UNIVERSIDAD POLITÉCNICA DE MADRID
Escuela Técnica Superior de Ingeniería Aeronáutica y del Espacio

Aeroelastic Analysis and Stability of a Hose-Drogue System with Aerodynamic Grid Fins for Aerial Refueling

D O C T O R A L T H E S I S

Submitted for the degree of Doctor by:

Andrés Keyvan Salehi Paniagua
MSc. in Aeronautical Engineering

Madrid, 2024

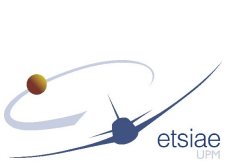


UNIVERSIDAD POLITÉCNICA DE MADRID
Escuela Técnica Superior de Ingeniería Aeronáutica y del Espacio

Doctorado en Ingeniería Aeroespacial

Aeroelastic Analysis and Stability of a Hose-Drogue System with Aerodynamic Grid Fins for Aerial Refueling

D O C T O R A L T H E S I S

Submitted for the degree of Doctor by:

Andrés Keyvan Salehi Paniagua
MSc. in Aeronautical Engineering

Under the supervision of:
Dr. Pablo García-Fogeda Núñez

Madrid, 2024

Title: Aeroelastic Analysis and Stability of a Hose-Drogue System with Aerodynamic Grid Fins for Aerial Refueling

Author: Andrés Keyvan Salehi Paniagua

Doctoral Programme: Doctorado en Ingeniería Aeroespacial

Thesis Supervision:

Dr. Pablo García-Fogeda Núñez, Full Professor, Escuela Técnica Superior de Ingeniería Aeronáutica y del Espacio, Universidad Politécnica de Madrid(Supervisor)

External Reviewers:

Thesis Defense Committee:

Thesis Defense Date:

Sciencia Potentia est

Contents

Acknowledgement

No ha sido fácil resumir años de trabajo en un puñado de páginas, como tampoco lo es expresar, en unas cuantas líneas, mi agradecimiento a todas las personas que de una forma u otra han contribuido a esta tesis doctoral. No obstante, intentaré hacerlo:

En primer lugar, a mi tutor, Pablo García-Fogeda, por su constante apoyo, guía y dedicación a lo largo de todos estos años. Le estaré eternamente agradecido por todo lo que me ha enseñado sobre aeroelasticidad, dinámica estructural, aerodinámica no estacionaria... Pero, sobre todo, le agradezco todo lo aprendido de él en lo referente a la ética profesional, al respeto por el conocimiento y a la forma de entender la docencia y la investigación, valores que siempre llevaré conmigo.

A mis compañeros de Unidad Docente: a Marcos Chimeno, quien (además de soportarme muchas horas todos los días) me ha enseñado y me sigue enseñando cómo ser un buen profesor y cómo enfrentar, con filosofía y tranquilidad, la infinita cantidad de problemas con los que nos encontramos. A Félix Arévalo, a quien debo en gran medida no solo la realización de esta tesis, sino también mi vocación por el mundo de la aeroelasticidad.

A todos mis compañeros de la ETSIAE, con quienes comparto el día a día y sin cuya compañía sería muy difícil mantener la energía y las ganas de enfrentar las crecientes dificultades del sistema universitario. Especialmente, quiero mencionar a Isma y a Víctor por su apoyo y amistad durante estos años.

Durante el año 2023 tuve la oportunidad de realizar una estancia en el Politecnico di Milano, una experiencia enriquecedora que me permitió abrir horizontes y conocer cómo se trabaja fuera de "casa". Estaré siempre enormemente agradecido a Sergio Ricci y a Francesco Toffol por su cálida acogida, así como a todas las personas que tuve la suerte de conocer durante esos meses. Grazie mille!

Fuera del ámbito profesional, no puedo dejar de mencionar a los amigos, sin cuya compañía muchas veces habría sido difícil seguir adelante: Rodri, Jaime, Luis, Jorge, Germán, César, Yago, Manu, Álvaro, Dani, Pablo, Domingo, Alan, Leo, Tamara, Ana... ¡y a todos los que me dejo!

Finalmente, a mi familia: a mi padre, a mi madre y a mis hermanas, por todo su apoyo y comprensión a lo largo de estos años. Espero que puedan sentirse un poco orgullosos de mí; yo, desde luego, me siento profundamente orgulloso de ellos.

Gracias a todos.
Madrid, octubre de 2024

Abstract

Aerial refueling extends the range, endurance and operational flexibility of military aircraft by allowing fuel transfer mid-flight from a tanker to a receiver aircraft. The hose-drogue system, one of the most widely used configurations for this purpose, relies on a flexible hose stabilized by a drogue at its end to guide the receiver aircraft during refueling. However, this setup is inherently susceptible to dynamic instabilities, particularly in turbulent or high-speed conditions, which can lead to severe oscillations, posing significant risks of structural failure and potentially jeopardizing the refueling operation.

The main purpose of this thesis is to develop a robust mathematical model to analyze the dynamic and aeroelastic behavior of the hose-drogue system, with a focus on identifying and characterizing its flutter boundaries. In addition, this study not only aims to provide the first in-depth flutter analysis for hose-drogue refueling systems but also proposes a method to improve stability by integrating a grid fins prototype attached at the hose-drogue junction. Grid fins consist of a lattice structure formed by a series of small aerodynamic surfaces arranged within a box-like frame, and their use has important advantages with respect to conventional planar fins.

The first stage of this research involves accurately characterizing the hose itself, as it is a complex structure with limited existing data. This characterization is achieved through static and dynamic tests, which provide key mechanical properties essential for the model's development. With these properties defined, a model for the hose-drogue system is developed, integrating both structural and aerodynamic considerations of the hose. This model enables the calculation of both the static equilibrium position of the system and its dynamic response to small perturbations. Using this foundation, a comprehensive aeroelastic analysis is conducted, allowing for the determination of flutter conditions, including speeds, frequencies, and modal shapes, under various flight conditions and hose configurations.

To assess the effect of grid fins, a detailed aerodynamic model is created, capturing both the steady and unsteady aerodynamic forces generated by these fins with a method based on a Doublet-Lattice code and the Unit-Grid Fin approach. Wind tunnel data is used to validate the steady-state forces. The grid fins are then integrated into the hose-drogue model. The enhanced hose-drogue-fins model allows for a comparative study of the aeroelastic behavior of the system with and without fins, illustrating how the inclusion of fins influences the flutter boundaries and stability margins of the system. This comparative analysis reveals that grid fins can significantly improve the stability of the system, thereby raising flutter thresholds.

Additionally, the study investigates the behavior of the system during the critical phase when the drogue makes contact with the receiver aircraft. While the primary analysis focuses on the flutter conditions of the free hose, understanding the dynamic response during contact is essential, as this phase is crucial for successful fuel transfer.

In summary, this thesis provides a novel, validated model for the analysis of the aeroelastic stability in hose-drogue refueling systems, with a specific focus on flutter conditions and the study of a new configuration with a grid fins prototype included. The results offer important insights into the role of aeroelastic interactions in refueling operations, potentially guiding the development of more resilient refueling systems and informing future studies into active control mechanisms, additional phases of the refueling process, and alternative stabilizing configurations.

Resumen

El reabastecimiento en vuelo extiende el alcance y la flexibilidad operativa de las aeronaves militares mediante la transferencia de combustible en vuelo desde un avión tanquero a una aeronave receptora. El sistema de cesta-manguera, uno de los más utilizados, emplea una manguera flexible estabilizada por una cesta en su extremo para guiar a la aeronave receptora durante el reabastecimiento. Sin embargo, este sistema es inherentemente susceptible a inestabilidades dinámicas, especialmente en condiciones de turbulencia o alta velocidad, lo que puede provocar oscilaciones severas que representan un riesgo de fallo estructural y comprometen la operación de reabastecimiento.

El principal objetivo de la tesis es desarrollar un modelo matemático robusto para analizar el comportamiento dinámico y aeroelástico de un sistema cesta-manguera, centrado principalmente en caracterizar sus condiciones de flameo. Asimismo, este estudio no solo pretende ofrecer el primer análisis profundo de flameo de sistemas cesta-manguera para reabastecimiento en vuelo, sino también proponer un método para mejorar la estabilidad del sistema mediante la integración de un prototipo de aletas tipo rejilla. Estas aletas consisten en una estructura formada por una serie de pequeñas superficies aerodinámicas, y su uso presenta importantes ventajas con respecto a las aletas planas convencionales.

La primera fase de esta investigación implica caracterizar con precisión la manguera, ya que se trata de una estructura compleja con datos muy limitados. Esta caracterización se logra mediante ensayos estáticos y dinámicos que proporcionan propiedades mecánicas esenciales para el desarrollo posterior del trabajo. Con estas propiedades definidas, se desarrolla un modelo para el sistema cesta-manguera, integrando tanto las consideraciones estructurales como aerodinámicas de la manguera. Este modelo permite calcular la posición de equilibrio estático del sistema y su respuesta dinámica ante pequeñas perturbaciones. Con estos resultados, se realiza un análisis aeroelástico exhaustivo para determinar las condiciones de flameo (velocidades, frecuencias y formas modales) bajo diversas condiciones de vuelo y configuraciones de manguera. Asimismo, se estudia el comportamiento del sistema durante la fase en la que la cesta hace contacto con el receptor. Aunque el análisis principal se centra en el flameo de la manguera libre, entender la respuesta dinámica durante el contacto es de gran importancia, ya que esta fase es crucial para el éxito de la transferencia de combustible.

Para evaluar el efecto de las aletas de rejilla, se crea un modelo aerodinámico detallado que incluye tanto las fuerzas aerodinámicas estacionarias como no-estacionarias generadas por estas aletas, mediante un método basado en un código Doublet-Lattice y el concepto de aleta de rejilla unitaria. Las fuerzas estacionarias se validan mediante datos experimentales de ensayos en túnel de viento. Las aletas se integran en el sistema cesta-manguera, creando una nueva configuración modificada de manguera-cesta-aletas. Este modelo mejorado permite un estudio comparativo del comportamiento dinámico y aeroelástico del sistema con y sin aletas, revelando que su inclusión puede mejorar significativamente el margen de estabilidad del sistema, retrasando la aparición de flameo.

En resumen, esta tesis proporciona un modelo novedoso y validado para analizar la estabilidad aeroelástica de los sistemas de reabastecimiento con cesta-manguera, con un enfoque específico en las condiciones de flameo y el estudio de una nueva configuración con un prototipo de aletas de rejilla. Los resultados ofrecen valiosas perspectivas sobre el papel de las interacciones aeroelásticas en las operaciones de reabastecimiento, lo que podría guiar el desarrollo de sistemas más resilientes y analizar futuros estudios sobre mecanismos de control activo, fases adicionales del proceso de reabastecimiento y configuraciones estabilizadoras alternativas.

List of Figures

List of Tables

Chapter 1

Introduction

1.1 Aerial refueling systems

Since the early days of aviation, fuel requirements represent one of the most critical factors both in design and during flight operations. The need for fuel not only serves as a primary source of energy for sustaining flight but also adds considerable weight, which affects the overall performance. In commercial aviation, given the typical size of the aircraft and design considerations, carrying large quantities of fuel onboard is generally manageable and does not pose significant challenges. However, in military fighter aircraft designed for extended-range missions, fuel requirements can become a major limiting factor, constraining mission capabilities and operational performance.

While one potential solution is the use of auxiliary fuel tanks which can be configured in various ways, these tanks come with notable drawbacks: the additional weight and drag introduced increase the fuel consumption, decrease the maneuverability, and reduce the aircraft top speed. Furthermore, even with extra fuel storage, fighter aircraft may still lack sufficient range for long-distance missions. Consequently, the only feasible solution for extending mission range for the aircraft is to receive additional fuel during flight.

The process of transferring fuel from one aircraft - the tanker -, to another - the receiver -, during the flight is referred as Aerial Refueling, or Air-to-Air Refueling, and is the most effective method of increasing the endurance and range of aircraft. Although its development and use have grown exponentially since the late years of the last century and the early years of the current one, the first ideas about performing aerial refueling are almost as old as the earliest powered flights. The concept of aerial refueling has a history spanning over 90 years, with its roots dating back to World War I. During this war, pilots experienced a significant decrease in combat effectiveness due to the limited endurance of fighter aircraft, highlighting the need for a refueling system that could extend flight duration's without requiring a return to base. The idea of transferring fuel from one aircraft to another while in flight was conceived as a solution.

The first practical steps towards aerial refueling were taken in 1917 by Russian-American engineer Alexander de Seversky [Thomas et al., 2014], who envisioned the concept. This was followed by experimental demonstrations in the 1920s, involving a 15-meter rubber hose and manual flow valve. However, the first successful aerial refueling was accomplished

on June 27, 1923, by Captain Lowell Smith and Lieutenant John P. Richter of the United States Army Air Service. Using a pair of Airco DH-4B biplanes (see Figure 1.1), they manually trailed and coupled a refueling hose mid-air, marking a significant milestone [Nawrocki, 1996]. This achievement was soon followed by an endurance record in August 1923, when a DH-4B remained airborne for over 37 hours through nine mid-air refuelings, demonstrating the potential of aerial refueling.

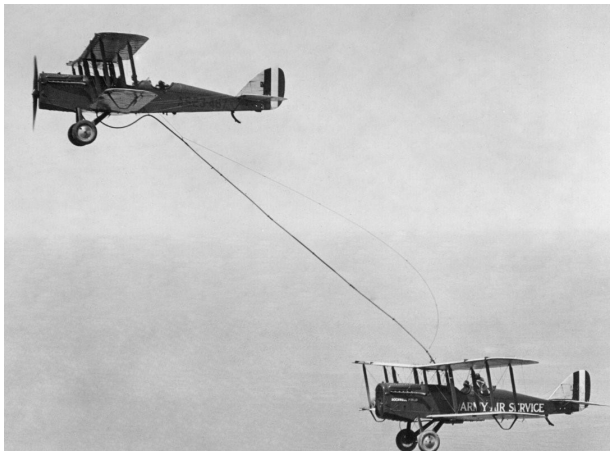

Figure 1.1: First aerial refueling process.

Throughout the late 1920s and 1930s, the technology advanced significantly [Smith, 1998]. Key developments included the creation of spill-free nozzles by Fred and Al Key in 1935, which improved the safety during the process. These innovations led to the establishment of Flight Refuelling Ltd (FRL) by Sir Alan Cobham in 1934, which played a pivotal role in the evolution of aerial refueling technology. Cobham's Grappled-Line Looped-Hose system, developed around 1934, allowed a receiver aircraft to trail a steel cable that could be grappled by a line shot from the tanker, see Figure 1.2. Once connected, the tanker would climb above the receiver to allow fuel to flow under gravity. Originally intended for long-range commercial flights, this system later became exclusively used in military applications.

Figure 1.2: Grappled-Line Looped-Hose Air-to-Air Refueling in 1935.

The outbreak of World War II temporarily interrupted experimentation with aerial refueling. However, post-war efforts resumed, and the Grappled-Line Looped-Hose system was successfully deployed, notably facilitating the first non-stop around-the-world flight in 1949 by the B-50 Superfortress "Lucky Lady II". Recognizing the limitations of the looped-hose system, FRL began developing the Probe and Drogue Refueling (PDR) system in 1948, an advancement that revolutionized aerial refueling practices. The PDR, along with the Boom Receptacle Refueling (BRR) system, became primary methods for

aerial refueling. The PDR was the first system used in combat during the Korean War in the 1950s, mainly in refueling F-84 fighter-bombers.

Figure 1.3: KB-29P from the 91st Air Refueling Squadron, Barksdale Air Force Base, La.

Aerial refueling has since been continuously refined and employed in endurance flights. However, while it has become a crucial capability for military aviation, for the moment it has never reached commercial aviation. Nonetheless, the technological advancements made since its inception have laid the foundation for modern aerial refueling practices, ensuring that aircraft can achieve extended flight times and operational ranges. In recent years, the interest in Autonomous Air-to-Air Refueling (AAAR) has grown due to ongoing research into Unmanned Aerial Vehicles (UAV). The development of AAAR has become increasingly important as UAVs are expected to perform many of the same functions as manned aircraft, including extended range and endurance capabilities provided by in-flight refueling [Thomas et al., 2014]. The emergence of UAVs has driven a resurgence of interest in aerial refueling, prompting numerous programs and advancements aimed at automating the refueling process. This has led to a wealth of research and academic publications addressing the theoretical and practical aspects of AAAR, covering aircraft control, sensor systems, and their integration. To support these efforts, simulation models have been developed with varying levels of fidelity, from simple parameterized representations to complex physical models that account for aircraft dynamics, aerodynamic disturbances, atmospheric effects, and refueling apparatus interactions.

Figure 1.4: MQ-25A Unmaned Aerial Tanker refuels Super Hornet.

Significant milestones in AAAR have been achieved in recent years. The first successful in-flight refueling of a UAV occurred on April 22, 2015, when Northrop Grumman and the United States Navy demonstrated full PDR using an X-47B UAV [Ren and Quan, 2024]. This pioneering achievement sparked new advancements in autonomous refueling technology. On May 9, 2017, Airbus Defence and Space conducted the first autonomous refueling demonstration using a flying boom system, successfully refueling a fighter aircraft.

Figure 1.5: Airbus A310-MRTT refueling using the PDR system.

The development of dedicated unmanned tanker aircraft has further advanced AAAR capabilities. A notable breakthrough was the introduction of the Boeing MQ-25 Stingray, the first operational unmanned tanker aircraft, which has been in service with the United States Navy since June 2021. The MQ-25 T1 is capable of refueling various combat jets, including the F/A-18 Super Hornet and F-35C fighters, using the PDR system. Additionally, recent AAAR initiatives have continued to push the boundaries of autonomous refueling. In November 2023, Airbus's Auto'Mate A4R AAAR program conducted its second flight test campaign, successfully simulating a refueling operation with five unmanned Airbus DT-25s, guided by Artificial Intelligence under the control of an A310 MRTT tanker. These advancements underscore the rapid evolution and growing capabilities of AAAR, setting the stage for fully autonomous refueling operations in the near future.

Future prospects for aerial refueling indicate sustained growth in the adoption of these systems. The global aerial refueling market is forecast to reach 781.2 millions of dollars in 2033, with a compound annual growth rate of 3.28% from 2023 to 2033 (data extracted from *https://www.sphericalinsights.com/reports/air-refueling-market*). As part of broader military initiatives of modernization, numerous countries are upgrading their aerial refueling capabilities. This includes fleet upgrades, investments in advanced technologies and the acquisition of new tanker aircraft. Key drivers for this demand include the need to support long-range missions and expeditionary operations, along with the aging tanker fleets for several countries. Figure 1.6 shows the growth expectation of the global aerial refueling market in the next decade.

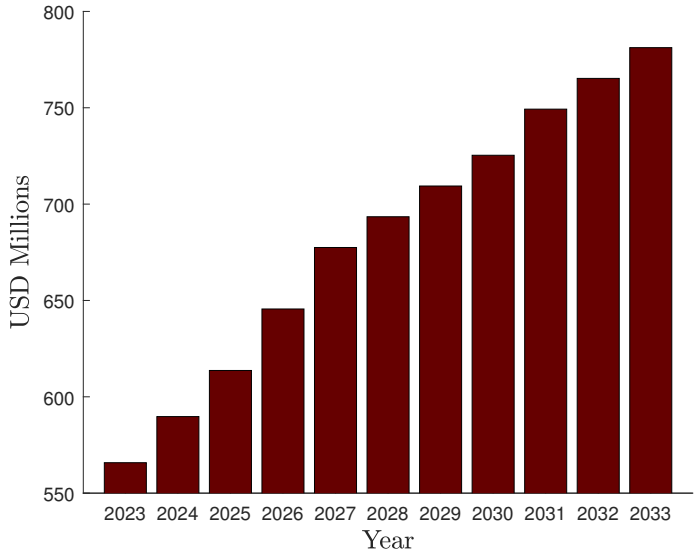

Figure 1.6: Growth expectation of the global aerial refueling market. Extracted from *www.sphericalinsights.com*

Although the evolution of aerial refueling is extensive, encompassing numerous trials, methods, and configurations, it is worth noting that from the outset, efforts in aerial refueling have focused on refining two main systems: the boom receptacle refueling system and hose and drogue system. These systems have been continuously improved to enhance their safety, efficiency, and compatibility with evolving aircraft technologies.

The flight boom system (see Figure 1.7) consists on using a fixed pole (or boom) between the tanker and the receiver to transfer fuel. The boom is guided by an operator in coordination with the tanker pilot to make a connection with the receptacle on the receiver aircraft. Due to its stiffness, the boom system offers a relatively fast fuel transfer. However, it has significant limitations, generally related to its low adaptability to different types of aircraft. On contrast, the hose and drogue system (see Figure 1.8) consists on using a trailing hose with a drogue at the end. The tanker aircraft deploys the hose behind it, with the drogue (typically a cone whose drag keeps the hose in a stable position) at the end. The receiver aircraft approaches the drogue with a probe, which is inserted into the drogue to connect the fuel systems [Zhu, 2008]. The hose is retracted when not in use, and its retraction is easier compared to the flying boom. The main advantage of this method is its easier adaptation, making it more suitable for use with different aircraft designs.

Figure 1.7: Aerial refueling process with flying boom system. Extracted from [Sahin, 2010].

Figure 1.8: Aerial refueling process with hose and drogue system. Extracted from *Naval Aviation News*.

Comparing both refueling systems, the flying Boom, known for its larger size, weight, and cost, contrasts sharply with the lighter and more versatile hose-drogue system. The rigid, telescoping boom design requires substantial infrastructure and specialized equipment, whereas the simplicity of the hose system makes it a more cost-effective option that can be easily integrated into a wide range of aircraft with minimal modifications. Operationally, the Boom system is limited to refueling one aircraft at a time, while the hose-drogue system allows for multiple hoses to be deployed simultaneously from a single tanker, enabling the refueling of several aircraft in one mission. This capability gives the hose-drogue system a significant advantage in scenarios requiring rapid refueling of multiple aircraft.

While the Boom system offers precise maneuvering and alignment during refueling, using controllable flaps to counteract aerodynamic disturbances and enhance stability, the hose-drogue system extends its versatility by being able to refuel helicopters — a capability not supported by the BRR system. This makes the hose-drogue system suitable for a broader range of aircraft types and mission profiles. The workload distribution also differs between the two systems. Boom operations distribute the workload between the receiver pilot and the boom operator, allowing for efficient and coordinated refueling. In contrast, the hose-drogue system demands greater pilot effort, as the receiver must accurately guide its probe into the drogue, adding complexity and potentially reducing efficiency compared to the more controlled boom operation. Table 2.1 extracted from [Thomas et al., 2014] summarizes these main differences between the flying boom and the hose-drogue systems.

Table 1.1: Comparison of flying boom and hose-drogue refueling systems, from [Thomas et al., 2014].

Flying boom system	**Hose and drogue system**
Larger size, weight and cost	Light and compact
Restricted to unary servicing	Multiple systems operable on one tanker, simultaneous servicing
Controllable via flaps	Passive, more susceptible to aerodynamic disturbances
Can use a boom-drogue adaptor to refuel probe-mounted receivers	Restricted to probe-mounted receivers
Not suitable for helicopters	Low speed drogues can be used to refuel helicopters
Workload is shared between receiver pilot and boom controller	Substantial pilot workload required to capture the drogue

In this thesis, the refueling process studied will be with a hose-drogue system. This type of aerial refueling operation involves several sequential steps, each with specific requirements and challenges to ensure a safe and efficient refueling process [García-Fogeda et al., 2018]. The operation can be divided into the following phases:

- **Initial Tanker Stabilized Flight Condition**: The operation begins with the tanker aircraft reaching a steady flight condition suitable for refueling. This involves stabilizing the tanker at a constant speed and altitude to create a predictable and controlled environment for the receiver aircraft. Light to moderate turbulence conditions are usually acceptable, but severe turbulence could pose a safety risk and make the process unfeasible.

- **Hose Deployment Phase**: Once the tanker is stabilized, the mission systems operator starts the deployment of the hose. This part of the process consists on extending the hose from a storage drum within the tanker pod. A control system manages the extraction rate of the hose, which is driven by an electric or hydraulic motor. The deployment rate is carefully regulated to prevent excessive oscillations or tangling of the hose. The conical drogue, situated at the end of the hose, acts as an aerodynamic stabilizer by creating drag, which helps keep the hose in a relatively steady position.

- **Pre-Contact Hose-Deployed Condition**: In this phase the hose is fully deployed but before the contact between the drogue and the receiver aircraft. However, this is an important phase of the process, as after the hose is fully deployed, the system usually experiences transient oscillations as it seeks to reach a stable equilibrium position. These oscillations can arise from several sources, like tanker rigid body motion, wake or atmospheric turbulences... The hose and drogue system must dampen these oscillations to reach a steady-state equilibrium position before the receiver aircraft approaches for refueling. The ability of the hose-drogue system to stabilize quickly is critical to minimizing the waiting time and ensuring safe coupling. Additionally, in this phase, stability issues can arise from the equilibrium position that the system reaches before contact occurs.

- **Drogue-Receiver Contact**: Once the hose and drogue system has achieved a

stable position, the receiver aircraft is cleared to approach. The receiver pilots must carefully align the probe on their aircraft with the drogue. This step requires precise control, as the probe must be guided into the drogue to establish a secure connection. When the probe successfully couples with the drogue, the fuel transfer can commence. Throughout this phase, any sudden movements by the tanker or receiver, or unexpected turbulence, can complicate the connection process, requiring the receiver to abort and retry.

The entire refueling procedure involves complex interactions between the aircraft and the environment. Ensuring safe and efficient operations requires thorough understanding and management of these factors. Various studies may be conducted to improve the process, including aerodynamic analysis to optimize drogue stability, aeroelastic evaluations to assess hose dynamics, and even economic feasibility studies to determine cost-effectiveness for different aircraft and mission profiles. As will be discussed in the following sections, this thesis primarily focuses on the dynamic and aeroelastic analysis of the aerial refueling system. It is crucial to emphasize this scope because, as highlighted throughout this chapter, the process of aerial refueling can be studied and approached from various perspectives, each with different objectives and methodologies. However, before starting with the specific aims of the thesis, it is essential to provide an overview of recent advancements in aerial refueling technology.

The development of new automated aerial refueling models, coupled with the ongoing need to execute the refueling process as quickly and precisely as possible, has necessitated the introduction of certain external control systems. These systems, which operate independently of the refueling components themselves (such as the hose and drogue), are designed to enhance the stability of the operation. Additionally, the evolution of long-endurance unmanned aerial systems has further driven the demand for AAAR methods explained previously. Conventional drogues, when exposed to non-uniform wind conditions or atmospheric turbulence while the receiver aircraft approaches, often exhibit high disturbances and instabilities, which can lead to mission failure. To address these challenges, several stabilization methods have been proposed over the past decade.

Many of these methods focus on the design and development of controllable drogues in order to minimize the motion induced by atmospheric disturbances. Notable research in this area includes the works of [Kuk and Ro, 2013], [Ro and Kamman, 2009], [Williamson et al., 2010] or [Yuan et al., 2017], who have explored various approaches to mitigate drogue instability (In Chapter 2 all of these references will be mentioned again and explained with more details). Alternatively, other studies have investigated the use of reel systems integrated into the refueling pod to improve stability, as proposed by [Vassberg et al., 2003]. There has also been significant research into the implementation of automated control surfaces to stabilize the drogue. For instance, [García-Fogeda et al., 2018] explores the use of small aerodynamic surfaces to generate corrective forces, thereby enabling the drogue to maintain a stable position in the presence of external perturbations. These efforts aim to reduce the adverse effects of atmospheric disturbances and improve the overall reliability of the refueling process.

Building on many of these previous studies and with the aim of presenting and analyzing a control system that has not been previously applied in aerial refueling, this thesis introduces a novel approach by integrating a grid fins prototype at the junction between

the hose and the drogue.

1.2 Grid fins

Grid fins (also known as lattice fins) have emerged as a widely used non-conventional aerodynamic control surface in missiles and rockets. These fins consist of a lattice structure formed by a series of small aerodynamic surfaces arranged within a box-like frame. Grid fins have several advantages with respect to conventional planar fins, including a shorter chord length that enables them to be folded along the missile body, resulting in a lower hinge moment, a higher stall angle of attack, and a very high strength-to-weight ratio. However, grid fins also have some disadvantages, including increased drag and reduced efficiency specially at transonic speeds [Washington and Miller, 1993], [Washington and Miller, 1998].

The origins of grid fins can be traced back to the 1970s, when they were first introduced in Soviet ballistic missiles. The earliest extensive study of grid fins was published in the 1980s by Sergey Belotserkovsky, who presented a comprehensive research on their aerodynamic properties, structural behavior, and manufacturing characteristics [Belotserkovsky et al., 1985]. The aerodynamic performance of grid fins has been the main subject of extensive research since the 1980s, starting by the U.S. Army Missile Research and Development Center (MRDEC) in Huntsville, Alabama [Washington and Miller, 1993]. These studies have highlighted some of the advantages of grid fins over planar fins. Grid fins maintain lift at higher angles of attack due to their distinct stall characteristics and produce much smaller hinge moments, allowing for the use of smaller control actuators. Their ability to fold against the missile body provides a storage advantage, although they generally exhibit higher drag compared to planar fins. Techniques for reducing drag through modifications to the grid fin frame's cross-sectional shape have been investigated to address this drawback. Since then, grid fins have become a conventional control device in the missile industry and have been the subject of intensive research worldwide, particularly throughout the 1990s as their use expanded across various missile and rocket systems.

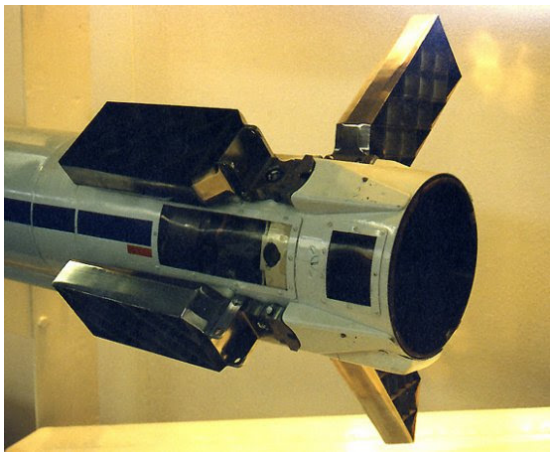

Figure 1.9: Massive Ordnance Air Blast bomb equipped with grid fins, extracted from *santoshaerospace.blogspot.com*.

Initially, grid fins were utilized as air brake systems, especially by the Soviets on the Soyuz launch escape spacecraft. However, their use as control surfaces has since gained

prominence. Well-known applications include the U.S.-developed "Massive Ordnance Air Blast (MOAB)" bomb and the Russian-made "Vympel R-77" air-to-air missile (see Figures 1.9 and 1.10). More recently, grid fins have been even adopted by SpaceX on the Falcon 9 reusable launch vehicle, where they function as maneuvering surfaces during the final reentry stage.

Figure 1.10: Grid fins prototype at the Vympel R-77 missile.

In high-speed agile missiles, such as air-to-air missiles, aerodynamic control surfaces are exposed to significant forces and moments throughout the flight envelope, posing challenges in structural design. The need for lower hinge moments, effective control within the flight regime, and compact packaging due to carriage constraints makes grid fins an ideal choice for these applications. Their shorter chord length minimizes variation in the center of pressure, resulting in reduced hinge moments. Additionally, grid fins possess superior lift and stall characteristics, enhancing a missile's control capabilities. Their lattice structure also provides a high strength-to-weight ratio, enabling the fins to withstand substantial aerodynamic forces, while their foldable design facilitates efficient storage along the missile body.

Figure 1.11: Folding grid fins of the R-77, extracted from *santoshaerospace.blogspot.com*.

Chapter 2 will provide a comprehensive review of the state of the art in studies focused on the aerodynamics of grid fins. As will be discussed, numerous research efforts have investigated various configurations, applications, and methods for determining the aerodynamic forces associated with grid fins. These approaches range from panel-based methods and Computational Fluid Dynamics (CFD) techniques to semi-empirical models correlated

with experimental data.

It is worth noting that the computation of the aerodynamic forces for this type of fin is complex, and a significant portion of grid fin prototype development is dedicated to accurately characterizing these forces. In this thesis, a grid fin model will be employed for integration into the aerial refueling system, making the aerodynamic characterization of the fins one of the key aspects of the research. Understanding and accurately predicting the aerodynamic behavior of the grid fins will be crucial for the successful implementation of the refueling system.

1.3 Objectives of the thesis

The main objective of this thesis is to develop a model for analyzing the aeroelastic behavior of an aerial refueling system based on a hose-drogue configuration. This analysis will be focused on the flutter conditions of the system: Among the phenomena associated with fluid-structure interaction problems, flutter is arguably the most significant instability, as well as the most challenging to predict. Flutter is a self-excited vibration in which the structure extracts energy from the external flow. If the energy supplied by the flow exceeds the system's dissipation capacity, this can result in an unstable motion that ultimately leads to structural failure [Fung, 1993]. The flutter analysis of hose-drogue systems has not been previously studied, making the findings of this research potentially valuable for understanding the fluid-structure instabilities of these processes. As previously explained, the refueling system can become unstable without a control mechanism, potentially jeopardizing the refueling operation. Thus, a grid fin model will be incorporated into the hose-drogue system to enhance stability. This thesis will therefore examine the aeroelastic behavior of the hose-drogue system both with and without grid fins, allowing for a detailed analysis of how the inclusion of grid fins affects system stability. However, this primary objective necessitates defining a series of secondary requirements or objectives to enable this comprehensive analysis.

To accurately study and analyze the system, it is essential to determine certain key properties of the hose-a complex structure for which detailed information is not readily available. Therefore, the first step before analyzing the behavior of the system will be to characterize several key mechanical properties of the hose. This will involve conducting two tests on a real sample of the hose: a static tension test and a vibration test. Results of these tests will allow to reliably estimate some mechanical properties of the hose, which are not easily calculated or obtained from existing studies but are essential for developing the model proposed in this thesis.

To perform the aeroelastic analysis of the hose-drogue system, a mathematical model that offers significant improvements over existing studies will be developed. This model will enable an in-depth study of the system during the refueling phase with the hose fully deployed, both before and during contact between the drogue and the receiver. Using this model, the static equilibrium position of the system will be first determined. Then, the dynamic properties will be obtained by solving the unsteady problem of small perturbations relative to this equilibrium position. In this way, both the static and dynamic behavior of the hose-drogue system will be studied, as well as the influence of various

parameters.

With the developed static and dynamic model, the aeroelastic stability of the hose-drogue system will be analyzed. The flutter boundaries of the system will be determined, which will show significant differences from the classical wing flutter. Additionally, the influence of numerous parameters on the flutter conditions will be examined. As the aeroelastic flutter analysis for this type of system is entirely novel, this study will provide valuable insights into potential instabilities arising from fluid-structure interactions during the refueling process.

Although the main goal is the aeroelastic study of the system, conducted during the phase when the hose is fully deployed and before fuel transfer begins, the developed model also enables an analysis of response of the system to the drogue-receiver contact — when the drogue couples with the receiver aircraft to initiate fuel transfer. Therefore, another objective of this research will be to examine how this contact between the drogue and the receiver may impact in the hose.

Once the hose-drogue system has been studied, the next step will be to analyze the inclusion of the fins model and the behavior of the new hose-drogue-fins configuration. However, a proper aerodynamic characterization of the fins is required beforehand. Therefore, using a model specifically developed to calculate aerodynamic forces on grid fins, both steady and unsteady forces will be obtained and analyzed. For the steady forces, wind tunnel test data will be available to validate the model.

With the aerodynamic forces on the fins determined, the analysis of the new hose-drogue-fins configuration can be conducted. The goal will be again to obtain the flutter conditions of this new setup and examine how the fins influence the aeroelastic stability of the system. This analysis will follow the same procedure used in the flutter study of the system without fins, first calculating the steady-state configuration of the complete system, then examining its dynamic behavior, and finally determining the flutter conditions.

It is important to mention that some parts of the model analyzed and developed in this thesis originates from the HDA3R project, a collaboration between the Polytechnic University of Madrid and Airbus Defence and Space. Although this will be referenced throughout the work, certain calculations and studies in this thesis were made possible by the data provided through this project. In particular, the hose sample used in the mechanical property characterization tests and the static wind tunnel test data for the fins prototype were supplied by this collaboration.

1.4 Thesis Outline

Based on the objectives presented previously, this thesis is organized into seven chapters, mainly grouped in two different parts. These two parts represent the main topics of the conducted research: the analysis of the hose-drogue model (Chapters 3 and 4) and the study of the hose-drogue-grid fins model (Chapters 5 and 6). A brief chapter-by-chapter summary is presented below. In addition, Figure 1.12 shows a flowchart of the general

scheme of the thesis chapters.

Chapter 2 provides a review of the existing state of the art in the two main topics addressed in this thesis: the dynamic study of an aerial refueling process with a hose-drogue system and the aerodynamic characterization and behavior of the grid fins. The main works in these fields will be presented in chronological order, highlighting how they have contributed to the development of the model proposed in this thesis.

Chapter 3 presents the hose characterization tests: it covers the development and results of the two tests conducted on a hose sample—a static tensile/compression test and a dynamic vibration test.

In Chapter 4 the hose-drogue model is fully developed: The mathematical model of the system is presented, including the derivation of both structural and aerodynamic forces on the hose, the static and dynamic problems, the aeroelastic analysis, and finally, the system's response to drogue-receiver contact.

Chapter 5 introduces the grid fins prototype used in the thesis: its main parameters and its geometry, and the obtention and computation of the steady and unsteady aerodynamic forces generated by the fins.

With the validated and developed hose-drogue model and grid fin model, in Chapter 6 the new hose-drogue-fins configuration is implemented. The process will follow a similar approach to that in Chapter 4, including mathematical modeling, static and dynamic analysis, and, finally, the aeroelastic study. Throughout this development, emphasis will be placed on the differences that arise when grid fins are included in the aerial refueling system.

Chapters 7 and 8 concludes discussing how the main contributions pursue the main objective of the thesis, suggesting in addition possible future works for all the topics covered.

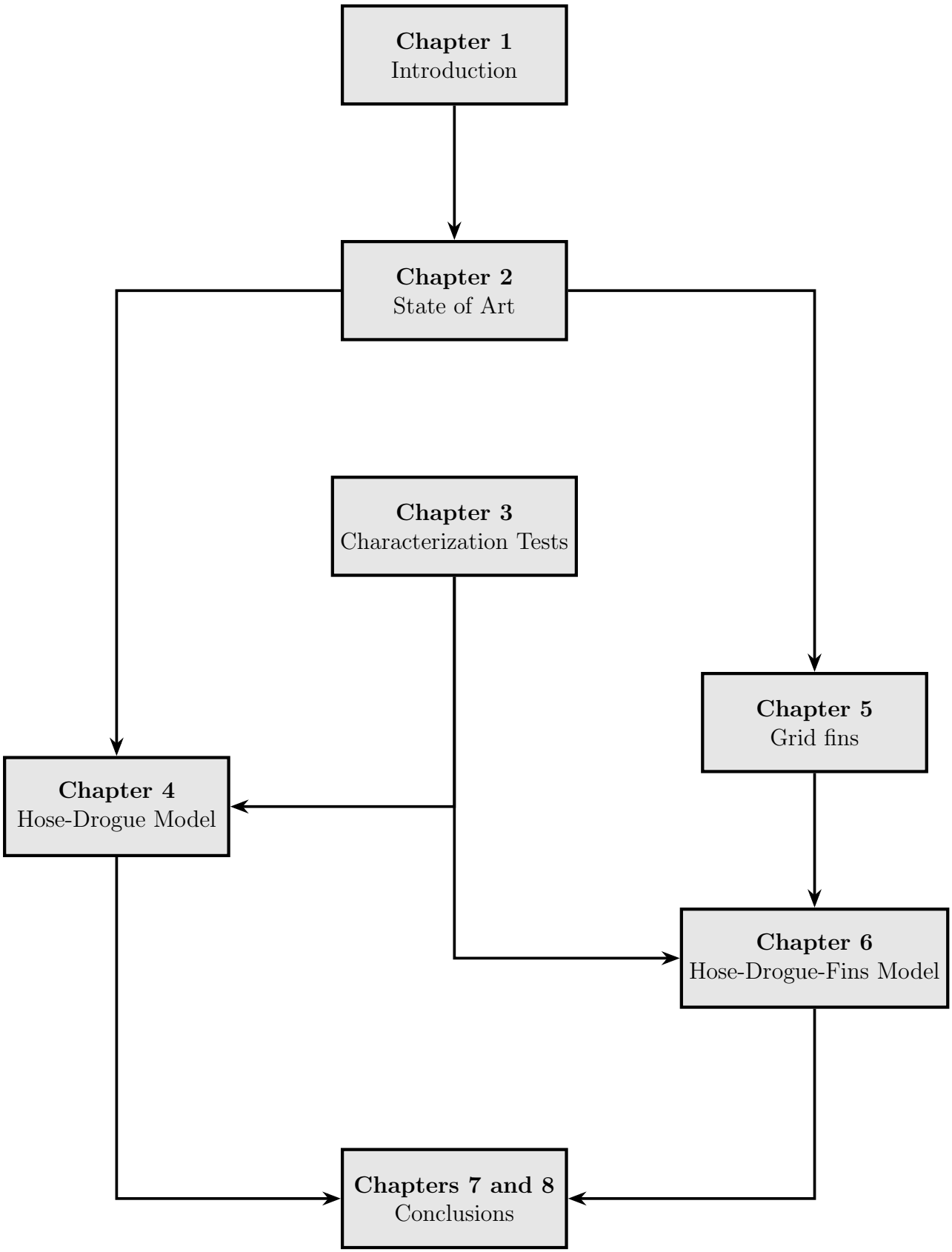

Figure 1.12: General scheme of the thesis.

Chapter 2

Literature Review

Once the focus and primary objectives of this thesis have been established, this chapter will present a review of the existing state of the art in the field of the work. Although this thesis covers a wide range of topics and technical disciplines, this review will be focused on the two main topics of the thesis: the modeling of an aerial refueling system with the hose-drogue (Section 2.1) and the aerodynamic behavior of grid fins (Section 2.2). In both sections, the most influential references in the development of the thesis models will be highlighted and explained.

It is important to note that not all references used in this thesis will appear in the literature review. As explained, only those focused on the two main topics are included here. However, throughout the development of the thesis document in subsequent chapters, various subjects (such as aeroelasticity, modal analysis, unsteady aerodynamics, etc.) will be addressed, incorporating additional key references that contributed to the construction of the thesis models.

In both sections (refueling with hose-drogue and grid fins), an explanatory summary of the main references and their focus areas will be provided, followed by a chronological list of all relevant references, highlighting each one's primary contribution to the field of study.

2.1 Hose-drogue refueling systems

As presented in Chapter 1, the evolution of aerial refueling processes spans the last hundred years. However, focusing specifically on the modeling of hose-drogue systems, the development of all relevant works dates back to the late 20th century and primarily the 21st century.

Numerous studies and research lines have focused on various aspects of hose-drogue systems in aerial refueling. One of the pioneering initiatives is [Eichler, 1978], which provides an early model for analyzing the static stability of the hose-drogue system during refueling, marking a foundational contribution to understanding refueling dynamics. This study set the groundwork for analyzing stability in varying aerodynamic conditions. Complementing this foundational work, more recent studies, such as [Bloy and Khan, 2002] or [Zhu,

2008], analyze the dynamic response of hose-drogue systems under operational conditions, investigating how oscillations and aerodynamic loads influence the system's performance. Other pioneering works in the analysis of hose-drogue refueling include [Bloy and Trochalidis, 1989] and [Bloy and Trochalidis, 1990], which focus on modeling the dynamic interactions between the tanker and receiver aircraft throughout the refueling process.

In parallel, specific studies address reel mechanisms or other strategies to control the hose tension, which could be crucial for stability during contact. Works by [Vassberg et al., 2003] and [Ribbens et al., 2012] incorporate reel dynamics to adjust hose tension in response to environmental and operational changes, a feature that enhances stability and safety by preventing hose whip or sudden motion. This approach is further developed in [Wu et al., 2003], where nonlinear vibrations in cable systems are analyzed, which can be applied to the aerial refueling field. Extending the complexity, studies like [Yamashiro et al., 2011] incorporate nonlinear effects to model hose response under large deformations, offering a more accurate representation of the hose behavior. For a comprehensive overview of the advancements and state of the art in aerial refueling, [Thomas et al., 2014] provides a thorough review, highlighting the evolution and technical progress in AAR systems and methodologies.

As explained during Chapter 1, an aerial refueling process with hose-drogue can be divided in four phases: stabilized flight, hose deployment, hose-deployed phase and the drogue-receiver contact. In the third phase, stability is critical, as it determines the likelihood of a successful attachment. Given the challenges associated with this phase, recent studies have proposed various strategies for controlling both the drogue and the hose after deployment. Studies by [Williamson et al., 2010], [Ro et al., 2010], and [Kuk and Ro, 2013] present methods for automatic control of the refueling drogue, with [García-Fogeda and Arévalo, 2015] and [García-Fogeda et al., 2018] exploring an active control strategy that uses automatic control surfaces to enhance drogue stability. Another works addressing this aspect includes [Dai et al., 2016], which examine oscillatory motion in worst-case scenarios involving environmental turbulence. Meanwhile, [Goyal and Perkins, 2007] uses a hybrid rod-catenary model to capture hose dynamics under low- and high-tension conditions, offering a computationally efficient way to assess stability and mitigate whip effects. Despite the importance of aeroelastic effects in AAR systems, limited research exists in this area, with [Erickson and Richards, 2019] being one of the few studies to analyze aeroelastic hose behavior under high-tension and whipping conditions.

Various models for hose-drogue systems have incorporated different dynamic effects to capture the system's complex behavior accurately. The foundational model by [Eichler, 1978] considers the hose under tension without bending or damping effects, establishing a simplified framework for initial analysis. Later, [Bloy and Khan, 2002] extends this work by including induced fluid perturbations from both the tanker and receiver, offering a more comprehensive understanding of static stability. Building on previous models, [Ro and Kamman, 2009] and [Ro et al., 2010] present a dynamic representation using rigid links connected by ball-and-socket joints, accounting for external forces such as tanker wake effects and receiver forebody aerodynamics, which are essential for real-time operational accuracy.

Several researchers, including [Yamashiro et al., 2011], have investigated hose dynamics

under large displacement scenarios, using Finite Element Methods frameworks and providing detailed insights into nonlinear hose behaviors. The work of [Zhu and Meguid, 2006, Zhu and Meguid, 2007, Zhu, 2008] employs finite element modeling, introducing a three-noded beam element to capture the flexibility and response of the hose under various operational loads. Additionally, [Meng and Chen, 2012] applies vortex-induced vibration principles from marine riser dynamics to address fatigue and stability challenges in aerial refueling hoses, particularly under high-tension scenarios.

Research also extends to drag and aerodynamic effects, which will be crucial for AAR. In [Vachon and Ray, 2004], drag variations in refueling assemblies are quantified, providing essential data for precision drag modeling in autonomous systems. In [Ng and Tan, 2009] simulations of transient fuel behaviors and pressure variations are presented, enhancing safety and reliability by identifying critical pressure points in the refueling phase. Furthermore, historical development and standardization of hose-drogue systems are detailed in [Purdy, 2010], which highlights NATO standards that ensure compatibility across various aircraft types, solidifying the hose-drogue method's role in both military and civil aviation.

Autonomous Aerial Refueling (AAAR) and UAVs, as explained in Chapter 1, present specific challenges. [Jackson et al., 2007] validates downwash effects through flight tests, contributing data crucial for developing UAV-specific docking protocols. Additional works by [Fravolini et al., 2004] or [Hansen et al., 2004] investigates effects such as drogue response under various flight conditions, enhancing control strategies for UAV refueling adaptations. In related research, [Thomas et al., 2014] and [Fezans and Jann, 2017] review technological advancements in autonomous docking, emphasizing challenges in control system development and aerodynamic modeling for precision refueling. Other works focused on AAAR control strategies include [Xun and Xinguo, 2013] and, more recently, [Hao and Quan, 2021]. Moreover, in recent years there are some works which start to focus on new techniques such as the machine learning approaches to control the refueling process, see [Wang et al., 2017] or [Dai et al., 2018].

In addition, recent studies start to explore energy-efficient civilian refueling models. The cruiser-feeder concept developed by [Price et al., 2014] suggests a 14% fuel reduction by enabling mid-flight refueling for larger aircraft, which could enhance environmental efficiency.

All of the mentioned articles together with some others relevant in the same field are presented at Table 2.1 organized chronologically with the year and with a concise summary of each article contribution. As demonstrated, in the aerial refueling field, the majority of studies focusing on the dynamic behavior of hose-drogue systems have been published primarily since the start of the 21st century. This trend indicates that the analysis and understanding of hose-drogue dynamics, essential for optimizing stability and reliability in refueling operations, is a relatively recent research area. Given the complex interactions of aerodynamic forces, turbulence, and mechanical control systems involved, this field presents significant opportunities for exploration. Future research can expand upon existing models, develop new control strategies, and further integrate autonomous capabilities, ensuring advancements in safety and efficiency for both manned and unmanned aerial refueling systems.

Table 2.1: Chronological review of relevant articles on aerial refueling with hose-drogue.

Year	Authors	Contribution
1978	[Eichler, 1978]	Analyzed the dynamics of a hose-drogue system.
1985	[Kamman and Huston, 1985]	Developed a model for low-tension cable dynamics.
1989	[Bloy and Trochalidis, 1989]	Study the receiver's stability during the refueling process.
1990	[Bloy and Trochalidis, 1990]	Analysis of the interference between tanker and receiver during the refueling process.
1995	[Bloy and Jouma'a, 1995]	Addressed stability and control in aerial refueling dynamics.
1999	[Koh et al., 1999]	Modeled low-tension cable dynamics in hose stability.
2000	[Gates and McCarthy, 2000]	Analyzed USMC tanker fleet needs with simulation models.
2001	[Bloy and Khan, 2001]	Modeled receiver aircraft wake effects for training simulations.
2003	[Vassberg et al., 2003]	Developed KC-10 hose whip control model for safety.
2003	[Wu et al., 2003]	Studied nonlinear vibrations in cables considering loosening.
2004	[Vachon and Ray, 2004]	Measured drag on refueling assemblies for better design.
2004	[Yamamoto et al., 2004]	Applied vortex dynamics to hose stability.
2004	[Fravolini et al., 2004]	Fuzzy sensor fusion for UAV docking in aerial refueling.
2004	[Hansen et al., 2004]	Flight test approach in UAV refueling systems.
2007	[Goyal and Perkins, 2007]	Modeled cable dynamics using rod and catenary elements.
2007	[Jackson et al., 2007]	Validated downwash effects for UAV refueling.
2007	[Zhu and Meguid, 2007]	Highlighted wave propagation's role in hose stability.
2007	[Khanafseh and Pervan, 2007]	Develop a model for GPS blockage caused by the tanker in autonomous refueling.

Continued on the next page

Year	Authors	Contribution
2008	[Zhu, 2008]	Recommended designs for short hoses prone to oscillations.
2008	[Dogan et al., 2008]	Modeling of wake-induced wind effects on a receiver in automated aerial refueling.
2009	[Ng and Tan, 2009]	Enhanced fuel behavior modeling for safety and reliability.
2009	[Ro and Kamman, 2009]	Modeled dynamic effects for UAV-specific refueling.
2010	[Purdy, 2010]	Documented probe-and-drogue system evolution and standards.
2010	[Williamson et al., 2010]	Enhanced drogue stability with adjustable LQR control.
2010	[Weinerfelt and Nilsson, 2010]	Simulated complex drogue dynamics in the refueling process.
2011	[Styuart et al., 2011]	Simulated hose whip, emphasizing robust probe design.
2012	[Meng and Chen, 2012]	Modeled fatigue in flexible hoses under high-tension.
2012	[Ribbens et al., 2012]	Improved hose whip control in probe-and-drogue refueling.
2013	[Kuk and Ro, 2013]	Tested drogue stability using aerodynamic surfaces.
2013	[Xun and Xinguo, 2013]	Efficient aerial refueling control method with a Kalman filter.
2014	[Thomas et al., 2014]	Reviewed autonomous refueling and docking challenges.
2014	[Wang et al., 2014]	Enhanced hose whip control using backstepping methods.
2014	[Price et al., 2014]	Proposed cruiser-feeder refueling for eco-efficiency.
2016	[Dai et al., 2016]	Modeled bow wave effects on drogue stability for UAVs.
2017	[Fezans and Jann, 2017]	Optimized automated refueling stability for UAVs.
2017	[He et al., 2017]	Developed control method for hose tension in complex refueling.
2017	[Yuan et al., 2017]	Reduced drogue swing with PID control in turbulence.

Continued on the next page

Year	Authors	Contribution
2017	[Wang et al., 2017]	Developed a robust method for real-time in autonomous aerial refueling..
2018	[Vess et al., 2018]	Validated simulation model for safer refueling operations.
2018	[García-Fogeda et al., 2018]	Enhanced drogue stability with automated control surfaces.
2018	[Dai et al., 2018]	Iterative learning control method in hose–drogue refueling.
2019	[Erickson and Richards, 2019]	Simulated aeroelastic hose behavior.
2021	[Hao and Quan, 2021]	Efficient rendezvous scheduling strategy for autonomous aerial refueling.
2024	[Ren and Quan, 2024]	Reviewed autonomy challenges in refueling technology.

2.2 Grid fins

As explained in Chapter 1, the concept of grid fins dates back to Soviet ballistic missiles developed in the 1970s. However, it was in the 1990s when grid fin studies began to proliferate for use in various missiles and rockets.

Focusing on the aerodynamics of grid fins, numerous studies have explored different configurations, applications, and methods for determining the aerodynamic forces. Analytical and empirical results for the aerodynamic coefficients of different grid fin configurations are presented in [Brooks and Burkhalter, 1989] and [Burkhalter and Frank, 1996]. These studies provided foundational data through wind tunnel and vortex theory approaches, respectively, enabling predictive models for control effectiveness at varying angles of attack. Additionally, experimental validations and comparisons with analytical and numerical methods appear in [Miller and Washington, 1994] and [Theerthamalai and Nagarathinam, 2006], demonstrating the drag reduction potential in grid fins and the adaptability of shock-expansion theory for high-speed aerodynamic predictions.

Further empirical insights are provided in [Washington and Miller, 1993], one of the first relevant works in the field, where experiments confirm that grid fins achieve a high strength-to-weight ratio and exhibit hinge moments conducive to stability across a range of Mach numbers. There are a lot of studies focusing on advanced numerical methods, especially CFD, to assess grid fin aerodynamics. Among them, the works of [Despirito et al., 2004], [Cai, 2009], [Reynier et al., 2004], [Chavan et al., 2022], and [DeSpirito et al., 2000] can be highlighted. For instance, [DeSpirito et al., 2000] verified CFD-derived predictions at Mach 2.5, highlighting grid fins' stability at high angles of attack, while [Reynier et al., 2004] applied the actuator disc concept, simplifying computational requirements while retaining accuracy. Additionally, vortex theory, applied in [Burkhalter and Frank, 1996] and later expanded through vortex lattice method ap-

proaches in [Burkhalter et al., 1995] and [Theerthamalai, 2007], offered new perspectives on grid fin dynamics, with [Theerthamalai, 2007] specifically addressing subsonic flow and efficiency limitations near transonic speeds.

Comparisons between grid fins and conventional planar fins are documented in [Fournier, 2001], or more recently at [Debiasi, 2020] and [Munawar, 2010]. These two studies confirm grid fins' superior control efficacy at high speeds. Detailed analyses of complete grid fin-missile configurations through both numerical simulations and experimental tests are explored in [Kiyak et al., 2014] and [Ledlow and Burkhalter, 2015]. These studies examine design optimizations to improve missile trajectory control and strike accuracy, with [Kiyak et al., 2014] leveraging an ant colony algorithm to optimize grid fin geometry for tactical performance. Experimental data for various grid fin angles are systematically provided in [Dupuis and Berner, 2001], offering insights into grid fin performance in flight and varying angle configurations. Aerodynamic coefficients derived from CFD simulations, combined with missile stability analyses for configurations with both canard and grid fins, are discussed in [Despeyroux et al., 2015]. Additionally, the effect of grid fins on missile stability in canard-controlled configurations appears in [Despirito et al., 2003], which emphasizes improved roll control at supersonic speeds.

Static and dynamic aeroelastic behavior of grid fins has also been examined in recent years. The work of [Ye et al., 2022] identifies bending-torsion coupling as a significant source of instability, particularly at transonic speeds where aeroelastic challenges intensify. Moreover, [Tripathi et al., 2019] and [Tripathi et al., 2020] characterizes grid fins' lift and stall behavior across different gap-to-chord ratios in subsonic flows, demonstrating how this parameter influences aerodynamic stability. Other recent studies, such as [Dinh et al., 2023], tested multiple grid fin pattern configurations, revealing reductions in drag and improvements in control when optimizing specific pattern geometries. A simplified numerical model introduced in [Dikbas et al., 2018] further contributes by simulating grid fin aerodynamic forces with reduced computational cost, making it viable for preliminary aerodynamic studies and design iterations.

All of the mentioned articles, along with others in the same field, are organized chronologically and presented in Table 2.2, which provides a concise summary of each article contribution. As shown, as in the aerial refueling field the majority of works were published after the start of the 21st century, indicating that the analysis and study of grid fins is a relatively recent field with significant room for exploration in the coming years.

Table 2.2: Chronological review of relevant articles on grid fins.

Year	Authors	Contribution
1989	[Brooks and Burkhalter, 1989]	Developed a model showing grid fins provide control at high angles with reduced actuator needs.
1993	[Washington and Miller, 1993]	Demonstrated that grid fins offer strength-to-weight benefits and low hinge moments.

Continued on the next page

Year	Authors	Contribution
1994	[Miller and Washington, 1994]	Identified drag reduction potential by modifying grid fin frame shape and thickness.
1995	[Burkhalter et al., 1995]	Confirmed grid fins maintain control effectiveness at high angles with low hinge moments.
1996	[Burkhalter and Frank, 1996]	Used vortex theory to predict grid fin behavior at moderate angles of attack.
2000	[DeSpirito et al., 2000]	Validated through CFD that grid fins maintain control at high angles.
2001	[Dupuis and Berner, 2001]	Wind tunnel tests for Mach numbers of 0.6–3.0 of missiles with grid fins.
2001	[Fournier, 2001]	Comparisons of grid fins and planar fins in wind tunnel tests on projectiles.
2003	[Despirito et al., 2003]	Showed grid fins enhance roll control in supersonic canard-controlled missiles.
2003	[Lin and Huang, 2003]	Validated grid fin designs reduce drag and hinge moments through simulations.
2004	[Despirito et al., 2004]	Found grid fins less effective for roll control at subsonic speeds due to flow choking.
2004	[Reynier et al., 2004]	Introduced actuator disc concept to simplify grid fin simulations in CFD.
2006	[Reynier et al., 2006]	Enhanced actuator disc model improved accuracy of grid fin simulations in supersonic flow.
2006	[Theerthamalai and Nagarathinam, 2006]	Predicted that grid fins remain effective for control in supersonic flows at high angles.
2007	[Theerthamalai, 2007]	Characterized grid fins at subsonic speeds, showing low hinge moments and efficient lift.
2009	[Cai, 2009]	Designed swept grid fins that reduce choked flow drag in transonic regimes.
2010	[Munawar, 2010]	Demonstrated grid fins outperform conventional fins for high-speed control in CFD studies.

Continued on the next page

Year	Authors	Contribution
2014	[Kiyak et al., 2014]	Development of an ant colony algorithm to optimize missile trajectories with grid fins.
2015	[Despeyroux et al., 2015]	Showed grid fins reduce pitch damping in transonic flow while effective in supersonic regimes.
2015	[Ledlow and Burkhalter, 2015]	Demonstrated that grid fins improve accuracy in target strikes despite added drag.
2018	[Dikbas et al., 2018]	Proposed a unit grid fin concept to simulate aerodynamic forces with lower costs.
2019	[Tripathi et al., 2019]	Analyzed grid fins in subsonic flow, showing increased lift and delayed stall at varying gap ratios.
2020	[Tripathi et al., 2020]	Identifies optimal grid fin patterns at subsonic speeds.
2020	[Debiasi, 2020]	Demonstrated that swept grid fins improve deployment and maintain flow at transonic speeds.
2022	[Chavan et al., 2022]	Developed a sharp-edged grid fin model that reduces turbulence, enhancing control.
2022	[Ye et al., 2022]	A model for identifying flutter and bending-torsion instability in grid fins.
2023	[Dinh et al., 2023]	Tested grid patterns, finding reduced drag and improved control with optimized designs.

Chapter 3

Characterization of the hose and drogue model

In this Chapter, preceding the development of the hose and drogue model, two characterization tests will be presented in order to obtain reliable reference values of some important mechanical properties of the hose.

For an homogeneous structure, such for example a metallic beam or a cable, the estimation of its mechanical properties would be straightforward. However, the hose and the drogue are sophisticated structures, for which little reference data is available to study their behavior.

The hose is composed of a rubber core and a metallic mesh embedded within, and a metallic helicoid running along its length (in order to stiffen the structure). It is supplied by Airbus Defence and Space, and manufactured by Cobham, a British manufacturing company, specialized in aerial refueling. A sketch of the hose is presented in Figure 3.1.

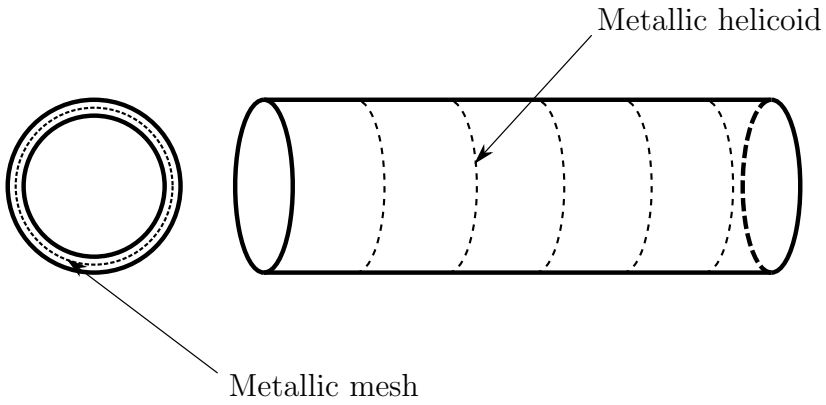

Figure 3.1: Sketch of the hose.

To obtain reliable values of certain properties of the hose, two different tests will be performed:

- **Static test**: A tension test will be performed with the objective of obtaining the

value of the Young Modulus, or Elastic Modulus, of the hose. A reliable value of this property is essential, since the bending forces acting on the hose depend linearly on this parameter. Due to the unusual composition of the hose, there are no references values in the literature for even a preliminary reliable first estimation of this Modulus.

- **Dynamic test**: The dynamic test, in particular a vibration test of a sample of the hose, aims to estimate the structural damping coefficient of the hose. This estimation is of great importance because, as will be seen in following Chapters, when combined with the aerodynamic damping, it determines the dynamic stability of the hose and drogue system.

These tests help relate the analysis to real flight conditions for aerial refueling systems. First, the static tension test to obtain the Elastic Modulus E will be presented, and, subsequently, the dynamic vibration test to obtain the structural damping coefficient c, which always has to be determined experimentally due to the uncertainties on theoretical models for evaluation of this coefficient.

3.1 Static test

The objective of this test is to obtain the value of the Young Modulus of the hose E. As previously mentioned, the hose is made of an uncommon material, which has a metallic helicoid along the length. Therefore, an analytical estimation is challenging and the test should be performed with special care, because the isotropic properties that exist in other structures are not fulfilled in this one. Next, the procedure to perform the tension test will be given.

3.1.1 Experimental setup

The test was conducted using a piece of the studied hose. In order to test it correctly on the tension machine, the process of the test was the following: First, two concentric metallic cylinders were placed inside the hose, with two smaller cylinders protruding on both sides to allow proper attachment to the machine of the tension test. Then, to correctly hold these two metallic pieces to the hose, two screws were placed on both sides, completely piercing the hose and the metallic pieces. The selection of the points where the screws are placed is not arbitrary; special care must be taken to avoid interfering with the metallic helicoid running through the hose.

The hose piece used for the test, as well as the two clamps for the connection to the tension machine and the two screws can be seen in Figure 3.2.

Figure 3.2: Piece of hose used in the tension test.

The machine used in the test is the *Instron Model 4204*, a universal testing machine specifically designed for tensile tests. It is controlled by a computer and is capable to perform a variety of tests based on tension and compression. The computer provides automated control, data acquisition and analysis. Figure 3.3 shows the hose placed in the machine before being tested.

Figure 3.3: Piece of hose and tension machine before the test.

3.1.2 Methodology of the test

The objective of this test is to measure the deformations of the hose when a known force is applied. Once the hose is securely attached to the machine, an extensometer is placed for measuring the deformations on the hose.

Testing a structure with uniform properties would typically require only a single test. However, due to the complexity of the hose, multiple tests were performed to obtain reliable estimates. The extensometer was placed in different positions for each test. In particular, three positions were considered. A fourth test was also performed to verify the consistency of the results, by maintaining the position of the extensometer but changing the force applied by the machine. The four tests are the following:

- **Test 1**: The extensometer is placed on the left side of the hose, once the hose has been attached to the machine. The maximum applied force by the machine is 2013 N.

- **Test 2**: The extensometer is placed in the center side of the hose, with a maximum applied force of 2548 N.
- **Test 3**: The extensometer is placed on the right side of the hose. The maximum applied force by the machine is 2019 N.
- **Test 4**: The extensimeter remains on the right side of the hose, but the maximum applied force by the machine is approximately twice that of in the previous test: 4102 N.

The process to estimate the Elastic Modulus is as follows:

1. In each of the tests, starting with a null load, a traction force is applied through the machine on both sides of the piece of hose, and the extensometer measures the resulting elongation.
2. Knowing the hose effective area A, and the applied force F_M, the stress is calculated as $\sigma_M = F_M/A$.
3. With the nominal length of the piece of hose l_0, and with the elongation Δl, the deformation is obtained as $\epsilon_M = \Delta l/l_0$.
4. Finally, with the hypothesis that the stress-strain curve is a straight line, the Elastic Modulus of the hose is estimated as the slope of that straight line:

$$\sigma_M = E \cdot \epsilon_M \Longrightarrow E = \frac{\sigma_M}{\epsilon_M}. \tag{3.1}$$

3.1.3 Results

In Figures 3.4 and 3.5 the results for the Elastic Modulus E for each of the tests are presented. In addition, Table 3.1 provides a summary of the results.

As can be seen in Table 3.1, the results obtained for each of the three tests provides significantly different values of the Elastic Modulus. Therefore, as expected, it is verified that the properties of the hose are different depending on the direction. However, the order of magnitude of the Elastic Modulus ($\simeq 10^8$) is consistent across all the tests, against the values found in some literature. Therefore, it can be concluded the values used by other works are not representative or the type of hose is very different to the one considered in this thesis.

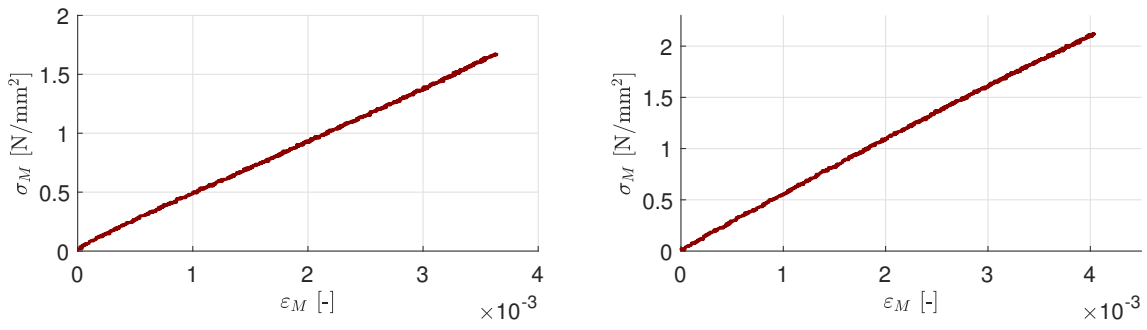

Figure 3.4: Stress-strain curve for Tests 1 and 2.

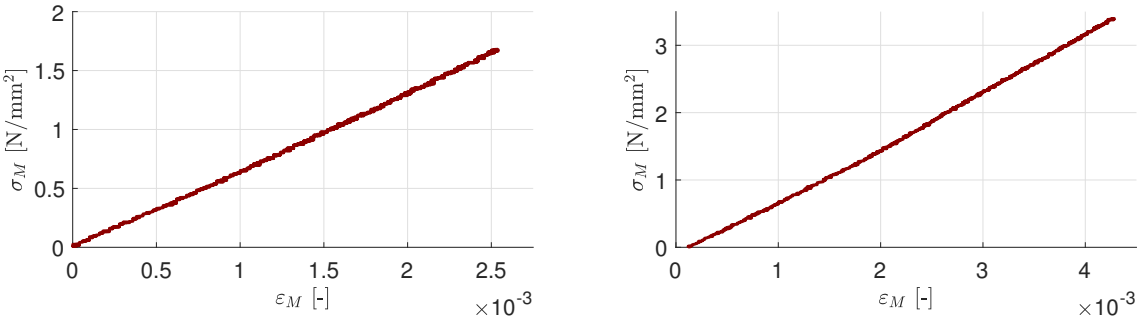

Figure 3.5: Stress-strain curve for Tests 3 and 4.

An interesting behavior is observed in Test 4. In this test, when the extensimeter is placed in the same position as in the third one, it should give very similar results, although the maximum applied force is different, the slope of the stress-strain curve should be the same. However, the result is different. Specifically, it is an 18% higher in the fourth test than in the third one. As no further tests have been able to be performed to verify these results, it is not possible to confirm with complete certainty the reason for this change. However, the fact that the result has a significant variation from Test 3 to 4 may mean that, after the Test 3, the hose did not returned to the original position, i.e., the results of Test 4 depend of the results of Test 3. The verification of this hypothesis could be done by performing a new test with the same characteristics (extensometer position and maximum force) as the Test 4, but without having previously performed any other test. This reasoning can explain the behavior of Figure 3.5, in which, as can be seen, for zero load the extensometer is already measuring a small deformation, meaning that at the beginning of the test the hose is already slightly deformed.

If the objective of this test had been to obtain a result as accurate as possible for the Elastic Modulus, these considerations would be fundamental, and the results obtained could not be assumed to be valid. However, as explained above, the objective was to be able to make a reliable estimation of the Elastic Modulus, with the aim to achieve adequate results when the bending of the hose is considered. Therefore, from the results of Table 3.1, an Elastic Modulus of $E = 600$ MPa will be used throughout this Thesis.

Table 3.1: Results of the tension test.

Test	F_{max} [N]	Δl [mm]	σ_{max} [MPa]	ϵ_{max} [-]	E [MPa]
1	2013	0.182	1.676	$3.64{\cdot}10^{-3}$	461.84
2	2548	0.202	2.121	$4.04{\cdot}10^{-3}$	534.28
3	2019	0.127	1.681	$2.54{\cdot}10^{-3}$	653.28
4	4102	0.214	3.415	$4.28{\cdot}10^{-3}$	771.16

3.2 Vibration test

Next, the vibration test is presented. As previously explained, the objective of this test is to estimate the structural damping coefficient of the hose. Vibration tests, or modal tests,

are based on generating an excitation at one or more points on a structure and measuring the response at these or other points. The theoretical foundation of this test is based on establishing a relationship between the excitation (input) and the response (output) in the form of frequency response functions, see [Ewins, 1984]. To obtain these functions, excitation and response measurements must typically be taken at various points on the structure. In general, the excitation is measured by means of a force transducer at the point where this excitation is applied and the response by means of accelerometers or similar sensors.

Since the frequency range of the hose specimen response is not known, the tests will be performed using a shaker. First, the experimental setup, equipment and materials necessary for the test are presented. Then, the test methodology and the process for obtaining results are explained. Finally, the results for the damping coefficients are presented.

3.2.1 Experimental setup

The objective of this test is to excite a piece of hose. This hose piece is held by two clamps, which hold it to a shaker. Between the shaker and the structure a load cell is placed, in order to measure the produced excitation. The response is measured with different accelerometers placed along the hose piece. Both the load cell and the accelerometers are connected to a signal analyzer, where the results are recorded. A general scheme of the test is shown in Figure 3.6. The equipment and materials used in the test are the following:

- A sample of the hose.
- Two cylindrical clamping structures, located in the middle of the piece of the hose.
- Seven accelerometers, placed along the hose piece.
- A load cell, placed between the hose and the shaker.
- The shaker, which generates the force to excite the desired frequency range.
- The data acquisition system (signal analyzer): RT Pro Focus program.

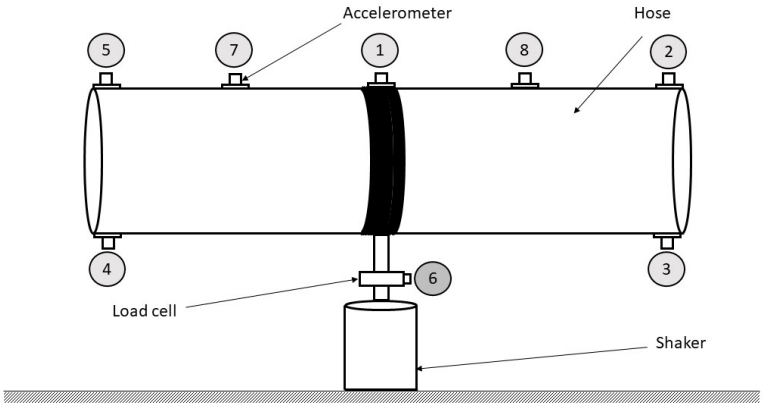

Figure 3.6: General scheme of the vibration test.

Most of the technical equipment can be seen in Figure 3.7.

Figure 3.7: Experimental setup for the vibration test.

It is important to note that the numbering of the accelerometers and the load cell have the following meaning: On the one hand, they represent the channels through which the collected data are sent to the signal analyzer, and, on the other hand, also serve as the sub-indexes of the frequency response functions.

Piece of hose and clamping structures

As in the static test presented before, a piece of hose of 500 mm of length is used. Since this is a much smaller piece than the complete hose, it is important to point out that the damping coefficients obtained will not directly correspond to those for the entire hose. However, the objective of this test is to obtain a reference value for the structural damping of the system, ensuring it is correctly characterized.

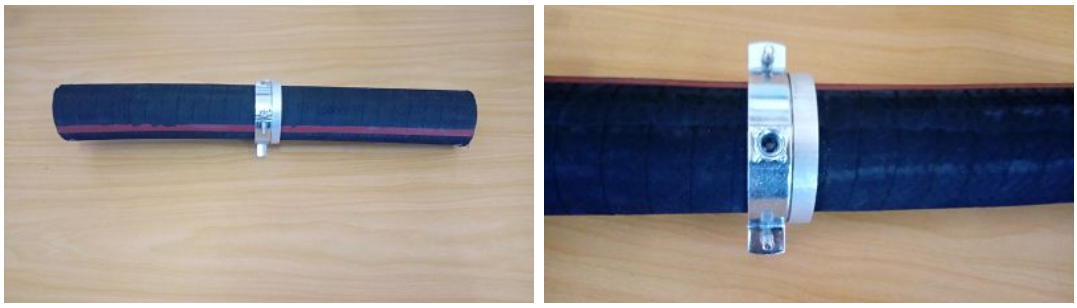

Figure 3.8: Piece of hose and clamping structures for the vibration test.

In order to correctly excite the structure, it must be firmly attached to the shaker to ensure that the excitation force is perfectly transmitted. Two cylindrical clamps, joined by two screws, are used to fix the structure to the load cell and to the shaker. The hose piece and the clamping structures are presented in Figure 3.8.

Accelerometers

Seven accelerometers from two different brands (Brüel & Kjær and PCB) are used, placed at different positions along the hose specimen. Figure 3.9 shows accelerometers of both brands. The serial numbers and sensitivities of each of the accelerometers are summarized in Table 3.2.

Table 3.2: Serial number and sensitivity of the accelerometers used in the vibration test.

Channel	**Accelerometer**	**Sensitivity [mV/g]**
1	Brüel & Kjær 65627	102.18
2	Brüel & Kjær 30905	100.22
3	Brüel & Kjær 31224	102.60
4	PCB 32686	21.51
5	Brüel & Kjær 65626	101.70
7	PCB 35873	20.00
8	PCB 35874	20.39

The method for attaching the accelerometers to the hose piece must consider factors such as location, surface roughness, accessibility, and portability. Due to the ease of assembly and the high quality of the measurements, the adhesive attachment has been chosen.

Figure 3.9: Accelerometers used in the vibration test. On the left side, Brüel & Kjær, and on the right side, PCB.

The different positions of each accelerometer, which can be seen in Figure 3.6, have been selected based on the following criteria:

- In order to be able to analyze modes along the entire length of the hose piece, five accelerometers are placed along its length, on the top-side.
- In order to distinguish whether the modes are symmetric or anti-symmetric respect to the attachment, two accelerometers are placed on the left side and other two on the right side, in identical positions relative to the fastening of the structure.
- To check if the motion at both sides of the hose piece is in the same direction, two more accelerometers have been placed on the bottom side of the hose. These two positions are very important, as they will allow to differentiate typical bending modes from other more complex modes.
- Finally, to check that the force is transmitted correctly through the clamps, one of the five top-side accelerometers has been placed on one of the clamp (in the center of the structure).

Shaker and load cell

The shaker used in the test (Figure 3.10) is the *V406* from *LDS Test and Measurement*. Table 3.3 summarizes some important technical specifications of this shaker.

Table 3.3: Technical specifications of the shaker.

Useful frequency range	[5-9000] Hz
Armature resonance frequency	9000 Hz
Mass	14.1 kg
Effective mass of moving element	0.20 kg
Sine force peak	98.0 N
Max. working ambient temperature	30 ^{o}C
Max. acoustic noise	82 dB

Figure 3.10: Shaker used in the vibration test.

With respect to the load cell, it is located between the shaker and the hose specimen, just below the clamps that hold the hose. This cell measures the force transmitted from the shaker and records it in the signal analyzer. Their sensitivity is 23.71 mV/N, and it is assigned to Channel 6 of the signal analyzer (the one with not appear at Table 3.2). Figure 3.11 shows the load cell together with the structure of attachment to the shaker.

Figure 3.11: Load cell used in the vibration test.

Signal analyzer

The signal analyzer used for the tests is the RT Pro Focus program. This analyzer can handle multiple channels simultaneously and provides accurate results. For this test, eight channels are used: Seven for the signals of the accelerometers, i.e., the outputs of the system, and the last one for the load cell, i.e., the input. The channel assignments can be seen in Figure 3.6.

Before conducting the test, the analyzer allows the user to select different options for data analysis and visualization. It allows the selection of the maximum excitation frequency to be reached during the test: different tests have been performed until this frequency has been set to 1100 Hz. Although the program selects that frequency range, it calculates the results up to a slightly higher frequency, around 1125 Hz. It is important to mention that at approximately the first 5 Hz the analyzer is not able to read the signal. Thus, the results in this low range of frequency are not considered.

The program also allows the user to select the number of points, i.e., the amount of data to be stored and processed. To ensure an appropriate time step and avoid aliasing

problems, 2560 points were selected. In addition, it is possible to choose the number of data averages. To obtain results with minimal noise, the number of averages was fixed at 300. Finally, the program also allows to select the option of use Window Functions. However, it was decided not to use them. Table 3.4 summarizes the main parameters used in the signal analyzer. A general view of the analyzer is shown in Figure 3.12.

Table 3.4: Parameters used in the signal analyzer.

Time step	$3.91{\cdot}10^{-4}$ s
Sampling time	$9.99{\cdot}10^{-1}$ s
Frequency step	1 Hz
Sampling frequency	2560 Hz
Frequency range	0-1100 Hz
Averages	300

Figure 3.12: Signal analyzer: RT Pro Focus program.

3.2.2 Test methodology

Once the experimental setup has been cleared up, the methodology followed in the tests is now presented. This section outlines the step-by-step experimental procedure and the data analysis process to obtain the results.

Experimental procedure

The steps to perform the test are the following:

1. Preparation of the hose surface: Sand and clean the surface to ensure correct attachment of the accelerometers.
2. Assembly: The load cell is placed on the shaker and the hose is placed through the clamps, on top of the load cell. Both the accelerometers and the cell are connected to the analyzer in their respective channels. It is crucial to ensure that the structure is firmly fixed and the accelerometers are correctly stuck in their designated positions.
3. Configuration of the signal analyzer: The parameters are adjusted and the type of excitation is selected. In this test, a white noise excitation signal is used with a frequency range presented in Table 3.4.

4. Execution of the test: The shaker generates the excitation, the load cell measures it, and the accelerometers measure the accelerations at each point. All data are sent to the analyzer.

5. Data Analysis: The data are analyzed as will be explained next and it is decided if the test has been valid or not.

6. Disassembly: If the test is valid, the accelerometers and the piece of hose are disassembled, and the surface cleaned. If the test is not been valid, step 3 is repeated (if it is needed to change certain parameters) or step 4 (if the test can be done again directly).

Data analysis

Next the data obtained from the test are analyzed. This involves examining the module and the phase of the Frequency Response Function (FRF) of the system.

The analyzer outputs files containing records of the applied load and the accelerations measured at each point. Thus, the computation of the FRF matrix of the system is given in terms of acceleration per unit force. In the frequency domain, the relation between the FRF matrix in terms of acceleration/force $\boldsymbol{A}(\omega)$ to the FRF in terms of displacement/force $\boldsymbol{H}(\omega)$ is [García-Fogeda Núñez and Sanz Andrés, 2014]:

$$\boldsymbol{A}(\omega) = -\omega^2 \boldsymbol{H}(\omega). \tag{3.2}$$

An arbitrary element of this matrix is denoted as A_{jk}, which has the meaning of the response at point j for a unit force applied at point k:

$$A_{jk}(\omega) = \frac{\tilde{q}_j(\omega)}{\tilde{p}_k(\omega)}, \tag{3.3}$$

where $\tilde{q}_j(\omega)$ are the accelerations measured by the accelerometers and $\tilde{p}_k(\omega)$ the measurements of the applied force, both in the frequency domain. In this test, subscript j varies for the seven accelerometers, while k (the input) is fixed.

Assuming a viscous damping model [García-Fogeda Núñez and Sanz Andrés, 2014] both FRF matrices $\boldsymbol{H}(\omega)$ and $\boldsymbol{A}(\omega)$ for small values of the damping coefficient can be approximated as:

$$H_{jk}(\omega) \simeq \sum_{r=1}^{N} \frac{\Phi_{jr}\Phi_{kr}^*}{-\omega^2 + \omega_r^2 + 2i\gamma_r\omega\omega_r}, \tag{3.4}$$

$$A_{jk}(\omega) \simeq \sum_{r=1}^{N} \frac{\Phi_{jr}\Phi_{kr}^*}{\left(\frac{\omega}{\omega_r}\right)^2 - 1 - 2i\gamma_r\frac{\omega}{\omega_r}} \cdot \left(\frac{\omega}{\omega_r}\right)^2, \tag{3.5}$$

where Φ is the mode, r is the number of modes, ω_r the frequencies and γ_r the damping coefficients.

In this case the information of the whole response function is not needed; only the information in the neighborhood of the frequencies to be analyzed. Therefore, $A_{jk}(\omega)$ can be

adjusted via the Peak-Picking method [Ewins, 1984]. This method assumes the response function near a frequency behaves like that of a one degree-of-freedom system. This approach usually gives accurate results as long as the frequencies are not too close together. With this approach, $A_{jk}(\omega)$ can be rewritten as:

$$A_{jk}(\omega) \simeq \sum_{r=1}^{N} \frac{\Phi_{jr}\Phi_{kr}^{*}}{\left(\frac{\omega}{\omega_r}\right)^2 - 1 - 2i\gamma_r\frac{\omega}{\omega_r}} \cdot \left(\frac{\omega}{\omega_r}\right)^2 \simeq \frac{\Phi_{jr}\Phi_{kr}^{*}}{\left(\frac{\omega}{\omega_r}\right)^2 - 1 - 2i\gamma_r\frac{\omega}{\omega_r}} \cdot \left(\frac{\omega}{\omega_r}\right)^2. \quad (3.6)$$

With the FRF of the system modeled as a one degree-of-freedom system, typical considerations for such systems can be applied. In particular, if small damping coefficients are assumed ($\gamma < 0.05$), this coefficient can be estimated as follows:

1. The maximum of the response function is located near $\Omega \simeq \omega_0$.
2. For $\gamma << 1$, the frequencies at which $1/\sqrt{2}$ of the maximum value is reached are $\Omega_1 = \omega_0(1-\gamma)$ and $\Omega_2 = \omega_0(1+\gamma)$.
3. The damping coefficient is then obtained as:

$$\gamma \simeq \frac{\Omega_2 - \Omega_1}{2\omega_0}. \quad (3.7)$$

To avoid the influence of the noise in measurements for the determination of the damping coefficient, which is usually a very small number, averages on the measurements are taken (300 in this case, as presented in Table 3.4).

The next step is, from the data obtained in these tests, to decide among the modes obtained in that test which are worthwhile to calculate the damping coefficient. First, the peaks in the module of the response functions, meaning the values of the natural frequencies, must be identified.

Figure 3.13 presents the module of the element $A_{4,6}$ of the FRF matrix. In this Figure, four different peaks can be clearly observed. The first one, close to 0 Hz, is discarded directly, since, as explained previously, at approximately the first 5 Hz the analyzer is not able to read the signal. Thus, three peaks are suitable for estimating the damping coefficient.

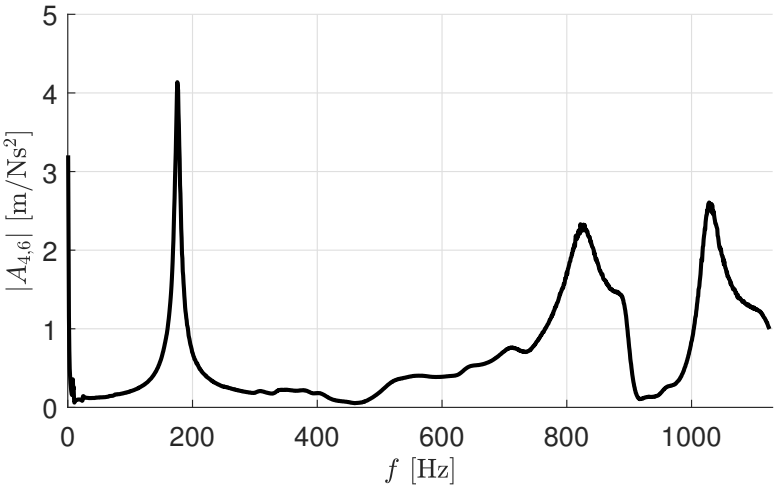

Figure 3.13: Module of the FRF $A_{4,6}$.

With the aim to determine the modal shapes of each of the three modes, the results of the FRF phases are also used. With the accelerometers located at different points of the piece of hose, the sign of the phase in each of the functions in the peak neighborhood provides the information of the direction in which each of the points is moving. By comparing phase signs across different points, it is possible to get the information of the modal shapes. Figure 3.14 presents the FRF phases for all the measured points.

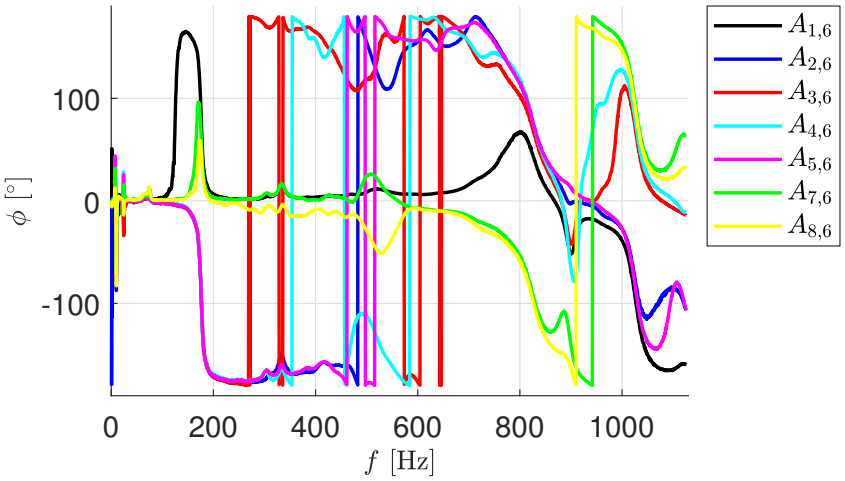

Figure 3.14: FRF phases of the system.

Analyzing Figure 3.14, it is possible to obtain the sign of the phases in the neighborhood of each of the three frequencies:

- **First frequency, f $\simeq$ 175 Hz**. The signs of the phases for each response function, and, therefore, for each position of the piece of hose in the neighborhood of the first frequency are outlined in Figure 3.15.

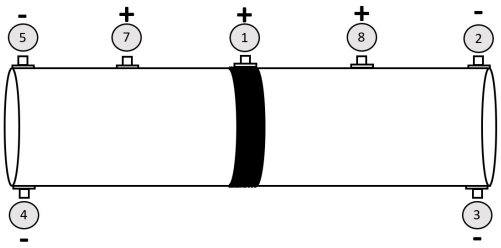

Figure 3.15: Signs of FRF phases in each position, mode at 175 Hz.

As can be seen in Figure 3.15, the motions at locations 5 and 4, as well as at locations 2 and 3, are in phase. This indicates that these two pairs of points move in the same direction. It is interesting to mention that this mode is equivalent to the one expected in a beam under similar boundary conditions. In particular, if the modes of a free-free beam are analyzed [Timoshenko, 1945], it is possible to see that the results obtained are equivalent. In Figure 3.16 an approximation of the modal shape is sketched.

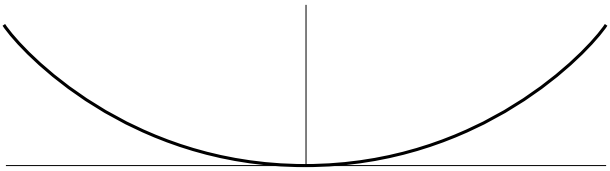

Figure 3.16: Approximate shape of the first mode.

- **Second frequency, f $\simeq$ 825 Hz**. The signs of the phases for each position of the piece of hose in the neighborhood of the second mode are outlined in Figure 3.17. In this case, in a similar way than the previous mode, the motions in locations 5 and 4, and in locations 2 and 3, are in phase. In addition, the motions in locations 7 and 8 are in against-phase to the previous ones, but the motion in location 1 now is in phase, which is the difference with respect to the first mode. With this information, it is possible to conclude that this mode is the second symmetrical mode of a free-free beam. Figure 3.18 shows an approximation of the modal shape.

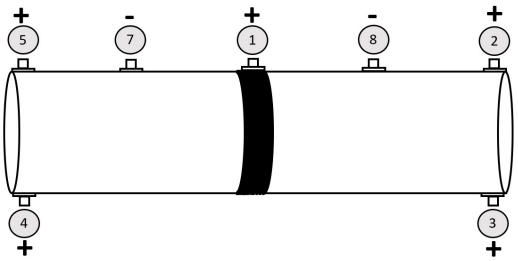

Figure 3.17: Signs of FRF phases in each position, mode at 825 Hz.

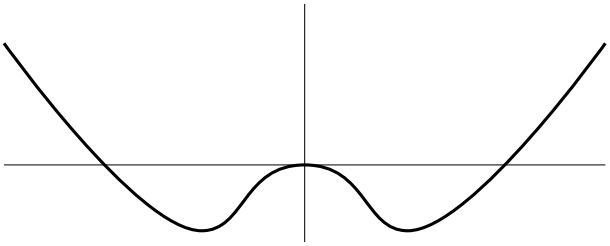

Figure 3.18: Approximate shape of the second mode.

- **Third frequency, f $\simeq$ 1025 Hz**. In Figure 3.19, the signs of the phases for each position of the piece of hose in the neighborhood of the third frequency are presented. As can be seen, in this mode the up and down points on both ends of the piece of hose move in different directions. This means that at this excitation frequency the hose is deformed in radial direction. As this motion will not be considered in the studied hose, this third mode is discarded for the estimation of the damping coefficient.

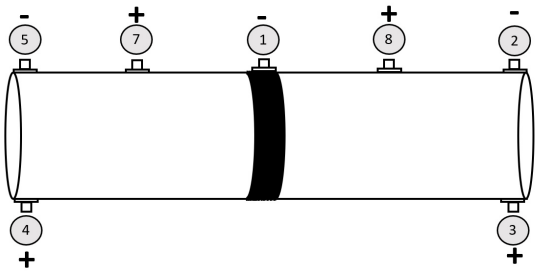

Figure 3.19: Signs of FRF phases in each position, mode at 1025 Hz.

From the results presented it is clear that the first two modes represent the bending deformation, and therefore in these two modes the damping coefficient is calculated by Eq.(3.7). The results obtained are summarized in the following section.

3.2.3 Results

The results obtained in the tests are presented below. In each of the two modes, the frequency estimation and the damping coefficients are given. The frequencies were estimated from the peaks of the FRF module, and those two peaks are the ones to be used for the estimation of the damping coefficient using Eq.(3.7).

As shown in Table 3.5, the adjustment for the first mode yields a consistent frequency and, except for the first function, an identical damping coefficient. By averaging all cases, the damping coefficient for the first mode is estimated to be $\gamma_1 \simeq 2.24\%$. For the second mode, the damping coefficient is estimated to be $\gamma_2 \simeq 3.93\%$ and the frequency is $f_2 \simeq 826.33$ Hz.

With the results of the vibration test, it is concluded that the estimation of the structural damping of the hose for the two modes is reliable. assuming that the coefficient of the first mode γ_1 is small enough, a conservative approach would be used: to assume the smallest value of γ_1 directly as the structural damping coefficient. Hence, a value of 2.22% will be used for the structural damping of the hose.

Table 3.5: Results of the vibration test: First and second mode.

FRF	f_1 (Hz)	γ_1 (%)	f_2 (Hz)	γ_2 (%)
$A_{1,6}$	175,6	2,30	—	—
$A_{2,6}$	175,6	2,22	826,9	4,02
$A_{3,6}$	175,6	2,22	828,8	4,49
$A_{4,6}$	175,6	2,22	821,9	3,64
$A_{5,6}$	175,6	2,22	826,9	3,94
$A_{7,6}$	—	—	826,9	3,26
$A_{8,6}$	—	—	826,9	4,21

3.2.4 Elastic Modulus checking

Finally, with the results from the dynamic test, in particular the two frequencies obtained, the Elastic Modulus of the hose can also be estimated. This process can be used to validate the results of the static test.

As explained above, the two modes obtained from the hose piece are equivalent to the first two symmetrical modes of a beam in a free-free condition. The dimensionless eigenfrequencies of an equivalent beam with these boundary conditions ξ_i can be defined as:

$$\xi_i = \sqrt[4]{\frac{\rho_H l^4 \omega_i^2}{EI}}, \tag{3.8}$$

where ρ_H is the mass per unit of length of the hose, l the length of the piece, ω_i the frequencies (in rad/s), and I the moment of inertia. Following [Timoshenko, 1945], these non-dimensional coefficients have an analytical solution, whose values for a free-free beam are:

- First mode $\Longrightarrow \xi_1 = 4.73004074$.
- Second mode $\Longrightarrow \xi_2 = 10.9956078$.

Therefore, the Elastic Modulus can be calculated as:

$$E = \frac{\rho_H l^4 \omega^2}{\xi^4 I}. \tag{3.9}$$

With Eq.(3.9) it is possible to obtain a estimation of the Elastic Modulus. The results are:

- First mode $\Longrightarrow E \simeq 665.5$ MPa.
- Second mode $\Longrightarrow E \simeq 505.3$ MPa.

As can be seen, the results are very similar to those obtained in the static test. Therefore, it can be concluded that a value of 600 MPa is a reliable estimation for the Elastic Modulus of the hose.

Chapter 4

Hose-Drogue model

In this chapter the hose-drogue model without the influence of the grid fins will be set forth. The model encompasses both static and dynamic results for the system and serves as a foundational framework, essential for gaining detailed insights into the behavior of the hose-drogue system. Moreover, it provides a basis for the subsequent analysis of how the incorporation of grid fins will impact in the behavior of the system.

As discussed in the literature review (see Chapter 2), numerous studies have explored models to study the dynamics of the hose as it is done in this thesis. However, this work introduces significant innovations, including a refined model of the aerodynamic forces acting on the hose and an aeroelastic analysis of the system. The chapter is structured into different sections, each serving a specific purpose:

In the first section, the mathematical model will be outlined in a general manner, providing an overview of the equations governing the motion of the hose-drogue system. This model integrates both structural and aerodynamic considerations, offering a foundational understanding of the problem at hand, with a particular focus on the aerodynamics of the hose.

Following the establishment of the general equations, the static equilibrium problem is first considered. This analysis delves into determining the equilibrium position that the hose-drogue system maintains once deployed and just before engaging with the receiver aircraft. Solving this static problem entails addressing a nonlinear system of equations, incorporating various considerations that will be detailed later.

Once the static equilibrium position is defined, the chapter proceeds to obtain the dynamic equations of the system assuming small perturbations with respect to the static equilibrium position. Inertia, damping and stiffness matrices of the system will be presented, as well as the whole process of obtaining them. Furthermore, the chapter explores the free vibration characteristics of the system, including its natural frequencies, damping coefficients, and eigenmodes, with an examination of how different parameters influence on these dynamic properties.

Then, the focus shifts to conducting an aeroelastic stability analysis of the system. The flutter boundaries, i.e., the dynamic instabilities of the hose-drogue-surrounding air system, are calculated using the tracing of the roots method, exploring the influence of various parameters on flutter occurrence. This analysis provides crucial insights into the potential for flutter in a refueling system akin to the one described in this thesis, highlighting key factors that affect system stability and performance.

In the final section of the chapter, a response problem based on the contact between the drogue and the receiver aircraft will be studied, using the dynamic properties of the system obtained previously.

4.1 Hose and drogue mathematical formulation

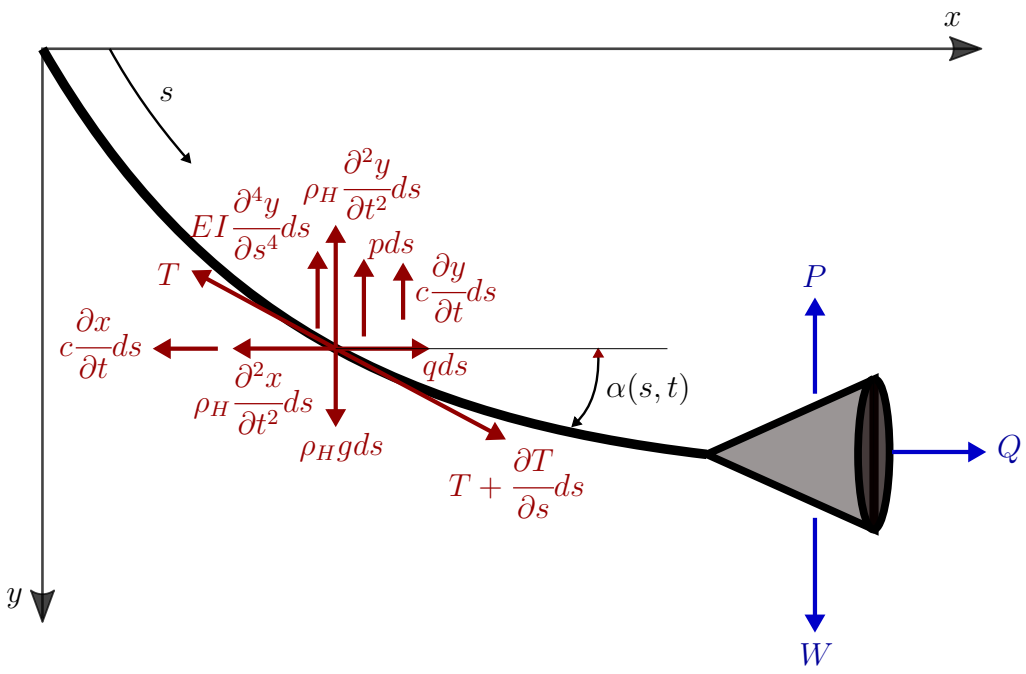

Figure 4.1: Acting forces on the hose (red) and on the drogue (blue).

Figure 4.1 shows the hose-drogue model, as well as the acting forces on a differential hose element of length ds (highlighted in red) and on the drogue (highlighted in blue). The reference system which defines the hose position (x, y, z) is defined by the x-axis aligned opposite to the flight direction, the y-axis pointing downwards (toward the earth) and the z-axis forming right-handed Cartesian axes. The motion of the hose and drogue system is considered within a vertical plane (x, y) due to the symmetry of the system. Consequently, neither forces nor perturbations outside that plane will be considered in this part of the thesis. However, it is worth noting that although the static and dynamic models will be developed in this two-dimensional space, one advantage of this formulation is its straightforward extension to three dimensions, allowing for inclusion of the lateral motion z (which will be done in the model with the aerodynamic grid fins, as will be presented in following chapters). Thus, in this chapter it is considered the null existence of any force acting in the z-direction, and aerodynamic effects like the wake of the wing tanker in the z-direction is also neglected in the following development.

The variables of Figure 4.1 are defined as follows: s represents the coordinate along the hose, ρ_H is the hose mass per unit of length, c is the structural damping coefficient (estimated from the dynamic tests presented in Chapter 3), T the hose tension, EI the hose bending stiffness, q and p are the aerodynamic drag and lift forces per unit of length on the hose, respectively, P and Q are the drogue lift and drag, respectively, and W the drogue weight. The different forces that appear in the system will be defined later. It is important

to mention that the hose is considered non stretchable and under tension in every moment.

The general formulation to be developed in this Section will focus on the equations for the three unknowns of the system:

- Horizontal position of the hose $x(s,t)$.
- Vertical position of the hose $y(s,t)$.
- Hose tension $T(s,t)$.

However, before the development of the general equations, an initial analysis of the hose angle of attack, defined as the angle between the hose and the x-axis and represented by $\alpha(s,t)$ will be carried out.

4.1.1 Hose angle of attack. Downwash effect

To formulate the equations of the system it is necessary to express the angle of attack of any section of the hose as a function of its position, i.e., as a function of the unknowns $x(s,t)$ and $y(s,t)$. As the angle of attack of the hose will also be influenced by the downwash angle induced by the wake of the tanker, this effect will be considered first.

The downwash angle due to to the wake of the tanker ε is evaluated using of the Lifting Line Theory, see [Bertin and Smith, 1979]. Assuming negligible oscillatory motion for the tanker this angle remains steady and approximately constant along of the hose. Its effect can be incorporated into the equations of motion through the angle of attack of the hose as:

$$\alpha(s,t) = \alpha_{\varepsilon=0}(s,t) + \varepsilon, \tag{4.1}$$

where $\alpha_{\varepsilon=0}(s,t)$ represents the hose angle of attack without the effect of the downwash angle. The downwash angle will be assumed to be very small for all the configurations analyzed. Therefore, only linear terms in ε are kept in the formulation of the model.

The sine and cosine of the angle of attack in a hose section s and at the adjacent section $s + ds$ can be expressed as a function of the local x and y positions of the hose and of ε using the following approximations:

$$\cos\alpha(s,t) \simeq \frac{\partial x}{\partial s}(s,t) - \varepsilon\frac{\partial y}{\partial s}(s,t), \tag{4.2}$$

$$\cos\alpha(s+ds,t) \simeq \frac{\partial x}{\partial s}(s,t) - \varepsilon\frac{\partial y}{\partial s}(s,t) + \left(\frac{\partial^2 x}{\partial s^2}(s,t) - \varepsilon\frac{\partial^2 y}{\partial s^2}(s,t)\right) ds, \tag{4.3}$$

$$\sin\alpha(s,t) \simeq \frac{\partial y}{\partial s}(s,t) + \varepsilon\frac{\partial x}{\partial s}(s,t), \tag{4.4}$$

$$\sin\alpha(s+ds,t) \simeq \frac{\partial y}{\partial s}(s,t) + \varepsilon\frac{\partial x}{\partial s}(s,t) + \left(\frac{\partial^2 y}{\partial s^2}(s,t) + \varepsilon\frac{\partial^2 x}{\partial s^2}(s,t)\right) ds. \tag{4.5}$$

These approximations enable the incorporation of the downwash angle effect into subsequent analyses of the hose-drogue system dynamics, facilitating a more complete understanding of its behavior under operational conditions.

4.1.2 General equations

The equations of the motion in the horizontal and vertical axes for a hose element of length ds are:

$$-\rho_H \frac{\partial^2 x}{\partial t^2}(s,t) - c\frac{\partial x}{\partial t}(s,t) + q(s,t) - T(s,t)\cos\alpha(s,t) + \left(T(s,t) + \frac{\partial T}{\partial s}(s,t)ds\right)\cos\alpha(s+ds,t) = 0, \tag{4.6}$$

$$-\rho_H \frac{\partial^2 y}{\partial t^2}(s,t) - c\frac{\partial y}{\partial t}(s,t) - p(s,t) + \rho_H g - T(s,t)\sin\alpha(s,t) + \left(T(s,t) + \frac{\partial T}{\partial s}(s,t)ds\right)\sin\alpha(s+ds,t) - EI\frac{\partial^4 y}{\partial s^4}(s,t) = 0. \tag{4.7}$$

Eqs.(4.6) and (4.7) can be rewritten using the angle of attack with the downwash angle effect defined in Eqs.(4.2)-(4.5):

$$-\rho_H \frac{\partial^2 x}{\partial t^2}(s,t) - c\frac{\partial x}{\partial t}(s,t) + q(s,t) + \frac{\partial}{\partial s}\left[T(s,t)\left(\frac{\partial x}{\partial s}(s,t) - \varepsilon\frac{\partial y}{\partial s}(s,t)\right)\right] = 0, \tag{4.8}$$

$$-\rho_H \frac{\partial^2 y}{\partial t^2}(s,t) - c\frac{\partial y}{\partial t}(s,t) - p(s,t) + \rho_H g + T(s,t) + \frac{\partial}{\partial s}\left[T(s,t)\left(\frac{\partial y}{\partial s}(s,t) + \varepsilon\frac{\partial x}{\partial s}(s,t)\right)\right] - EI\frac{\partial^4 y}{\partial s^4}(s,t) = 0. \tag{4.9}$$

The boundary conditions at the hose-to-tanker junction, $s = 0$, are:

$$x(0,t) = X_T(t), \tag{4.10}$$

$$y(0,t) = Y_T(t), \tag{4.11}$$

where $X_T(t)$ and $Y_T(t)$ represent the motion of the hose-to-tanker junction (rear part of the refueling pod) in both axes and are assumed to be known.

The boundary conditions at the hose-to-drogue junction $s = s_0$ are obtained from the equilibrium of the acting forces in the x and y directions:

$$-T(s_0,t)\cos\alpha(s_0,t) + Q = 0, \tag{4.12}$$

$$T(s_0,t)\sin\alpha(s_0,t) + P - W - \frac{W}{g}\frac{\partial^2 y(s_0,t)}{\partial t^2} + EI\frac{\partial^3 y(s_0,t)}{\partial s^3} = 0, \tag{4.13}$$

$$EI\frac{\partial^2 y(s_0,t)}{\partial s^2} \simeq 0. \tag{4.14}$$

As can be seen, it is assumed that the hose-to-drogue junction is a perfect ball joint and no moments are transmitted from the drogue to the hose. Eqs.(4.12) and (4.13) can be rewritten using the expressions for the hose angle of attack:

$$-T(s_0,t)\left(\frac{\partial x}{\partial s}(s_0,t) - \varepsilon\frac{\partial y}{\partial s}(s_0,t)\right) + Q = 0, \tag{4.15}$$

$$T(s_0,t)\left(\frac{\partial y}{\partial s}(s_0,t) + \varepsilon\frac{\partial x}{\partial s}(s_0,t)\right) + P - W - \frac{W}{g}\frac{\partial^2 y(s_0,t)}{\partial t^2} + EI\frac{\partial^3 y(s_0,t)}{\partial s^3} = 0. \tag{4.16}$$

In addition, a compatibility equation for the non stretchable hose condition must be included:

$$dx^2 + dy^2 = ds^2 \Longrightarrow \left(\frac{\partial x}{\partial s}\right)^2 + \left(\frac{\partial y}{\partial s}\right)^2 = 1. \tag{4.17}$$

4.1.3 Aerodynamic forces on the hose

In the formulation of the general motion equations for the hose, it is crucial to accurately model the aerodynamic forces $p(s,t)$ and $q(s,t)$ acting on the hose. Previous studies focused on the static or dynamic analysis of a hose, like for example [Eichler, 1978], have often used oversimplified models for these forces.

In order to find a more accurate model, a first option could be to search for models of high complexity, completely numerical and based on the use of CFD simulation programs. This approach would require a huge amount of computational time, and it is out of the objectives of this thesis. Therefore, the goal is to achieve a formulation that, being analytical and fast to execute, provides an accurate and reliable model for the correct characterization of the aerodynamic forces. For that reason, the models considered focuses on aerodynamic forces acting on inclined cylinders with surrounding air. This approach is suitable due to the similarities of the flow dynamics around inclined cylinders with the hose-drogue system.

Among the different references that studied the aerodynamics forces acting on inclined cylinders, the work of [Poulin and Larsen, 2007] must be highlighted. In this reference, loads on an inclined cylinder similar to the system of this work are analyzed both analytically and experimentally to determine the corresponding aerodynamic coefficients. The model presented in [Poulin and Larsen, 2007] has been generalized with insights from [Hoerner, 1965] to enhance its applicability for the later use in this thesis. The study configuration of the aerodynamic forces acting on inclined cylinders presented in [Poulin and Larsen, 2007] is shown at Figure 4.2.

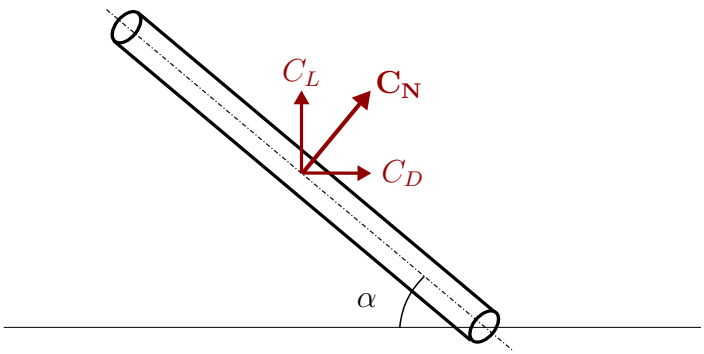

Figure 4.2: Aerodynamic forces in an inclined cylinder.

Focusing on the equivalent inclined cylinder of Figure 4.2, their normal force coefficient C_N can be expressed as a function of the angle of attack:

$$C_N = C_{D0} \sin^2 \alpha, \tag{4.18}$$

where C_{D0} is the drag coefficient without lift. This coefficient can be obtained following [Poulin and Larsen, 2007] as a function of the angle of attack and of the Reynolds number based on the diameter of the cylinder $Re_d \equiv Re$:

$$C_{D0} = \begin{cases} 1.2, & \text{if } Re\sin\alpha \leq 3\cdot 10^5, \\ -2\cdot 10^{-6} Re\sin\alpha + 1.8, & \text{if } 3\cdot 10^5 < Re\sin\alpha \leq 5\cdot 10^5, \\ 0.8, & \text{if } Re\sin\alpha > 5\cdot 10^5, \end{cases} \tag{4.19}$$

where $Re = \rho_\infty U_\infty d/\mu$, being ρ_∞ and U_∞ the air density and the speed at the prescribed flight condition, d the external diameter of the cylinder, and μ the viscosity of the air, fixed in a typical value of $1.79{\cdot}10^{-5}$ N·s/m^2 [Hoerner, 1965]. Results of Eq.(4.19) have been compared with [Hoerner, 1965], where the experimental variation of the coefficient as a function of the Reynolds Number is presented for different graphs, and it has been possible to conclude that the results are very similar.

Then, from Eq.(4.18), projecting on both axes:

$$C_L = C_N \cos\alpha = C_{D0}\sin^2\alpha\cos\alpha, \tag{4.20}$$
$$C_D = C_N \sin\alpha = C_{D0}\sin^3\alpha. \tag{4.21}$$

Eq.(4.20) provides the lift coefficient of the cylinder as a function of C_{D0} and α. However, Eq.(4.21) only provides one of the components of the drag coefficient: the pressure drag term C_{DP} [Hoerner, 1965]. For a complete analysis, it is necessary to add another important contribution [Roskam and Edward Lan, 1997], the term due to the friction drag C_{Df}. Although it will have a lower value than C_{DP}, this term is still fundamental to be able to characterize adequately the system, because it is the drag term which does not depend on the angle of attack (i.e., it is a constant term). For the estimation of the friction drag coefficient, the analysis presented in [Roskam and Edward Lan, 1997] will be followed, via the flat plate analogy:

$$C_{Df} = \sum FF \cdot C_{Df,i} \cdot \frac{S_{wet,i}}{S_{ref,C}}, \tag{4.22}$$

where FF is a form factor, based on the geometry of the configuration, $C_{Df,i}$ is the friction coefficient of each contribution, $S_{wet,i}$ the wet surface and $S_{ref,C}$ the reference surface. This contributions are added depending on whether the configuration is in laminar or turbulent state:

$$C_{Df} = FF\left(C_{Df,lam}\frac{S_{wet,lam}}{S_{ref,C}} + C_{Df,t}\frac{S_{wet,t}}{S_{ref,C}}\right). \tag{4.23}$$

The transition from laminar to turbulent state can be defined from a certain Reynolds number, called Transition Reynolds. Setting this value to $Re_{lt} = 10^5$, it is possible to define the transition point as $x_{lt} = Re_{lt}\mu/\rho_\infty U_\infty$. Depending on where that point is along the cylinder, the coefficients can be obtained as:

$$C_{Df,lam} = \begin{cases} \dfrac{0.664}{\sqrt{Re_{LT}}}, & \text{if } x_{lt} < l, \\ \dfrac{0.664}{\sqrt{Re_l}}, & \text{if } x_{lt} > l, \end{cases} \tag{4.24}$$

$$C_{Df,t} = \begin{cases} 0.288 \log(Re_l)^{-2.45}, & \text{if } x_{lt} < l, \\ 0, & \text{if } x_{lt} > l, \end{cases} \tag{4.25}$$

where l is the length of the cylinder, and Re_l is the Reynolds Number based on this length $Re_l = \rho_\infty U_\infty l/\mu$. Wet surfaces can be defined in a similar way:

$$S_{wet,lam} = \begin{cases} \pi d x_{lt}, & \text{if } x_{lt} < l, \\ \pi d(l - x_{lt}), & \text{if } x_{lt} > l, \end{cases} \tag{4.26}$$

$$S_{wet,t} = \begin{cases} \pi d l, & \text{if } x_{lt} < l, \\ 0, & \text{if } x_{lt} > l\text{-} \end{cases} \tag{4.27}$$

Finally, the reference surface is $S_{ref} = \pi d l$, and, following [Torenbeek, 1982], the form factor can be obtained as:

$$FF = 1 + \frac{60}{(l/d)^3} + \frac{l/d}{400}. \tag{4.28}$$

Then, the total drag coefficient is given by:

$$C_{D_{total}} = C_{Df} + C_{DP} = C_{Df} + C_{D0} \sin^3 \alpha. \tag{4.29}$$

Using the inclined cylinder lift and total drag coefficients, Eqs.(4.20) and (4.29), the two aerodynamic forces per unit length on the hose are:

$$p(s,t) = \frac{1}{2}\rho_\infty U_\infty^2 l_{ref} C_L(s,t), \tag{4.30}$$

$$q(s,t) = \frac{1}{2}\rho_\infty U_\infty^2 l_{ref} C_{D_{total}}(s,t), \tag{4.31}$$

where $l_{ref} = d/2$. Now the variables are function of s and t, since the hose angle of attack is also a function of these independent variables. Starting with the drag force $q(s,t)$, if we expand the coefficients:

$$q(s,t) = \frac{1}{2}\rho_\infty U_\infty^2 l_{ref} [C_{Df} + C_{D0} \sin^3 \alpha(s,t)],$$

which can also be expressed as:

$$q(s,t) = k_1 + k_2 \sin^3 \alpha(s,t), \tag{4.32}$$

where the constants k_1 and k_2 can be defined as follows:

$$k_1 = \frac{1}{2}\rho_\infty U_\infty^2 l_{ref} C_{Df}, \tag{4.33}$$

$$k_2 = \frac{1}{2}\rho_\infty U_\infty^2 l_{ref} C_{D0}. \tag{4.34}$$

In a similar way for the lift coefficient:

$$p(s,t) = \frac{1}{2}\rho_\infty U_\infty^2 l_{ref} C_{D0} \sin^2 \alpha(s,t) \cos \alpha(s,t),$$

or,

$$p(s,t) = k_2 \sin^2 \alpha(s,t) \cos \alpha(s,t). \tag{4.35}$$

And using the relationships of Eqs.(4.2)-(4.5) the aerodynamic forces on the hose can finally be expressed as:

$$p(s,t) = k_2 \left[\left(\frac{\partial y}{\partial s}(s,t) \right)^2 \frac{\partial x}{\partial s}(s,t) + 2\varepsilon \frac{\partial y}{\partial s}(s,t) \left(\frac{\partial x}{\partial s}(s,t) \right)^2 - \varepsilon \left(\frac{\partial y}{\partial s}(s,t) \right)^3 \right], \tag{4.36}$$

$$q(s,t) = k_1 + k_2 \left[\left(\frac{\partial y}{\partial s}(s,t) \right)^3 + 3\varepsilon \left(\frac{\partial y}{\partial s}(s,t) \right)^2 \frac{\partial x}{\partial s}(s,t) \right]. \tag{4.37}$$

4.1.4 Linearization

Eqs.(4.8) and (4.9) along with the boundary conditions given by Eqs.(4.10)-(4.11) and Eqs.(4.15)-(4.16) and with the aerodynamic forces defined in Eqs.(4.36) and (4.37) represent a system of nonlinear partial differential equations. Considering the applicability of this formulation to the complete process of aerial refueling - specifically, the pre-contact and post-contact deployed conditions of the hose - it is reasonable to assume small amplitude for external excitations from the static equilibrium position of the system. Examples of such external excitations can include oscillations of the tanker aircraft, a non-uniformity of the incident flow, the presence of a gust... This way to solve the equations aligns with strategies employed in references like [García-Fogeda et al., 2018] or [Ribbens et al., 2012], where the dynamic problem is solved starting from the static equilibrium position with small perturbations. However, if the amplitude of the motion cannot be considered small, a direct solution to the dynamic problem becomes necessary. This way is performed, for example, in [Goyal and Perkins, 2007].

Under this assumption of small perturbation the dynamic motion of the system can be expressed as a small amplitude oscillation with respect to the static equilibrium position. Therefore, the three unknowns of the system can be written as:

$$x(s,t) = x_e(s) + \delta_1 \cdot \xi(s,t), \tag{4.38}$$

$$y(s,t) = y_e(s) + \delta_1 \cdot \eta(s,t), \tag{4.39}$$

$$T(s,t) = T_e(s) + \delta_1 \cdot \tau(s,t), \tag{4.40}$$

where $y_e(s)$, $x_e(s)$ and $T_e(s)$ are the static equilibrium coordinates of the system and the static hose tension, respectively, δ_1 is the small amplitude unsteady perturbation (being always $\delta_1 << 1$), and $\eta(s,t)$, $\xi(s,t)$ and $\tau(s,t)$ are the perturbed values of the coordinates and the hose tension, respectively.

The hose angle of attack $\alpha(s,t)$ can also be split into two different contributions: The steady angle of attack $\alpha_e(s)$ and the angle of attack due to unsteady effects $\alpha_1(s,t)$:

$$\alpha(s,t) = \alpha_e(s) + \delta_1 \cdot \alpha_1(s,t), \tag{4.41}$$

where the effect of the downwash angle ε is included in the steady angle $\alpha_e(s)$. Considering the unsteady effect due to the oscillatory motion of the system, and assuming the

hypothesis of small angles, the unsteady angle of attack can be expressed as the ratio of the vertical speed of the hose $v(s,t)$ to the free-stream speed U_∞:

$$\alpha_1(s,t) = \frac{v(s,t)}{U_\infty} = \frac{\partial \eta}{\partial s}(s,t) + \frac{1}{U_\infty}\frac{\partial \eta}{\partial t}(s,t). \tag{4.42}$$

It should be noted that in Eq.(4.42) other terms must be added if other different unsteady effects were considered, such as, for example, a gust causing a non-uniformity in the incident airflow [García-Fogeda et al., 2018].

Projecting the angle of attack on both axes as presented in Eqs.(4.2)-(4.5), the aerodynamic forces given at Eqs.(4.37) and (4.36) can already be separated into a static term and a term of order δ_1. Thus, the drag can be expressed as:

$$q(s,t) = q_e(s) + \delta_1 \left.\frac{dq}{d\alpha}\right|_{\alpha_e}(s) \cdot \alpha_1(s,t), \tag{4.43}$$

where

$$q_e(s) = k_1 + k_2\left(\frac{dy_e}{ds}\right)^3 + 3\varepsilon k_2\left(\frac{dy_e}{ds}\right)^2\frac{dx_e}{ds}, \tag{4.44}$$

$$\left.\frac{dq}{d\alpha}\right|_{\alpha_e}(s) = 3k_2\left(\frac{dy_e}{ds}\right)^2\frac{dx_e}{ds}. \tag{4.45}$$

And in a similar way for the lift:

$$p(s,t) = p_e(s) + \delta_1 \left.\frac{dp}{d\alpha}\right|_{\alpha_e}(s) \cdot \alpha_1(s,t), \tag{4.46}$$

where

$$p_e(s) = k_2\left(\frac{dy_e}{ds}\right)^2\frac{dx_e}{ds} + \varepsilon k_2\left[2\frac{dy_e}{ds}\left(\frac{dx_e}{ds}\right)^2 - \left(\frac{dy_e}{ds}\right)^3\right], \tag{4.47}$$

$$\left.\frac{dp}{d\alpha}\right|_{\alpha_e}(s) = k_2\left[2\frac{dy_e}{ds}\left(\frac{dx_e}{ds}\right)^2 - \left(\frac{dy_e}{ds}\right)^3\right]. \tag{4.48}$$

Substitutions of Eqs.(4.39)-(4.48) into the original equations allows splitting the steady problem from the unsteady one (given by the terms of order δ_1). Consequently, the steady problem comprises a system of coupled nonlinear equations, while the unsteady problem is linearized and must be solved once the static equilibrium position of the system has been determined.

4.2 Static problem

This section focuses on analyzing the equilibrium position of the hose and drogue system. Due to the influence of the static equilibrium position on the dynamic motion of the hose-drogue system, it is critical to verify how different parameters affect to the steady position

of the system. Of particular importance is the vertical distance between the tanker and the drogue $y_e(s)$. The *Cobham's* catenary requirement, as referenced in [Liggieri, 2012], establishes a theoretical limit beyond which the system in the static equilibrium should not exceed. Achieving this limit can be challenging, especially under flight conditions at not very high speeds. In such cases, alternative strategies must be considered to reduce this distance. In following Chapters, this point will be again addressed.

The governing equations for the static coordinates of the hose $x_e(s)$, $y_e(s)$ and for the static tension $T_e(s)$ are:

$$q_e(s) + \frac{d}{ds}\left[T_e(s)\left(\frac{dx_e}{ds}(s) - \varepsilon\frac{dy_e}{ds}(s)\right)\right] = 0, \tag{4.49}$$

$$-p_e(s) + \rho_H g + \frac{d}{ds}\left[T_e(s)\left(\frac{dy_e}{ds}(s) + \varepsilon\frac{dx_e}{ds}(s)\right)\right] - EI\frac{d^4y_e}{ds^4}(s) = 0, \tag{4.50}$$

where $q_e(s)$ and $p_e(s)$ were defined in Eqs.(4.44) and (4.47). The boundary conditions at the hose-to-tanker junction are:

$$x_e|_0 = X_{T_e}, \tag{4.51}$$

$$y_e|_0 = Y_{T_e}, \tag{4.52}$$

and at the hose-to-drogue junction:

$$-T_e|_{s_0}\left(\left.\frac{dx_e}{ds}\right|_{s_0} - \varepsilon\left.\frac{dy_e}{ds}\right|_{s_0}\right) + Q = 0, \tag{4.53}$$

$$T_e|_{s_0}\left(\left.\frac{dy_e}{ds}\right|_{s_0} + \varepsilon\left.\frac{dx_e}{ds}\right|_{s_0}\right) + EI\left.\frac{d^3y_e}{ds^3}\right|_{s_0} - W + P = 0, \tag{4.54}$$

$$EI\left.\frac{d^2y_e}{ds^2}\right|_{s_0} \simeq 0. \tag{4.55}$$

The compatibility equation for the non-stretchable hose is:

$$\left(\frac{dx_e}{ds}(s)\right)^2 + \left(\frac{dy_e}{ds}(s)\right)^2 = 1. \tag{4.56}$$

In certain references such as [Eichler, 1978] or [García-Fogeda et al., 2018], a preliminary analytical integration of Eqs.(4.49)-(4.56) was feasible to solve for $dx_e/ds(s)$, $dy_e/ds(s)$ and $T_e(s)$. Afterwards, a second numerical integration was applied to determine the static equilibrium position $x_e(s)$ and $y_e(s)$. However, the inclusion of the hose bending force, the downwash angle effect and the present model of the aerodynamic forces presented previously renders a first analytical integration impractical in this formulation.

To address this challenge, the system of Eqs.(4.49)-(4.56) is reformulated into a first-order non-linear ordinary differential equation system. Solving this system with the boundary conditions at the end of the hose Eqs.(4.53)-(4.55), yields $dx_e/ds(s)$, $dy_e/ds(s)$ and $T_e(s)$. Finally, a second numerical integration is performed with the boundary conditions at the beginning of the hose Eq.(4.51), resulting in the determination of the static equilibrium position of the hose-drogue system.

4.3 Dynamic problem

In this section the dynamic response of the system to small perturbations respect to the static position is studied. These perturbations can arise from various sources, for example due to responses to gusts, oscillations of the hose reel, turbulence effects, and more, as noted in [García-Fogeda et al., 2018]. However, this work specifically analyzes the effect of a force of low intensity applied at the drogue. Therefore, under the assumption of small perturbations for dynamics, equations will be linearized following the approach outlined in [Ribbens et al., 2012]. Thus, large-amplitude oscillations, as investigated in studies such as [Goyal and Perkins, 2007], are not studied in this work.

By obtaining the dynamic properties of the hose and drogue system, including natural frequencies and damping coefficients, a comprehensive evaluation can be conducted to identify and analyze differences that emerge in the system's behavior.

4.3.1 Perturbed equations

From Eqs.(4.8) and (4.9), using the linearization presented in Eqs.(4.38)-(4.40) and retaining only terms of order δ_1, the governing equations for the perturbed coordinates of the hose $\xi(s,t)$, $\eta(s,t)$ and the perturbed tension $\tau(s,t)$ are:

$$-\rho_H \frac{\partial^2 \xi}{\partial t^2}(s,t) - c\frac{\partial \xi}{\partial t}(s,t) + \left.\frac{dq}{d\alpha}\right|_{\alpha_e}(s)\alpha_1(s,t) + \tau(s,t)\frac{d^2 x_e}{ds^2}(s) + \frac{dT_e}{ds}(s)\frac{\partial \xi}{\partial s}(s,t) + T_e(s)\frac{\partial^2 \xi}{\partial s^2}(s,t) + \frac{\partial \tau}{\partial s}(s,t)\frac{dx_e}{ds}(s) = 0, \tag{4.57}$$

$$-\rho_H \frac{\partial^2 \eta}{\partial t^2}(s,t) - c\frac{\partial \eta}{\partial t}(s,t) - \left.\frac{dp}{d\alpha}\right|_{\alpha_e}(s)\alpha_1(s,t) - EI\frac{\partial^4 \eta}{\partial s^4}(s,t) + \tau(s,t)\frac{d^2 y_e}{ds^2}(s) + \frac{dT_e}{ds}(s)\frac{\partial \eta}{\partial s}(s,t) + T_e(s)\frac{\partial^2 \eta}{\partial s^2}(s,t) + \frac{\partial \tau}{\partial s}(s,t)\frac{dy_e}{ds}(s) = 0. \tag{4.58}$$

Where the unsteady angle of attack $\alpha_1(s,t)$ has been defined in Eq.(4.42). The boundary conditions at the beginning of the hose are:

$$\xi(0,t) = \Delta X_T(t), \tag{4.59}$$

$$\eta(0,t) = \Delta Y_T(t), \tag{4.60}$$

where ΔX_T and ΔY_T are the unsteady prescribed motions of the tanker, which, as explained previously, are assumed to be known. The boundary conditions at the end of the hose are:

$$\tau(s_0,t)\left.\frac{dy_e}{ds}\right|_{s_0} + T_e|_{s_0}\frac{\partial \eta}{\partial s}(s_0,t) - \frac{W}{g}\frac{\partial^2 \eta}{\partial t^2}(s_0,t) + EI\frac{\partial^3 \eta}{\partial s^3}(s_0,t) = 0, \tag{4.61}$$

$$-\tau(s_0,t)\left.\frac{dx_e}{ds}\right|_{s_0} - T_e|_{s_0}\frac{\partial \xi}{\partial s}(s_0,t) = 0, \tag{4.62}$$

$$EI\frac{\partial^2 \eta}{\partial s^2}(s_0,t) \simeq 0. \tag{4.63}$$

Eqs.(4.57) and (4.58) together with the boundary conditions given by Eqs.(4.59)-(4.63), constitute the set of differential equations that must be solved to obtain the free-vibration response of the system. It is important to highlight that the linear terms involving the downwash angle, which were present in previous sections, do not appear in these equations as they are now considered second-order effects.

Eqs.(4.57) and (4.58) reveal three unknowns: the horizontal and vertical motions of the hose relative to its static position, and the variation in the hose tension from its steady-state value. Focusing the analysis on this last term, an important hypothesis will be performed: Given the phase of the refueling process being analyzed (the fully deployment of the hose) and the assumption of small oscillations around the equilibrium position, it is reasonable to consider the unsteady effects on hose tension negligible. Therefore, for the remainder of the analysis, the value of $\tau(s,t) \simeq 0$ will be assumed. The work of [Zhu and Meguid, 2007] supports this hypothesis. In another works, such as [Eichler, 1978] or [García-Fogeda et al., 2018], the assumption of $\tau = 0$ is also made. It is important to note, however, that this assumption may not hold in other phases of the refueling process (e.g., the hose deploying or the hose retrieval). Under this hypothesis, the horizontal and vertical dynamic equations for the perturbed motion can be reformulated as follows:

$$-\rho_H \frac{\partial^2 \xi}{\partial t^2}(s,t) - c\frac{\partial \xi}{\partial t}(s,t) + \left.\frac{dq}{d\alpha}\right|_{\alpha_e}(s)\left(\frac{\partial \eta}{\partial s}(s,t) + \frac{1}{U_\infty}\frac{\partial \eta}{\partial t}(s,t)\right) + \frac{\partial}{\partial s}\left(T_e(s)\frac{\partial \xi}{\partial s}(s,t)\right) = 0, \tag{4.64}$$

$$-\rho_H \frac{\partial^2 \eta}{\partial t^2}(s,t) - c\frac{\partial \eta}{\partial t}(s,t) - \left.\frac{dp}{d\alpha}\right|_{\alpha_e}(s)\left(\frac{\partial \eta}{\partial s}(s,t) + \frac{1}{U_\infty}\frac{\partial \eta}{\partial t}(s,t)\right) - EI\frac{\partial^4 \eta}{\partial s^4}(s,t) + \frac{\partial}{\partial s}\left(T_e(s)\frac{\partial \eta}{\partial s}(s,t)\right) = 0. \tag{4.65}$$

And the boundary conditions:

$$\xi(0,t) = \Delta X_T(t) \equiv 0, \tag{4.66}$$

$$\eta(0,t) = \Delta Y_T(t) \equiv 0, \tag{4.67}$$

$$T_e|_{s_0}\frac{\partial \eta}{\partial s}(s_0,t) - \frac{W}{g}\frac{\partial^2 \eta}{\partial t^2}(s_0,t) + EI\frac{\partial^3 \eta}{\partial s^3}(s_0,t) = 0, \tag{4.68}$$

$$T_e|_{s_0}\frac{\partial \xi}{\partial s}(s_0,t) = 0, \tag{4.69}$$

$$EI\frac{\partial^2 \eta}{\partial s^2}(s_0,t) = 0, \tag{4.70}$$

where, as can be seen in Eqs.(4.66) and (4.67), the unsteady prescribed motions of the tanker is assumed equal to zero on both axes.

4.3.2 Lag in the unsteady aerodynamic forces

The model presented in the previous subsection allows for the dynamic analysis of the hose-drogue system. However, in order to update the model with a more physical accuracy and reliability, some improvements will be included in the aerodynamic terms of the

equations.

Classical references such as [Theodorsen, 1934] indicate that the unsteady aerodynamic forces acting on a vibrating structure will have a certain lag with respect to its vibration motion. The inclusion of this lag between structure and aerodynamics can be approached from different perspectives. Theoretically, a formulation based on the solution for the Navier-Stokes equations, accounting for fluid detachment around the oscillating hose, would be necessary. Although accurate, this way would render the computation of the hose and drogue system dynamics and stability prohibitively time-consuming or even unfeasible. This challenge has been overcome in this thesis with an alternative approach: In complex fluid-structure interactions, the phase lag angle is often introduced into the model and the stability of the system is determined with this angle as a parameter. This resolution strategy is very similar to approaches for stall flutter problems, as can be seen for example in [Dowell, 2015].

To estimate this parameter, among various existing references in this field, the work of [Sarpkaya, 2004] is selected. In this reference a comprehensive review of the vortex-induced vibrations phenomena in cylinders is performed. Following this work, we estimate the phase lag angle ψ between the unsteady aerodynamic forces on the hose and its motion as:

$$\tan\psi = \frac{2cf_{vac}f_{com}}{f_{vac}^2 - f_{com}^2}, \tag{4.71}$$

where:

- c is the structural damping coefficient of the hose, obtained from the dynamic test presented in Chapter 3 and used previously in the equations of this chapter.
- f_{vac} is the frequency in vacuum of the system. Since Eq.(4.71) is obtained from a single degree-of-freedom model, see [Sarpkaya, 2004], there is only one frequency, unlike this work, where, as will be seen later, a large number of frequencies are obtained. However, it has been proved that the use of the first frequency in vacuum for f_{vac} provides a conservative estimation (yielding the largest value of ψ) and therefore that value will be used.
- f_{com} represent the frequency of the system including the fluid effect. As in the case of f_{vac}, the first frequency obtained will be used for f_{com} to ensure a conservative estimation.

Once the frequencies of the hose with and without fluid effects are known, an estimation of the phase angle ψ can be obtained with this simplified expression. Further details on these estimates and how the parameter affects the results will be presented at the end of this chapter.

4.3.3 FEM model

4.3.4 Equations for the spatial domain

Focusing on the perturbed variables $\xi(s,t)$ and $\eta(s,t)$, applying separation of variables they can be written as:

$$\xi(s,t) = X(s) \cdot e^{\lambda t}, \tag{4.72}$$

$$\eta(s,t) = N(s) \cdot e^{\lambda t}, \tag{4.73}$$

where $X(s)$ and $N(s)$ represent the spatial part of the horizontal and vertical motions, respectively, and the exponential term with the eigenvalue λ represents the temporal part.

The resolution process will consist of using the separation of variables in the dynamic equations of the system, Eqs.(4.64) and (4.65), and in the boundary conditions Eqs.(4.66)-(4.70). As detailed in the previous Section, the phase lag in the unsteady aerodynamic forces is included as a parametric-type phase angle ψ. This angle enters into the formulation through the unsteady angle of attack of the hose as:

$$\alpha_1(s,t) = \left(N'(s) + \frac{\lambda}{U_\infty} N(s) \right) \cdot e^{\lambda t + i\psi}, \tag{4.74}$$

where the perturbed variable $\eta(s,t)$ of Eq.(4.73) has been modified to consider the phase angle ψ, i.e., $\eta(s,t) = N(s) \cdot \exp(\lambda t + i\psi)$. Substitution in Eqs.(4.64) and (4.65) yields:

$$-\rho_H \lambda^2 X(s) - c\lambda X(s) + \left.\frac{dq}{d\alpha}\right|_{\alpha_e}(s) \left(N'(s) + \frac{\lambda}{U_\infty} N(s) \right) \cdot e^{i\psi} + \frac{d}{ds}[T_e X'(s)] = 0. \tag{4.75}$$

$$-\rho_H \lambda^2 N(s) - c\lambda N(s) - \left.\frac{dp}{d\alpha}\right|_{\alpha_e}(s) \left(N'(s) + \frac{\lambda}{U_\infty} N(s) \right) \cdot e^{i\psi}$$

$$- EI \cdot N^{IV}(s) + \frac{d}{ds}[T_e N'(s)] = 0. \tag{4.76}$$

Eqs.(4.75) and (4.76) form a system of ordinary differential equations with two unknowns: $X(s)$ and $N(s)$. The first term in both equations (the one multiplying λ^2) represents the inertia of the system. The terms multiplying λ represent the damping, while the constant terms represent the stiffness. It is interesting to mention that the vertical motion is decoupled from the horizontal, but not vice-versa. The boundary conditions in the split variables $X(s)$ and $N(s)$ are now:

$$X(0) = N(0) = 0, \tag{4.77}$$

$$T_e|_{s_0} X'(s_0) = 0, \tag{4.78}$$

$$T_e|_{s_0} N'(s_0) - \frac{W}{g} \lambda^2 N(s_0) + EI \cdot N'''(s_0) = 0, \tag{4.79}$$

$$EI \cdot N''(s_0) = 0. \tag{4.80}$$

In Eq.(4.77) is shown that the prescribed motion of the tanker is assumed equal to zero. Eqs.(4.75) and (4.76) can be written in a compact matrix form grouping the terms according to their dependence on the eigenvalue λ as:

$$\lambda^2 \boldsymbol{A_1}(s) + \lambda \boldsymbol{A_2}(s) + \boldsymbol{A_3}(s) = \boldsymbol{0}, \tag{4.81}$$

where:

$$\boldsymbol{A_1}(s) = \begin{bmatrix} -\rho_H X(s) & 0 \\ 0 & -\rho_H N(s) \end{bmatrix} \tag{4.82}$$

$$\boldsymbol{A_2}(s) = \begin{bmatrix} -cX(s) & \dfrac{1}{U_\infty}\dfrac{dq}{d\alpha}\Big|_{\alpha_e}(s)e^{i\psi}N(s) \\ 0 & -cN(s) - \dfrac{1}{U_\infty}\dfrac{dp}{d\alpha}\Big|_{\alpha_e}(s)e^{i\psi}N(s) \end{bmatrix} \tag{4.83}$$

$$\boldsymbol{A_3}(s) = \begin{bmatrix} \dfrac{d}{ds}[T_e X'(s)] & \dfrac{dq}{d\alpha}\Big|_{\alpha_e}(s)e^{i\psi}N'(s) \\ 0 & \dfrac{d}{ds}[T_e N'(s)] - \dfrac{dp}{d\alpha}\Big|_{\alpha_e}(s)e^{i\psi}N'(s) - EI \cdot N^{IV}(s) \end{bmatrix} \tag{4.84}$$

Hose Discretization: Weighted Residual Method

Eq.(4.81) together with the boundary conditions Eqs.(4.77)-(4.80) represents a system of ordinary differential equations. The solution of these equations will be computed by discretizing the hose into a number of elements high enough to ensure the convergence of the solution. Spatial discretization can be approached in various ways, with the Finite Element Method (FEM) being the most common. However, this thesis adopts a broader approach by the use of the Weighted Residual Method, detailed in [Finlayson, 1972]. This method, which is based on assuming approximate solutions that should accomplish certain conditions, is more versatile than the Finite Element Method, since through its use a FEM problem can be generated.

First, approximates solutions of the horizontal and vertical spatial motions of the hose, denoted as $\hat{X}(s)$ and $\hat{N}(s)$ respectively, which meet the boundary conditions at the beginning of the hose, Eq.(4.77), are defined. Eq.(4.81) is reformulated as:

$$\lambda^2 \hat{\boldsymbol{A}}_{\boldsymbol{1}}(s) + \lambda \hat{\boldsymbol{A}}_{\boldsymbol{2}}(s) + \hat{\boldsymbol{A}}_{\boldsymbol{3}}(s) = \hat{\boldsymbol{R}}(s), \tag{4.85}$$

where the matrices $\hat{\boldsymbol{A}}_{\boldsymbol{1}}(s)$, $\hat{\boldsymbol{A}}_{\boldsymbol{2}}(s)$ and $\hat{\boldsymbol{A}}_{\boldsymbol{3}}(s)$ are the approximate values of $\boldsymbol{A_1}(s)$, $\boldsymbol{A_2}(s)$ and $\boldsymbol{A_3}(s)$, and $\hat{\boldsymbol{R}}(s)$ denotes the non-zero residue of the approximate solution, also called the residue function.

The hose is discretized into elements along its length. The Weighted Residual Method applies the following condition to the residue function defined in Eq.(4.85):

$$\int_{s_j}^{s_{j+1}} [\varphi_k(s) R_l(s) ds] + \varphi_k(s_0) r_l(s_0) = 0; \quad k = 1, \cdots, N_s; \quad l = x, y, \tag{4.86}$$

where $\varphi_k(s)$ are weighted functions (or form functions) of each element of the hose, $r_l(s_0)$ the residue function of the boundary conditions at the end of the hose (in the last element) and N_s the number of elements. By replacing for every element Eq.(4.85) in Eq.(4.86) the discretized dynamic equations of the system are obtained. The form functions to be used depend on the degrees of freedom assigned to each node of the hose after it has been discretized. These functions should be as simple as possible without compromising the physical sense of the approach. For this reason, different form functions will be employed depending on the terms that appear in the equations:

- **Linear functions** $\varphi^{(1)}(s)$: Suitable for terms related to the tension on the hose, as well as the rest of the terms except the ones related to the hose bending, linear form functions can be utilized because, as will be verified later, do not include derivatives of higher order than one. They are defined as:

$$\varphi_j^{(1)}(s) = \begin{cases} \dfrac{s - s_{j-1}}{s_j - s_{j-1}}, & \text{if } s_{j-1} \leq s \leq s_j, \\ \dfrac{s_{j+1} - s}{s_{j+1} - s_j}, & \text{if } s_j \leq s \leq s_{j+1}, \end{cases} \tag{4.87}$$

  where $j = 1, \cdots, N_s$. These functions must satisfy the following values at the ends of each element:

$$\varphi_j^{(1)}(s_{j-1}) = 0, \qquad \varphi_j^{(1)}(s_j) = 1, \qquad \varphi_j^{(1)}(s_{j+1}) = 0. \tag{4.88}$$

  These functions will be used in all the terms of the equations except the ones associated to the hose bending. Therefore, the approximation of the spatial part of the perturbed variables, $\hat{X}(s)$ and $\hat{N}(s)$ in all of these terms can be written as:

$$\hat{X}(s) = \sum_{j=1}^{N_s+1} v_j \cdot \varphi_j^{(1)}(s), \tag{4.89}$$

$$\hat{N}(s) = \sum_{j=1}^{N_s+1} w_j \cdot \varphi_j^{(1)}(s), \tag{4.90}$$

  where v_j and w_j are the horizontal and vertical displacements of the each node of the hose.

- **Cubic functions** $\varphi^{(3)}(s)$: For bending terms, which involve higher derivatives, the linear form functions cannot be used. Therefore, it is necessary to use cubic functions, as they are the lowest-order functions that can satisfy the boundary conditions associated with bending. Moreover, a new distinction must be made between these functions, since, unlike the rest of the terms, the bending degrees of freedom encompass both vertical displacement and hose rotation. Although, as will be discussed later, the rotational degrees of freedom for each element of the hose will not appear in the final equations, they must be considered in the formulation at this stage.The form functions for the hose displacement are:

$$\varphi_{j,d}^{(3)}(s) = \begin{cases} -2\left(\dfrac{s - s_{j-1}}{s_j - s_{j-1}}\right)^3 + 3\left(\dfrac{s - s_{j-1}}{s_j - s_{j-1}}\right)^2, & \text{if } s_{j-1} \leq s \leq s_j, \\ -2\left(\dfrac{s_{j+1} - s}{s_{j+1} - s_j}\right)^3 + 3\left(\dfrac{s_{j+1} - s}{s_{j+1} - s_j}\right)^2, & \text{if } s_j \leq s \leq s_{j+1}, \end{cases} \tag{4.91}$$

and for the hose rotation:

$$\varphi_{j,r}^{(3)}(s) = \begin{cases} \dfrac{(s-s_{j-1})^3}{(s_j-s_{j-1})^2} - \dfrac{(s-s_{j-1})^2}{s_j-s_{j-1}}, & \text{if } s_{j-1} \leq s \leq s_j, \\ \dfrac{(s_{j+1}-s)^3}{(s_{j+1}-s_j)^2} - \dfrac{(s_{j+1}-s)^2}{s_{j+1}-s_j}, & \text{if } s_j \leq s \leq s_{j+1}, \end{cases} \tag{4.92}$$

Therefore, in this case the manipulation of the equations will be different depending on the degrees of freedom analyzed. The form functions for each element presented in Eqs.(4.91) and (4.92) have been chosen to meet the boundary conditions presented in Table 4.1.

Table 4.1: Boundary conditions for the cubic form functions.

	Displac., d		Rotation, r	
	$s_{j\pm1}$	s_j	$s_{j\pm1}$	s_j
$\varphi_j^{(3)}(s)$	0	1	0	0
$\varphi_j^{'(3)}(s)$	0	0	0	1

The vertical perturbed variable $\hat{N}(s)$ in the bending term can be written as:

$$\hat{N}(s) = \sum_{j=1}^{N_s+1} [w_j \cdot \varphi_{j,d}^{(3)}(s) + \theta_j \cdot \varphi_{j,r}^{(3)}(s)], \tag{4.93}$$

where θ_j are the rotations of each node of the hose.

Once all the form functions were defined, the WRM condition, Eq.(4.86), is applied to Eq.(4.81). The boundary conditions coming from the bending term will be multiplied by their respective form functions, i.e., the forces equilibrium condition goes with the displacements, and the momentum equilibrium condition goes with the rotations.

With these considerations, applying the Weighted Residual Method to the horizontal and vertical dynamic equations Eqs.(4.75) and (4.76) and approaching $\hat{X}(s)$ and $\hat{N}(s)$ (as well as their respective derivatives) with the different form functions, as can be seen with detail in the Appendix A, the formulation of the problem can finally be expressed as:

$$(\lambda^2 \boldsymbol{M} + \lambda \boldsymbol{B} + \boldsymbol{K})\boldsymbol{u} = \boldsymbol{0}, \tag{4.94}$$

where $\boldsymbol{M}$, $\boldsymbol{B}$ and $\boldsymbol{K}$ are the inertia, damping and stiffness matrices, respectively, and $\boldsymbol{u}$ the vector which represents the degrees-of-freedom of the system. As has been shown, the degrees of freedom at each node of the hose include horizontal displacement, vertical displacement, and rotation. However, the vector $\boldsymbol{u}$ will contain only the horizontal and vertical displacements. This is because, as will be explained below, a reduction in the degrees of freedom of the system will be performed, excluding the rotational degree of freedom associated with the bending of the hose. Next, the different matrices will be presented. Further details of the derivation of Eq.(4.94) as well as the development of the following matrices are presented in Appendix A.

Inertia matrix

Considering the different contributions the inertia matrix can be expressed as:

$$\boldsymbol{M} = \begin{bmatrix} \boldsymbol{M^{xx}} & \mathbf{0} \\ \mathbf{0} & \boldsymbol{M^{yy}} \end{bmatrix}, \tag{4.95}$$

where $\boldsymbol{M^{xx}}$ and $\boldsymbol{M^{yy}}$ are the inertia matrices of the horizontal and the vertical motion of the hose, respectively, and are obtained from the first term associated to Eqs.(A.6) and (A.7). The development of each term of the inertia matrix is showed in Appendix A.

Damping matrix

The damping matrix can be expressed as:

$$\boldsymbol{B} = \begin{bmatrix} \boldsymbol{B^{xx}} & \boldsymbol{B^{xy}} \\ \mathbf{0} & \boldsymbol{B^{yy}} \end{bmatrix}, \tag{4.96}$$

where $\boldsymbol{B^{xx}}$ and $\boldsymbol{B^{yy}}$ are the damping matrices of the horizontal and the vertical motion, and $\boldsymbol{B^{xy}}$ represents the horizontal damping matrix due to the vertical motion (the fourth term of Eq.(A.6)). As can be seen, there is coupling in the horizontal motion with the vertical but not vice versa. This fact was already seen in Eq.(4.75).

It is important to note that the damping matrices incorporate two sources of damping: structural damping (terms multiplied by the coefficient c) and aerodynamic damping (terms arising from the aerodynamic forces of the hose). This fact has also been seen throughout the development of the equations in this chapter. The details of the sub-matrices are presented in Appendix A.

Stiffness matrix

The stiffness matrix is expressed as:

$$\boldsymbol{K} = \begin{bmatrix} \boldsymbol{K^{xx}} & \boldsymbol{K^{xy}} \\ \mathbf{0} & \boldsymbol{K^{yy}} \end{bmatrix}, \tag{4.97}$$

As previously mentioned, coupling terms between horizontal and vertical motion appear in both damping and stiffness. However, these terms are present only in the horizontal motion, Eq.(4.75), while they do not appear in the vertical motion, Eq.(4.76). In other words, the horizontal motion is coupled with the vertical motion, but not vice versa. Thus, it is possible to solve the vertical motion of the system independently of the horizontal.

Eigenvalues problem

With all the matrices defined, the equation of the system Eq.(4.94) can be solved. That equation, set to zero, represents the free vibration problem of the hose-drogue system.

Since the objective of this part of the thesis is to obtain the dynamic properties of the system (frequencies and damping coefficients), the eigenvalue problem derived from the equation will be solved. The eigenvalue problem is based on computing the determinant associated to Eq.(4.94):

$$||\lambda^2 \boldsymbol{M} + \lambda \boldsymbol{B} + \boldsymbol{K}|| = 0. \tag{4.98}$$

From the resulting complex eigenvalues λ_i, the natural frequencies and damping coefficients can be obtained as:

$$\omega_i = \mathrm{Im}(\lambda_i), \tag{4.99}$$

$$\gamma_i = \frac{\mathrm{Re}(\lambda_i)}{2\mathrm{Im}(\lambda_i)}, \tag{4.100}$$

where $\mathrm{Re}(\lambda_i)$ and $\mathrm{Im}(\lambda_i)$ are the real and the imaginary parts of the eigenvalues, respectively.

4.4 Aeroelastic analysis

After obtaining the inertia, damping and stiffness matrices of the system, and therefore its dynamic properties, the next step is to analyze the aeroelastic stability of the system. In particular, the obtention of the flutter speeds, frequencies and modal shapes under different flight conditions and parameters. As described previously, the system is statically nonlinear but dynamically linear, being coupled static and dynamic problems. Therefore, ensuring the accuracy of both static and dynamic solutions are crucial in order to analyze the aeroelastic stability of the system.

With respect to the flutter computation, unlike the classical linear flutter (see, for example, the book of [Fung, 1993]), in this work the static equilibrium position influence on the dynamic forces. Therefore, the flutter solution will depend on the non-linearity effects of the static or steady configuration equilibrium.

There are several studies focused on non-linearities in aeroelastic problems. Among them, some analyze non-linearities from the structural point of view (see for example [Crespo da Silva et al., 1991]), while others discuss limit cycle oscillations or aerodynamic flows with shock waves (see for example [Dowell, 2015]), or applications in non-linear analysis to High-Altitude Long-Endurance aircrafts (like the work of [Patil et al., 2001]). However, for the validation of the present model, references like [Tang and Dowell, 2001], [Cestino et al., 2019] or [Romeo et al., 2006] are particularly noteworthy. These studies provide detailed analyses of the effect of the deformed equilibrium position on the highly flexible wings flutter with respect to the undeformed position. The results of these works allow validating the procedure of the computation of flutter instabilities on the hose and drogue system with a nonlinear static model.

Regarding the dynamic problem, linearization of the equations from the equilibrium position will significantly affect the stability of the system. Examples of time linearization can be found in certain studies focused on other types of aeroelastic instabilities. For

example, works like [Zhang et al., 2012] or [Kreiselmaier and Laschka, 2000], where an aeroelastic analysis with linearized Euler equations is performed, show that the calculation from linearized dynamic equations is sufficiently reliable to predict accurately the flutter boundary.

The stability of the system will be obtained for different flight conditions (altitudes and speeds), as well as for different values of the lag angle ψ. As discussed previously, this angle is included in the model as a parameter, although it is possible to perform an estimation from the results of the frequencies of the system by the use of Eq.(4.71). The process for calculating flutter on the system is summarized as follows:

1. The value of the phase lag angle ψ is fixed. The process will start at $\psi = 0$ and will increase until the system becomes unstable. As will be seen in the results Section below, the inclusion of the lag angle will produce remarkable changes in the dynamic properties of the system.

2. The flight altitude H_∞ is fixed, starting at the maximum altitude at which the refueling process can be safely performed (30000 ft, 9144 m) and will decrease to the minimum (5000 ft, 1424 m).

3. For each lag angle and flight altitude a sweep in the flight speed U_∞ is performed, starting from the lowest speed for refueling (see [García-Fogeda et al., 2018]) until a value high enough to cover all possible flight envelopes.

4. For each flight altitude and flight speed, the static equilibrium position of the system is obtained.

5. For each lag angle, flight altitude and flight speed the dynamic problem is solved following the development presented along the chapter. Inertia, damping and stiffness matrices of the system are obtained. Then, the eigenvalues given by the solution of Eqs.(4.99) and (4.100) and therefore the frequencies and damping coefficients of the system are computed.

6. Flutter speeds are search by means of the Tracing of the Roots method. Therefore, if all the eigenvalues calculated are with real part negative (all the damping coefficients are negative) the system will be stable at this flight condition and this value of ψ, and the process will start again at point 1. However, if the real part of any of the eigenvalues becomes positive, flutter will occur for that flight condition and lag angle. In that case, the speed at which the damping coefficient of the mode associated with that eigenvalue, see Eq.(4.100), is equal to zero will be the flutter speed of the system under these conditions. The frequency corresponding to this speed will be the flutter frequency, and the eigenvector associated to the corresponding eigenvalue will be the flutter mode of the system.

7. Once the flutter boundaries have been obtained, the last step would be to asess if in the corresponding flight condition the actual phase angle of the system can reach the assumed values. As explained previously, for this purpose an estimation of the angle based on the frequencies of the system is performed using Eq.(4.71). If the estimated value is less than the value assumed for flutter computation, it can be concluded that the system will be stable at this flight condition.

4.5 Response of the system due to the drogue-receiver contact

The hose and drogue model developed allows not only to study the stability of the system, but to analyze another types of relevant dynamic problems which can appear during the refueling process. Among them, the response when the drogue comes into contact with the receiver aircraft was selected to be studied once the aeroelastic analysis has been performed. This phase of the refueling has not been studied at any point in the thesis until now, as all static and dynamic calculations have been carried out for the hose in a fully deployed state but before the contact between the drogue and the receiver aircraft. Nonetheless, it is worth noting that once the inertia, damping, and stiffness matrices and the dynamic properties of the system are obtained, in addition to studying the aeroelastic stability, analyzing how the hose responds when the drogue makes contact with the receiver is not particularly challenging.

Other authors which present results of this contact are, for example, [Zhu and Meguid, 2006], which presents the effect of non-linearities due to the contact in the system, or [Yamashiro et al., 2011], which shows that the force transmitted into the drogue could cause a reduction in the value of the hose tension to almost zero. However, in this model only linear terms for the dynamic response will be retained, and the perturbation on the system will be analyzed using first a simple vertical impulse and then a realistic profile of speeds from the receiver aircraft. Hence, with the dynamic properties of the system it is possible to study the displacements and maximum forces that this contact can produce in the hose and in the drogue accurately.

The external input to the system will come from the speed profiles of the receiver V_x and V_y once the contact with the drogue takes place (see Figure 4.3). It is assumed that at the instant of contact, the hose-drogue system is in equilibrium.

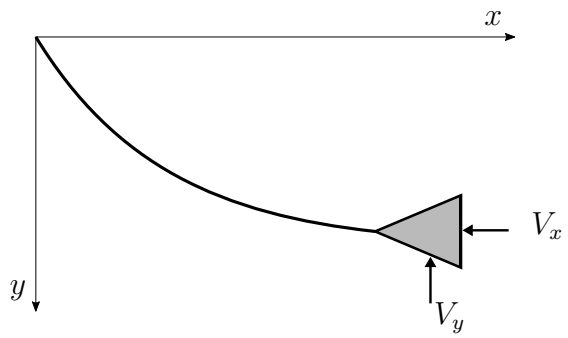

Figure 4.3: Drogue-Receiver contact speed.

Two different cases due to the receiver contact will be considered: First, the response to an instantaneous impulse in the vertical speed will be analyzed. This case will be useful for analyzing the system's behavior and drawing interesting conclusions about certain parameters of the model, particularly the effect of including bending forces. Then, the response to a realistic velocity profile of the receiver provided by Airbus Defence and Space within the HDA3R refueling project will be analyzed, and the hose displacements

and the force transmitted to it upon contact will be obtained.

With the inertia, damping and stiffness matrices attained from Eqs.(4.95)-(4.97) and with the speed receiver profile to be used the response of the system to the contact is a initial conditions problem:

The dynamic response of the hose-drogue system to the contact with the receiver is an initial conditions problem which can be expressed as:

$$\boldsymbol{M}\ddot{\boldsymbol{u}}(t) + \boldsymbol{B}\dot{\boldsymbol{u}}(t) + \boldsymbol{K}\boldsymbol{u}(t) = \boldsymbol{0}, \tag{4.101}$$

$$\boldsymbol{u}(0) = \boldsymbol{u_0}, \tag{4.102}$$

$$\dot{\boldsymbol{u}}(0) = \dot{\boldsymbol{u}}_{\boldsymbol{0}}, \tag{4.103}$$

where the matrices were defined at Eqs.(4.95)-(4.97), $\boldsymbol{u}(t) = \{\boldsymbol{u_x}(t)\ \boldsymbol{u_y}(t)\}^T$ are the horizontal and vertical displacements of the system after contact. As $\boldsymbol{u}$(t) is defined as the motion from the static equilibrium position of the drogue defined previously, the initial condition in the displacements $\boldsymbol{u_0}$ will be zero. The initial condition in the speeds $\dot{\boldsymbol{u}}_{\boldsymbol{0}}$ will be also zero for all the nodes except on the last node (last term in $\boldsymbol{u_x}$ and last term in $\boldsymbol{u_y}$), which will be equal to the receiver speed profile considered.

4.5.1 Response due to an instantaneous impulse

First, the response due to a vertical impulse in $t = 0$ will be studied. The initial conditions for this case are:

$$\boldsymbol{u}(0) = \boldsymbol{u_0}, \tag{4.104}$$

$$\dot{\boldsymbol{u}}(0) = \begin{Bmatrix} 0 \\ \vdots \\ V_{0y} \end{Bmatrix}, \tag{4.105}$$

where V_{0y} is the vertical speed difference between the receiver aircraft and the hose and drogue system. The approach for solving this initial conditions problem is based on expressing the equation in modal coordinates (see [Shabana, 1991]). The relationship between the physical and modal coordinates is as follows:

$$\boldsymbol{u}(t) = \boldsymbol{\phi} \cdot \boldsymbol{u_h}(t), \tag{4.106}$$

where $\boldsymbol{u_h}$ are the modal coordinates, and $\boldsymbol{\phi}$ is the modal matrix of the system obtained from the normal modes (the eigenvectors of Eq.(4.98)), which in this case (with non-zero damping) is a complex matrix. The modes are normalized with the mass matrix. In order to write Eq.(4.101) in the modal space, it must be pre-multiplied by the conjugated transposed modal matrix as follows:

$$\boldsymbol{\phi^*}^T \cdot \boldsymbol{M} \cdot \boldsymbol{\phi} \cdot \ddot{\boldsymbol{u}}(t) + \boldsymbol{\phi^*}^T \cdot \boldsymbol{B} \cdot \boldsymbol{\phi} \cdot \dot{\boldsymbol{u}}(t) + \boldsymbol{\phi^*}^T \cdot \boldsymbol{K} \cdot \boldsymbol{\phi^*} \cdot \boldsymbol{u}(t) = \boldsymbol{0}, \tag{4.107}$$

Eq.(4.107) can be expressed as:

$$\boldsymbol{M_{hh}}\ddot{\boldsymbol{u}}_{\boldsymbol{h}}(t) + \boldsymbol{B_{hh}}\dot{\boldsymbol{u}}_{\boldsymbol{h}}(t) + \boldsymbol{K_{hh}}\boldsymbol{u_h}(t) = \boldsymbol{0}, \tag{4.108}$$

where $\boldsymbol{M_{hh}}$, $\boldsymbol{B_{hh}}$ and $\boldsymbol{K_{hh}}$ are the inertia, damping and stiffness matrices in the modal space, respectively. Applying Eq.(4.106) to the initial conditions:

$$\boldsymbol{u}(0) = \boldsymbol{\phi} \cdot \boldsymbol{u_h}(0), \tag{4.109}$$

$$\dot{\boldsymbol{u}}(0) = \boldsymbol{\phi} \cdot \dot{\boldsymbol{u}}_{\boldsymbol{h}}(0) \tag{4.110}$$

and pre-multiplying by $\boldsymbol{\phi}^{*T}\boldsymbol{M}$:

$$\boldsymbol{I} \cdot \boldsymbol{u_h}(0) = \boldsymbol{u_{h_0}} = \boldsymbol{\phi}^{*T}\boldsymbol{M}\boldsymbol{u_0} = \boldsymbol{0}, \tag{4.111}$$

$$\boldsymbol{I} \cdot \dot{\boldsymbol{u}}_{\boldsymbol{h}}(0) = \dot{\boldsymbol{u}}_{\boldsymbol{h_0}} = \boldsymbol{\phi}^{*T}\boldsymbol{M}\dot{\boldsymbol{u}}(0). \tag{4.112}$$

In order to reduce the computational cost of the numerical simulation, the number of active modes can be reduced as long as the convergence of the solution is ensured. After some tests, for this system it is possible to conclude that 50 modes is enough for convergency. Then, the equations in the modal space are solved numerically in order to get the response of the system to the initial speed condition. With respect to the value of the receiver speed at the end of the hose, a value of V_{0y}= 10 m/s has been selected to visualize the hose motion.

One of the main parameters of the numerical resolution is the simulation time. After carrying out different tests, it was decided to simulate 40 seconds, in order to analyze the evolution of the response. In particular, to be able to see how in the last few seconds the system returns to its original position. In addition, it is important to perform an accurate estimation of the time step used in the numerical solution, which is a fundamental factor in order to achieve reliable results. In general, the time step Δt is defined from the maximum display frequency f_{max} through the Shannon-Nyquist Theorem [Shannon, 1949], which states that:

$$\Delta t = \frac{1}{2f_{max}}. \tag{4.113}$$

However, in order to ensure that the number of points is sufficient, an even smaller time step was used:

$$\Delta t = \frac{1}{5f_{max}}. \tag{4.114}$$

As 50 modes have been selected, the maximum frequency is that of the mode 50th. From the results obtained in the dynamic problem, the value of this frequency is $f_{50} \simeq 70$ Hz. Therefore, applying Eq.(4.114), a time step of $\Delta t \simeq 2.857 \cdot 10^{-3} = 1/350$ s is obtained. That is, 350 points per second. As the simulation time is 40 seconds, finally a total of 14000 points are needed in order to solve the problem reliably.

4.5.2 Response due to a receiver speed profile

Next, the response of the system due to the speed profile of the receiver (instead of an instantaneous impulse) will be studied. The speed profile of the receiver considered is:

$$V_x[\text{m/s}] = \begin{cases} 1 & \text{for} \quad t \leq 1\text{s} \\ 0.12 & \text{for} \quad 1\text{s} < t \leq 2\text{s} \\ 0 & \text{for} \quad t > 2\text{s} \end{cases} \qquad V_y[\text{m/s}] = \begin{cases} 0.15 & \text{for} \quad t \leq 2\text{s} \\ 0 & \text{for} \quad t > 2\text{s} \end{cases} \tag{4.115}$$

Then for $t > 0$ both horizontal and vertical speed at the last node of the hose are known, and therefore by integration the position of that point is prescribed. Therefore, the solution of this case will then be treated as a forced motion, with the force exerted at the last node.

While the previous case is solved using modal coordinates, in this case, the problem will be addressed directly through numerical integration in physical coordinates. Eq.(4.101) can be written as a function of the sub-matrices of the horizontal and vertical motions defined previously during the development of the dynamic equations:

$$\begin{bmatrix} \boldsymbol{M^{xx}} & \mathbf{0} \\ \mathbf{0} & \boldsymbol{M^{yy}} \end{bmatrix} \begin{Bmatrix} \ddot{\boldsymbol{u}}_{\boldsymbol{x}} \\ \ddot{\boldsymbol{u}}_{\boldsymbol{y}} \end{Bmatrix} + \begin{bmatrix} \boldsymbol{B^{xx}} & \boldsymbol{B^{xy}} \\ \mathbf{0} & \boldsymbol{B^{yy}} \end{bmatrix} \begin{Bmatrix} \dot{\boldsymbol{u}}_{\boldsymbol{x}} \\ \dot{\boldsymbol{u}}_{\boldsymbol{y}} \end{Bmatrix} + \begin{bmatrix} \boldsymbol{K^{xx}} & \boldsymbol{K^{xy}} \\ \mathbf{0} & \boldsymbol{K^{yy}} \end{bmatrix} \begin{Bmatrix} \boldsymbol{u}_{\boldsymbol{x}} \\ \boldsymbol{u}_{\boldsymbol{y}} \end{Bmatrix} = \begin{Bmatrix} \mathbf{0} \\ \mathbf{0} \end{Bmatrix}. \quad (4.116)$$

With respect to the initial conditions, it will be zero except in the last node of the hose in both horizontal and vertical directions, for which the speed profile of Eq.(4.115) is imposed. Then, the initial condition in the displacements will be:

$$\boldsymbol{u}(0) = \{\boldsymbol{u_x}(0)\ \boldsymbol{u_y}(0)\}^T : \quad (4.117)$$

$$\boldsymbol{u_x}(0) = \begin{Bmatrix} 0 \\ \vdots \\ V_x \cdot t \end{Bmatrix}, \quad (4.118)$$

$$\boldsymbol{u_y}(0) = \begin{Bmatrix} 0 \\ \vdots \\ V_y \cdot t \end{Bmatrix}, \quad (4.119)$$

and in the speeds:

$$\dot{\boldsymbol{u}}(0) = \{\dot{\boldsymbol{u}}_{\boldsymbol{x}}(0)\ \dot{\boldsymbol{u}}_{\boldsymbol{y}}(0)\}^T : \quad (4.120)$$

$$\dot{\boldsymbol{u}}_{\boldsymbol{x}}(0) = \begin{Bmatrix} 0 \\ \vdots \\ V_x \end{Bmatrix}, \quad (4.121)$$

$$\dot{\boldsymbol{u}}_{\boldsymbol{y}}(0) = \begin{Bmatrix} 0 \\ \vdots \\ V_y \end{Bmatrix}, \quad (4.122)$$

Since in this case the motion of the last node of the hose is known, these equations can be reformulated: With N being the number of nodes of the hose, the problem can be transformed from a free vibration problem with N degrees of freedom and non-zero initial conditions to a forced vibration problem with $N-1$ degrees of freedom and zero initial conditions. Therefore, Eq.(4.116) can be written including the forced motion of the end of the hose:

$$\begin{bmatrix} \bar{\boldsymbol{M}}^{\boldsymbol{xx}} & \mathbf{0} \\ \mathbf{0} & \bar{\boldsymbol{M}}^{\boldsymbol{yy}} \end{bmatrix} \begin{Bmatrix} \ddot{\boldsymbol{u}}_{\boldsymbol{x}} \\ \ddot{\boldsymbol{u}}_{\boldsymbol{y}} \end{Bmatrix} + \begin{bmatrix} \bar{\boldsymbol{B}}^{\boldsymbol{xx}} & \bar{\boldsymbol{B}}^{\boldsymbol{xy}} \\ \mathbf{0} & \bar{\boldsymbol{B}}^{\boldsymbol{yy}} \end{bmatrix} \begin{Bmatrix} \dot{\boldsymbol{u}}_{\boldsymbol{x}} \\ \dot{\boldsymbol{u}}_{\boldsymbol{y}} \end{Bmatrix} + \begin{bmatrix} \bar{\boldsymbol{K}}^{\boldsymbol{xx}} & \bar{\boldsymbol{K}}^{\boldsymbol{xy}} \\ \mathbf{0} & \bar{\boldsymbol{K}}^{\boldsymbol{yy}} \end{bmatrix} \begin{Bmatrix} \boldsymbol{u}_{\boldsymbol{x}} \\ \boldsymbol{u}_{\boldsymbol{y}} \end{Bmatrix} = \begin{Bmatrix} \boldsymbol{P}_{\boldsymbol{x}} \\ \boldsymbol{P}_{\boldsymbol{y}} \end{Bmatrix}, \quad (4.123)$$

where all the matrices with the superscript − represent the previous matrices but without their last row and column, which are now in the forced terms vectors $\boldsymbol{P_x}$ and $\boldsymbol{P_y}$. These forces can be defined from the speed profiles and from the last row and column elements of the different matrices as:

$$P_x^j = -B_{xx}^{j,N} V_x - K_{xx}^{j,N} V_x t - B_{xy}^{j,N} V_y - K_{xy}^{j,N} V_y t. \tag{4.124}$$

$$P_y^j = -B_{yy}^{j,N} V_y - K_{yy}^{j,N} V_y t, \tag{4.125}$$

where j=1,...,$N-1$. As the motion of the last node is now included as a forced term, the initial conditions will be zero:

$$\boldsymbol{u}(0) = \mathbf{0}, \tag{4.126}$$

$$\dot{\boldsymbol{u}}(0) = \mathbf{0}. \tag{4.127}$$

In this case, the resulting system of equations will be solved numerically directly in the time domain (without applying the modal approximation explained in the first part of the section). To do this, the equation must be obtained for the different time intervals defined from the receiver's velocity profile of Eq.(4.115), ensuring compatibility in displacements and velocities (i.e., through the initial conditions) so that the end of each interval is the starting point of the next one.

For the speed profile of the receiver given by Eq.(4.115) it can be found that for of for $t > 2$ the speed of the receiver becomes zero. Thus, the last node of the hose and therefore the drogue remains fixed, and the forces defined in Eqs.(4.124) and (4.125) will be constants. However, once the last node is fixed a result of great importance is the reaction force generated in the drogue as a consequence of the end point fixed position. From Eq.(4.116), the expression of this force for both horizontal and vertical motion can be obtained. Thus for the vertical force:

$$F_y = M_{yy}^{N,N-1} \ddot{u}_y^{N-1} + B_{yy}^{N,N-1} \dot{u}_y^{N-1} + K_{yy}^{N,N-1} u_y^{N-1} + K_{yy}^{N,N} u_y^N. \tag{4.128}$$

It can be observed that at Eq.(4.128) there are four different contributions to the force in the drogue:

- Acceleration term $\Rightarrow M_{yy}^{N,N-1} \ddot{u}_y^{N-1}$
- Velocity term $\Rightarrow B_{yy}^{N,N-1} \dot{u}_y^{N-1}$
- Oscillatory term $\Rightarrow K_{yy}^{N,N-1} u_y^{N-1}$
- Constant term (the position u_y^N is known) $\Rightarrow K_{yy}^{N,N} u_y^N$

The horizontal force can be defined similarly, but with the cross terms of the vertical motion:

$$\begin{aligned} F_x = {} & M_{xx}^{N,N-1} \ddot{u}_x^{N-1} + B_{xx}^{N,N-1} \dot{u}_x^{N-1} + K_{xx}^{N,N-1} u_x^{N-1} + K_{xx}^{N,N} u_x^N \\ & + B_{xy}^{N,N-1} \dot{u}_y^{N-1} + K_{xy}^{N,N-1} u_y^{N-1} + K_{xy}^{N,N} u_y^N. \end{aligned} \tag{4.129}$$

Again, four contributions to the force appear:

- Acceleration term $\Rightarrow M_{xx}^{N,N-1}\ddot{u}_x^{N-1}$
- Velocity terms $\Rightarrow B_{xx}^{N,N-1}\dot{u}_x^{N-1}$ and $B_{xy}^{N,N-1}\dot{u}_y^{N-1}$
- Oscillatory terms $\Rightarrow K_{xx}^{N,N-1}u_x^{N-1}$ and $K_{xy}^{N,N-1}u_y^{N-1}$
- Constant terms $\Rightarrow K_{yy}^{N,N}u_y^N$ and $K_{xy}^{N,N}u_y^N$

4.6 Results

This section presents the main results obtained from the hose and drogue model analysis. The results are organized following the structure of this chapter: First, the static equilibrium position for different flight conditions is presented. Then, natural frequencies and damping coefficients also for different flight conditions are discussed. And finally, the aeroelastic analysis of the system in terms of the flutter boundaries and how some parameters as the lag angle influence on these boundaries is studied. In addition, the flutter modes and frequencies are found out.

Table 4.2: Parameters of the hose and drogue model.

Hose length, s_0	25.90 m
Hose external diameter, d_{ext}	0.0676 m
Hose internal diameter, d_{int}	0.0551 m
Mass per unit length of the hose empty, ρ_H	2.50 kg/m
Mass per unit length of the hose with fuel, $\rho_{H,fuel}$	4.90 kg/m
Young Modulus of the hose, E	600 MPa
Moment of inertia of the hose empty, I	$5.71{\cdot}10^{-7}$ m^4
Moment of inertia of the hose with fuel, I_{fuel}	$1.03{\cdot}10^{-6}$ m^4
Drag without lift coefficient of the hose, C_{D0}	1.2
Friction drag coefficient of the hose, C_{Df}	$4.5995{\cdot}10^{-4}$
Drogue weight, W	101.80 N
Drogue drag, Q	925.01 N
Number of hose elements, N_s	600

One of the main computational advantages of the developed model is its ability to easily adjust and study variations in the flight condition (altitude and speed) as well as the values of the parameters. Regarding the flight condition, a broad range of flight speeds and flight altitudes have been studied:

- Flight speeds ranging from 45 m/s (defined as the minimum speed required for the aerial refueling process) to 300 m/s.
- Flight altitudes from 5000 ft (1424 m) to 30000 ft (9144 m) are computed.

Regarding to the rest of the parameters exposed in the model, while most of them remain constant throughout the analysis, others will have some variations:

- With respect to the hose, two cases will be considered: the hose empty (the pre-contact deployed phase) and the hose full of fuel (the post-contact phase begins once the effects associated with the contact between the drogue and the receiver aircraft have dissipated). The approach to represent the hose filled with fuel will be carried out by incorporating the effect of the fuel mass into the hose's properties.
- The impact of the downwash angle induced by the tanker aircraft. Results are presented for certain values of this angle, which show the different conditions for refueling including the zero-angle case to investigate the effect of neglecting this angle.
- One of the main novelties of the model is the inclusion of bending force in the hose. Therefore, the results will be compared with those that would have been obtained if it had not been considered.
- The phase lag angle is another parameter needed to be varied since this angle is included without numerical computation to the model.

The main parameters of the hose and drogue model, as well as some numerical parameters used in the computations, are summarized in Table 4.2.

4.6.1 Static equilibrium

Eqs.(4.49)-(4.56) yield the equilibrium position of the system and the hose tension. The results are obtained for the range of flight speeds and flight altitudes explained previously, as well as for the values of the system parameters presented in the Table 4.2.

In order to illustrate the variations that appear in the equilibrium position under different flight conditions, Figure 4.4 displays the equilibrium positions for two specific flight scenarios with the same speed, $U_\infty = 56.59$ m/s, but different altitudes: $H_\infty = 5000$ ft (1524 m) and $H_\infty = 30000$ ft (9144 m). These flight altitudes represent the minimum and maximum altitudes to be able to perform the refueling process safely, respectively. The hose is empty of fuel.

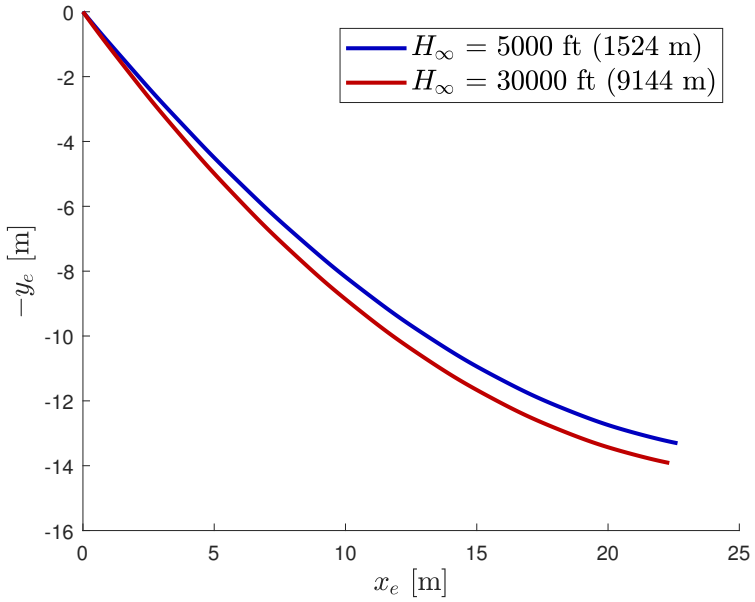

Figure 4.4: Static equilibrium position of the system for different flight altitudes.

As depicted in Figure 4.4, changes in flight altitude result in relatively small differences in the equilibrium position of the system. For instance, variations in the vertical position are approximately 4.5% at the junction between the hose and the drogue.

To further analyze the impact of the flight speed, two scenarios with the same flight altitude ($H_\infty = 5000$ ft) but different flight speeds ($U_\infty = 56$ m/s and $U_\infty = 240$ m/s) and again with the hose empty of fuel are computed and presented in Figure 4.5. As can be seen, increasing the flight speed leads to significant changes in the equilibrium. In particular, the hose-drogue junction vertical position changes of more than 100% appear. From these two Figures it can be concluded that, as expected, the air density barely affects to the dynamic pressure while the flight speed strongly influence it. Although not applied in this work, the assumption of constant density flow could be adopted without compromising the results.

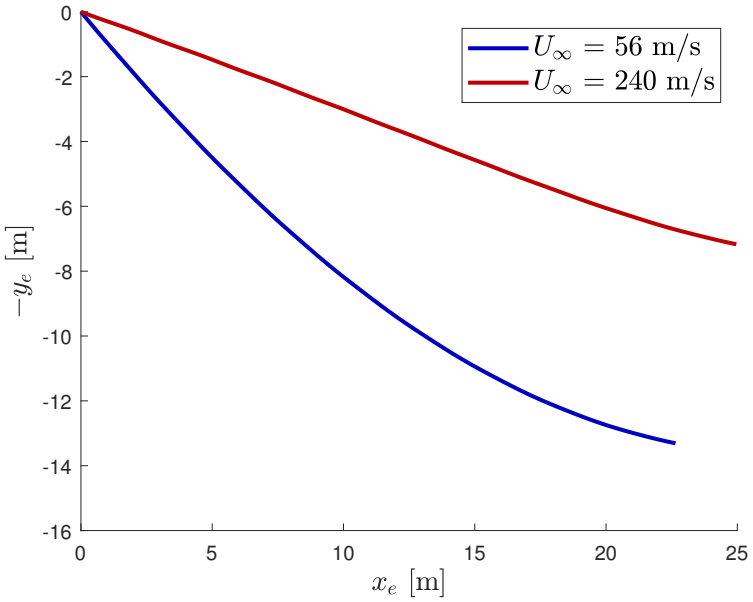

Figure 4.5: Static equilibrium position of the system for different flight speeds.

As mentioned earlier, the hose is studied in two distinct phases: before the contact between the drogue and the receiver, and after. Figure 4.6 shows the static equilibrium position for the same flight condition (a flight altitude of 5000 ft and a flight speed of 100 m/s and) with the hose empty (orange line) and with the hose filled with fuel (green line). As can be seen, the hose with fuel descends more than when it is empty. This behavior is expected, as the mass per unit length of the hose nearly doubles, as shown Table 4.2. However, the effect is less pronounced than one might anticipate because the bending forces in the hose filled with fuel also increase (due to the increased moment of inertia). The variation in the vertical position at the hose-drogue junction is approximately 10%.

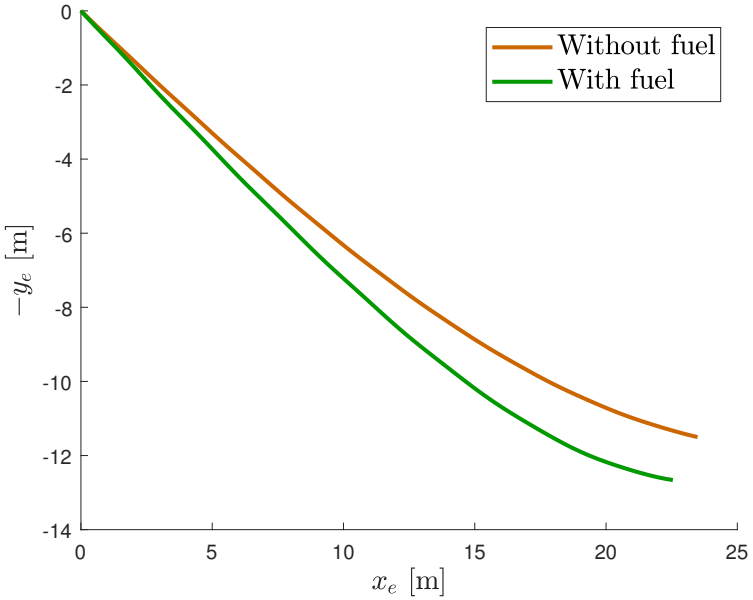

Figure 4.6: Static equilibrium position of the system with the hose empty and with the hose with fuel.

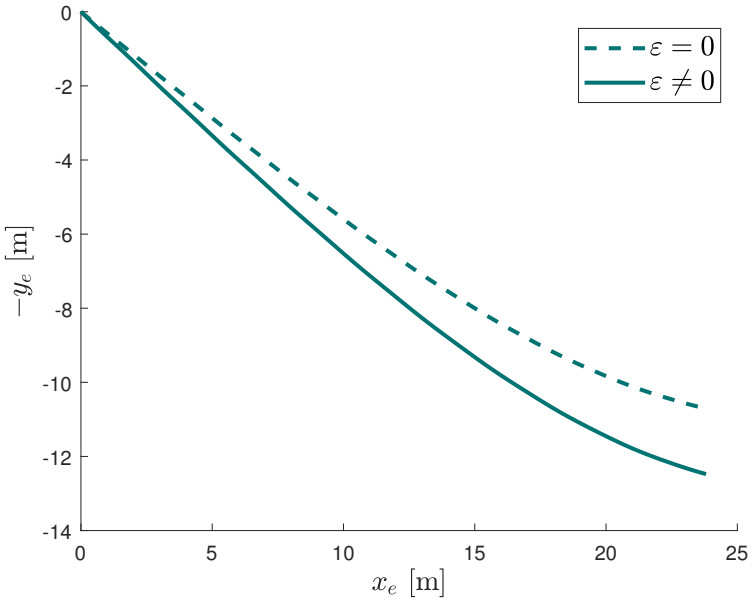

Figure 4.7: Static equilibrium position of the system with and without the downwash angle effect.

In addition, is very interesting to examine the influence of the downwash angle generated by the tanker on the static equilibrium position. For this purpose, a flight condition with $H_\infty = 20000$ ft (6096 m) and $U_\infty = 150$ m/s is considered. The static equilibrium position with and without ε is illustrated in Figure 4.7.

It is observed that significant differences appear when the downwash angle is included. The effect of the angle is to lower the equilibrium position of the hose. This effect involves a larger vertical distance between the tanker and the receiver, along with a more pronounced steady angle of attack on the hose, which, as will be seen later, markedly influence the dynamics of the system. The end position of the hose is lowered a 15% due to this angle (an effect much more pronounced than the one due to the air density).

Finally, the effect of the hose bending on the static equilibrium position is analyzed in Figure 4.8, where two cases are presented: one with hose bending included and the other without it. The flight condition is the same as in the analysis of the downwash angle: $H_\infty = 20000$ ft (6096 m) and $U_\infty = 150$ m/s. As expected, the bending force results in a reduction in the vertical distance between the tanker and the drogue. Additionally, it can be observed that the hose is slightly stiffer (particularly towards the end, where the hose angle of attack is smaller with bending than without bending). This outcome is also expected due to the increased stiffness of the hose when considering bending forces.

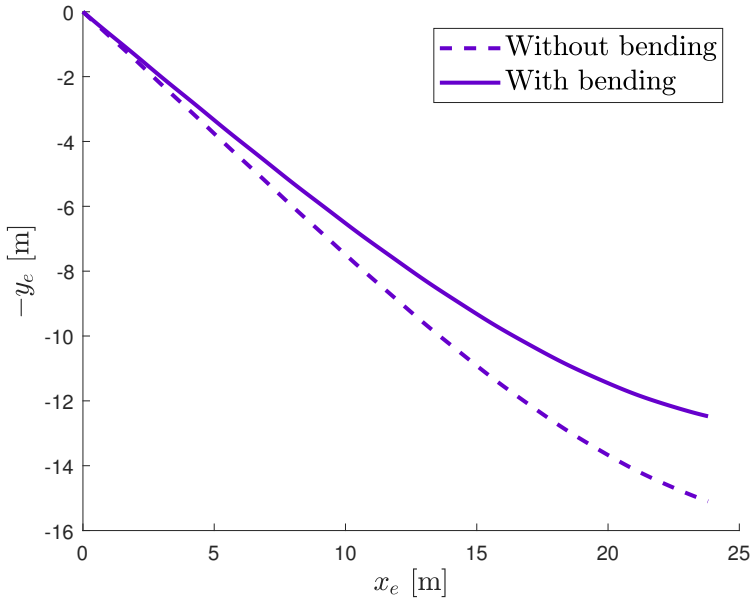

Figure 4.8: Static equilibrium position of the system with and without bending forces.

4.6.2 Dynamic properties of the system

The dynamic properties of the system (frequencies, damping coefficients, and natural modes) will be presented next, in a similar way to the static results.

Flight condition effects

From Eq.(4.98) the eigenvalues and eigenvectors of the dynamic problem, and therefore the frequencies, damping coefficients and mode shapes can be obtained. Natural frequencies and damping coefficients for different flight conditions and values of some parameters are presented below. In this way, the effect of some of the parameters on these results can be analyzed and the order of magnitude of these results can be seen. The results are presented for the same three cases studied previously:

- $U_\infty = 56$ m/s and $H_\infty = 5000$ ft (1524 m).
- $U_\infty = 56$ m/s and $H_\infty = 30000$ ft (9144 m).
- $U_\infty = 240$ m/s and $H_\infty = 5000$ ft (1524 m).

As in the results presented in the static analysis, differences between the first and the second case allows for studying the effect of the flight altitude, while differences between the first and the third cases allows for analyze the effect of the flight speed. The first six natural frequencies of the system are presented in Table 4.3. In addition, Table 4.4 shows the first six damping coefficients. It is important to mention that in this Table the structural damping of the hose has been neglected, in order to analyze only the aerodynamic source of damping. However, the total damping coefficients can be obtained by adding the value of the structural damping c to the results of this Table.

Table 4.3: Natural frequencies of the hose-drogue system for different flight conditions.

	U_∞=56 m/s H_∞ = 5000 ft	U_∞=56 m/s H_∞ = 30000 ft	U_∞=240 m/s H_∞ = 5000 ft
f_1 [Hz]	0.1282	0.1234	0.1412
f_2 [Hz]	0.1893	0.1812	0.3283
f_3 [Hz]	0.3381	0.3341	0.3438
f_4 [Hz]	0.3839	0.3813	0.5261
f_5 [Hz]	0.5364	0.5309	0.6123
f_6 [Hz]	0.6079	0.6011	0.9204

Table 4.4: Damping coefficients of the hose-drogue system for different flight conditions.

	U_∞=56 m/s H_∞ = 5000 ft	U_∞=56 m/s H_∞ = 30000 ft	U_∞=240 m/s H_∞ = 5000 ft
γ_1 [-]	-0.0000	-0.0000	-0.0000
γ_2 [-]	-0.0432	-0.0389	-0.0352
γ_3 [-]	-0.0000	-0.0000	-0.0000
γ_4 [-]	-0.0243	-0.0211	-0.0273
γ_5 [-]	-0.0000	-0.0000	-0.0000
γ_6 [-]	-0.0161	-0.0139	-0.0131

Tables 4.3 and 4.4 present the results for the first six modes of the system. The first mode corresponds to the horizontal motion. The second mode represents the first vertical motion mode (typically referred to as the pendulum mode). The third and fifth modes are the second and third horizontal motion modes, respectively. The fourth and sixth modes represent the second and third vertical motion modes, analogous to the first two bending modes of a beam. As explained in Chapter 3, these vertical motion modes were used in the dynamic tests of the hose to estimate the structural damping. It is important to remember that the vertical motion is entirely decoupled from the horizontal motion, as demonstrated at Eq.(4.94). On the other hand, horizontal motion present coupling terms with the vertical one in terms of inertia and damping. However, these coupling terms are relatively small compared to the other terms in the equations.

With respect to the natural frequencies presented in Table 4.3, as can be seen the first three modes associated with horizontal motion (modes 1, 3 and 5) show lower frequencies compared to those associated with vertical motion (modes 2, 4 and 6). This outcome is expected, since the horizontal stiffness sub-matrix has lower values than the vertical one (note that vertical motion includes bending and aerodynamic stiffness forces). In addition, the frequencies of the horizontal modes hardly vary with either flight altitude or flight speed. The behavior is very different in the frequencies of the vertical modes, where with increasing speed their values show a large growth. This behavior is also expected, as the aerodynamic effect in the horizontal motion problem is practically negligible.

Table 4.4 presents the damping coefficients. The main point to note is that, as expected, the coefficients associated with the horizontal modes are zero (recall that the structural damping, which was the sole damping source for horizontal motion, has been excluded from these results).

The lack of variation in the results of the horizontal motion with the flight speed, together with the fact that the vertical problem can be solved independently of the horizontal one, leads to conclude that, for the aeroelastic analysis of the following section, only the frequencies, damping coefficients and modes of the vertical motion will be considered. As will be demonstrated later, this approach is valid because flutter issues arise only with these modes. Thus, focusing the analysis on the vertical motion, the first three modal shapes for the flight conditions previously analyzed are presented in Figures 4.9-4.11.

Figure 4.9 shows the first vertical mode of the hose and drogue system. As can be seen, the effect of the flight speed is much larger than the effect of the flight altitude. For high speeds, the mode has a greater amplitude towards the end of the hose. In Figure 4.10 the second vertical mode of the system is presented. Again is shown that the effect of flight speed is much more relevant than that of altitude. For high speeds, as in the first mode, the amplitude is greater. However, it is interesting to note that the nodal point hardly suffers any variation between the three cases. Figure 4.11 shows the third vertical mode of the system. Similar trend to the other modes is observed: higher amplitudes at higher speeds and the nodal points practically remain constant.

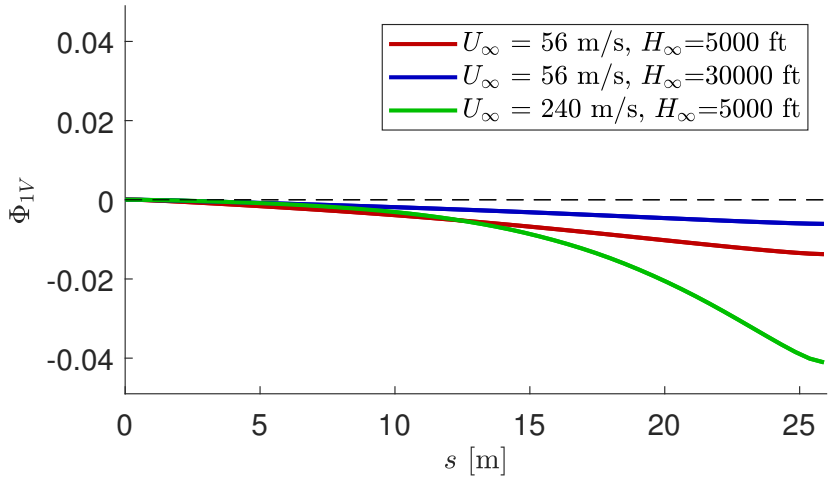

Figure 4.9: First vertical mode of the hose-drogue system for different flight conditions.

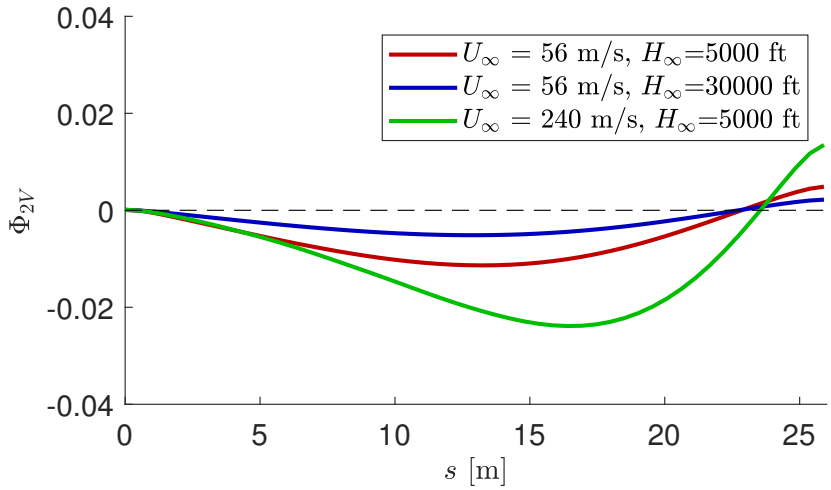

Figure 4.10: Second vertical mode of the hose-drogue system for different flight conditions.

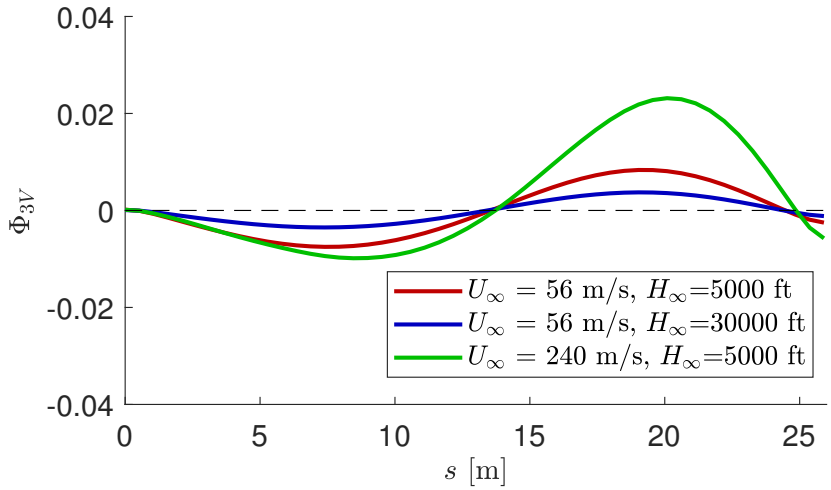

Figure 4.11: Third vertical mode of the hose-drogue system for different flight conditions.

Fuel effect

In Table 4.5 the frequencies and damping coefficients of the system are obtained with the hose empty and with the hose full of fuel. The flight condition is H_∞=5000 ft and U_∞=100 m/s. For the reasons mentioned above, the analysis will be performed only on the vertical motion modes.

Table 4.5: Natural frequencies and damping coefficients of the system with the hose empty and with the hose with fuel.

	Hose empty	Hose with fuel		Hose empty	Hose with fuel
f_{1V} [Hz]	0.1933	0.1672	γ_1 [-]	-0.0452	-0.0376
f_{2V} [Hz]	0.4720	0.4442	γ_2 [-]	-0.0252	-0.0135
f_{3V} [Hz]	0.7889	0.7386	γ_3 [-]	-0.0180	-0.0078

As mentioned earlier, when the hose is filled with fuel, two significant changes occur: an

increase in the inertia of the system (due to the higher mass of the hose) and an increase in the stiffness (as a result of the greater bending force of the hose). Table 4.5 shows that frequencies are lower when the hose contains fuel compared to when it is empty, indicating that the effect of the added mass is more significant than the change in the moment of inertia. Regarding the damping coefficients, an important decrease appears when there is fuel in the hose, which is again expected based on the aforementioned changes. The first three vertical mode shapes with the hose empty and with the hose with fuel are presented in Figures 4.12-4.14. As can be seen, in all three modes differences are small. However, in all three modes the modal amplitude in the hose with fuel is less than in the hose empty.

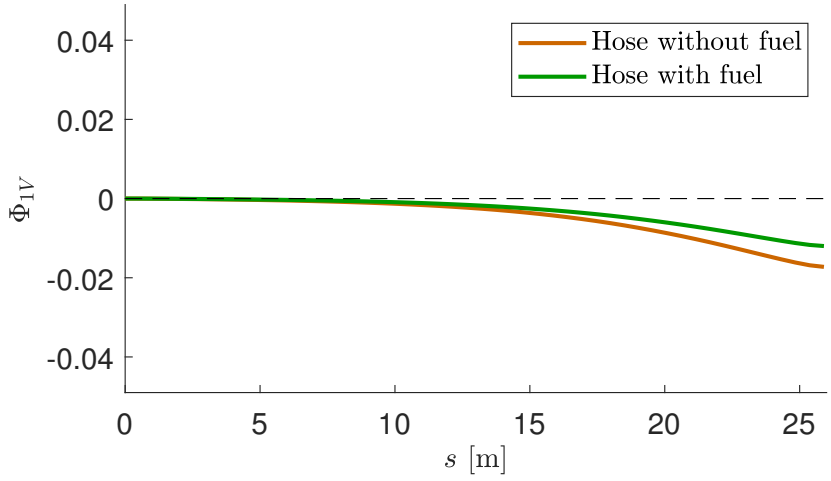

Figure 4.12: First vertical mode of the hose-drogue system with the hose empty and with the hose with fuel.

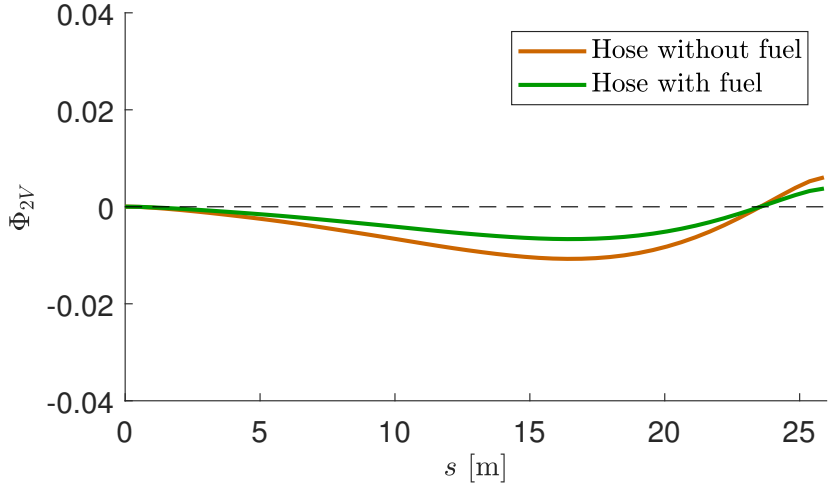

Figure 4.13: Second vertical mode of the hose-drogue system with the hose empty and with the hose with fuel.

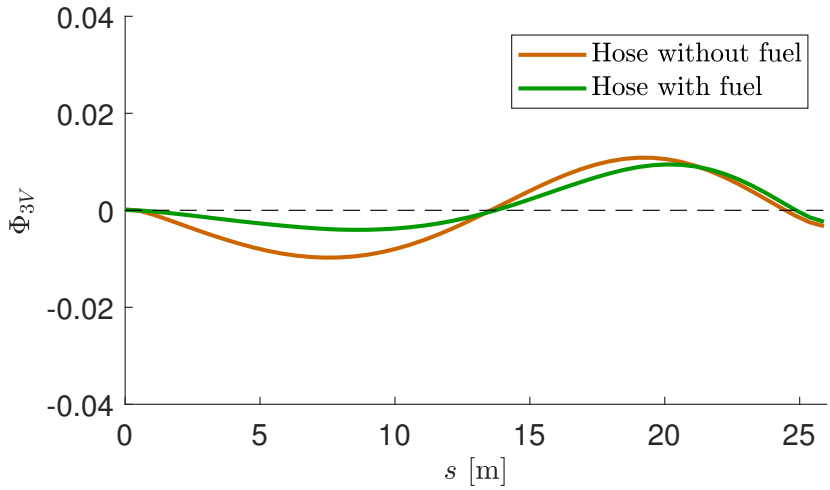

Figure 4.14: Third vertical mode of the hose-drogue system with the hose empty and with the hose with fuel.

Downwash angle effect

Next, the influence of the downwash angle on the natural frequencies and aerodynamic damping coefficients is briefly analyzed. In order to obtain values in conditions other than those seen above, this analysis will be carried out for a flight condition of $H_\infty = 20000$ ft (6096 m) and $U_\infty = 150$ m/s. Results are summarized in Table 4.6, for the first three vertical modes.

Table 4.6: Natural frequencies and damping coefficients of the system with and without the downwash angle effect.

	$\varepsilon = 0°$	$\varepsilon \neq 0°$		$\varepsilon = 0°$	$\varepsilon \neq 0°$
f_{1V} [Hz]	0.2289	0.2225	γ_1 [-]	-0.0286	-0.0338
f_{2V} [Hz]	0.5474	0.4830	γ_2 [-]	-0.0159	-0.0195
f_{3V} [Hz]	0.8200	0.8056	γ_3 [-]	-0.0140	-0.0171

The downwash angle effect results in an increase of the total angle of attack, and, therefore, in a slight increase on the aerodynamic forces on the hose, as can be seen in Eqs.(4.36) and (4.37). The increase in the aerodynamic forces causes, in turn, an increase in the aerodynamic damping. Thus, as shown in Table 4.6, the natural frequencies fall slightly with the downwash angle effect, and the absolute values of the damping coefficients are higher. This behavior is because the influence of the downwash angle through the term $\frac{dp}{d\alpha}\Big|_{\alpha_e}$ is to reduce the stiffness of the system, and therefore to reduce the value of the natural frequencies and to increase the absolute value of the damping coefficients. The values of the natural frequencies presented in Table 4.6 are similar to the results obtained by [Zhu and Meguid, 2007].

Figures 4.15-4.17 show the first three vertical modal shapes with and without the downwash angle. As can be seen, differences in all the modes are negligible.

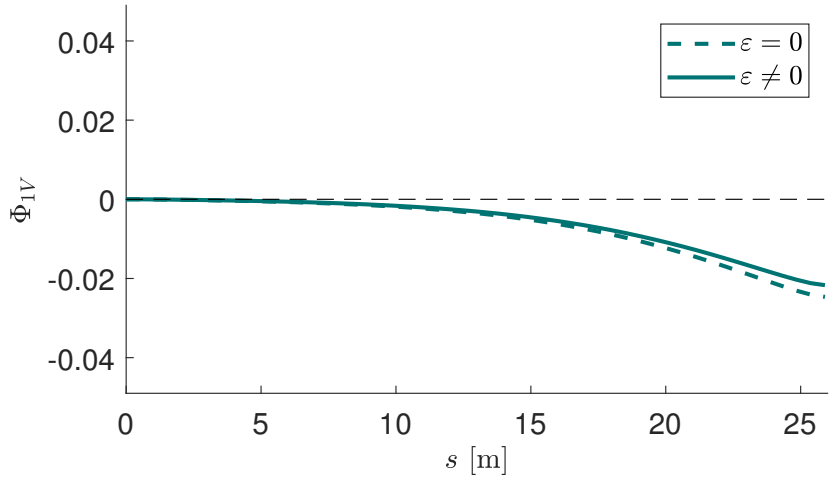

Figure 4.15: First vertical mode of the hose-drogue system with and without the downwash angle effect.

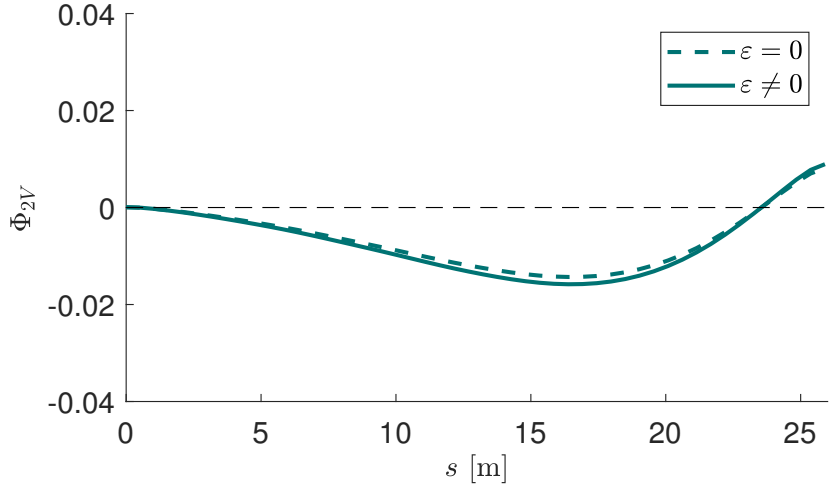

Figure 4.16: Second vertical mode of the hose-drogue system with and without the downwash angle effect.

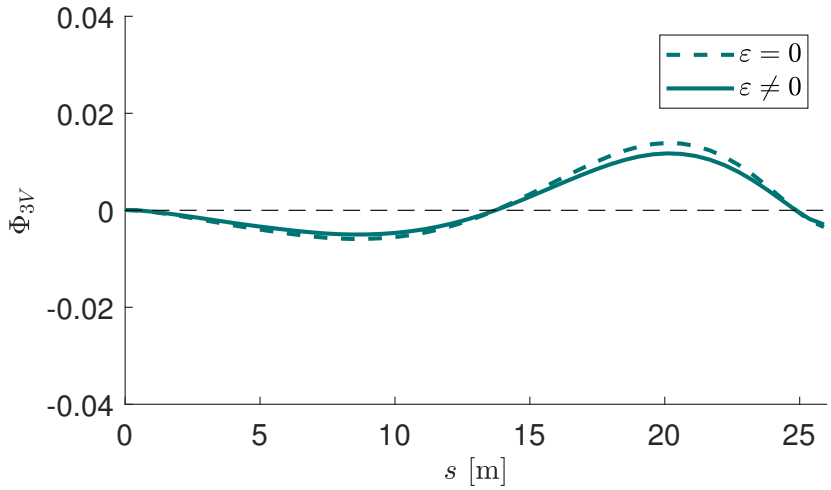

Figure 4.17: Third vertical mode of the hose-drogue system with and without the downwash angle effect.

Bending effect

Following the same procedure as in the static results analysis, now the influence of the bending force of the hose on the natural frequencies and aerodynamic damping coefficients will be studied. This analysis will be carried out for a flight condition at a speed of 150 m/s and an altitude of 20000 ft. Results for the first three vertical modes are summarized in Table 4.7.

Table 4.7: Natural frequencies and damping coefficients of the system with and without the bending force included.

	Without bending	With bending		Without bending	With bending
f_{1V} [Hz]	0.1705	0.2225	γ_1 [-]	-0.0479	-0.0338
f_{2V} [Hz]	0.4488	0.4830	γ_2 [-]	-0.0217	-0.0195
f_{3V} [Hz]	0.7496	0.8056	γ_3 [-]	-0.0185	-0.0171

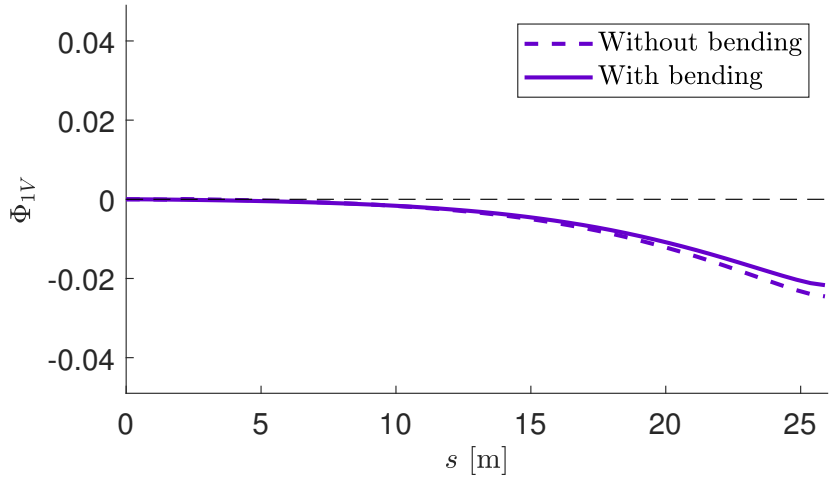

Figure 4.18: First vertical mode of the hose-drogue system with and without the bending force of the hose.

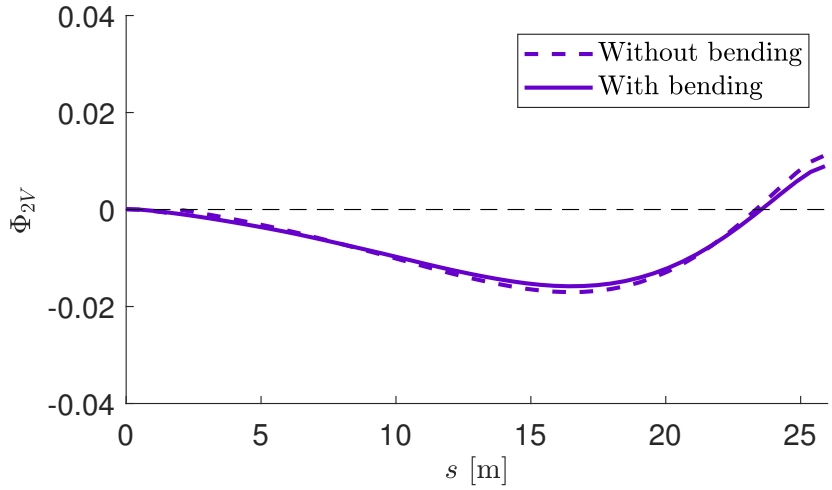

Figure 4.19: Second vertical mode of the hose-drogue system with and without the bending force of the hose.

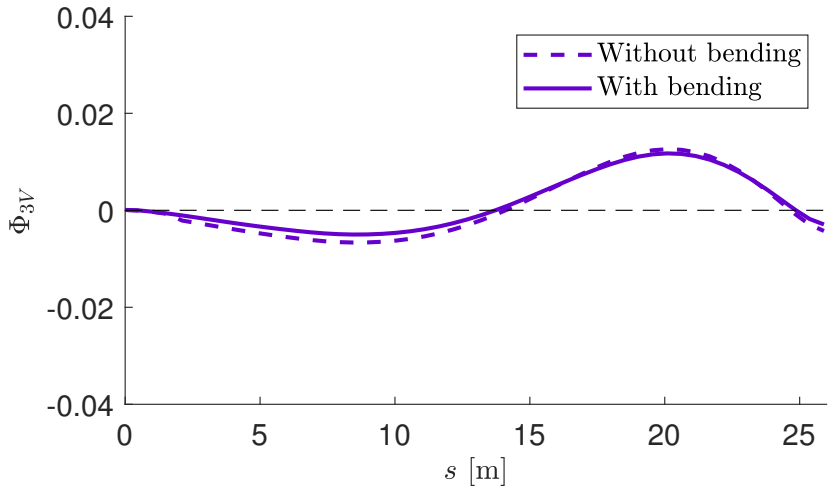

Figure 4.20: Third vertical mode of the hose-drogue system with and without the bending force of the hose.

As can be seen in Table 4.7, including the bending of the hose produces a significant increase in the frequencies of the system. These results are expected: as demonstrated above, accounting for the bending of the hose leads to an increase in the stiffness of the system. This conclusion is of great importance, since it shows that neglecting the bending term in the hose-drogue system leads to oversimplified results, resulting in significantly lower frequencies than would be observed if the bending were considered.

With respect to the damping coefficients, is shown that the system is slightly less damped when the bending force is taken into account. These results are expected: as explained previously, including the bending term for the hose results in an increase in the system's stiffness. If the inertia and damping matrices of the system remain constant, this increase in stiffness leads to a decrease in the damping coefficient [García-Fogeda Núñez and Sanz Andrés, 2014]. This is highly significant because neglecting the bending of the hose can lead to the assumption of higher damping coefficients than those that would be obtained if bending were considered. This can be dangerous in flutter analysis, as it may result in non-conservative predictions of flutter speeds.

Figures 4.18-4.20 present the first three vertical modal shapes with and without the bending force on the hose. As can be observed, the differences in all three modes are very small.

4.6.3 Phase lag angle effect on the system dynamic instability

Next, the effect of the phase lag angle ψ on the natural frequencies and damping coefficients of the system will be evaluated.

When this parameter is set to zero, $\psi = 0$, the matrices $\boldsymbol{M}$, $\boldsymbol{B}$ and $\boldsymbol{K}$ obtained from Eq.(4.94), are real. Therefore, the eigenvalues obtained from solving Eq.(4.98) are complex conjugates.

However, when $\psi \neq 0$, the aerodynamic terms in both the damping and stiffness matrices

$\boldsymbol{F}$ and $\boldsymbol{K}$ (which are the ones that include aerodynamic terms) become complex. This results in the eigenvalues of Eq.(4.98) no longer being complex conjugates. Consequently, the number of natural frequencies and damping coefficients defined in Eqs.(4.99) and (4.100) are doubled with respect to the case without the lag angle effect. For instance, the first vertical frequency with $\psi = 0$, f_{1V}, splits into two distinct values when $\psi \neq 0$, denoted as f_{1V}^{+} and f_{1V}^{-}. The same behavior applies to the other frequencies and damping coefficients of the system. This phenomenon is crucial for interpreting the results obtained.

To illustrate this effect, the following test case is considered:

- Hose with fuel.
- $H_\infty = 15.000$ ft (4572 m).
- $U_\infty = 250$ m/s.
- Zero structural damping.

The first three natural frequencies and damping coefficients of the vertical motion for several values of the phase lag angle are provided in Table 4.8 and 4.9.

In addition, Figures 4.21 and 4.22 shows the unfold produced by the phase angle in the frequencies and damping coefficients of the vertical motion. To focus the analysis, these Figures include a more specific range of lag (up to 10°) and only the first two vertical modes.

Table 4.8: Natural frequencies of the system for different values of the lag angle.

	$\psi = 0°$	$\psi = 5°$	$\psi = 10°$	$\psi = 15°$
f_{1V}^{-} [Hz]	0.2837	0.2816	0.2783	0.2751
f_{1V}^{+} [Hz]		0.2847	0.2855	0.2863
f_{2V}^{-} [Hz]	0.4959	0.4941	0.4915	0.4889
f_{2V}^{+} [Hz]		0.4970	0.4974	0.4979
f_{3V}^{-} [Hz]	0.7841	0.7821	0.7795	0.7768
f_{3V}^{+} [Hz]		0.7855	0.7862	0.7869

Table 4.9: Damping coefficients of the system for different values of the lag angle.

	$\psi = 0°$	$\psi = 5°$	$\psi = 10°$	$\psi = 15°$
γ_{1V}^{-} [-]	-0.0307	-0.0525	-0.0744	-0.0963
γ_{1V}^{+} [-]		-0.0091	0.0125	0.0341
γ_{2V}^{-} [-]	-0.0182	-0.0026	-0.0328	-0.0629
γ_{2V}^{+} [-]		-0.0123	-0.0064	-0.0004
γ_{3V}^{-} [-]	-0.0135	-0.0174	-0.0212	-0.0251
γ_{3V}^{+} [-]		-0.0096	-0.0056	-0.0017

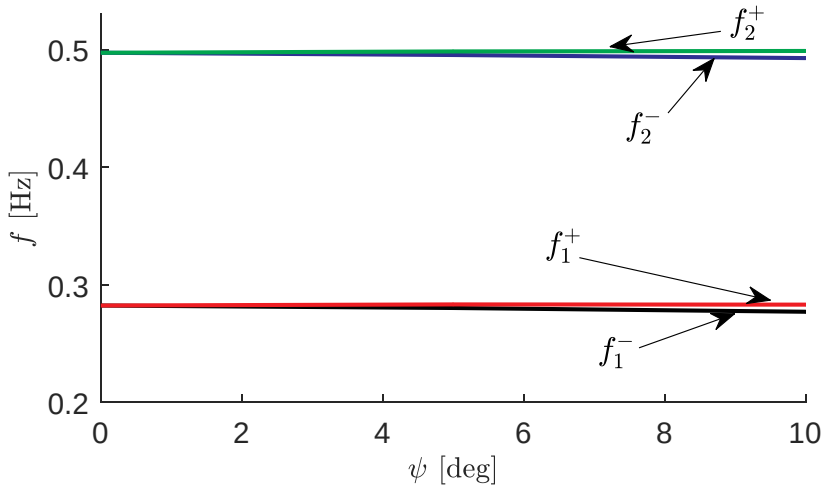

Figure 4.21: Effect of the lag angle on the natural frequencies of the system.

As can be seen in Figures 4.21 and 4.22 the natural frequencies are barely affected by the phase angle (the influence is very small, below of 0.5%). However, the effect on the damping coefficients is much more significant. In particular, the coefficient γ_{1V}^+, associated with the first vertical mode, becomes positive at a phase angle of around 7°. Therefore, the system would become unstable under these flight conditions if the phase angle could reach this value. If the approximate expression for ψ given in [Sarpkaya, 2004], Eq.(4.71), is used for this test case, the phase angle estimation would be $\psi \simeq 2.8°$, far from the value of $\psi \simeq 7°$ identified in this analysis. Thus, it can be concluded that the system at this flight condition will remain stable since the value of 7° is far from the estimated value. It is important to note that the mode shapes are not represented, as the differences between the modes after the splitting occurs are negligible.

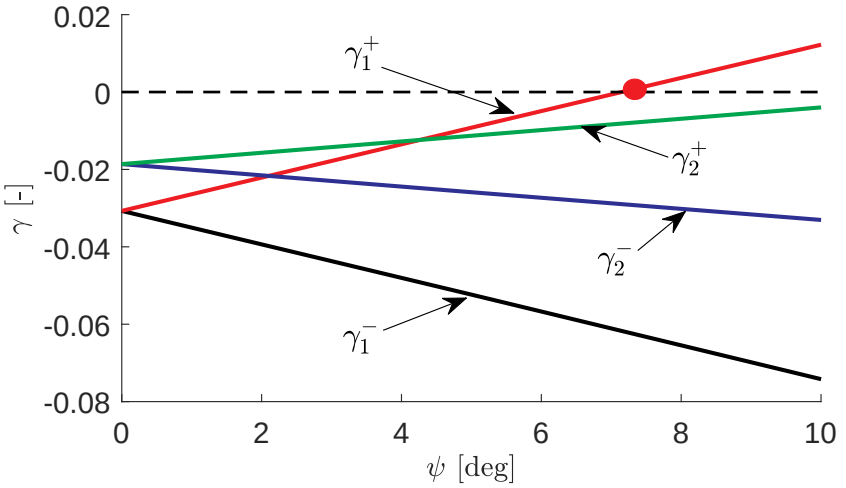

Figure 4.22: Effect of the lag angle on the damping coefficients of the system.

4.6.4 Flutter results

Frequencies and damping coefficients as a function of flight speed

To illustrate the procedure for determining the flutter speeds, for a fixed phase lag angle ψ the frequencies and damping coefficients are plotted as a function of the flight speed U_∞. As explained previously, the flutter speed corresponds to the first for which a damping coefficient becomes positive. Three different scenarios are depicted in Figures 4.23-4.25, with the phase lag angles set to $\psi = 0°$, $\psi = 5°$ and $\psi = 10°$. The other parameters remain constant across all cases:

- Hose without fuel.
- $H_\infty = 10.000$ ft (3048 m).
- Zero structural damping.

As can be seen, for the values of $\psi = 0°$ and $\psi = 5°$ (Figures 4.23 and 4.24) the damping coefficients remain negative and, therefore, there is no flutter. However, for the case of $\psi = 10°$ (Figure 4.25) the coefficient γ_{1V}^{+} changes its sign. By linear interpolation between two computed data points, the flutter speed U_F can be determined. The value of $U_F = 206$ m/s for this case is achieved.

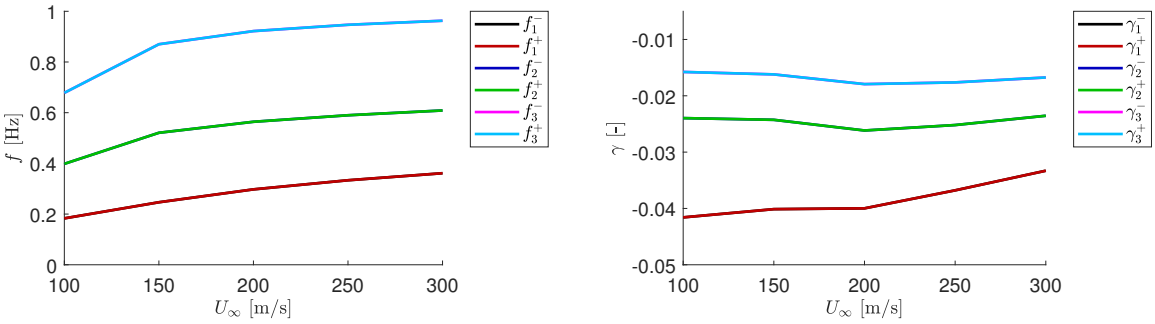

Figure 4.23: Frequencies and damping coefficients as a function of the flight speed U_∞ with $\psi = 0°$.

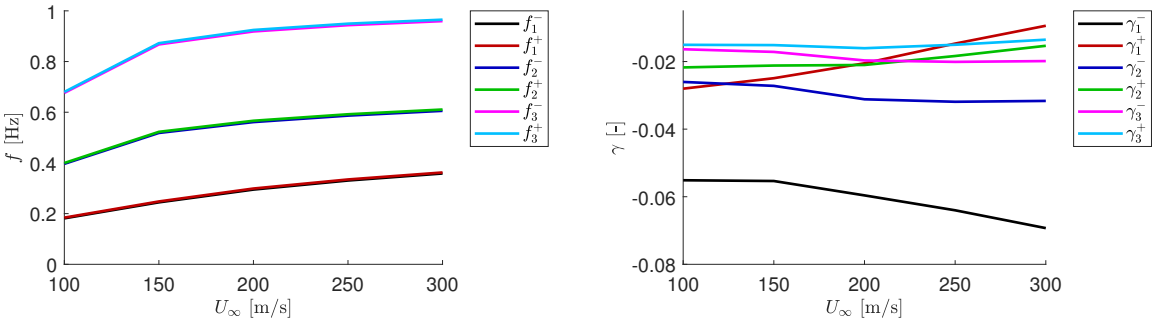

Figure 4.24: Frequencies and damping coefficients as a function of the flight speed U_∞ with $\psi = 5°$.

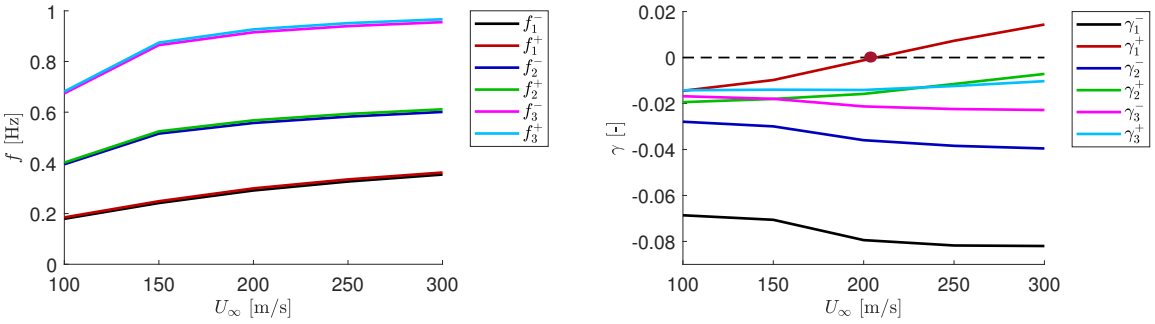

Figure 4.25: Frequencies and damping coefficients as a function of the flight speed U_∞ with $\psi = 10°$.

Flutter boundaries

The results of the flutter speeds, frequencies and modes of the system are presented below. In order to analyze the effects of both the phase lag angle ψ and the flight altitude H_∞ on the flutter speeds, frequencies and modes, three different test cases will be considered throughout this Section. Table 4.10 outlines the details of these cases. It is important to note that, unlike previous results, the structural damping of the hose is considered non-zero (with the value estimated in the dynamic test presented in Chapter 3) in these analyses. As a result, the outcomes presented here differ from those where zero structural damping was assumed. In all three cases, the flutter conditions are presented with the hose empty, and the bending force and downwash angle included. The effect of these parameters on the flutter of the system will be presented at the end of this Section.

Table 4.10: Test cases for the flutter results.

Test case 1	$H_\infty = 5000$ ft	$\psi = 10°$
Test case 2	$H_\infty = 5000$ ft	$\psi = 15°$
Test case 3	$H_\infty = 30000$ ft	$\psi = 10°$

As can be seen from the values in Table 4.10, the possible differences between cases 1 and 2 will allow to analyze the effect of the lag angle in the flutter results, while the comparison between cases 1 and 3 provides insights into the effect of the flight altitude.

Next, the results of the flutter speeds are presented. As described previously, the flutter boundaries have been calculated using the Tracing of the Roots method for each combination of flight speed, flight altitude and phase lag angle. This way of obtaining the instability of the system allows to represent effectively both the evolution of the frequencies and damping coefficients with varying flight speeds. These results will be focused on the three test cases presented in Table 4.10.

It is important to highlight that flutter in the hose-drogue system always occurs by a single mode, since no coupling between modes has been observed. Examples of single-mode flutter can be found, for example, in stall flutter scenarios (see [Dowell, 2015]). As

will be shown, the flutter mode in all cases studied corresponds to the first vertical mode (pendulum mode) of the system. The remaining eigenvalues for vertical motion and all eigenvalues for horizontal motion remain stable.

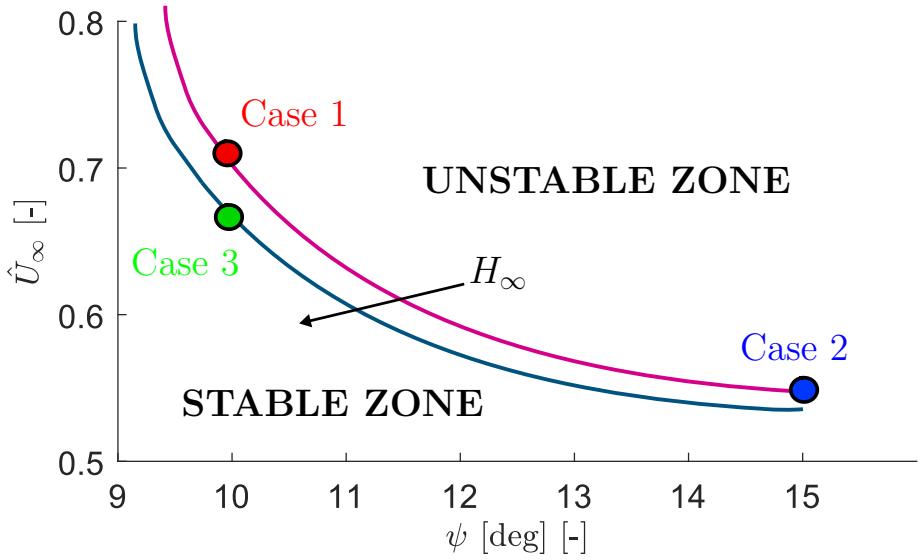

Figure 4.26: Non-dimensional flutter speed as a function of the lag angle and the flight altitude.

Figure 4.26 presents the non-dimensional flutter speed as a function of the phase lag angle and the flight altitude, with the three test cases marked. The dimensionless speed is defined as $\hat{U}_\infty = U_\infty / U_{max}$, where $U_{max} = 300$ m/s. As can be seen, the first unstable case occurs for a phase angle of approximately 9°. The impact of the lag angle on flutter boundaries is evident: as the angle increases, the flutter speed decreases. This reduction is more pronounced at lower values of ψ and becomes less significant at higher values of ψ.

Regarding the flight altitude, an increase in its value leads to a slight decrease in flutter speed. This behavior can be attributed to minor changes in the equilibrium position of the hose due to altitude variations. This result, as mentioned earlier and as will be shown again below, highlights one of the main conclusions of the flutter study in a hose-drogue system: the static equilibrium position of the system affects its aeroelastic stability.

Figure 4.27 shows the flutter mechanism for the three test cases. The mode involved in the flutter mechanism is for all cases the first one (corresponding to the pendulum mode of the hose-drogue system, as presented previously in Figure 4.9). As can be seen, the effects on the flutter mode due to changes in the lag angle (comparing test case 1, red line, with test case 2, blue line) are minimal. Similarly, the flutter mode is barely affected by variations in flight altitude (difference between test case 1, red line, and test case 3, green line).

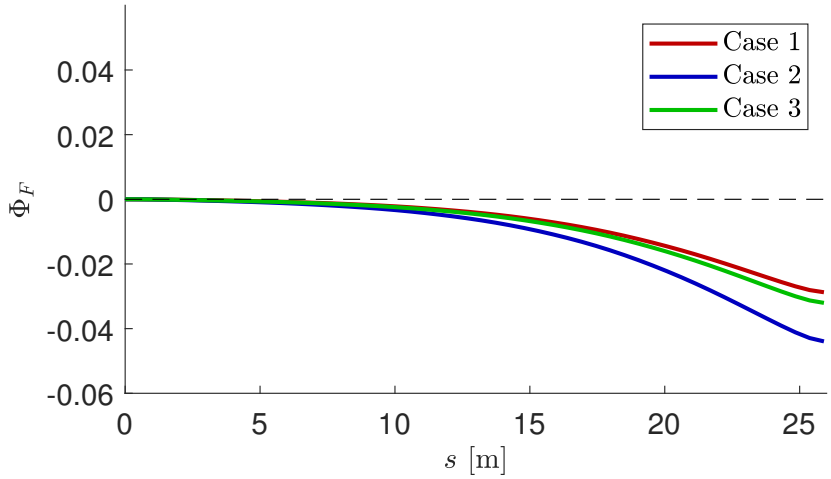

Figure 4.27: Flutter mode for each test case.

Figures 4.28-4.30 show the evolution with the non-dimensional flight speed of the frequencies and damping coefficients for the first three modes in each test case. It is possible to see, as explained previously, that the flutter occurs in all cases by a single mode. In particular, the first mode of the vertical motion. The results presented correspond to only one of the mode branches (the one identified above with the + symbol). Table 4.11 summarizes the results.

Table 4.11: Flutter speeds and frequencies for the test cases.

Test case 1	$\hat{U}_F = 0.71$	$f_F = 0.315$ Hz
Test case 2	$\hat{U}_F = 0.55$	$f_F = 0.255$ Hz
Test case 3	$\hat{U}_F = 0.67$	$f_F = 0.284$ Hz

With respect to the evolution of the frequency with speed, there is a smooth increase in frequency as flight speed increases across all three test cases. With respect to the damping coefficients, is shown that the evolution with flight speed for the damping of Mode 1 is similar for cases 1 and 2, while for case 3 there is a steeper variation with $\hat{U}_\infty$. The flutter speeds for each case are $U_F = 0.71U_{max}$ for case 1, $U_F = 0.55U_{max}$ for case 2 and $U_F = 0.67U_{max}$ for case 3. As already shown in Figure 4.26, the case with the highest lag angle (case 2) presents the lowest flutter speed. In addition, it can be observed that the phase lag ψ has a more significant impact on the flutter speed than the flight altitude.

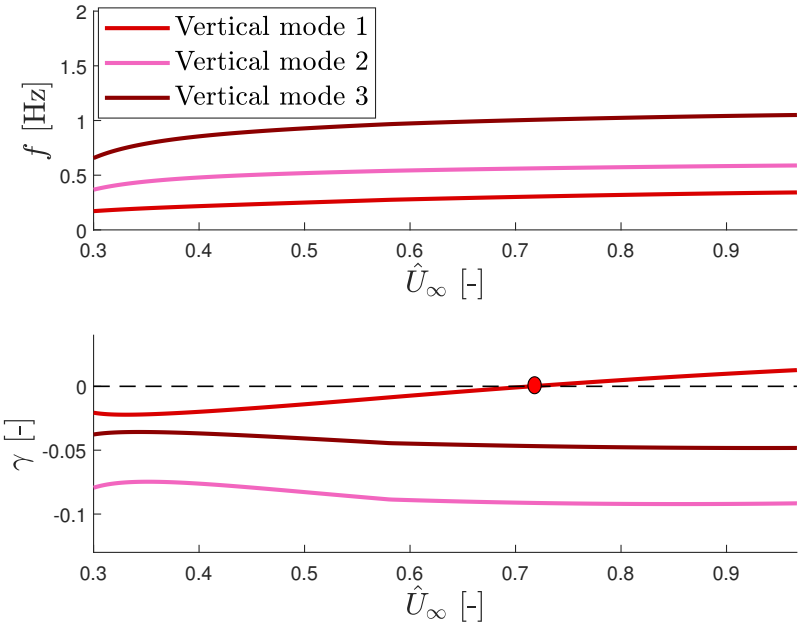

Figure 4.28: $V - g - f$ diagram for the test case 1.

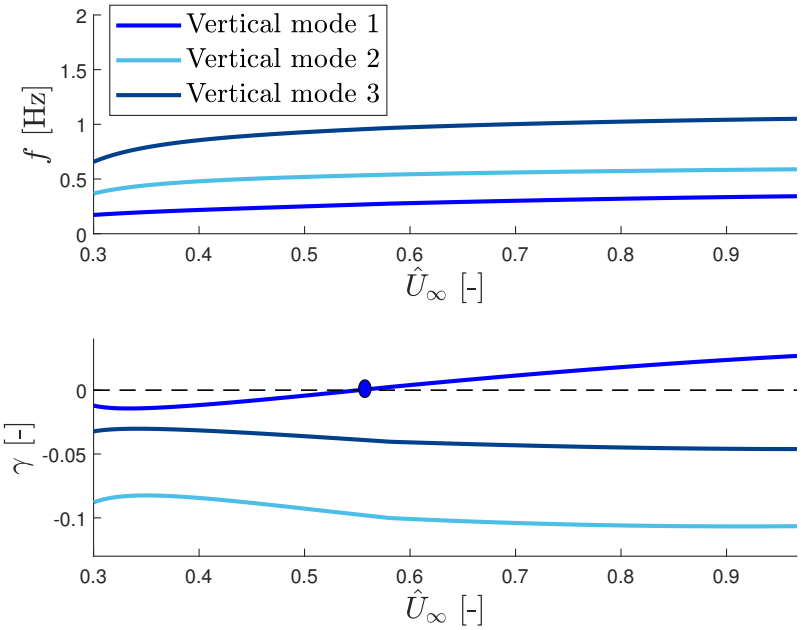

Figure 4.29: $V - g - f$ diagram for the test case 2.

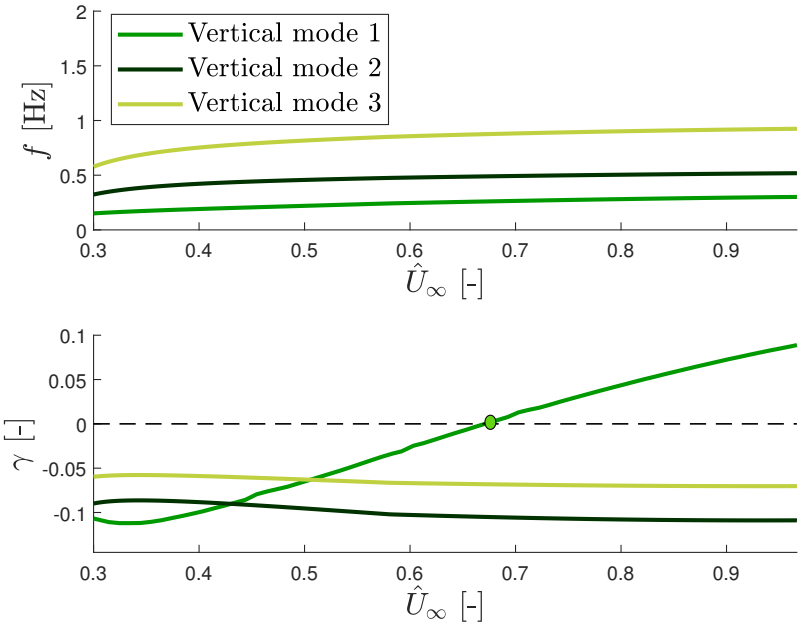

Figure 4.30: $V - g - f$ diagram for the test case 3.

Figures 4.31-4.33 present the root locus for the flutter mode of each test case. The figures show the static equilibrium position for speeds below the flutter speed, at the flutter speed, and above the flutter speed for each case.

Is shown that the static position changes significantly with the flight speed, as presented previously in Figure 4.5. Therefore, its influence on the results is of great importance. By comparing the Figures, it can be concluded that the evolution of the eigenvalue with flight speed is similar in all three test cases. However, in case 2, the evolution of the root for speeds below the flutter speed is much closer to the zero real part line than in the other two cases, reaching the flutter boundary at a lower speed. The differences between cases 1 and 3 (those associated with the difference in altitudes) are significantly smaller.

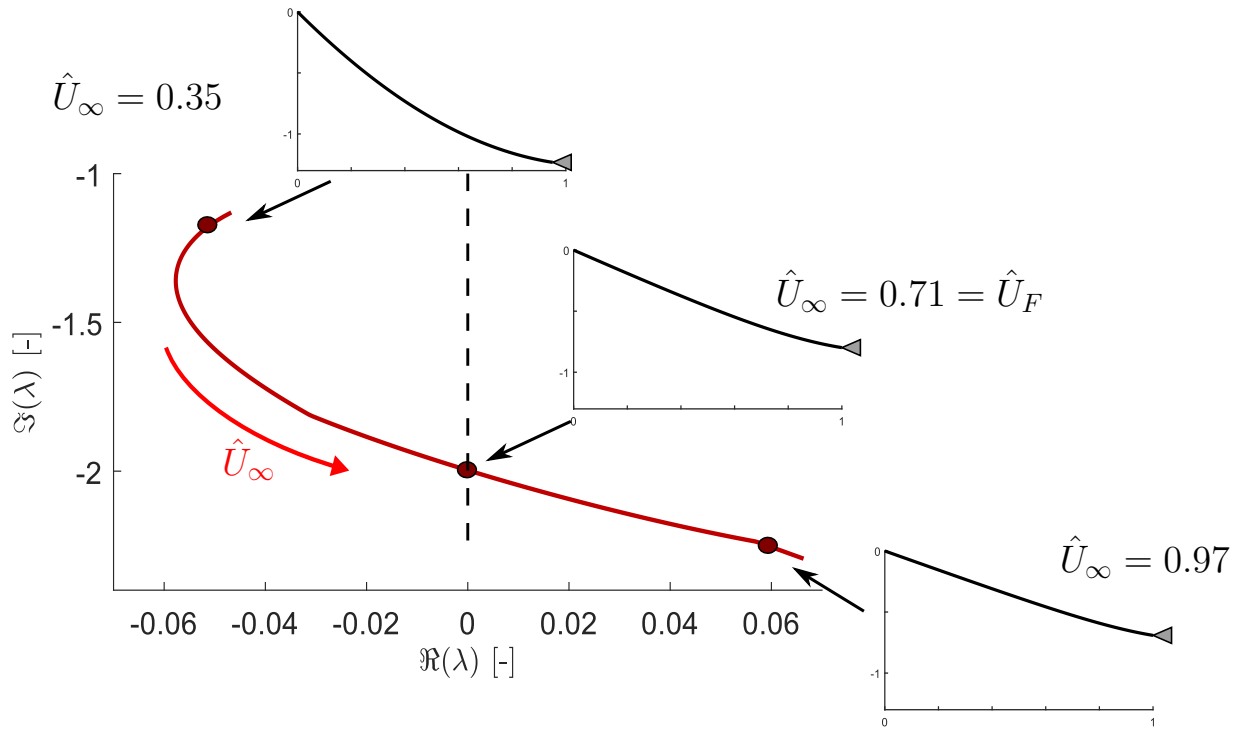

Figure 4.31: Root locus for the test case 1.

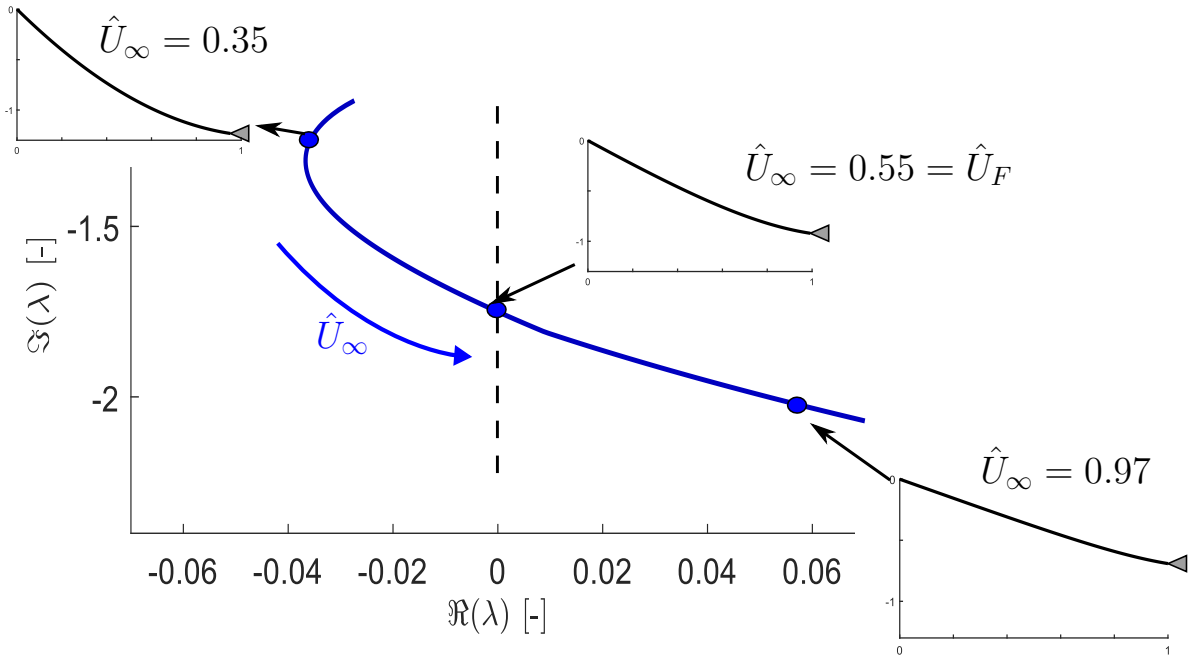

Figure 4.32: Root locus for the test case 2.

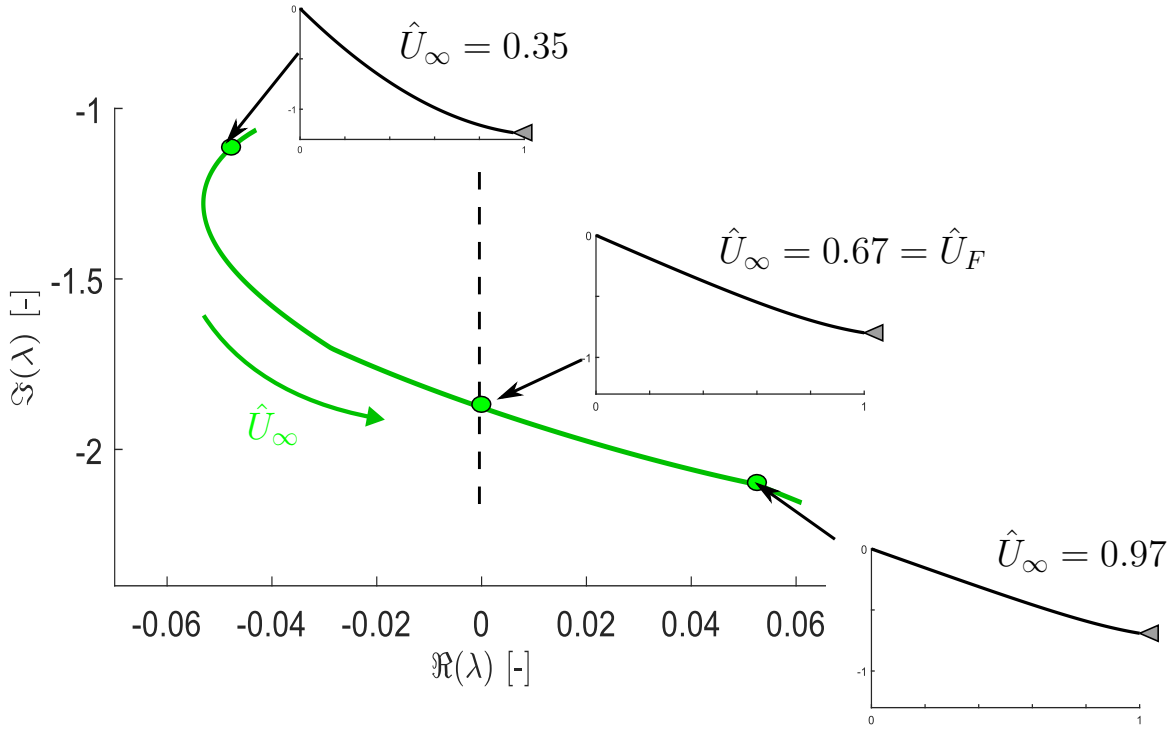

Figure 4.33: Root locus for the test case 3.

Finally, a brief analysis of the effect of certain parameters on the aeroelastic stability of the system will be conducted. These parameters will be the same as those previously analyzed in the static position results and in the system's dynamic characteristics: whether the hose is empty or filled with fuel, the downwash angle, and the bending forces. Test case 2 will be used as a reference for this analysis.

Fuel effect

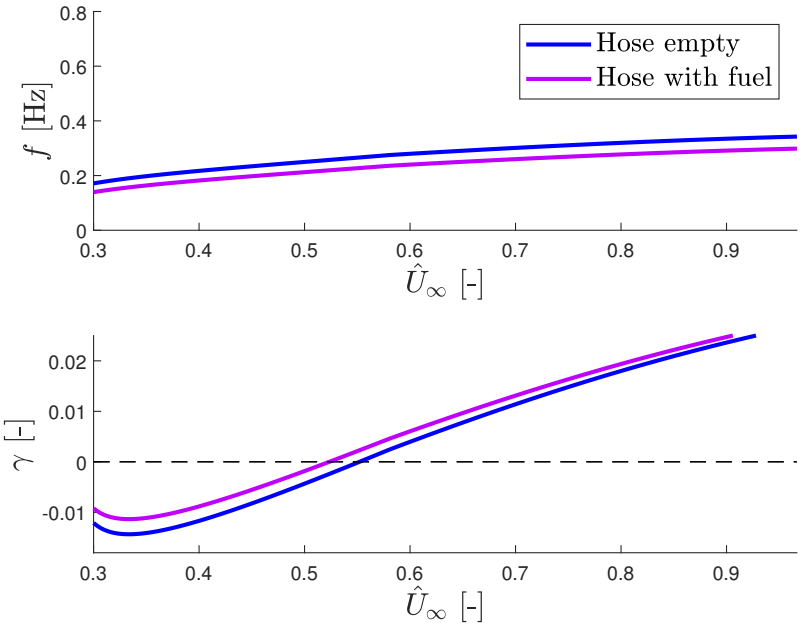

Figure 4.34: $V-g-f$ diagram for the test case 2 with the hose empty and with the hose with fuel.

As shown in Table 4.5, when the hose is filled with fuel, the system's frequencies and damping coefficients decrease. The V-g diagram of the flutter onset mode for test case 2, with the hose both empty and filled with fuel, is presented in Figure 4.34. As can be seen, the flutter speed is lower when the hose is filled compared to when it is empty. Specifically, the dimensionless flutter speed decreases from $\hat{U}_\infty$=0.55 to $\hat{U}_\infty$=0.52, which represents a 5.5% reduction. This result aligns with the fact that the filled hose is slightly less damped, making the mode unstable at a somewhat lower speed. The flutter frequency also decreases slightly.

Downwash angle effect

The effect of the downwash angle on the frequencies and damping coefficients of the system was presented in Table 4.6, where it was shown that the downwash angle increases the system's damping, while slightly reducing the frequencies. The V-g diagram for test case 2, with and without the downwash angle included, is presented in Figure 4.35. The flutter speed of the system without considering the downwash angle is slightly lower than when this angle is included in the model: $\hat{U}_\infty$=0.53 instead of $\hat{U}_\infty$=0.55. This result is again expected based on the damping results, as including the downwash angle introduces additional aerodynamic damping to the system, resulting in a slightly higher flutter speed.

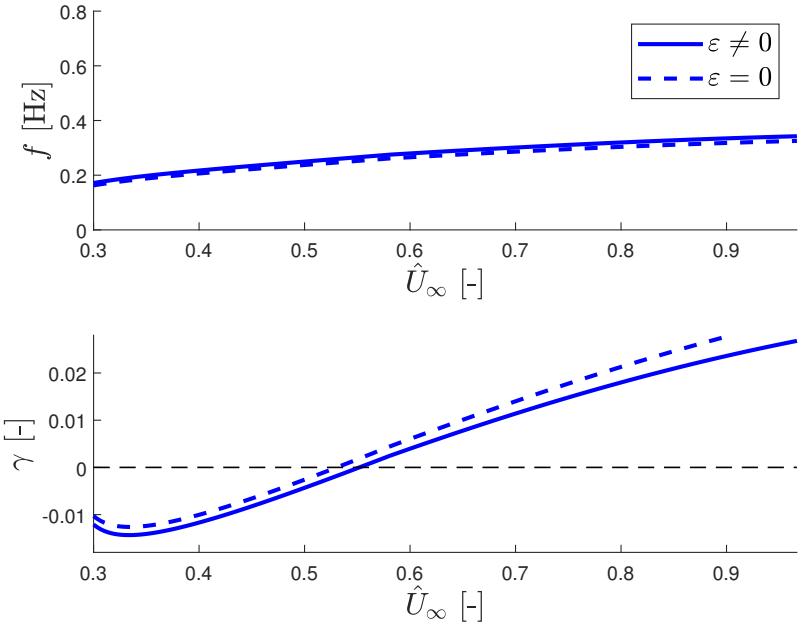

Figure 4.35: $V-g-f$ diagram for the test case 2 with and without the downwash angle effect.

Bending effect

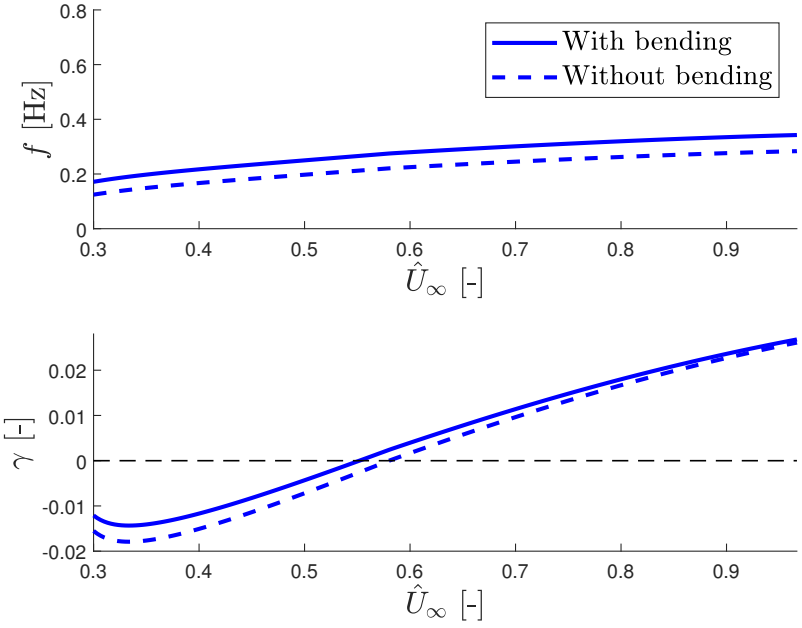

Figure 4.36: $V-g-f$ diagram for the test case 2 with and without the bending force of the hose.

Finally, the effect of the bending on the flutter boundaries of the system is studied. Table 4.7 showed that the inclusion of bending forces in the hose resulted in an increase in frequencies and a decrease in the damping coefficients of the system. The V-g diagram for test case 2, with and without hose bending included, is presented in Figure 4.36.

As can be seen, excluding the bending force in the hose leads to a higher flutter speed: $\hat{U}_\infty$=0.58 instead of $\hat{U}_\infty$=0.55. This behavior is due to the fact that excluding bending, as previously explained, results in slightly smaller damping coefficients than what would actually be obtained. This result is of great importance, as it demonstrates the significance of including hose bending from an aeroelastic stability perspective: failing to do so may lead to non-conservative flutter predictions.

4.6.5 Response of the system due to the drogue-receiver contact

Next, the results for the system's response to the contact between the receiver aircraft and the drogue will be presented. First, the results associated with the case of the receiver's instantaneous vertical velocity will be analyzed, followed by the study of those related to the velocity profile case.

4.6.6 Response due to an instantaneous impulse

The response of the hose due to the instantaneous vertical impulse in the drogue will be presented. First, the position of the complete hose will be studied for different instants of time. After that, the motion for some characteristic points along the hose will be shown as a function of time. The results are presented with and without the bending forces on the hose included. It is important to point out that in the next Figures the results have been obtained with a high value of V_0, in order to visualize as much as possible the effect of the perturbation. However, during a real case of aerial refueling, the speed would probably be much lower, and, therefore, the hose displacements would also be lower. Results will be presented for a flight altitude of $H_\infty = 5000$ ft and a flight speed of $U_\infty = 175$ m/s, and with the hose full of fuel.

Figure 4.37 shows the evolution of the hose position at different times with the hose-drogue model without bending forces. As can be seen, the initial speed condition generates a wave that travels back and forth along the hose. However, this wave is only visible during the initial moments after the contact, as it becomes damped afterward. Despite this, the hose is still moving, but with decreasing amplitude, until in the final stages of the simulation the hose returns to its original position. To analyze the first instants after the perturbation in more detail, the results for the two first seconds of simulation are presented in Figure 4.38, where it is possible to clearly see the motion of the wave generated after the perturbations, which moves through the hose from the point where the initial speed is applied. As can be observed, the wave is generated immediately after contact and travels along the hose from the drogue to the tanker. 1.4 seconds after the contact, as shown in Figure 4.38(e), it has nearly traversed the entire length of the hose, after which it returns toward the drogue's position.

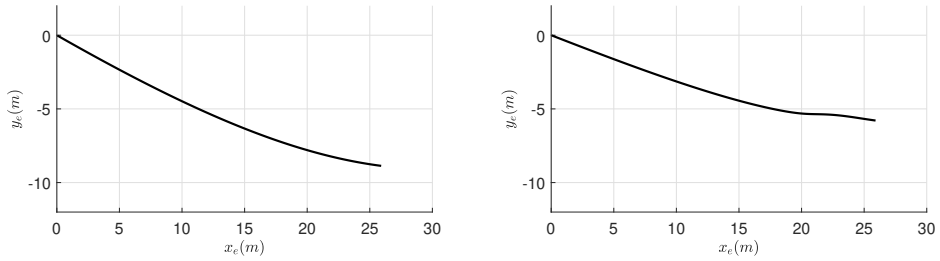

(a) t=0 s

(b) t=3 s

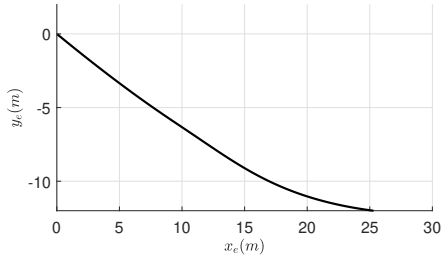

(c) t=8 s

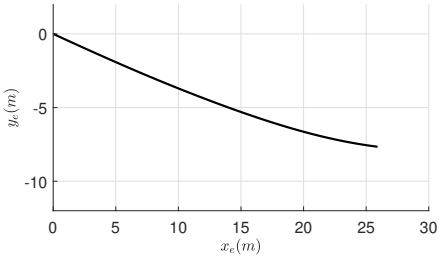

(d) t=15 s

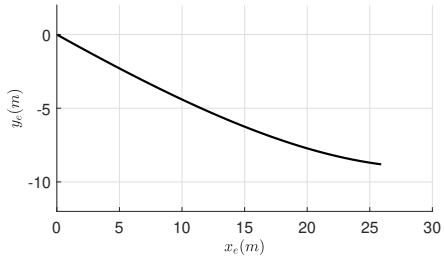

(e) t=25 s

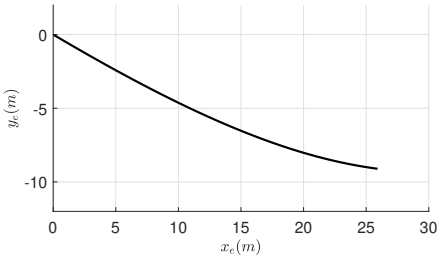

(f) t=40 s

Figure 4.37: Position of the hose after perturbation in the initial speed of the drogue without bending forces considered.

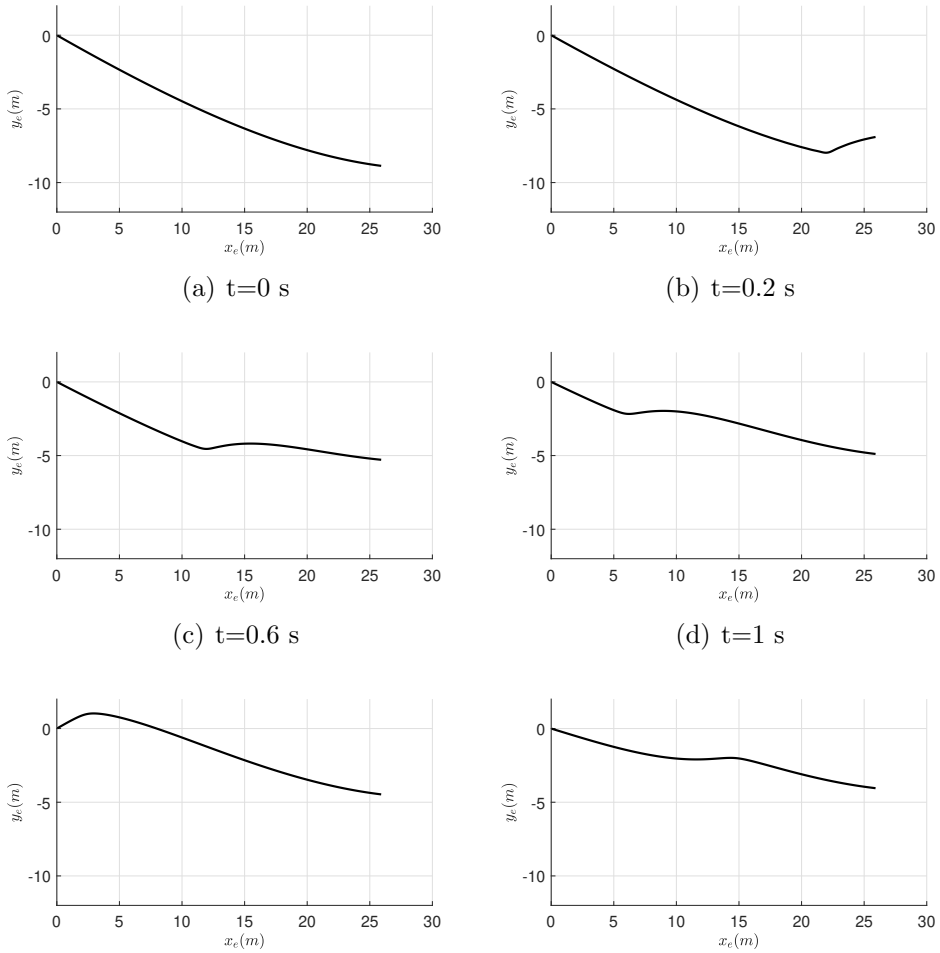

(a) t=0 s (b) t=0.2 s

(c) t=0.6 s (d) t=1 s

(e) t=1.4 s (f) t=2 s

Figure 4.38: Position of the hose after perturbation in the initial speed of the drogue (initial stages of the simulation) without bending forces considered.

Figure 4.39 shows the evolution of the hose position for different times with the bending forces included. As can be seen, the bending term causes relevant differences with respect to the previous results: In this case, more than one wave appears, all of them moving along the hose from the drogue to the tanker. However, as in the model without bending, the waves are quickly damped and at the final stages of the simulation the hose is returned to its original position. Thus, the effect of the contact can only be seen again in the first few instants of time. Likewise, in both cases it can be observed that as time increases the oscillations are of smaller amplitude. Another important difference is that the speed at which the waves move is different in this case than in the case without bending. As can be seen when Figures 4.37 and 4.39 are compared, at the same instant of time the position of the hose is different in each case. In addition, the amplitude of the hose motion is less than in the model without bending. This fact is expected: As presented above, the bending term produces an increment of the stiffness along the hose.

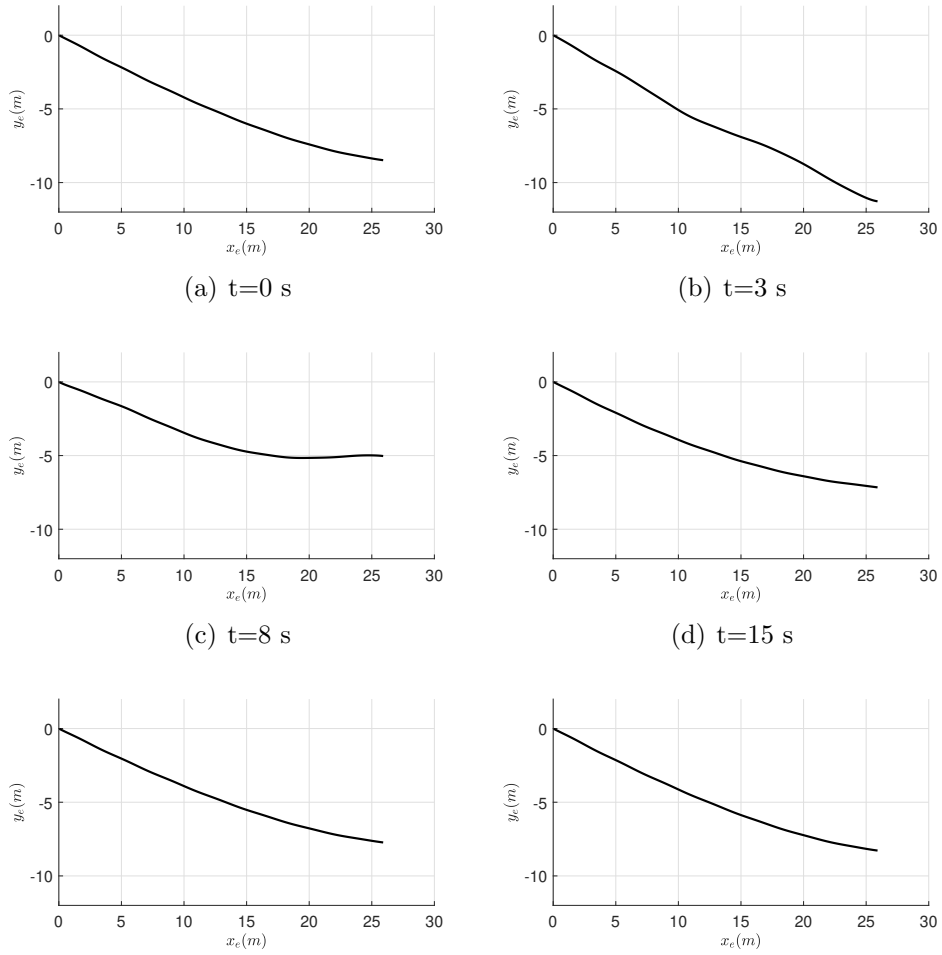

(a) t=0 s (b) t=3 s

(c) t=8 s (d) t=15 s

(e) t=25 s (f) t=40 s

Figure 4.39: Position of the hose after perturbation in the initial speed of the drogue with bending forces considered.

Again, with the aim of analyze the first instants after the perturbation, Figure 4.40 shows the results in the two first seconds of simulation. It can be seen how in the first instants of time similar behavior to the case without bending appears: The contact generates a wave which advances towards the beginning of the hose from the drogue position. However, as can be seen in Figure 4.40(e), once the wave has traversed the entire hose, a second wave is generated, which also passes through the hose from one side to the other. The comparison between Figure 4.40 and Figure 4.38 is of great interest, as it highlights that in the model with bending, the speed of the initial wave generated is higher than that of the single wave produced in the model without bending. As shown in 4.40(d), after 1 second of simulation, the wave has almost reached the beginning of the hose, whereas in the model without bending, this occurs approximately half a second later, see Figure 4.38(e). This conclusion is important, as it demonstrates that analyzing the response to contact between the drogue and the receiver in the hose-drogue system without including bending forces can lead to inaccurate assessments regarding the impact of the contact at the beginning of the hose.

Next, the evolution with time of specific points of the hose with and without the bending included are presented. In particular, three nodes of the hose will be considered: the last

node (where the initial speed is applied), the central node, and the first non-fixed node.

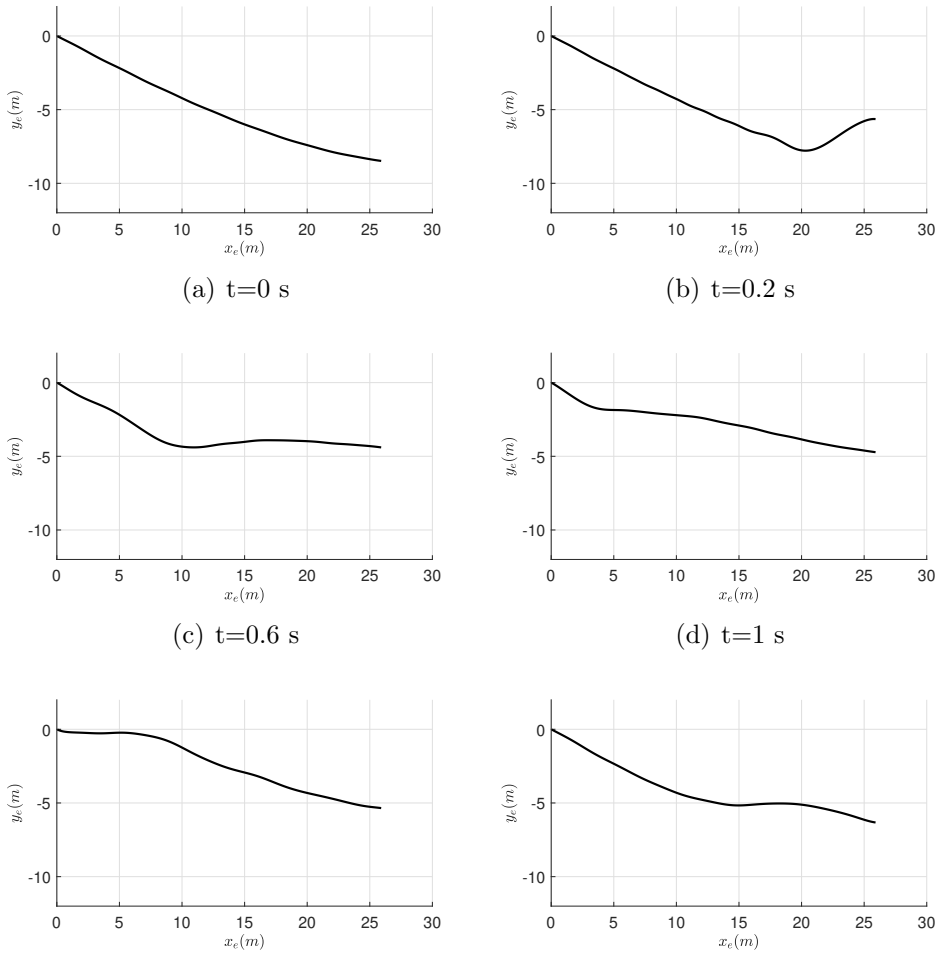

(a) t=0 s (b) t=0.2 s

(c) t=0.6 s (d) t=1 s

(e) t=1.4 s (f) t=2 s

Figure 4.40: Position of the hose after perturbation in the initial speed of the drogue (initial stages of the simulation) with bending forces considered.

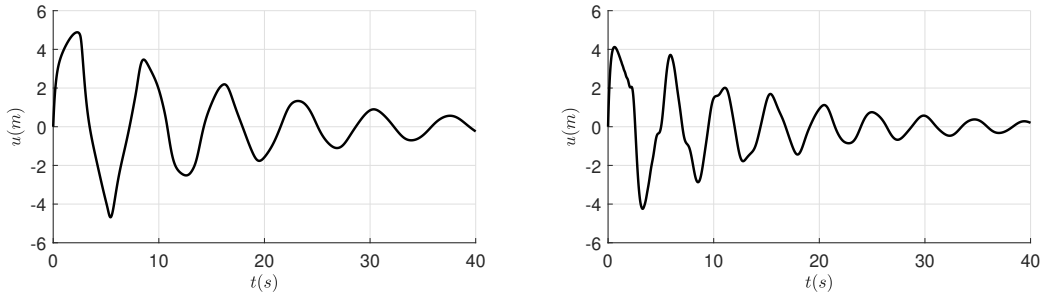

(a) Without bending (b) With bending

Figure 4.41: Evolution of the end of the hose position after perturbation in the initial speed of the drogue.

In Figure 4.41 the response to the perturbation at the end of the hose is presented. As can

be seen, the results are similar to those that would be obtained in the response to a percussion by a linear system [García-Fogeda Núñez and Sanz Andrés, 2014]. The maximum amplitude of motion is approximately 4.5 m in the case without bending, and slightly less, around 4 m, in the case with bending. Both cases are damped, thus, the amplitude decreases over time. However, this reduction is higher in the case without bending, since, as mentioned above, its damping coefficient is higher.

It can also be seen that when bending force is considered more peaks in the response can be observed. This is due to the conclusion explained before: With bending, the perturbation in initial conditions produces more than one wave that propagates through the hose. In addition, at Figure 4.41 it is possible to check that in the case with bending the amplitude of motion is smaller and decreases faster that in the case without bending.

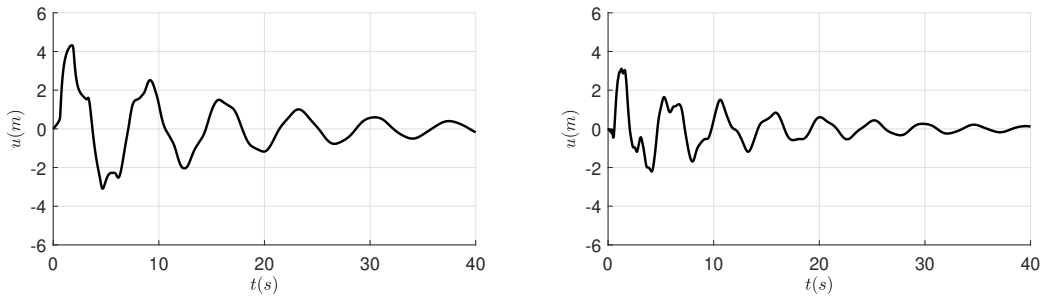

(a) Without bending (b) With bending

Figure 4.42: Evolution of the middle of the hose position after perturbation in the initial speed of the drogue.

Figure 4.42 shows the response for the node in the middle position of the hose. It can be seen that the amplitude of the motion is slightly less than the point at the end of the hose. In particular, around 4 m in the case without bending, and around 3 m in the case with bending. It is observed again that in the case with bending more peaks appear, as there is more than one wave.

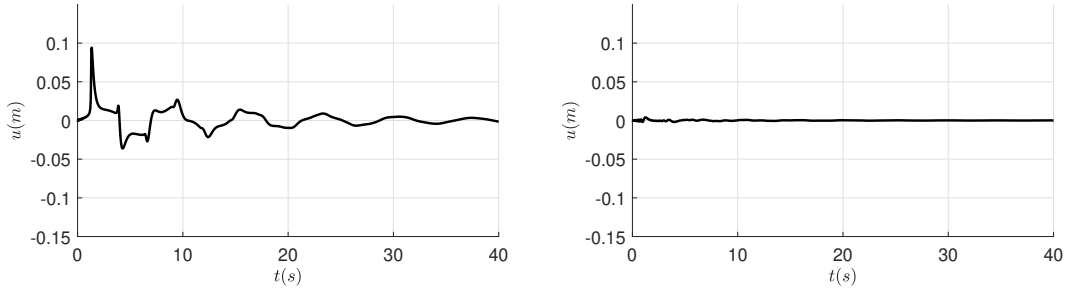

(a) Without bending (b) With bending

Figure 4.43: Evolution of the beginning of the hose position after perturbation in the initial speed of the drogue.

Finally, the evolution of the first node of the hose with motion is showed in Figure 4.43.

As can be seen, at this point the hose practically does not move. Particularly, in the case with bending, where the maximum amplitude is of the order of 10^{-3} m.

4.6.7 Response due to a receiver speed profile

The results obtained for the velocity profile of the receiver given at Eq.(4.115) will be analyzed next. In this case, the bending forces are always included, and the results are obtained for a flight speed of $U_\infty = 90$ m/s, a flight altitude of $H_\infty = 5000$ ft and with the hose filled with fuel.

Figures 4.44 and 4.45 show the horizontal and vertical displacements (u_x and u_y, respectively) of different points along the hose (the arrow with s represents the hose coordinate along the hose) as a function of the time after the contact between the receiver and the drogue has taken place. As shown in both Figures, the motion of the last node of the hose (red line) is prescribed by the speed profile Eq.(4.115) as explained during the development of this response problem. Once contact has taken place and the receiver speed becomes zero (for $t > 2$ s) u_x and u_y remain fixed for the last node of the hose. Likewise, both Figures show how the displacements for the rest of the nodes are damped with time, being, as expected, of smaller amplitude the closer the node is to the hose-tanker junction. It is interesting to note that the vertical motion is damped faster than the horizontal one. This fact was to be expected, since the damping in the vertical motion is higher (it has two contributions: structural and aerodynamic), while the horizontal has only structural damping.

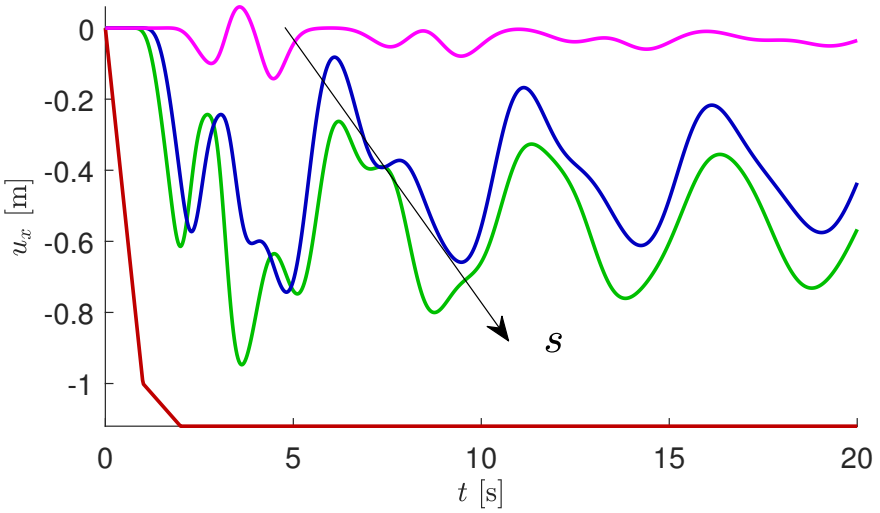

Figure 4.44: Horizontal displacements in different points of the hose after the receiver-drogue contact.

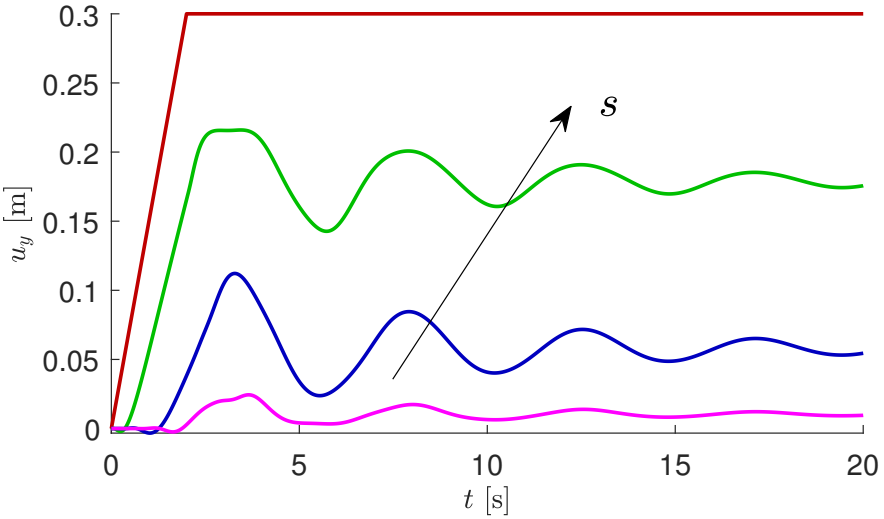

Figure 4.45: Vertical displacements in different points of the hose after the receiver-drogue contact.

In addition, the transmitted forces to the drogue in both axes once the receiver speed becomes zero (for $t > 2$ s) and therefore the drogue is fixed are presented at Figures 4.46 and 4.47. These forces were defined in Eqs.(4.128) and (4.129), and will be presented dimensionless with a nominal value $F_{ref} = 1600$ N.

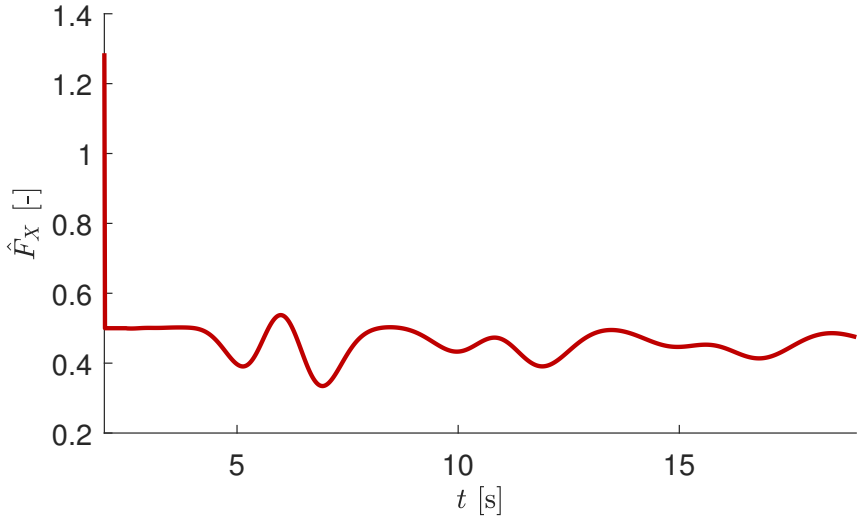

Figure 4.46: Horizontal force in the drogue after the receiver-drogue contact.

Figure 4.46 shows the transmitted dimensionless force in the horizontal direction $\hat{F}_x$. As observed, the maximum force value, approximately $\hat{F}_{X,max} = 1.28$, appears at the exact moment when the drogue becomes fixed. From this point, the force rapidly dampens, approaching a steady value of around $\hat{F}_X = 0.4$. The minimum force value is reached 7 seconds after the contact, with a value of $\hat{F}_{X,min} = 0.32$.

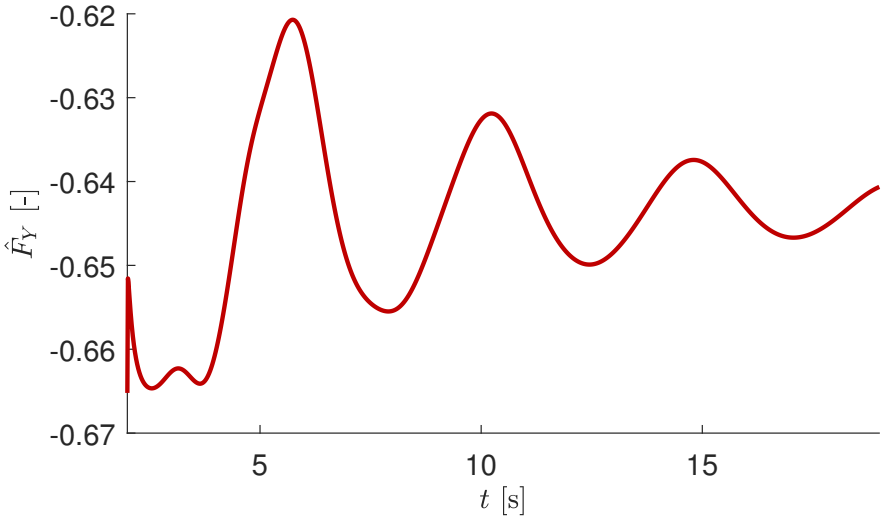

Figure 4.47: Vertical force in the drogue after the receiver-drogue contact.

The dimensionless vertical force $\hat{F}_Y$ is shown in Figure 4.47. Compared to the horizontal force, the vertical force shows much smaller fluctuations and is quickly dampened (as previously mentioned, the damping in the vertical motion is higher than in the horizontal). The maximum value occurs approximately 3 seconds after contact, with an absolute value of $|\hat{F}_{Y,max}| = 0.665$, while the minimum value appears 6 seconds post-contact, with a value of $|\hat{F}_{Y,min}| = 0.62$. Finally, the steady-state value toward which the force converges is approximately $|\hat{F}_{Y,max}| = 0.64$.

Chapter 5

Grid fins characterization

The hose-drogue system developed in previous chapters represents a promising approach for successfully executing the aerial refueling process. As explained in Chapter 1, the stability of the system during the pre-contact hose-deployed phases is crucial to ensure a successful attachment. To enhance the performance of the refueling process, a control strategy to stabilize the drogue is desirable. Grid fins, also known as lattice fins, are non-conventional aerodynamic control surfaces commonly used in missiles and rockets. These fins consist of a lattice of small aerodynamic surfaces arranged within a box structure. In Chapter 1 a general review of grid fins and its advantages over conventional planar fins were presented.

In this chapter, with the goal of integrating the grid fin model into the complete hose-drogue system, a new aerodynamic modeling approach for the fins will be introduced. This approach is based on the Doublet-Lattice Method (DLM) and the "Unit Grid Fin" (UGF) concept for calculating steady and unsteady aerodynamic forces on the fins. Although several works have focused on the CFD analysis of grid fins for preliminary design, such calculations are computationally expensive (typically requiring several hundred hours, as reported by [Despirito et al., 2004]). This significantly limits the ability to compare different configurations or fin models, leading to the consideration of alternative methods.

In the DLM, the aerodynamic surface is divided into small trapezoidal panels arranged in columns parallel to the free-stream, with a distribution of acceleration potential doublets of uniform intensity on each panel. While the DLM is an efficient and reliable strategy for calculating aerodynamic forces, computing a complete fin configuration still requires significant computational resources. Therefore, a method that achieves accurate results with lower computational costs is needed. In this thesis, the method based on the UGF concept presented in [Dikbas et al., 2018] will be generalized to include the computation of dynamic force coefficients using the DLM, as explained in the following sections. The method presented in this reference combines efficiency and reliability, making it an ideal tool for the aerodynamic characterization of the grid fins. The unsteady forces on the fins will be computed with low computational cost while maintaining reliability, as will be demonstrated through comparisons with other methods and experiments.

In the first section, the prototype of grid fins used will be outlined in a general manner. Then, the UGF method will be presented and developed and, finally, both the steady and

unsteady aerodynamic coefficients of the fins will be obtained and analyzed.

5.1 Grid fins prototype

First, the prototype of the grid fins used in this study is presented. Several configurations and positions for grid fins are discussed in the literature; for example, two horizontal grid fins, four in a cross configuration, four at forty-five degrees... In this thesis, the prototype used is the one developed by Airbus Defence and Space within the HDA3R project, as shown in Figure 5.1.

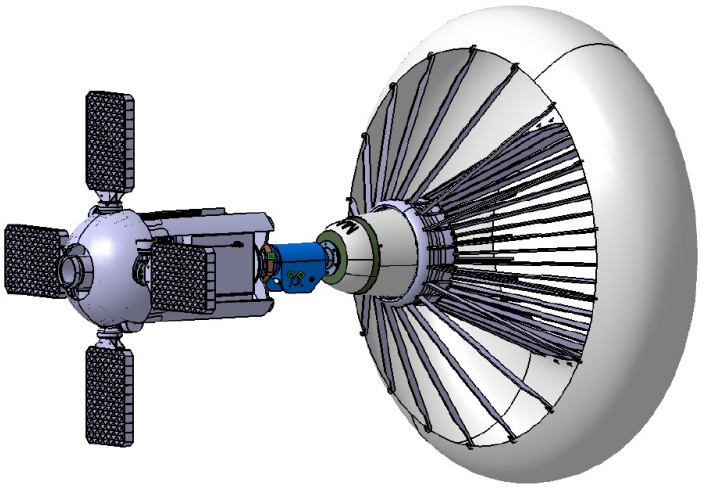

Figure 5.1: Grid fins Prototype.

As can be seen, the prototype consists of four grid fins arranged in a cross configuration, with two fins positioned vertically and two horizontally. The model also includes a control unit and the drogue (which is the same as presented in previous chapters). The four fins are rigidly attached to the control unit. The configuration of each fin is detailed in Figure 5.2, where a_f, b_f and c_f are the fin span, height and chord, respectively. The reference coordinate system (x, y, z) will be the same as defined in the previous Chapter.

As illustrated, there are two fins in vertical position (fins 1 and 3) and two fins in horizontal position (fins 2 and 4). Each of these fins can rotate around its own axis (θ_i angles). These rotations, combined with the motion of the complete model at the hose-drogue-fins junction (pitch α and yaw β), allow for the definition of a local fins angle of attack (rotation around the z-axis) and a local fins angle of sideslip (rotation around the y-axis) for each fin, denoted as α_i^F and β_i^F, for $i = 1, ..., 4$:

$$\alpha_1^F = \alpha; \qquad \beta_1^F = \beta + \theta_1, \tag{5.1}$$

$$\alpha_2^F = \alpha + \theta_2; \qquad \beta_2^F = \beta, \tag{5.2}$$

$$\alpha_3^F = \alpha; \qquad \beta_3^F = \beta - \theta_3, \tag{5.3}$$

$$\alpha_4^F = \alpha - \theta_4; \qquad \beta_4^F = \beta. \tag{5.4}$$

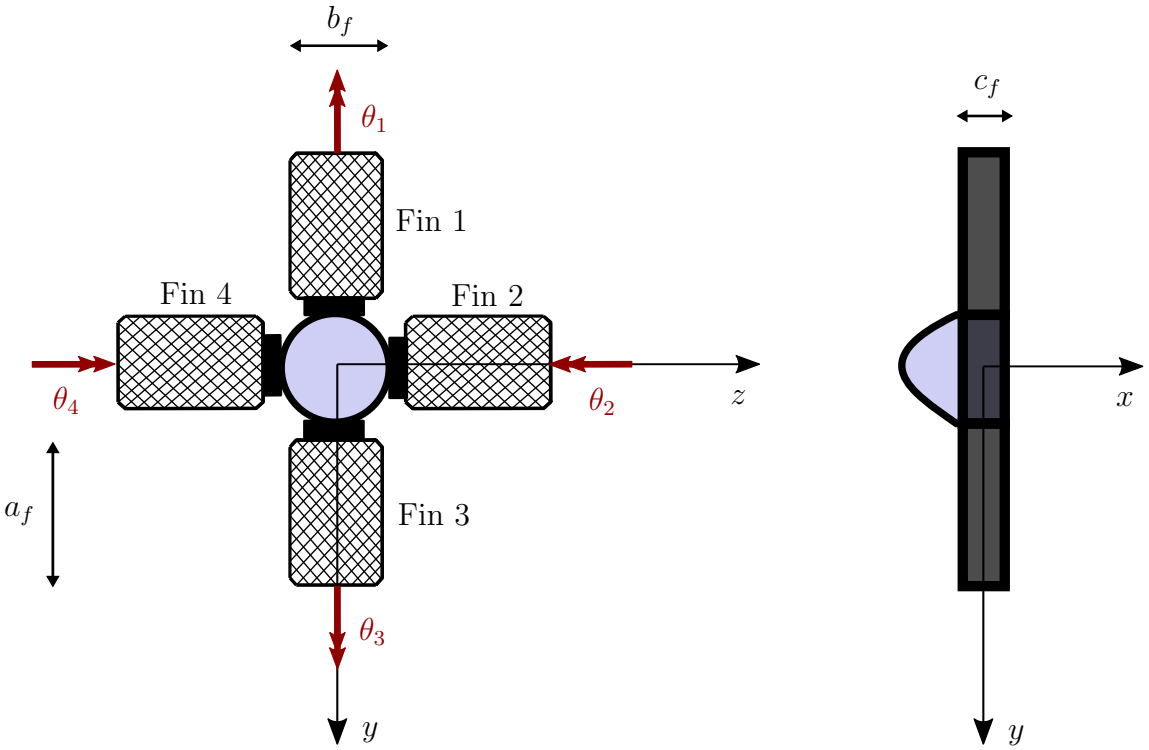

Figure 5.2: Grid fins prototype.

The main characteristics of the grid fins used in the prototype are provided in Table 5.1.

Table 5.1: Grid fin parameters.

Fins span, a_f	190 mm
Fins height, b_f	270 mm
Fins chord, c_f	30 mm
Cavity side length, l	18.8 mm
Grid thickness, t_1	0.2 mm
Frame thickness, t_2	0.8 mm
Fin surface S_{fin}	51300 mm^2
Radial distance from prototype to fin's c.p., r_{ref}	304.9 mm
X-body distance from MRC to fin's c.p., x_{ref}	593.9 mm

5.2 UGF Method

5.2.1 Introduction to the UGF concept

The method for obtaining the aerodynamic forces on each fin is based on the Unit Grid Fin (UGF) concept introduced by [Dikbas et al., 2018], which has been extended in this study to include the unsteady aerodynamic coefficients of grid fins. In this ingenious

approach, the complete fin is divided into individual UGFs, as illustrated in Figure 5.3. The aerodynamic forces on each UGF are computed individually, and the total force coefficient on the fin is obtained by multiplying the net forces acting on each UGF by the total number of equivalent UGFs, as will be seen later.

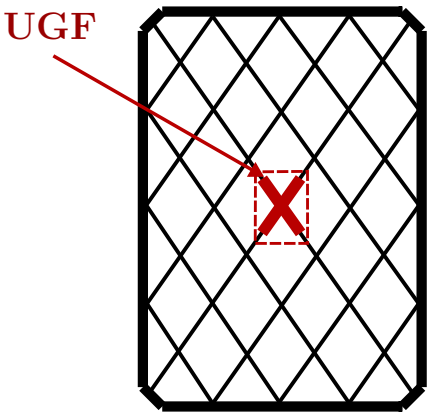

Figure 5.3: Unit Grid Fin example.

In [Dikbas et al., 2018] the UGF-based approach is validated by comparing it with forces calculated for the complete fin, demonstrating very good accuracy in the subsonic regime for steady forces. In this thesis, this procedure is generalized to compute both steady and unsteady aerodynamic forces. While in [Dikbas et al., 2018] the steady aerodynamic forces of the UGF are achieved by a CFD code, in this thesis, since the interest also lies in computing the unsteady aerodynamic forces, will be obtained with a DLM code.

Using the DLM each of the generalized aerodynamic forces, for example the UGF normal force coefficient $C_{N\alpha}^{UGF}$ is computed as a function of the Mach number M_∞ and the reduced frequency of the unsteady motion of the system $k = \omega c_{UGF}/2U_\infty$.

5.2.2 Complete Fin Aerodynamic Coefficients

Once the aerodynamic coefficient of the UGF, $C_{N\alpha}^{UGF}$, has been obtained, the next step is to determine the coefficients for the complete fin. This is achieved, as shown at [Dikbas et al., 2018], by determining the total number of equivalent UGFs for each fin. In this reference it is displayed that three different type of UGF can appear, see Figure 5.4, depending on the location on the fin of the UGF. Let N_{eq} represent the total number of UGFs (or equivalent nodes) for the fin. This value will vary depending on whether the fin is placed horizontally or vertically due to the effect of the frame. Therefore, the equivalent number of nodes will differ for vertical fins (subscript V) and for horizontal fins (subscript H) as follows:

$$N_{eq,V} = \xi_1 \cdot n_1 + \xi_2 \cdot n_2 + \xi_3 \cdot n_3 + N_{frame,V}, \tag{5.5}$$

$$N_{eq,H} = \xi_1 \cdot n_1 + \xi_2 \cdot n_2 + \xi_3 \cdot n_3 + N_{frame,H}, \tag{5.6}$$

where n_i is the total number of each type of node, N_{frame} is the number of equivalent nodes due to the fin frame (see Figure 5.4) and ξ_i is a correction factor for the different UGF nodes defined with the following criteria, which is based on how many webs each UGF has:

- UGF Type 1 $\Longrightarrow \xi_1 = 1$.
- UGF Type 2 $\Longrightarrow \xi_2 = 3/4$.
- UGF Type 3 $\Longrightarrow \xi_3 = 1/2$.

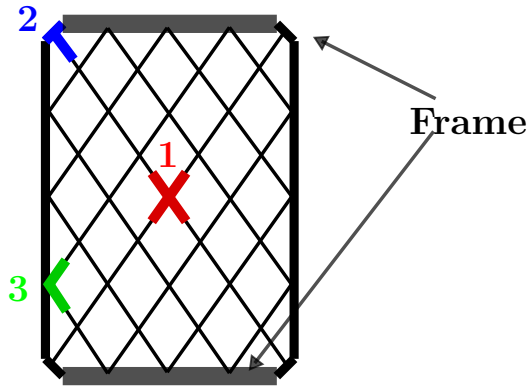

Figure 5.4: UGF types of nodes: Type 1 (center, red), Type 2 (corner, blue), Type 3 (side, green) and the part of the frame which contributes to the aerodynamics (grey).

Thus, with the approach of the UGF method the lift coefficient slopes on the vertical fins (1 and 3) and on the horizontal fins (2 and 4) can be expressed as:

$$C_{L\alpha 1} = C_{L\alpha 3} = C_{N\alpha}^{UGF} \cdot \frac{S_{UGF}}{S_{fin}} \cdot N_{eq,V}, \tag{5.7}$$

$$C_{L\alpha 2} = C_{L\alpha 4} = C_{N\alpha}^{UGF} \cdot \frac{S_{UGF}}{S_{fin}} \cdot N_{eq,H}, \tag{5.8}$$

where S_{UGF} is the reference surface of a UGF, S_{fin} is the reference surface of a complete fin, and $N_{eq,V}$ and $N_{eq,H}$ are the equivalent UGF for a vertical and an horizontal fin, respectively, which are estimated following Eqs.(5.5) and (5.6).

Due to the symmetry of the fin configuration, the side force coefficient slopes in the fins can be derived from the lift coefficients:

$$C_{Z\beta 1} = C_{Z\beta 3} \equiv C_{L\alpha 2} = C_{N\alpha}^{UGF} \cdot \frac{S_{UGF}}{S_{fin}} \cdot N_{eq,H}, \tag{5.9}$$

$$C_{Z\beta 2} = C_{Z\beta 4} \equiv C_{L\alpha 1} = C_{N\alpha}^{UGF} \cdot \frac{S_{UGF}}{S_{fin}} \cdot N_{eq,V}. \tag{5.10}$$

Once $C_{L\alpha}$ and $C_{Z\beta}$ have been determined, a formulation can be developed to calculate the aerodynamic forces on the complete fins. As will be presented in the following Section, contributions to the total forces, such as interference terms between the four fins and the rest of the prototype, are obtained from experimental data, while the DLM computations are strictly associated with the isolated fins. Although these additional interference contributions are typically minor compared to those of the fins themselves, they are included in the results used for the aerodynamic coefficients to enhance the reliability of the results.

5.2.3 Validation of the method

Before the development of the complete coefficients of the grid fins prototype, the UGF method will be validated. For this purpose, data from two different references already mentioned will be used:

- The work of [Dikbas et al., 2018] will serve as a reference for validating the DLM code employed to compute the aerodynamic UGF coefficients.
- The steady lift coefficient for an isolated fin will be compared with those presented in the work of [Burkhalter et al., 1995] and in the work of [Washington and Miller, 1998], which includes experimental results.

UGF coefficient validation

The steady UGF normal force coefficient obtained by the present method is compared with the results presented at [Dikbas et al., 2018]. As explained previously, Dikbas results are obtained using a CFD approach for the computations of the UGF forces while now the DLM is employed. The Mach Number is 0.7. The results are shown in Table 5.2. It can be observed that the difference between both methods is negligible (around 0.2%).

Table 5.2: Comparison of the steady UGF normal force coefficient with Dikbas [Dikbas et al., 2018].

	$C_{N\alpha}^{UGF}$
[Dikbas et al., 2018]	0.00925
Present work	0.00927

Fin coefficient validation

Figure 5.5 presents the comparison of the steady normal force coefficient for an isolated horizontal fin computed by the present method with the results of [Burkhalter et al., 1995], and experimental data from [Washington and Miller, 1998]. The coefficient is obtained as $C_N^{fin2} = C_{L\alpha 2} \cdot \alpha$, where $C_{L\alpha 2}$ has been defined in Eq.(5.8).

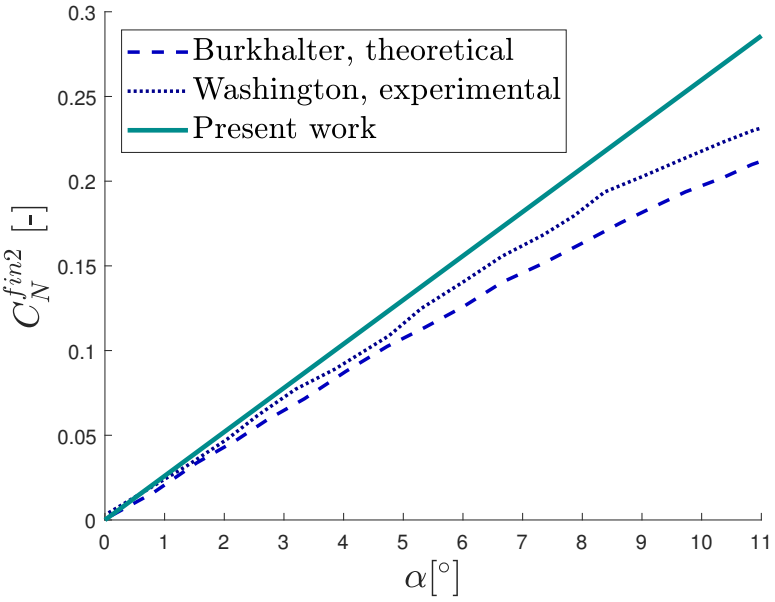

Figure 5.5: Comparison of the steady C_N^{fin2} with the results of [Burkhalter et al., 1995] and [Washington and Miller, 1998].

As can be seen in Figure 5.5, the agreement between the two sets of data is quite satisfactory up to angles of attack of 5^{o} or 6^{o}. When compared with experiments, for the angle of attack of 6^{o}, the present method overpredict the normal force by a 10% while the results of [Burkhalter et al., 1995] underpredict it by a 7%. The Mach Number for this case is 0.5. The results obtained through the DLM code and with the UGF method has no corrections for high angles of attack so it should be only valid in the linear angle of attack range, say up to 6°-7○. It should be emphasized that while the method of [Burkhalter et al., 1995] uses a compressibility correction, the present method remains fully valid within the subsonic Mach Number range. Therefore, as the Mach Number increases, the present method is expected to provide more accurate results than [Burkhalter et al., 1995].

5.3 Grid fins aerodynamic forces

In this section, the complete formulation of the aerodynamic coefficients for the fins will be developed. As previously explained, the fin prototype will be positioned at the hose-drogue junction, and it has the capability to pitch (rotation around the z-axis) and yaw (rotation around the y-axis). The aerodynamic forces acting on the fins are illustrated in Figure 5.6.

As shown in Figure 5.6, the grid fins generate three forces: lift L_F, drag D_F, and side force Z_F, along with two moments: pitching moment M_F and yawing moment N_F, with the positive signs shown in the Figure. Since the model does not account for torsional rotation, there is no aerodynamic moment around the x-axis. As will be discussed in the next Chapter, all these forces will be incorporated into the hose-drogue model as boundary conditions at the end of the hose. However, in this section the focus will be on obtaining these forces, while their integration into the complete hose-drogue model will

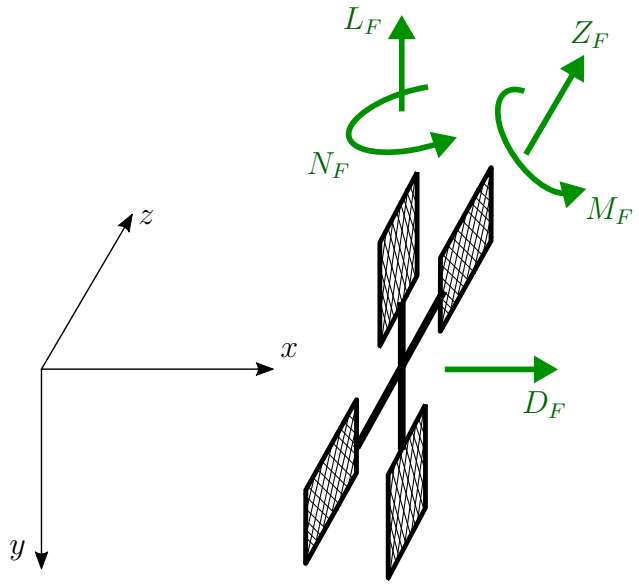

Figure 5.6: Acting forces on the grid fins.

be addressed in Chapter 6. Each force and moment will be defined as:

$$L_F = q_\infty \cdot S_{UGF} \cdot C_L^F, \tag{5.11}$$

$$Z_F = q_\infty \cdot S_{UGF} \cdot C_Z^F, \tag{5.12}$$

$$D_F = q_\infty \cdot S_{UGF} \cdot C_D^F, \tag{5.13}$$

$$M_F = q_\infty \cdot S_{UGF} \cdot c_f \cdot C_M^F. \tag{5.14}$$

$$N_F = q_\infty \cdot S_{UGF} \cdot c_f \cdot C_N^F, \tag{5.15}$$

where C_L^F, C_Z^F and C_D^F are the lift, side force and drag coefficients, respectively, C_M^F and C_N^F the pitch and yaw moment coefficients. These coefficients will be determined as functions of the local angles of attack and sideslip defined in Eqs.(5.1)-(5.4).

Similar to Chapter 2, a linearization will be performed around the static equilibrium position to obtain the unsteady aerodynamic coefficients, while the steady-state coefficients will be obtained using the UGF method explained in the previous section, along with the available experimental data. Therefore, the forces from Eqs.(5.11)-(5.15) will be split in a steady and an unsteady contribution.

The experimental data includes eleven distinct test cases, where the angles of attack and sideslip for each fin vary. In each case, the three force coefficients (lift, drag, and side force) and the pitching moment coefficient are calculated experimentally. Although the yawing moment does appear, as will be discussed in Chapter 6, it does not influence the results of the complete hose-drogue-fins model. Therefore, it will not be further developed in this section.

5.3.1 Lift coefficient

For the configuration presented in Figure 5.2, the lift force coefficient for each fin can be written as a function of the lift-force slopes and the local angles of attack and sideslip as:

$$C_{L1}^F = C_{L\alpha 1} \cdot \alpha_1^F \cdot \cos\beta_1^F, \tag{5.16}$$

$$C_{L2}^F = C_{L\alpha 2} \cdot \alpha_2^F \cdot \cos\beta_2^F, \tag{5.17}$$

$$C_{L3}^F = C_{L\alpha 3} \cdot \alpha_3^F \cdot \cos\beta_3^F, \tag{5.18}$$

$$C_{L4}^F = C_{L\alpha 4} \cdot \alpha_4^F \cdot \cos\beta_4^F, \tag{5.19}$$

where $C_{L\alpha 1}$, $C_{L\alpha 2}$, $C_{L\alpha 3}$ and $C_{L\alpha 4}$ were defined in Eqs.(5.7) and (5.8).

To obtain the total lift coefficient due to the fins, the first option could be to use the sum of each fin force coefficient. However, it is necessary to include previously the aerodynamic interference that appear between the four fins and with the control unit and the drogue. As experimental data is available, this interference will be added from the eleven experimental test cases to enhance the reliability of the results. For this purpose, a least-square fit using all the experimental data provided is performed. The total lift coefficient due to the fins C_L^F, once the interference factors have been included, must be equal to the coefficient obtained experimentally $C_{L,exp}^F$:

$$\hat{f}_{1L} C_{L1}^F + \hat{f}_{2L} C_{L2}^F + \hat{f}_{3L} C_{L3}^F + \hat{f}_{4L} C_{L4}^F \equiv C_{L,exp}^F, \tag{5.20}$$

where $\hat{f}_{1L}$, $\hat{f}_{2L}$, $\hat{f}_{3L}$ and $\hat{f}_{4L}$ are the interference factors for each grid fin, respectively. These factors are assumed to have three different contributions:

- Interference at null angle of attack and null angle of sideslip, defined as f_{0L}.
- Interference due to angle of attack at null angle of sideslip, defined as $f_{\alpha L}|\alpha_i|$.
  - Vertical fins (1 and 3) $\Longrightarrow f_{\alpha L,V}$
  - Horizontal fins (2 and 4) $\Longrightarrow f_{\alpha L,H}$
- Interference due to angle of sideslip at null angle of attack, defined as $f_{\beta L}|\beta_i|$.
  - Vertical fins (1 and 3) $\Longrightarrow f_{\beta L,V}$
  - Horizontal fins (2 and 4) $\Longrightarrow f_{\beta L,H}$

Thus, each interference factor can be written as:

$$\hat{f}_{1L} = f_{0L} + f_{\alpha L,V}|\alpha_1^F| + f_{\beta L,V}|\beta_1^F|, \tag{5.21}$$

$$\hat{f}_{2L} = f_{0L} + f_{\alpha L,H}|\alpha_2^F| + f_{\beta L,H}|\beta_2^F|, \tag{5.22}$$

$$\hat{f}_{3L} = f_{0L} + f_{\alpha L,V}|\alpha_3^F| + f_{\beta L,V}|\beta_3^F|, \tag{5.23}$$

$$\hat{f}_{4L} = f_{0L} + f_{\alpha L,H}|\alpha_4^F| + f_{\beta L,H}|\beta_4^F|. \tag{5.24}$$

Expanding Eq.(5.20) with Eqs.(5.21)-(5.24), it is possible to write the experimental lift coefficient as a function of the three interference contributions:

$$C^F_{L,exp} = A_{0L} \cdot f_{0L} + A_{\alpha L,V} \cdot f_{\alpha L,V} + A_{\beta L,V} \cdot f_{\beta L,V} + A_{\alpha L,H} \cdot f_{\alpha L,H} + A_{\beta L,H} \cdot f_{\beta L,H}, \quad (5.25)$$

where:

$$A_{0L} = C^F_{L1} + C^F_{L2} + C^F_{L3} + C^F_{L4}, \quad (5.26)$$

$$A_{\alpha L,V} = |\alpha^F_1| C^F_{L1} + |\alpha^F_3| C^F_{L3}, \quad (5.27)$$

$$A_{\beta L,V} = |\beta^F_1| C^F_{L1} + |\beta^F_3| C^F_{L3}, \quad (5.28)$$

$$A_{\alpha L,H} = |\alpha^F_2| C^F_{L2} + |\alpha^F_4| C^F_{L4}, \quad (5.29)$$

$$A_{\beta L,H} = |\beta^F_2| C^F_{L2} + |\beta^F_4| C^F_{L4}. \quad (5.30)$$

From Eq.(5.25), the three interference contributions are obtained with a least-square fit, using the available experimental results. With Eqs.(5.21)-(5.24) each interference factor is calculated, and finally the lift coefficient due to the fins can be written as:

$$C^F_L = \hat{f}_{1L} C^F_{L1} + \hat{f}_{2L} C^F_{L2} + \hat{f}_{3L} C^F_{L3} + \hat{f}_{4L} C^F_{L4}. \quad (5.31)$$

As mentioned previously, the interference factors are calculated from steady results, since all of the experimental cases have been obtained with the HDA3R model in static configuration. However, it will be assumed that this factors are valid in both steady and unsteady cases. This assumption amounts to say that the dynamic part of the interference factors of higher order can be neglected. It is also important to note that these eleven experimental cases are the ones used for the interference factors because they are the only available data from the grid fin prototype tests: If test data with even more fin configurations had been available, these factors would have been calculated using all of them.

5.3.2 Side force coefficient

With respect to the side force coefficient, it can be obtained applying an equivalent procedure as for the determination of the lift force. The coefficient for each fin is written as:

$$C^F_{Z1} = C_{Z\beta 1} \cdot (-\beta^F_1) \cdot \cos \alpha^F_1, \quad (5.32)$$

$$C^F_{Z2} = C_{Z\beta 2} \cdot (-\beta^F_2) \cdot \cos \alpha^F_2, \quad (5.33)$$

$$C^F_{Z3} = C_{Z\beta 3} \cdot (-\beta^F_3) \cdot \cos \alpha^F_3, \quad (5.34)$$

$$C^F_{Z4} = C_{Z\beta 4} \cdot (-\beta^F_4) \cdot \cos \alpha^F_4. \quad (5.35)$$

As for the lift force coefficient procedure, interference factors for each grid fin are defined to fulfill the following expression:

$$\hat{f}_{1Z} C^F_{Z1} + \hat{f}_{2Z} C^F_{Z2} + \hat{f}_{3Z} C^F_{Z3} + \hat{f}_{4Z} C^F_{Z4} \equiv C^F_{Z,exp}. \quad (5.36)$$

Again, the interference factors are assumed to have three different contributions:

- Interference at null angle of attack and null angle of sideslip f_{0Z}.
- Interference due to angle of sideslip at null angle of attack $f_{\beta Z}|\beta_i|$.
  - Vertical fins (1 and 3) $\Longrightarrow f_{\beta Z,V}$
  - Horizontal fins (2 and 4) $\Longrightarrow f_{\beta Z,H}$
- Interference due to angle of attack at null angle of sideslip $f_{\alpha Z}|\alpha_i|$.
  - Vertical fins (1 and 3) $\Longrightarrow f_{\alpha Z,V}$
  - Horizontal fins (2 and 4) $\Longrightarrow f_{\alpha Z,H}$

And each interference factor is written as:

$$\hat{f}_{1Z} = f_{0Z} + f_{\alpha Z,V}|\alpha_1^F| + f_{\beta Z,V}|\beta_1^F|, \tag{5.37}$$

$$\hat{f}_{2Z} = f_{0Z} + f_{\alpha Z,H}|\alpha_2^F| + f_{\beta Z,H}|\beta_2^F|, \tag{5.38}$$

$$\hat{f}_{3Z} = f_{0Z} + f_{\alpha Z,V}|\alpha_3^F| + f_{\beta Z,V}|\beta_3^F|, \tag{5.39}$$

$$\hat{f}_{4Z} = f_{0Z} + f_{\alpha Z,H}|\alpha_4^F| + f_{\beta Z,H}|\beta_4^F|, \tag{5.40}$$

The experimental side force coefficient can be written as a function of the three interference contributions:

$$C^F_{Z,exp} = A_{0Z} \cdot f_{0Z} + A_{\alpha Z,V} \cdot f_{\alpha Z,V} + A_{\beta Z,V} \cdot f_{\beta Z,V} + A_{\alpha Z,H} \cdot f_{\alpha Z,H} + A_{\beta Z,H} \cdot f_{\beta Z,H}, \tag{5.41}$$

where:

$$A_{0Z} = C^F_{Z1} + C^F_{Z2} + C^F_{Z3} + C^F_{Z4}, \tag{5.42}$$

$$A_{\alpha Z,V} = |\alpha_1^F|C^F_{Z1} + |\alpha_3^F|C^F_{Z3}, \tag{5.43}$$

$$A_{\beta Z,V} = |\beta_1^F|C^F_{Z1} + |\beta_3^F|C^F_{Z3}, \tag{5.44}$$

$$A_{\alpha Z,H} = |\alpha_2^F|C^F_{Z2} + |\alpha_4^F|C^F_{Z4}, \tag{5.45}$$

$$A_{\beta Z,H} = |\beta_2^F|C^F_{Z2} + |\beta_4^F|C^F_{Z4}. \tag{5.46}$$

Solving Eq.(5.41) with a least-square fit and with Eqs.(5.32)-(5.35), the side force coefficient due to the fins can be obtained as:

$$C^F_Z = \hat{f}_{1Z}C^F_{Z1} + \hat{f}_{2Z}C^F_{Z2} + \hat{f}_{3Z}C^F_{Z3} + \hat{f}_{4Z}C^F_{Z4}. \tag{5.47}$$

5.3.3 Drag force coefficient

As the proposed method is based on a DLM code, and therefore in a potential aerodynamic theory, it is not possible to calculate the drag in the fins. For that reason, the experimental drag force data provided will be used directly, and no induced drag is assumed in these coefficients. Therefore, the total drag force coefficient associated to the fins can be defined as the sum of each of them:

$$C^F_D = C^F_{D1} + C^F_{D2} + C^F_{D3} + C^F_{D4}, \tag{5.48}$$

where the drag coefficients for each fin are obtained from experimental data:

$$C_{D1}^F = C_{D1,exp}^F, \tag{5.49}$$

$$C_{D2}^F = C_{D2,exp}^F, \tag{5.50}$$

$$C_{D3}^F = C_{D3,exp}^F, \tag{5.51}$$

$$C_{D4}^F = C_{D4,exp}^F. \tag{5.52}$$

5.3.4 Pitching moment coefficient

To obtain the pitching moment coefficient of the grid fins it is necessary to have been previously obtained the lift and drag force coefficients in each of them. With the C_{Li}^F and C_{Di}^F coefficients and with the reference distances defined in Table 5.1, the pitching moment coefficient for each fin is defined as:

$$C_{M1}^F = \frac{r_{z1}}{a_f}\left(-\hat{f}_{1L}\cdot C_{L1}^F\cdot\sin\alpha_1^F + C_{D1}^F\cdot\cos\alpha_1^F\right) + \frac{x_{ref}}{a_f}\left(\hat{f}_{1L}\cdot C_{L1}^F\cdot\cos\alpha_1^F + C_{D1}^F\cdot\sin\alpha_1^F\right), \tag{5.53}$$

$$C_{M2}^F = -\frac{r_{z2}}{a_f}\left(-\hat{f}_{2L}\cdot C_{L2}^F\cdot\sin\alpha_2^F + C_{D2}^F\cdot\cos\alpha_2^F\right) + \frac{x_{ref}}{a_f}\left(\hat{f}_{2L}\cdot C_{L2}^F\cdot\cos\alpha_2^F + C_{D2}^F\cdot\sin\alpha_2^F\right), \tag{5.54}$$

$$C_{M3}^F = \frac{r_{z3}}{a_f}\left(-\hat{f}_{3L}\cdot C_{L3}^F\cdot\sin\alpha_3^F + C_{D3}^F\cdot\cos\alpha_3^F\right) + \frac{x_{ref}}{a_f}\left(\hat{f}_{3L}\cdot C_{L3}^F\cdot\cos\alpha_3^F + C_{D3}^F\cdot\sin\alpha_3^F\right), \tag{5.55}$$

$$C_{M4}^F = -\frac{r_{z4}}{a_f}\left(-\hat{f}_{4L}\cdot C_{L4}^F\cdot\sin\alpha_4^F + C_{D4}^F\cdot\cos\alpha_4^F\right) + \frac{x_{ref}}{a_f}\left(\hat{f}_{4L}\cdot C_{L4}^F\cdot\cos\alpha_4^F + C_{D4}^F\cdot\sin\alpha_4^F\right). \tag{5.56}$$

Where r_{zi} is defined as $r_{zi} = r_{ref}\cdot\sin(i\pi/2)$, being $i = 1, ..., 4$. In this case the interference corrections are already added through the lift coefficient. Therefore, the total pitching moment coefficient due to the fins is:

$$C_M^F = C_{M1}^F + C_{M2}^F + C_{M3}^F + C_{M4}^F. \tag{5.57}$$

5.3.5 Linearization

In a similar way to Eqs.(4.39)-(4.40) from Chapter 4, the angles of attack and sideslip of the grid fins can be split into a steady and an unsteady contribution (for a symmetric case of the grid fins configuration):

$$\alpha_i^F = \alpha_{e_i}^F + \delta_1\cdot\Delta\alpha_i^F, \tag{5.58}$$

$$\beta_i^F = \beta_{e_i}^F + \delta_1\cdot\Delta\beta_i^F, \tag{5.59}$$

where $\alpha_{e_i}^F$ and $\beta_{e_i}^F$ are the steady angle of attack and sideslip of each fin, $\Delta\alpha_i^F$ and $\Delta\beta_i^F$ the unsteady angle of attack and sideslip of each grid fin ($i = 1, ..., 4$) and δ_1 is the small amplitude unsteady perturbation (already presented in Chapter 4).

With this definition of the angles, the aerodynamic coefficients developed previously can be splitted in a steady and an unsteady contribution. However, regarding the drag coefficient, since it is derived directly from experimental data (which, as previously mentioned, are based on experiments with various static positions of the prototype), it will be assumed that all drag forces generated by the fins are steady.

Lift force coefficient

The lift coefficient for each fin, defined in Eqs.(5.16)-(5.19), can be rewritten as:

$$C_{Li}^F = C_{L\alpha i} \cdot (\alpha_{e_i}^F + \delta_1 \cdot \Delta\alpha_i^F) \cdot \cos(\beta_{e_i}^F + \delta_1 \cdot \Delta\beta_i^F). \tag{5.60}$$

By linearizing this expression in a similar manner to the procedure described in Chapter 3, the coefficients can be separated into a steady-state component and an unsteady one:

$$C_{Li}^F = C_{Le_i}^F + \delta_1 \cdot \Delta C_{Li}^F, \tag{5.61}$$

where

$$C_{Le_i}^F = C_{L\alpha i} \cdot \alpha_{e_i}^F \cdot \cos\beta_{e_i}^F, \tag{5.62}$$

$$\Delta C_{Li}^F = C_{L\alpha i}(\Delta\alpha_i^F \cos\beta_{e_i}^F - \alpha_{e_i}^F \Delta\beta_i^F \sin\beta_{e_i}^F). \tag{5.63}$$

Side force coefficient

The side force coefficient for each fin, defined in Eqs.(5.32)-(5.35), is rewritten as:

$$C_{Zi}^F = C_{Z\beta i}(-\beta_{e_i}^F - \delta_1 \cdot \Delta\beta_i^F) \cdot \cos(\alpha_{e_i}^F + \delta_1 \cdot \Delta\alpha_i^F). \tag{5.64}$$

Linearizing this expression, the coefficients are splitted into a steady-state component and an unsteady one:

$$C_{Zi}^F = C_{Ze_i}^F + \delta_1 \cdot \Delta C_{Zi}^F, \tag{5.65}$$

where

$$C_{Ze_i}^F = C_{Z\beta i} \cdot (-\beta_{e_i}^F) \cdot \cos\alpha_{e_i}^F, \tag{5.66}$$

$$\Delta C_{Zi}^F = C_{Z\beta i}(\Delta\beta_i^F \cos\alpha_{e_i}^F + \beta_{e_i}^F \Delta\alpha_i^F \sin\alpha_{e_i}^F). \tag{5.67}$$

Pitching moment coefficient

With respect to the pitching moment coefficient for each fin, a linearization can also be performed:

$$C_{Mi}^F = C_{Me_i}^F + \delta_1 \cdot \Delta C_{Mi}^F, \tag{5.68}$$

where the steady coefficient for each fin is:

$$C_{Me_i}^F = \frac{r_{zi}}{a_f}\left(-\hat{f}_{iL} \cdot C_{Lei}^F \cdot \sin\alpha_{e_i}^F + C_{Dei}^F \cdot \cos\alpha_{e_i}^F\right) + \frac{x_{ref}}{a_f}\left(\hat{f}_{iL} \cdot C_{Le_i}^F \cdot \cos\alpha_{e_i}^F + C_{Di}^F \cdot \sin\alpha_{e_i}^F\right),$$

(5.69)

and the unsteady:

$$\Delta C_{Mi}^F = \frac{r_{zi}}{a_f}\left(-\hat{f}_{iL}\cdot\sin\alpha_{e_i}^F\Delta C_{Li}^F - \hat{f}_{iL}\cdot C_{Le_i}^F\cdot\cos\alpha_{e_i}^F\cdot\Delta\alpha_i^F - C_{Di}^F\cdot\sin\alpha_{e_i}^F\cdot\Delta\alpha_i^F\right)+$$

$$\frac{x_{ref}}{a_f}\left(\hat{f}_{iL}C_{Lei}^F\cdot\sin\alpha_{e_i}^F\cdot\Delta\alpha_i + \hat{f}_{iL}\cdot\cos\alpha_{e_i}^F\cdot\Delta C_{Li}^F + C_{Dei}^F\cdot\cos\alpha_{e_i}^F\Delta\alpha_i^F\right). \tag{5.70}$$

As can be seen, Eqs.(5.69) and (5.70) are written as functions of the steady and unsteady lift coefficients for each fin $C_{Le_i}^F$ and ΔC_{Li}^F. Therefore, using Eqs.(5.62) and (5.63) the steady and unsteady pitching moment coefficient can finally be written as:

$$C_{Me_i}^F = \frac{r_{zi}}{a_f}\left(-\hat{f}_{iL}\cdot C_{L\alpha i}\cdot\alpha_{e_i}^F\cdot\cos\beta_{e_i}^F\cdot\sin\alpha_{e_i}^F + C_{Di}^F\cdot\cos\alpha_{e_i}^F\right)+$$

$$\frac{x_{ref}}{a_f}\left(\hat{f}_{iL}\cdot C_{L\alpha i}\cdot\alpha_{e_i}^F\cdot\cos\beta_{e_i}^F\cdot\cos\alpha_{e_i}^F + C_{Di}^F\cdot\sin\alpha_{e_i}^F\right), \tag{5.71}$$

$$\Delta C_{Mi}^F = \frac{r_{zi}}{a_f}\Big[-\hat{f}_{iL}\cdot\sin\alpha_{e_i}^F\cdot C_{L\alpha i}\cdot(\Delta\alpha_i^F\cos\beta_{e_i}^F - \alpha_{e_i}^F\Delta\beta_i^F\sin\beta_{e_i}^F)-$$

$$\hat{f}_{iL}\cdot C_{L\alpha i}\cdot\alpha_{e_i}^F\cdot\cos\beta_{e_i}^F\cdot\cos\alpha_{e_i}^F\cdot\Delta\alpha_i^F - C_{Dei}^F\cdot\sin\alpha_{e_i}^F\cdot\Delta\alpha_i^F\Big]+$$

$$\frac{x_{ref}}{a_f}\Big[\hat{f}_{iL}\cdot C_{L\alpha i}\cdot\alpha_{e_i}^F\cdot\cos\beta_{e_i}^F\cdot\sin\alpha_{e_i}^F\cdot\Delta\alpha_i^F+$$

$$\hat{f}_{iL}\cdot\cos\alpha_{e_i}^F\cdot C_{L\alpha i}\cdot(\Delta\alpha_i^F\cos\beta_{e_i}^F - \alpha_{e_i}^F\Delta\beta_i^F\sin\beta_{e_i}^F) + C_{Dei}^F\cdot\cos\alpha_{e_i}^F\cdot\Delta\alpha_i^F\Big]. \tag{5.72}$$

With all the coefficients for each fin, following the procedure developed in the previous sections, the total lift, side force and pitching moment coefficient can be also defined separated in a steady and an unsteady contribution:

$$C_L^F = C_{Le}^F + \delta_1\cdot\Delta C_L^F, \tag{5.73}$$

$$C_Z^F = C_{Ze}^F + \delta_1\cdot\Delta C_Z^F, \tag{5.74}$$

$$C_M^F = C_{Me}^F + \delta_1\cdot\Delta C_M^F. \tag{5.75}$$

It is necessary to highlight the three unsteady aerodynamic coefficients ΔC_L^F, ΔC_Z^F and ΔC_M^F: throughout their development, it has been observed that they depend on eight variables: the four unsteady angles of attack for each fin $\Delta\alpha_i^F$ and the four unsteady sideslip angles for each fin $\Delta\beta_i^F$. This fact, as will be discussed in chapter 6, becomes critically important when incorporating the unsteady fin forces into the complete hose-drogue system. Therefore, these coefficients can be expressed by grouping the terms that

depend on each of these eight variables in the following manner:

$$\Delta C_L^F = \sum_{i=1}^{4} (\Delta C_{L\alpha_i} \cdot \Delta\alpha_i^F + \Delta C_{L\beta_i} \cdot \Delta\beta_i^F), \tag{5.76}$$

$$\Delta C_Z^F = \sum_{i=1}^{4} (\Delta C_{Z\alpha_i} \cdot \Delta\alpha_i^F + \Delta C_{Z\beta_i} \cdot \Delta\beta_i^F), \tag{5.77}$$

$$\Delta C_M^F = \sum_{i=1}^{4} (\Delta C_{M\alpha_i} \cdot \Delta\alpha_i^F + \Delta C_{M\beta_i} \cdot \Delta\beta_i^F). \tag{5.78}$$

where all the coefficients that multiplies $\Delta\alpha_i^F$ and $\Delta\beta_i^F$ are defined from the previous expressions of each coefficient as:

$$\Delta C_{L\alpha_i} = C_{L\alpha i} \cdot \cos\beta_{e_i}^F, \tag{5.79}$$

$$\Delta C_{L\beta_i} = C_{L\alpha i} \cdot \alpha_{e_i}^F \cdot \sin\beta_{e_i}^F, \tag{5.80}$$

$$\Delta C_{Z\alpha_i} = C_{Z\beta i} \cdot \beta_{e_i}^F \cdot \sin\alpha_{e_i}^F, \tag{5.81}$$

$$\Delta C_{Z\beta_i} = C_{Z\beta i} \cdot \cos\alpha_{e_i}^F, \tag{5.82}$$

$$\Delta C_{M\alpha_i} = \frac{r_{zi}}{a_f}\left[-\hat{f}_{iL} \cdot \sin\alpha_{e_i}^F \cdot C_{L\alpha i} \cdot \cos\beta_{e_i}^F - \hat{f}_{iL} \cdot C_{L\alpha i} \cdot \alpha_{e_i}^F \cdot \cos\beta_{e_i}^F \cdot \cos\alpha_{e_i}^F - C_{Dei}^F \cdot \sin\alpha_{e_i}^F\right]$$

$$+ \frac{x_{ref}}{a_f}\left[\hat{f}_{iL} \cdot C_{L\alpha i} \cdot \alpha_{e_i}^F \cdot \cos\beta_{e_i}^F \cdot \sin\alpha_{e_i}^F + \hat{f}_{iL} \cdot \cos\alpha_{e_i}^F \cdot C_{L\alpha i} \cdot \cos\beta_{e_i}^F + C_{Dei}^F \cdot \cos\alpha_{e_i}^F\right], \tag{5.83}$$

$$\Delta C_{M\beta_i} = \frac{r_{zi}}{a_f} \cdot \hat{f}_{iL} \cdot \sin\alpha_{e_i}^F \cdot C_{L\alpha i} \cdot \alpha_{e_i}^F \cdot \sin\beta_{e_i}^F - \frac{x_{ref}}{a_f} \cdot \hat{f}_{iL} \cdot \cos\alpha_{e_i}^F \cdot C_{L\alpha i} \cdot \alpha_{e_i}^F \sin\beta_{e_i}^F. \tag{5.84}$$

Further development of these coefficients can be found at Appendix B. The complete development of each part of the total coefficients, as well as the coefficients for each fin are also presented with details in this Appendix.

Finally, the lift and side forces and the pitching moment can be written from its coefficients as:

$$L_F = L_{F_e} + \delta_1 \cdot \Delta L_F, \tag{5.85}$$

$$Z_F = Z_{F_e} + \delta_1 \cdot \Delta Z_F, \tag{5.86}$$

$$M_F = M_{F_e} + \delta_1 \cdot \Delta M_F. \tag{5.87}$$

5.3.6 Results for the steady forces

The results for the steady aerodynamic coefficients obtained with the proposed method are presented. The experimental cases provided by Airbus Defence and Space are used

as a reference. For the grid fins configuration presented previously, there are a total of eleven different cases. The angles of each case, together with the experimental results for the lift, side force and pitching moment coefficients are presented in Table 5.3.

The steady lift coefficients due to the fins are presented in Table 5.4. As can be seen, in every case (from 1 to 11) is shown the coefficient for each grid fin, as well as the interference factors and finally the total lift coefficient C_L^F. In addition, a comparison with respect to the experimental result $C_{L,exp}^F$ is given, as a percentage increment.

As shown in Table 5.4, results are very similar to those obtained experimentally. However, it is important to mention that in Case 1 a significantly lower coefficient than the experimental data is obtained. This fact is mainly due to the applicability of the interference factors, which are obtained on the basis of an adjustment with the eleven cases.

Table 5.3: Experimental aerodynamic coefficients for each case.

Case	$\alpha[^\circ]$	$\beta[^\circ]$	$\theta_1[^\circ]$	$\theta_2[^\circ]$	$\theta_3[^\circ]$	$\theta_4[^\circ]$	$C_{L,exp}^F$	$C_{Z,exp}^F$	$C_{M,exp}^F$
1	0	0	0	5	0	-5	0.9072	0.0000	2.8357
2	0	0	0	5	0	5	0.0000	0.0000	0.0000
3	0	0	5	0	-5	0	0.0000	-0.0972	0.0000
4	0	0	5	0	5	0	0.0000	0.0000	0.0000
5	0	0	7.5	7.5	-7.5	-7.5	1.3118	-1.3118	4.1005
6	5	0	5	5	-5	-5	1.8095	-0.8151	6.3105
7	-5	0	5	5	-5	-5	-0.1404	-0.8151	-2.8635
8	0	5	5	5	-5	-5	0.8151	-1.8095	2.5479
9	0	-5	5	5	-5	-5	0.8151	0.1404	2.5479
10	5	5	5	5	-5	-5	1.7321	-1.7321	6.0056
11	15	15	5	5	5	5	2.2999	-2.2999	9.5915

Table 5.4: Lift coefficient results.

Case	C_{Le1}^F	C_{Le2}^F	C_{Le3}^F	C_{Le4}^F	$\hat{f}_{1L}$	$\hat{f}_{2L}$	$\hat{f}_{3L}$	$\hat{f}_{4L}$	C_{Le}^F	C_{Le}^F (%)
1	0.0000	0.3009	0.0000	0.3009	0.9638	1.2202	0.9638	1.2202	0.7343	-19.05%
2	0.0000	0.3009	0.0000	-0.3009	0.9638	1.2202	0.9638	1.2202	0.0000	0.00%
3	0.0000	0.0000	0.0000	0.0000	0.2045	0.9638	0.2045	0.9638	0.0000	0.00%
4	0.0000	0.0000	0.0000	0.0000	0.2045	0.9638	0.2045	0.9638	0.0000	0.00%
5	0.0000	0.4514	0.0000	0.4514	-0.1752	1.3484	-0.1752	1.3484	1.2172	-7.32%
6	0.2848	0.6018	0.2848	0.6018	0.2307	1.4767	0.2307	1.4767	1.9087	5.48%
7	-0.2848	0.0000	-0.2848	0.0000	0.2307	0.9638	0.2307	0.9638	-0.1314	-6.40%
8	0.0000	0.2998	0.0000	0.2998	-0.5548	1.4357	-0.5548	1.4357	0.8608	5.60%
9	0.0000	0.2998	0.0000	0.2998	0.9638	1.4357	0.9638	1.4357	0.8608	5.60%
10	0.2815	0.5995	0.2815	0.5995	-0.5286	1.6922	-0.5286	1.6922	1.7314	-0.04%
11	0.8059	1.1626	0.8446	0.5813	-1.9946	2.6361	-0.4760	2.1232	2.2896	-0.45%

Next, the side force coefficients due to the fins are presented in Table 5.5, in a similar way to the case of the lift coefficient. As can be seen, the results are accurate enough when compared with the experimental data, for all the cases except Case 5, showing a difference of less than 10%.

Table 5.5: Side force coefficient results.

Case	C^F_{Ze1}	C^F_{Ze2}	C^F_{Ze3}	C^F_{Ze4}	$\hat{f}_{1Z}$	$\hat{f}_{2Z}$	$\hat{f}_{3Z}$	$\hat{f}_{4Z}$	C^F_{Ze}	C^F_{Ze} (%)
1	0.0000	0.0000	0.0000	0.0000	0.6803	0.2686	0.6803	0.2686	0.0000	0.00%
2	0.0000	0.0000	0.0000	0.0000	0.6803	0.2686	0.6803	0.2686	0.0000	0.00%
3	-0.3009	0.0000	-0.3009	0.0000	1.0633	0.6803	1.0633	0.6803	-0.1043	7.30%
4	-0.3009	0.0000	0.3009	0.0000	1.0633	0.6803	1.0633	0.6803	0.0000	0.00%
5	-0.4514	0.0000	-0.4514	0.0000	1.2548	0.0628	1.2548	0.0628	-1.1328	-13.65%
6	-0.2998	0.0000	-0.2998	0.0000	1.2320	-0.1430	1.2320	-0.1430	-0.7386	-9.38%
7	-0.2998	0.0000	-0.2998	0.0000	1.2320	0.6803	1.2320	0.6803	-0.7386	-9.38%
8	-0.6018	-0.2848	-0.6018	-0.2848	1.4464	0.0508	1.4464	0.0508	-1.7698	-2.20%
9	0.0000	0.2848	0.0000	0.2848	0.6803	0.2263	0.6803	0.2263	0.1289	-8.19%
10	-0.5995	-0.2815	-0.5995	-0.2815	1.6150	-0.3609	1.6150	-0.3609	-1.7333	0.07%
11	-1.1626	-0.8059	-0.5813	-0.8446	2.7185	-1.6199	1.9524	-0.7966	-2.3172	0.75%

The pitching moment coefficients due to the fins are presented in Table 5.6. The results compared with the experimental data are again satisfactory. In all cases except Case 1, the differences are less than 10%.

Table 5.6: Pitching moment coefficient results.

Case	C^F_{Me1}	C^F_{Me2}	C^F_{Me3}	C^F_{Me4}	C^F_{Me}	C^F_{Me} (%)
1	0.4306	1.2631	-0.4306	1.2631	2.5262	-10.91%
2	0.4305	1.2631	-0.4305	-1.2631	0.0000	0.00%
3	0.4999	0.0000	-0.4999	0.0000	0.0000	0.00%
4	0.4999	0.0000	-0.4999	0.0000	0.0000	0.00%
5	0.6177	1.9993	-0.6177	1.9993	3.9986	-2.49%
6	1.7308	2.2681	0.5871	2.2681	6.8541	7.93%
7	-0.9155	0.0000	-2.0280	0.0000	-2.9435	-2.79%
8	0.7793	1.2144	-0.7793	1.2144	2.4288	4.67%
9	0.4689	1.2144	-0.4689	1.2144	2.4288	4.67%
10	1.8504	2.0732	0.2375	2.0732	6.2343	3.81%
11	3.2667	2.6671	1.8900	1.8092	9.6330	2.57%

Finally, in Table 5.7 a summary of the comparison between all the results obtained with the experimental ones is presented.

Table 5.7: Comparison of the results with the experimental data.

Case	α_1^F	α_2^F	α_3^F	α_4^F	β_1^F	β_2^F	β_3^F	β_4^F	$C_{L,exp}^F$	C_{Le}^F	$C_{Z,exp}^F$	C_{Ze}^F	$C_{M,exp}^F$	C_{Me}^F
1	0	5	0	5	0	0	0	0	0.9072	0.7343 (-19.05%)	0	0.0000 (0.00%)	2.8357	2.5262 (-10.91%)
2	0	5	0	-5	0	0	0	0	0	0.0000 (0.00%)	0	0.0000 (0.00%)	0.0000	0.0000 (0.00%)
3	0	0	0	0	5	0	5	0	0	0.0000 (0.00%)	-0.0972	-0.1043 (7.30%)	0.0000	0.0000 (0.00%)
4	0	0	0	0	5	0	-5	0	0	0.0000 (0.00%)	0	0.0000 (0.00%)	0.0000	0.0000 (0.00%)
5	0	7.5	0	7.5	7.5	0	7.5	0	1.3118	1.2172 (-7.32%)	-1.3118	-1.1328 (-13.65%)	4.1005	3.9986 (-2.49%)
6	5	10	5	10	5	0	5	0	1.8095	1.9087 (5.48%)	-0.8151	-0.7386 (-9.38%)	6.3105	6.8541 (7.93%)
7	-5	0	-5	0	5	0	5	0	-0.1404	-0.1314 (-6.40%)	-0.8151	-0.7386 (-9.38%)	-2.8635	-2.9435 (-2.79%)
8	0	5	0	5	10	5	10	5	0.8151	0.8608 (5.60%)	-1.8095	-1.7698 (-2.20%)	2.5479	2.4288 (4.67%)
9	0	5	0	5	0	-5	0	-5	0.8151	0.8608 (5.60%)	0.1404	0.1289 (-8.19%)	2.5479	2.4288 (4.67%)
10	5	10	5	10	10	5	10	5	1.7321	1.7314 (-0.04%)	-1.7321	-1.7333 (0.07%)	6.0056	6.2343 (3.81%)
11	15	20	15	10	20	15	10	15	2.2999	2.2896 (-0.45%)	-2.2999	-2.3172 (0.75%)	9.5915	9.6330 (2.57%)

5.3.7 Results for the unsteady forces

Next, the results for the unsteady aerodynamic forces are presented. As the DLM code is executed as a function of the reduced frequency and the Mach number, the unsteady coefficients will first be presented as a function of the reduced frequency for a fixed value of the Mach number, followed by the reverse (a fixed reduced frequency varying the Mach number). In this way, the influence of both parameters in the results can be analyzed.

Sweep in the reduced frequency

Starting from the known results for $k = 0$, the DLM code is executed for a Mach number $M_\infty = 0.5$ and for several reduced frequencies. Then, an unsteady UGF normal force coefficient $C_{N\alpha,UGF}(M_\infty = 0.5, k)$ can be calculated. Using the previously explained UGF method, the unsteady coefficients $\Delta C_L^F(0.5, k)$, $\Delta C_Z^F(0.5, k)$ and $\Delta C_M^F(0.5, k)$, which are now complex numbers, are obtained.

In Figures 5.7-5.9, the module and phase of each coefficient are represented as a function of the reduced frequency. The results correspond to the Case 10 of the presented in Tables 5.3 and 5.7. As can be observed, the modules of the three aerodynamic coefficients decrease as the reduced frequency increases, up to a value close to $k = 2$. Beyond this point, the trend reverses and the modules start to increase with the reduced frequency. Regarding the phases, up to approximately $k = 1.5$ the phase in all three coefficients increases with the reduced frequency. However, from that value it decreases slightly as the reduced frequency increases.

Sweep in the Mach number

In addition to the results presented earlier, the variation of the unsteady aerodynamic coefficients with the Mach number M_∞ for a specific value of the reduced frequency has also been analyzed. By setting this value to $k = 0.2$, the DLM code is executed, performing a sweep across the Mach number M_∞. This process yields $C_{N\alpha,UGF}(M_\infty, k = 0.2)$. With the same procedure as in the previous case, $\Delta C_L^F(M_\infty, 0.2)$, $\Delta C_Z^F(M_\infty, 0.2)$ and $\Delta C_M^F(M_\infty, 0.2)$ are calculated.

The module and the phase of each coefficient as a function of the Mach number are shown in Figures 5.10-5.12. As in the previous case, the results correspond to the Case 10 of the presented in Tables 5.3 and 5.7. As can be seen, as the Mach number increases the modules of the three aerodynamic coefficients increase. The rate of increase becoming more pronounced at higher Mach numbers. Conversely, the phases present a slight increase with the Mach number. However, this increase is minimal, leading to the conclusion that the effect of Mach number on the phase of the aerodynamic coefficients is practically negligible.

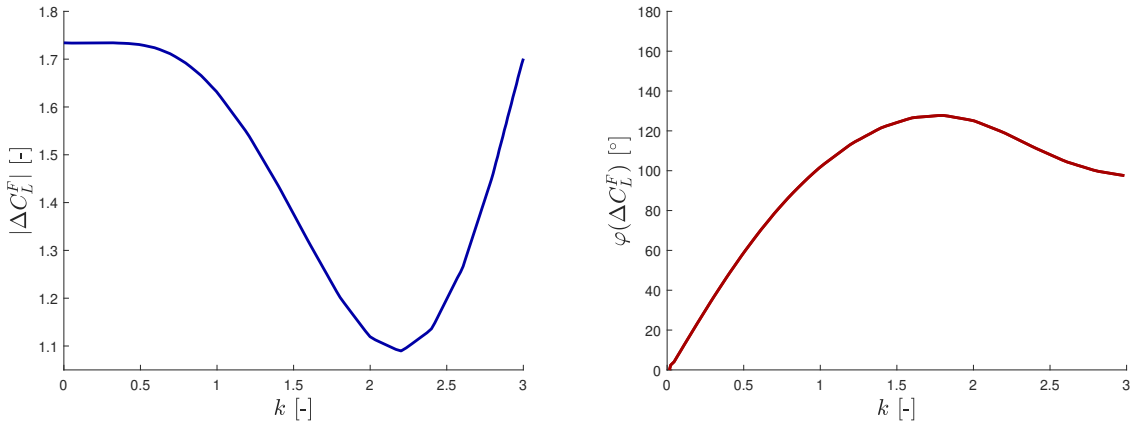

Figure 5.7: Module and phase of the lift coefficient as a function of the reduced frequency for $M_\infty = 0.5$.

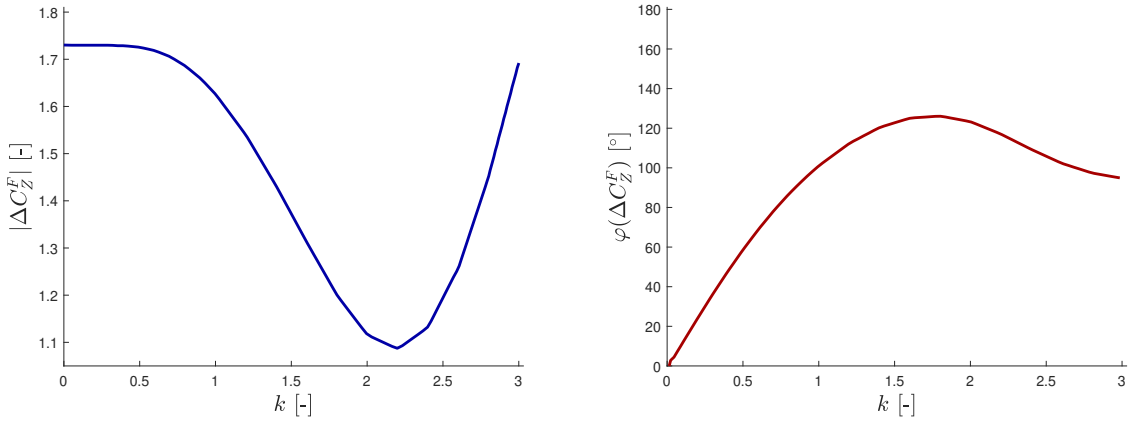

Figure 5.8: Module and phase of the side force coefficient as a function of the reduced frequency for $M_\infty = 0.5$.

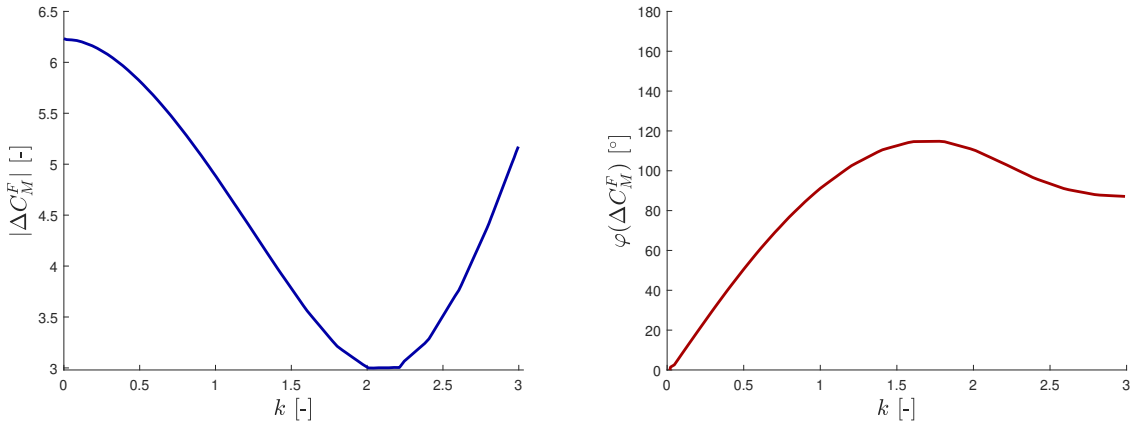

Figure 5.9: Module and phase of the pitching moment coefficient as a function of the reduced frequency for $M_\infty = 0.5$.

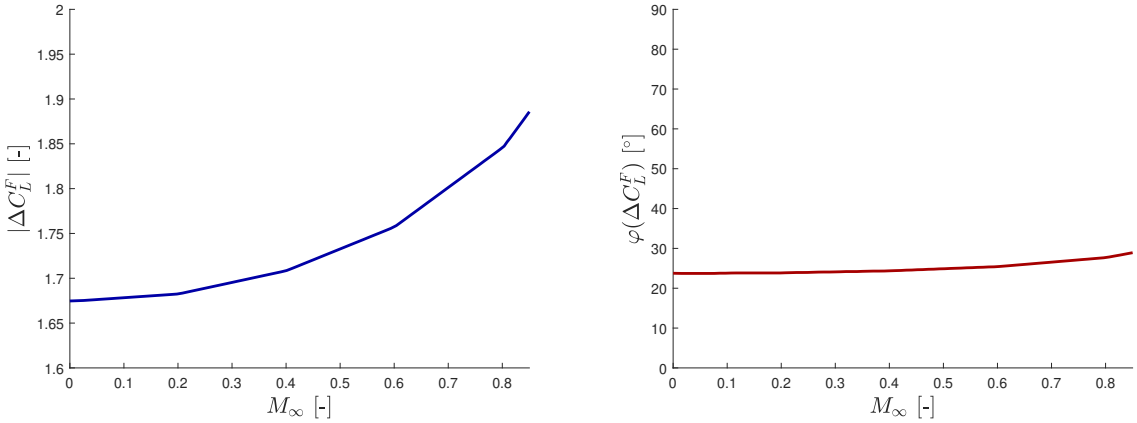

Figure 5.10: Module and phase of the lift coefficient as a function of the Mach number for $k = 0.2$.

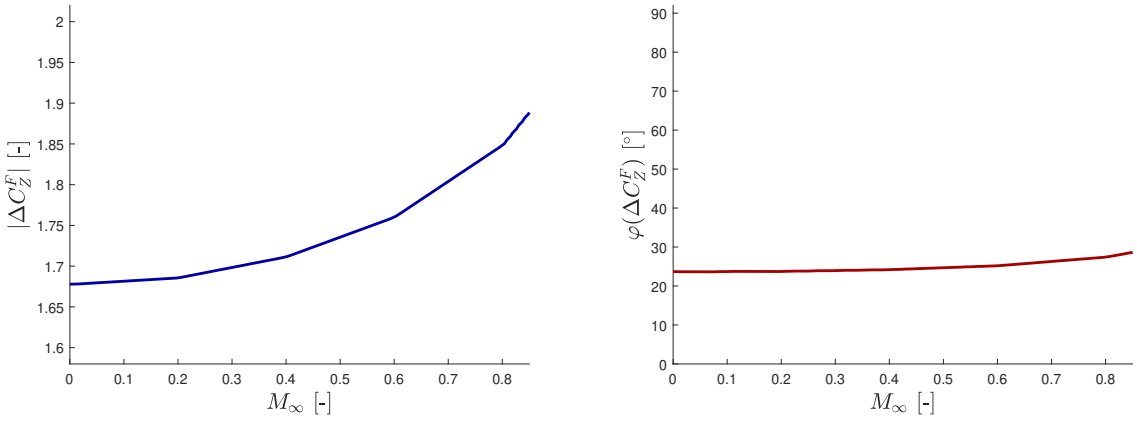

Figure 5.11: Module and phase of the side force coefficient as a function of the Mach number for $k = 0.2$.

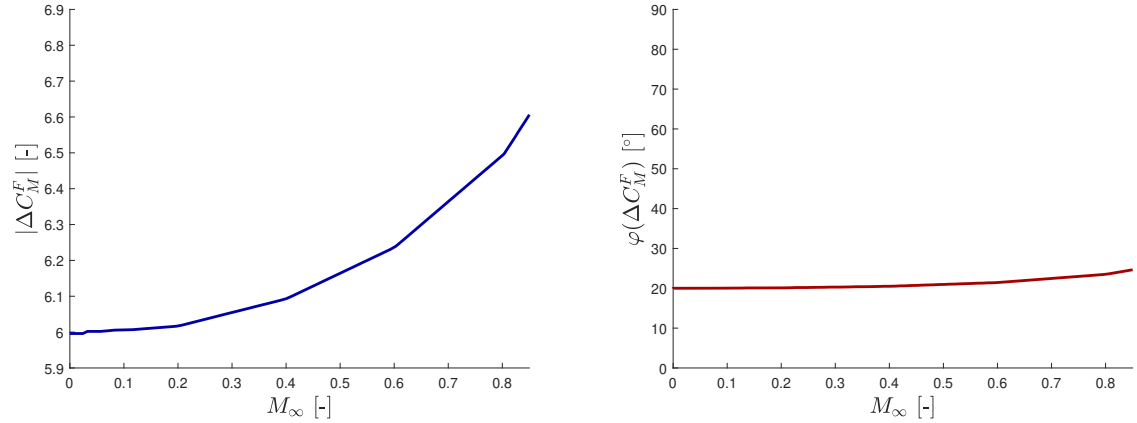

Figure 5.12: Module and phase of the pitching moment coefficient as a function of the Mach number for $k = 0.2$.

Chapter 6

Hose-Drogue-Grid Fins model

At this stage in the thesis, both the hose-drogue model and the grid fins prototype have been fully developed. Therefore, all the necessary elements are now in place to address, in this chapter, the static and dynamic analysis of the new hose-drogue-fins configuration for aerial refueling. The grid fins prototype is positioned between the hose and the drogue, and the objective is to analyze this new refueling model in a analogous manner to the system without fins as presented in Chapter 4. Consequently, the development that follows will adhere to the same approach. It is important to note that, since much of the structural and aerodynamic modeling of the system will be identical to that in Chapter 4, many of the matters discussed here will be covered with less detail than in that Chapter.

In the first section, the mathematical model will be outlined in a general manner. Then, the static equilibrium position that the hose-drogue-fins system maintains once deployed and just before engaging with the receiver aircraft will be analyzed.

Once the static equilibrium position is defined, the dynamic equations of the system will be obtained, assuming small perturbations with respect to the static equilibrium position. The inertia, damping, stiffness and aerodynamic fins forces matrices of the system will be put forward, along with the entire process of obtaining them.

Then, the aeroelastic stability analysis of the system will be performed. The flutter boundaries, that is, the dynamic instabilities of the hose-drogue-fins-surrounding air system, are calculated using the K-Method, exploring the influence of various parameters on flutter occurrence and analyzing the differences that arise in the system when the grid fins prototype is added compared to the model of Chapter 4.

6.1 Mathematical formulation

This section presents the development of the mathematical model for the complete hose-drogue-fins system. Before proceeding, it should be noted that many aspects of the development (specifically those related to the drogue and the hose) were already explained in detail when the hose-drogue model without the fins was introduced. Therefore, those aspects will not be further explained again.

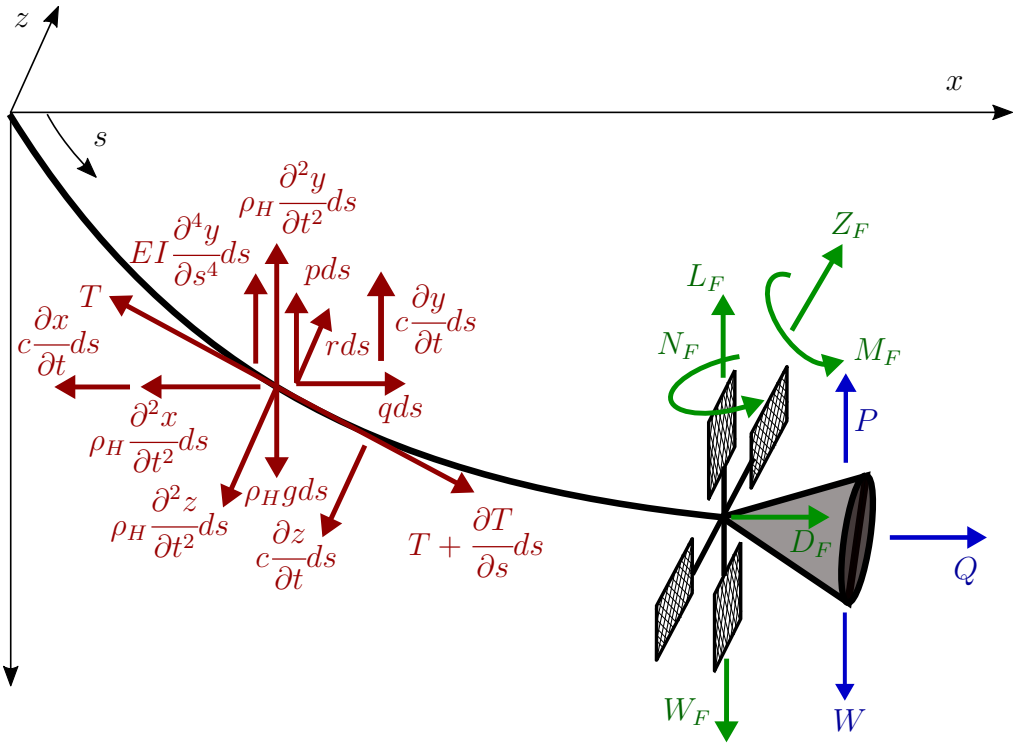

Figure 6.1: Acting forces on the hose-drogue-grid fins model.

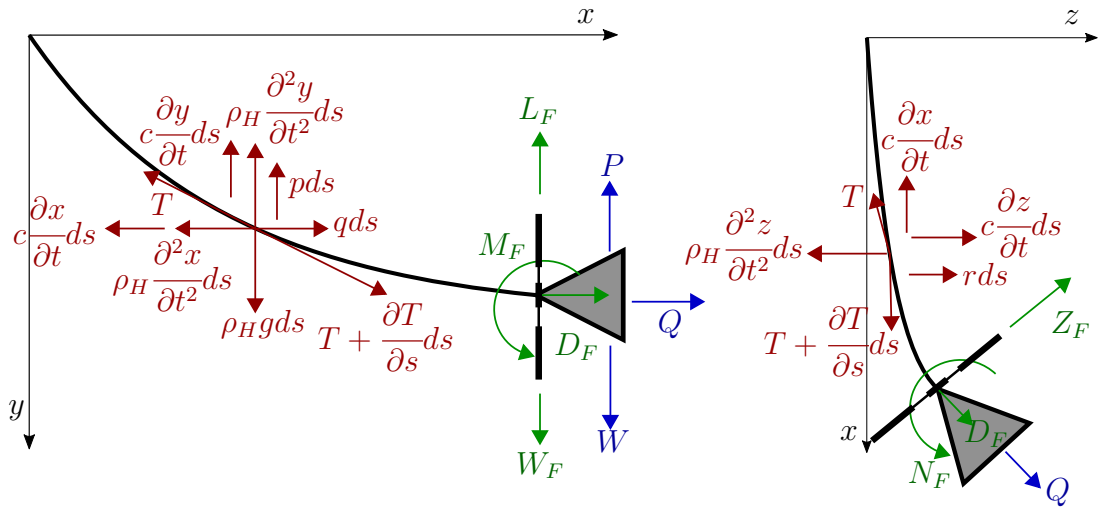

Figure 6.2: Acting forces on the hose-drogue-grid fins model, (x, y) and (z, x) planes.

Figure 6.1 presents the hose-drogue-fins model, with the acting forces on a differential hose element of length ds (highlighted in red), as well as on the hose-drogue-fins junction, with the grid fins forces highlighted in green and the drogue forces in blue. The main difference with respect to Chapter 4 is that, as shown during the development of the grid fins prototype, the fins are capable of generating lateral forces outside the vertical plane. The hose-drogue model without grid fins was assumed to stay at the (x, y) plane. Therefore, in order to analyze the system with the fins the formulation must be generalized to include the motion in the z-axis as well. The reference system (x, y, z) is defined again by the x-axis aligned opposite to the flight direction, the y-axis pointing downwards (toward the earth) and the z-axis forming right-handed Cartesian axes. Figure 6.1 can be projected in a vertical plane (x, y) and in an horizontal plane (z, x) to favor the analysis

of the forces, as shown in Figure 6.2.

The formulation will focus on the equations for the four unknowns of the system:

- Horizontal position of the hose $x(s,t)$.
- Vertical position of the hose $y(s,t)$.
- Lateral position of the hose $z(s,t)$.
- Hose tension $T(s,t)$.

The governing equations of the system are:

$$-\rho_H \frac{\partial^2 x}{\partial t^2}(s,t) - c\frac{\partial x}{\partial t}(s,t) + q(s,t) + \frac{\partial}{\partial s}\left[T(s,t)\left(\frac{\partial x}{\partial s}(s,t) - \varepsilon\frac{\partial y}{\partial s}(s,t)\right)\right] = 0, \tag{6.1}$$

$$-\frac{\partial^2 y}{\partial t^2}(s,t) - c\frac{\partial y}{\partial t}(s,t) - p(s,t) + \rho_H g + \frac{\partial}{\partial s}\left[T(s,t)\left(\frac{\partial y}{\partial s}(s,t) + \varepsilon\frac{\partial x}{\partial s}(s,t)\right)\right] - EI\frac{\partial^4 y}{\partial s^4}(s,t) = 0, \tag{6.2}$$

$$-\rho_H \frac{\partial^2 z}{\partial t^2}(s,t) - c\frac{\partial z}{\partial t}(s,t) + r(s,t) + \frac{\partial}{\partial s}\left(T(s,t)\frac{\partial z}{\partial s}(s,t)\right) = 0, \tag{6.3}$$

where the only new variable with respect to the formulation presented in Chapter 4 is the lateral aerodynamic force per unit length on the hose r. The rest of variables and parameters have been already defined.

With respect to these force, in general the configuration will be symmetrical with respect to the $z = 0$ plane. Only very small deviations due to the side forces generated by the grid fins are considered. These lateral forces, as will be shown in the results, are small. Therefore, the lateral force on the hose r can be assumed very small compared to the lift and the drag, and, in first approximation, it can be neglected (that is, is assumed that all the lateral aerodynamic force comes from the grid fins). With respect to the lift and drag per unit of length of the hose p and q are defined following the development of Chapter 4, obtaining again:

$$p(s,t) = k_2\left[\left(\frac{\partial y}{\partial s}(s,t)\right)^2\frac{\partial x}{\partial s}(s,t) + 2\varepsilon\frac{\partial y}{\partial s}(s,t)\left(\frac{\partial x}{\partial s}(s,t)\right)^2 - \varepsilon\left(\frac{\partial y}{\partial s}(s,t)\right)^3\right], \tag{6.4}$$

$$q(s,t) = k_1 + k_2\left[\left(\frac{\partial y}{\partial s}(s,t)\right)^3 + 3\varepsilon\left(\frac{\partial y}{\partial s}(s,t)\right)^2\frac{\partial x}{\partial s}(s,t)\right]. \tag{6.5}$$

The boundary conditions at the hose-tanker junction, $s = 0$, are:

$$x(0,t) = X_T(t), \tag{6.6}$$

$$y(0,t) = Y_T(t), \tag{6.7}$$

$$z(0,t) = Z_T(t), \tag{6.8}$$

where $X_T(t)$, $Y_T(t)$ and $Z_T(t)$ represent the prescribed motion at the hose-tanker connection. Eqs.(6.6)-(6.8) must be completed with geometric or kinematic boundary conditions on the derivatives of the variables at $s = 0$ as a function of the considered case of the connection (for example: pinned, clamped...).

The boundary conditions at the hose-drogue-fins junction are obtained from the equilibrium of the acting forces in $s = s_0$:

$$-T(s_0,t)\left[\frac{\partial x}{\partial s}(s_0,t) - \varepsilon\frac{\partial y}{\partial s}(s_0,t)\right] + Q + D_F - Z_F\frac{\partial z}{\partial s}(s_0,t) = 0, \tag{6.9}$$

$$T(s_0,t)\left[\frac{\partial y}{\partial s}(s_0,t) + \varepsilon\frac{\partial x}{\partial s}(s_0,t)\right] + P + L_F + EI\frac{\partial^3 y}{\partial s^3}(s_0,t)$$

$$-W_T - \frac{W_T}{g}\frac{\partial^2 y}{\partial t^2}(s_0,t) = 0, \tag{6.10}$$

$$T(s_0,t)\frac{\partial z}{\partial s}(s_0,t) + Z_F + D_F\frac{\partial z}{\partial s}(s_0,t) = 0, \tag{6.11}$$

$$EI\frac{\partial^2 y}{\partial s^2}(s_0,t) + M_F = 0. \tag{6.12}$$

where s_0 is the total hose length, W the drogue weight, P and Q the drogue lift and drag, respectively, W_T the total drogue+grid fins weight ($W_T = W + W_F$), L_F the grid fins lift, D_F the grid fins drag, Z_F the grid fins side force and M_F the grid fins pitching moment. All these forces and moments were defined in Chapter 5.

In a similar way to the system without grid fins, starting from an initial static equilibrium position, the system is perturbed with a small amplitude. Hence the four variables of the system can be expressed as:

$$x(s,t) = x_e(s) + \delta_1 \cdot \xi(s,t), \tag{6.13}$$

$$y(s,t) = y_e(s) + \delta_1 \cdot \eta(s,t), \tag{6.14}$$

$$z(s,t) = z_e(s) + \delta_1 \cdot \sigma(s,t), \tag{6.15}$$

$$T(s,t) = T_e(s) + \delta_1 \cdot \tau(s,t) \simeq T_e(s), \tag{6.16}$$

where $y_e(s)$, $x_e(s)$, $z_e(s)$ and $T_e(s)$ are the static equilibrium coordinates of the system and the static hose tension, respectively, δ_1 is the small amplitude unsteady perturbation parameter, and $\eta(s,t)$, $\xi(s,t)$, $\sigma(s,t)$ and $\tau(s,t)$ the perturbed values of the variables. The expression of the hose angle of attack is the same that in Chapter 4, and the aerodynamic forces on the hose are split into a steady and an unsteady contribution again in a similar way than in the model without grid fins:

$$q(s,t) = q_e(s) + \delta_1 \left.\frac{dq}{d\alpha}\right|_{\alpha_e}(s) \cdot \left(\frac{\partial \eta}{\partial s}(s,t) + \frac{1}{U_\infty}\frac{\partial \eta}{\partial t}(s,t)\right), \tag{6.17}$$

$$p(s,t) = p_e(s) + \delta_1 \left.\frac{dp}{d\alpha}\right|_{\alpha_e}(s) \cdot \left(\frac{\partial \eta}{\partial s}(s,t) + \frac{1}{U_\infty}\frac{\partial \eta}{\partial t}(s,t)\right), \tag{6.18}$$

where

$$q_e(s) = k_1 + k_2 \left(\frac{dy_e}{ds}\right)^3 + 3\varepsilon k_2 \left(\frac{dy_e}{ds}\right)^2 \frac{dx_e}{ds}, \tag{6.19}$$

$$\left.\frac{dq}{d\alpha}\right|_{\alpha_e}(s) = 3k_2 \left(\frac{dy_e}{ds}\right)^2 \frac{dx_e}{ds}, \tag{6.20}$$

$$p_e(s) = k_2 \left(\frac{dy_e}{ds}\right)^2 \frac{dx_e}{ds} + \varepsilon k_2 \left[2\frac{dy_e}{ds}\left(\frac{dx_e}{ds}\right)^2 - \left(\frac{dy_e}{ds}\right)^3\right], \tag{6.21}$$

$$\left.\frac{dp}{d\alpha}\right|_{\alpha_e}(s) = k_2 \left[2\frac{dy_e}{ds}\left(\frac{dx_e}{ds}\right)^2 - \left(\frac{dy_e}{ds}\right)^3\right]. \tag{6.22}$$

6.2 Static problem

The governing equations for the static coordinates of the hose $x_e(s)$, $y_e(s)$ and $z_e(s)$ and for the static tension $T_e(s)$ are:

$$q_e(s) + \frac{d}{ds}\left[T_e(s)\left(\frac{dx_e}{ds}(s) - \varepsilon\frac{dy_e}{ds}(s)\right)\right] = 0, \tag{6.23}$$

$$-p_e(s) + \rho_H g + \frac{d}{ds}\left[T_e(s)\left(\frac{dy_e}{ds}(s) + \varepsilon\frac{dx_e}{ds}(s)\right)\right] - EI\frac{d^4y_e}{ds^4}(s) = 0, \tag{6.24}$$

$$\frac{d}{ds}\left(T_e(s)\frac{dz_e}{ds}(s)\right) = 0, \tag{6.25}$$

$$\tag{6.26}$$

where $q_e(s)$ and $p_e(s)$ were defined at Eqs.(6.19) and (6.21). The boundary conditions at the hose-tanker junction are:

$$x_e|_0 = X_{T_e}, \tag{6.27}$$

$$y_e|_0 = Y_{T_e}, \tag{6.28}$$

$$z_e|_0 = Z_{T_e}, \tag{6.29}$$

and at the hose-fins-drogue junction:

$$-T_e|_{s_0}\left(\left.\frac{dx_e}{ds}\right|_{s_0} - \varepsilon\left.\frac{dy_e}{ds}\right|_{s_0}\right) + Q + D_{F_e} - Z_{F_e}\left.\frac{dz_e}{ds}\right|_{s_0} = 0, \tag{6.30}$$

$$T_e|_{s_0}\left(\left.\frac{dy_e}{ds}\right|_{s_0} + \varepsilon\left.\frac{dx_e}{ds}\right|_{s_0}\right) + P + L_{F_e} + EI\left.\frac{d^3y_e}{ds^3}\right|_{s_0} - W_T = 0, \tag{6.31}$$

$$T_e|_{s_0}\left.\frac{dz_e}{ds}\right|_{s_0} + Z_{F_e} + D_{F_e}\left.\frac{dz_e}{ds}\right|_{s_0} = 0, \tag{6.32}$$

$$EI \left. \frac{d^2 y_e}{ds^2} \right|_{s_0} + M_{F_e} = 0. \tag{6.33}$$

The compatibility equation for the non-stretchable hose complete the formulation and is:

$$\left(\frac{dx_e}{ds}(s) \right)^2 + \left(\frac{dy_e}{ds}(s) \right)^2 + \left(\frac{dz_e}{ds}(s) \right)^2 = 1. \tag{6.34}$$

The way to obtain the static equilibrium position is similar to the model without grid fins: the system of Eqs.(6.23)-(6.25) is reformulated into a first-order non-linear ordinary differential equation system. Solving this system with the boundary conditions at the end of the hose Eqs.(6.30)-(6.33), yields $dx_e/ds(s)$, $dy_e/ds(s)$, $dz_e/ds(s)$ and $T_e(s)$. Finally, a second numerical integration is performed with the boundary conditions at the beginning of the hose Eqs.(6.27)-(6.29), obtaining the static equilibrium position of the hose-drogue-fins system.

6.3 Grid fins unsteady forces incorporation in the model

In Chapter 5 was shown that one of the most relevant aspects of this thesis is the determination of the steady and unsteady aerodynamic forces acting on the fins. However, as a preliminary step to the unsteady problem of the complete hose-drogue-fins model, it is necessary to analyze how the unsteady fin forces will be integrated into the hose-drogue formulation.

As discussed in Chapter 5, there are three unsteady aerodynamic coefficients associated to the fins:

- The unsteady lift coefficient ΔC_L^F.
- The unsteady side force coefficient ΔC_Z^F.
- The unsteady pitching moment coefficient ΔC_M^F.

These coefficients were obtained as a function of eight unknowns: the four unsteady angles of attack of each fin $\Delta\alpha_i^F$ and the four unsteady angles of sideslip of each fin $\Delta\beta_i^F$, where $i = 1, ..., 4$. To be able to incorporate the fins forces into the complete model, it will be necessary to express $\Delta\alpha_i^F$ and $\Delta\beta_i^F$ in terms of some hose-drogue system variables. For this purpose, first the three unsteady aerodynamic coefficients of the fins must be expressed as a function of $\Delta\alpha_i^F$ and $\Delta\beta_i^F$ as in Eqs.(5.76)-(5.78). It is possible to write these expressions in a compact matrix form as a function of the unknowns:

$$\begin{Bmatrix} \Delta C_L^F \\ \Delta C_Z^F \\ \Delta C_M^F \end{Bmatrix} = \boldsymbol{\Delta Q}_{\alpha\beta} \cdot \boldsymbol{\Delta X_F}, \tag{6.35}$$

where the matrix $\boldsymbol{\Delta Q}_{\alpha\beta}$ contains each coefficient from Eqs.(5.76)-(5.78):

$$\boldsymbol{\Delta Q}_{\alpha\beta} = \begin{bmatrix} \Delta C_{L\alpha_1} & \Delta C_{L\beta_1} & \Delta C_{L\alpha_2} & \Delta C_{L\beta_2} & \Delta C_{L\alpha_3} & \Delta C_{L\beta_3} & \Delta C_{L\alpha_4} & \Delta C_{L\beta_4} \\ \Delta C_{Z\alpha_1} & \Delta C_{Z\beta_1} & \Delta C_{Z\alpha_2} & \Delta C_{Z\beta_2} & \Delta C_{Z\alpha_3} & \Delta C_{Z\beta_3} & \Delta C_{Z\alpha_4} & \Delta C_{Z\beta_4} \\ \Delta C_{M\alpha_1} & \Delta C_{M\beta_1} & \Delta C_{M\alpha_2} & \Delta C_{M\beta_2} & \Delta C_{M\alpha_3} & \Delta C_{M\beta_3} & \Delta C_{M\alpha_4} & \Delta C_{M\beta_4} \end{bmatrix}, \tag{6.36}$$

and $\boldsymbol{\Delta X_F}$ is the vector of unknowns:

$$\boldsymbol{\Delta X_F} = \{\Delta\alpha_1^F \ \Delta\beta_1^F \ \Delta\alpha_2^F \ \Delta\beta_2^F \ \Delta\alpha_3^F \ \Delta\beta_3^F \ \Delta\alpha_4^F \ \Delta\beta_4^F\}^T. \tag{6.37}$$

Each matrix coefficient of Eq.(6.36), as mentioned in Chapter 5, is defined in Appendix B.

Eq.(6.36) gives the generalized unsteady force matrix of the fins as a function of their unsteady angles of attack and sideslip. To couple the aerodynamic forces on the fins with the dynamic equations on the hose this matrix must be expressed as a function of the three perturbed variables of the unsteady problem $\eta(s,t)$, $\xi(s,t)$ and $\sigma(s,t)$. By analyzing the fins angles at the static equilibrium position, a relationship between these angles and the static variables can be found. Starting for example with fin 1, the following approximation can be used:

$$\sin\alpha_{e_1}^F \simeq \frac{dy_e}{ds}(s_0); \quad \cos\alpha_{e_1}^F \simeq \frac{dx_e}{ds}(s_0), \tag{6.38}$$

$$\sin\beta_{e_1}^F \simeq \frac{dz_e}{ds}(s_0); \quad \cos\beta_{e_1}^F \simeq \frac{dx_e}{ds}(s_0), \tag{6.39}$$

where it has been assumed that the angles in the hose-fins-drogue junction are small. Once the system is perturbed from their static position the total angles of attack and sideslip for fin 1 can be written expanding Eqs.(6.38) and (6.39) as:

$$\alpha_1^F = \alpha_{e_1}^F + \delta_1 \cdot \Delta\alpha_1^F = \frac{\dfrac{\partial y}{\partial s}(s_0,t)}{\dfrac{\partial x}{\partial s}(s_0,t)} = \frac{\dfrac{dy_e}{ds}(s_0) + \delta_1 \cdot \dfrac{\partial \eta}{\partial s}(s_0,t)}{\dfrac{dx_e}{ds}(s_0) + \delta_1 \cdot \dfrac{\partial \xi}{\partial s}(s_0,t)}, \tag{6.40}$$

$$\beta_1^F = \beta_{e_1}^F + \delta_1 \cdot \Delta\beta_1^F = \frac{\dfrac{\partial z}{\partial s}(s_0,t)}{\dfrac{\partial x}{\partial s}(s_0,t)} = \frac{\dfrac{dz_e}{ds}(s_0) + \delta_1 \cdot \dfrac{\partial \sigma}{\partial s}(s_0,t)}{\dfrac{dx_e}{ds}(s_0) + \delta_1 \cdot \dfrac{\partial \xi}{\partial s}(s_0,t)}, \tag{6.41}$$

and retaining terms of order δ_1 the unsteady angles of attack and sideslip are:

$$\Delta\alpha_1^F \simeq \frac{dx_e}{ds}(s_0) \cdot \frac{\partial \eta}{\partial s}(s_0,t) - \frac{dy_e}{ds}(s_0) \cdot \frac{\partial \xi}{\partial s}(s_0,t), \tag{6.42}$$

$$\Delta\beta_1^F \simeq \frac{dx_e}{ds}(s_0) \cdot \frac{\partial \sigma}{\partial s}(s_0,t) - \frac{dz_e}{ds}(s_0) \cdot \frac{\partial \xi}{\partial s}(s_0,t). \tag{6.43}$$

It is worth noting that the terms of order 1 have been already included in the static problem. Using the relationships of Eqs.(6.42) and (6.43), the unsteady angles of attack

and sideslip of each fin can be expressed as a function of the perturbed variables of the system at the hose-drogue-fins connection ($s = s_0$):

$$\Delta\alpha_i^F = \cos\alpha_{e_i}^F \cdot \frac{\partial\eta}{\partial s}(s_0,t) - \sin\alpha_{e_i}^F \cdot \frac{\partial\xi}{\partial s}(s_0,t), \tag{6.44}$$

$$\Delta\beta_i^F = \cos\beta_{e_i}^F \cdot \frac{\partial\sigma}{\partial s}(s_0,t) - \sin\beta_{e_i}^F \cdot \frac{\partial\xi}{\partial s}(s_0,t), \tag{6.45}$$

for $i = 1, ..., 4$. Eqs.(6.44) and (6.45) can be written as a transformation matrix $\boldsymbol{T}$ between the grid fins unsteady angles and the derivatives of the perturbed variables:

$$\boldsymbol{\Delta X_F} = \boldsymbol{T} \cdot \begin{Bmatrix} \frac{\partial\xi}{\partial s}(s_0,t) \\ \frac{\partial\eta}{\partial s}(s_0,t) \\ \frac{\partial\sigma}{\partial s}(s_0,t) \end{Bmatrix} \tag{6.46}$$

The expression of this matrix is easily obtained from Eqs.(6.44) and (6.45):

$$\boldsymbol{T} = \begin{bmatrix} -\sin\alpha_{e_1}^F & \cos\alpha_{e_1}^F & 0 \\ -\sin\beta_{e_1}^F & 0 & \cos\beta_{e_1}^F \\ -\sin\alpha_{e_2}^F & \cos\alpha_{e_2}^F & 0 \\ -\sin\beta_{e_2}^F & 0 & \cos\beta_{e_2}^F \\ -\sin\alpha_{e_3}^F & \cos\alpha_{e_3}^F & 0 \\ -\sin\beta_{e_3}^F & 0 & \cos\beta_{e_3}^F \\ -\sin\alpha_{e_4}^F & \cos\alpha_{e_4}^F & 0 \\ -\sin\beta_{e_4}^F & 0 & \cos\beta_{e_4}^F \end{bmatrix} \tag{6.47}$$

With this transformation matrix it is possible to write the unsteady coefficients of the fins as a functions of the three perturbed variables of the system at the hose-fins-drogue junction:

$$\begin{Bmatrix} \Delta C_L^F \\ \Delta C_Z^F \\ \Delta C_M^F \end{Bmatrix} = \boldsymbol{\Delta Q}_{\alpha\beta} \cdot \boldsymbol{\Delta X_F} = \boldsymbol{\Delta Q}_{\alpha\beta} \cdot \boldsymbol{T} \cdot \begin{Bmatrix} \frac{\partial\xi}{\partial s}(s_0,t) \\ \frac{\partial\eta}{\partial s}(s_0,t) \\ \frac{\partial\sigma}{\partial s}(s_0,t) \end{Bmatrix} = \boldsymbol{\Delta Q}_{xyz} \cdot \begin{Bmatrix} \frac{\partial\xi}{\partial s}(s_0,t) \\ \frac{\partial\eta}{\partial s}(s_0,t) \\ \frac{\partial\sigma}{\partial s}(s_0,t) \end{Bmatrix} \tag{6.48}$$

where, as can be seen, the unsteady aerodynamic coefficients of the fins matrix as a function of the hose unknowns $\boldsymbol{\Delta Q}_{xyz}$ is completed:

$$\boldsymbol{\Delta Q}_{xyz} = \begin{bmatrix} \Delta Q_{Lx} & \Delta Q_{Ly} & \Delta Q_{Lz} \\ \Delta Q_{Zx} & \Delta Q_{Zy} & \Delta Q_{Zz} \\ \Delta Q_{Mx} & \Delta Q_{My} & \Delta Q_{Mz} \end{bmatrix}, \tag{6.49}$$

Each coefficient of the matrix can be expressed using the definitions of the matrices of Eqs.(6.36) and (6.47):

$$\Delta Q_{Lx} = -\sum_{i=1}^{4}(\sin\alpha_{e_i}^F \cdot \Delta C_{L\alpha_i} + \sin\beta_{e_i}^F \cdot \Delta C_{L\beta_i}), \tag{6.50}$$

$$\Delta Q_{Ly} = \sum_{i=1}^{4}\cos\alpha_{e_i}^F \cdot \Delta C_{L\alpha_i}, \tag{6.51}$$

$$\Delta Q_{Lz} = \sum_{i=1}^{4}\cos\beta_{e_i}^F \cdot \Delta C_{L\beta_i}, \tag{6.52}$$

$$\Delta Q_{Zx} = -\sum_{i=1}^{4}(\sin\alpha_{e_i}^F \cdot \Delta C_{Z\alpha_i} + \sin\beta_{e_i}^F \cdot \Delta C_{Z\beta_i}), \tag{6.53}$$

$$\Delta Q_{Zy} = \sum_{i=1}^{4}\cos\alpha_{e_i}^F \cdot \Delta C_{Z\alpha_i}, \tag{6.54}$$

$$\Delta Q_{Zz} = \sum_{i=1}^{4}\cos\beta_{e_i}^F \cdot \Delta C_{Z\beta_i}, \tag{6.55}$$

$$\Delta Q_{Mx} = -\sum_{i=1}^{4}(\sin\alpha_{e_i}^F \cdot \Delta C_{M\alpha_i} + \sin\beta_{e_i}^F \cdot \Delta C_{M\beta_i}), \tag{6.56}$$

$$\Delta Q_{My} = \sum_{i=1}^{4}\cos\alpha_{e_i}^F \cdot \Delta C_{M\alpha_i}, \tag{6.57}$$

$$\Delta Q_{Mz} = \sum_{i=1}^{4}\cos\beta_{e_i}^F \cdot \Delta C_{M\beta_i}. \tag{6.58}$$

6.4 Dynamic problem

6.4.1 Perturbed equations

With the linearization proposed at Eqs.(6.13)-(6.16) a PDE system of equations is obtained, where the unknowns are the perturbed variables of the system:

$$-\rho_H \frac{\partial^2 \xi}{\partial t^2}(s,t) - c\frac{\partial \xi}{\partial t}(s,t) + \left.\frac{dq}{d\alpha}\right|_{\alpha_e}(s)\left(\frac{\partial \eta}{\partial s}(s,t) + \frac{1}{U_\infty}\frac{\partial \eta}{\partial t}(s,t)\right) + \frac{\partial}{\partial s}\left(T_e(s)\frac{\partial \xi}{\partial s}(s,t)\right) = 0, \tag{6.59}$$

$$-\rho_H \frac{\partial^2 \eta}{\partial t^2}(s,t) - c\frac{\partial \eta}{\partial t}(s,t) - \left.\frac{dp}{d\alpha}\right|_{\alpha_e}(s)\left(\frac{\partial \eta}{\partial s}(s,t) + \frac{1}{U_\infty}\frac{\partial \eta}{\partial t}(s,t)\right) - EI\frac{\partial^4 \eta}{\partial s^4}(s,t) + \frac{\partial}{\partial s}\left(T_e(s)\frac{\partial \eta}{\partial s}(s,t)\right) = 0, \tag{6.60}$$

$$-\rho_H \frac{\partial^2 \sigma}{\partial t^2}(s,t) - c\frac{\partial \sigma}{\partial t}(s,t) + \frac{\partial}{\partial s}\left(T_e(s)\frac{\partial \sigma}{\partial s}(s,t)\right) = 0. \tag{6.61}$$

The boundary conditions at the hose-tanker junction are:

$$\xi(0,t) = \Delta X_T(t), \tag{6.62}$$

$$\eta(0,t) = \Delta Y_T(t), \tag{6.63}$$

$$\sigma(0,t) = \Delta Z_T(t), \tag{6.64}$$

where ΔX_T, ΔY_T and ΔZ_T are the unsteady prescribed motions of the tanker, which will be assumed to be known an equal to zero for the time being. The boundary conditions at the hose-fins-tanker junction are obtained linearizing from Eqs.(4.53)-(4.55) and using the expressions of the aerodynamic forces of the fins defined previously at Eq.(6.49):

$$T_e(s_0)\frac{\partial \xi}{\partial s}(s_0,t) + Z_{F_e}\frac{\partial \sigma}{\partial s}(s_0,t) + \left.\frac{dz_e}{ds}\right|_{s_0} q_\infty S_{UGF}\left[\Delta Q_{Zx}\frac{\partial \xi}{\partial s}(s_0,t) + \Delta Q_{Zy}\frac{\partial \eta}{\partial s}(s_0,t) + \Delta Q_{Zz}\frac{\partial \sigma}{\partial s}(s_0,t)\right] = 0, \tag{6.65}$$

$$T_e(s_0)\frac{\partial \eta}{\partial s}(s_0,t) - \frac{W_T}{g}\frac{\partial^2 \eta}{\partial t^2}(s_0,t) + q_\infty S_{UGF}\left[\Delta Q_{Lx}\frac{\partial \xi}{\partial s}(s_0,t) + \Delta Q_{Ly}\frac{\partial \eta}{\partial s}(s_0,t) + \Delta Q_{Lz}\frac{\partial \sigma}{\partial s}(s_0,t)\right] + EI\frac{\partial^3 \eta}{\partial s^3}(s_0,t) = 0, \tag{6.66}$$

$$T_e(s_0)\frac{\partial \sigma}{\partial s}(s_0,t) + q_\infty S_{UGF}\left[\Delta Q_{Zx}\frac{\partial \xi}{\partial s}(s_0,t) + \Delta Q_{Zy}\frac{\partial \eta}{\partial s}(s_0,t) + \Delta Q_{Zz}\frac{\partial \sigma}{\partial s}(s_0,t)\right] + D_{F_e}\frac{\partial \sigma}{\partial s}(s_0,t) = 0, \tag{6.67}$$

$$EI\frac{\partial^2\eta}{\partial s^2}(s_0,t)+q_\infty S_{UGF}c_f\left[\Delta Q_{Mx}\frac{\partial\xi}{\partial s}(s_0,t)+\Delta Q_{My}\frac{\partial\eta}{\partial s}(s_0,t)+\Delta Q_{Mz}\frac{\partial\sigma}{\partial s}(s_0,t)\right]=0, \tag{6.68}$$

where ΔQ_{ij} are the unsteady grid fins force coefficients obtained from Eqs.(6.50)-(6.58).

6.4.2 Equations for the spatial domain

Applying separation of variables, the perturbed variables of the system can be expressed as:

$$\xi(s,t)=X(s)\cdot e^{\lambda t}, \tag{6.69}$$

$$\eta(s,t)=N(s)\cdot e^{\lambda t}, \tag{6.70}$$

$$\sigma(s,t)=\Gamma(s)\cdot e^{\lambda t}, \tag{6.71}$$

where $X(s)$, $N(s)$ and $\Gamma(s)$ are the spatial part of the horizontal, vertical and lateral motions, respectively, and the exponential term with the eigenvalue λ represents the temporal part. As in Chapter 4, the separation of variables will be used at the dynamic equations of the system and at the boundary conditions. Again, an improved model for the unsteady aerodynamic forces acting on the hose can be obtained by adding the phase lag angle ψ between the aerodynamics on the hose and its dynamic motion. This angle was defined in Eq.(4.71) during the development of the model without grid fins, and again will be included as a parametric-type phase angle. Therefore, applying separation of variables and with the effect of the lag angle Eqs.(6.59)-(6.61) can be rewritten as:

$$-\lambda^2\rho_H X(s)-c\lambda X(s)+\left.\frac{dq}{d\alpha}\right|_{\alpha_e}(s)\left(N'(s)+\frac{\lambda}{U_\infty}N(s)\right)\cdot e^{i\psi}+\frac{d}{ds}[T_e(s)X'(s)]=0, \tag{6.72}$$

$$-\lambda^2\rho_H N(s)-c\lambda N(s)-\left.\frac{dp}{d\alpha}\right|_{\alpha_e}(s)\left(N'(s)+\frac{\lambda}{U_\infty}N(s)\right)\cdot e^{i\psi}-$$

$$EI\cdot N^{IV}(s)+\frac{d}{ds}[T_e(s)N'(s)]=0, \tag{6.73}$$

$$-\lambda^2\rho_H\Gamma(s)-c\lambda\Gamma(s)+\frac{d}{ds}[T_e(s)\Gamma'(s)]=0. \tag{6.74}$$

And the boundary conditions:

$$X(0)=N(0)=\Gamma(0)=0, \tag{6.75}$$

$$T_e(s_0)X'(s_0)+Z_{F_e}\Gamma'(s_0)+\left.\frac{dz_e}{ds}\right|_{s_0}q_\infty S_{UGF}[\Delta Q_{Zx}X'(s_0)+$$

$$\Delta Q_{Zy}N'(s_0)+\Delta Q_{Zz}\Gamma'(s_0)]=0, \tag{6.76}$$

$$T_e(s_0)N'(s_0) - \lambda^2\frac{W_T}{g}N(s_0) + q_\infty S_{UGF}[\Delta Q_{Lx}X'(s_0) + \Delta Q_{Ly}N'(s_0) + \Delta Q_{Lz}\Gamma'(s_0)] + EI \cdot N'''(s_0) = 0, \tag{6.77}$$

$$T_e(s_0)\Gamma'(s_0) + q_\infty S_{UGF}[\Delta Q_{Zx}X'(s_0) + \Delta Q_{Zy}N'(s_0) + \Delta Q_{Zz}\Gamma'(s_0)] + D_{F_e}\Gamma'(s_0) = 0, \tag{6.78}$$

$$EI \cdot N''(s_0) + q_\infty S_{UGF}c_f[\Delta Q_{Mx}X'(s_0) + \Delta Q_{My}N'(s_0) + \Delta Q_{Mz}\Gamma'(s_0)] = 0. \tag{6.79}$$

6.4.3 Hose discretization: Weighted Residual Method

Eqs.(6.72)-(6.74) and their boundary conditions Eqs.(6.75)-(6.79) represent a system of ordinary differential equations. To solve it the hose will be discretized into a sufficient number of elements large enough to ensure the convergence of the solution.

In Chapter 4 the possible strategies for discretizing the hose were explained in detail, and the Weighted Residuals Method (WRM) was presented as the solution strategy for the system of equations. In this case, with the complete system (i.e., including the grid fins), the WRM will be used again with the same considerations than in the model without fins. Therefore, to avoid redundancy, the entire development of this method (its conditions, the form functions to be used, etc.) will not be repeated here, as it was already covered in Chapter 4.

However, for the hose-drogue-fins model there are two significant differences. The first one is that in the new model with grid fins the equations have been derived for the three axes (x, y, z), meaning they account for horizontal, vertical, and lateral motions, whereas in the hose-drogue model, the motion in z was not included. As discussed throughout the development of the equations, the inclusion of lateral motion has been handled similarly to the other two. Therefore, the adding of this motion in the lateral direction does not provide any difficulty in the formulation. The same form functions will be used for the lateral perturbed variable as for the other two. Consequently, the spatial part of the perturbed variables approximations $\hat{X}(s)$, $\hat{N}(s)$ and $\hat{\Gamma}(s)$ in all of terms except the bending ones can be written as:

$$\hat{X}(s) = \sum_{j=1}^{N_s+1} v_j \cdot \varphi_j^{(1)}(s), \tag{6.80}$$

$$\hat{N}(s) = \sum_{j=1}^{N_s+1} w_j \cdot \varphi_j^{(1)}(s), \tag{6.81}$$

$$\hat{\Gamma}(s) = \sum_{j=1}^{N_s+1} z_j \cdot \varphi_j^{(1)}(s), \tag{6.82}$$

where v_j, w_j and z_j are the horizontal, vertical and lateral displacements of each node of the hose. For the bending terms, which involve higher derivatives, the linear form

functions cannot be used and the vertical perturbed variable $\hat{N}(s)$ in these terms can be written as:

$$\hat{N}(s) = \sum_{j=1}^{N_s+1} [w_j \cdot \varphi_{j,d}^{(3)}(s) + \theta_j \cdot \varphi_{j,r}^{(3)}(s)], \tag{6.83}$$

where θ_j are the rotations of each node of the hose. All form functions were defined and explained in Chapter 4.

The second difference concerns the terms associated with the aerodynamic forces of the fins. These terms will indeed introduce a significant difference when solving the dynamic equations compared to the hose-drogue model in Chapter 4. However, for this part of the formulation, the WRM can still be applied to all terms associated with the aerodynamic forces of the fins. The main difference, as will be shown below, is that in addition to the inertia, damping, and stiffness matrices, an aerodynamic forces matrix associated to the fins will also come up.

Thus, by applying the WRM to the horizontal, vertical and lateral dynamic equations, Eqs.(6.72) and (6.74), and approaching $\hat{X}(s)$, $\hat{N}(s)$ and $\hat{\Gamma}(s)$ and their respective derivatives with the appropriate form functions, the formulation of the problem can finally be expressed as:

$$(\lambda^2 \boldsymbol{M} + \lambda \boldsymbol{B} + \boldsymbol{K} - q_\infty \boldsymbol{Q})\boldsymbol{u} = \boldsymbol{0}, \tag{6.84}$$

where $\boldsymbol{M}$, $\boldsymbol{B}$ and $\boldsymbol{K}$ are the inertia, damping and stiffness matrices, respectively, $\boldsymbol{Q}$ the grid fins force coefficient matrix and $\boldsymbol{u}$ the vector which represents the degrees-of-freedom of the system (the horizontal, vertical and lateral displacements). Next, the matrices will be presented. The application of the WRM to the dynamic equations as well as the complete development of the following matrices are presented in detail in the Appendix C.

Inertia matrix

Considering the different contributions the inertia matrix can be expressed by the following sub-matrices:

$$\boldsymbol{M} = \begin{bmatrix} \boldsymbol{M^{xx}} & \boldsymbol{0} & \boldsymbol{0} \\ \boldsymbol{0} & \boldsymbol{M^{yy}} & \boldsymbol{0} \\ \boldsymbol{0} & \boldsymbol{0} & \boldsymbol{M^{zz}} \end{bmatrix}, \tag{6.85}$$

where $\boldsymbol{M^{xx}}$, $\boldsymbol{M^{yy}}$ and $\boldsymbol{M^{zz}}$ are the inertia matrices of the horizontal, vertical and lateral motion of the hose, respectively.

Damping matrix

The damping matrix can be written as:

$$\boldsymbol{B} = \begin{bmatrix} \boldsymbol{B^{xx}} & \boldsymbol{B^{xy}} & \boldsymbol{0} \\ \boldsymbol{0} & \boldsymbol{B^{yy}} & \boldsymbol{0} \\ \boldsymbol{0} & \boldsymbol{0} & \boldsymbol{B^{zz}} \end{bmatrix}, \tag{6.86}$$

where $\boldsymbol{B^{xx}}$ and $\boldsymbol{B^{yy}}$ are the damping matrices of the horizontal and the vertical motion, which will have aerodynamic and structural contribution, and $\boldsymbol{B^{xy}}$ is the horizontal damping term due to the vertical motion. In this matrix there is a coupling between vertical and horizontal motion, as shown in Eq.(6.72). Concerning the lateral motion of the hose, it has no aerodynamic damping (fact that can be observed at Eq.(6.74)). For that reason, $\boldsymbol{B^{zz}}$ terms come only from the structural damping c. The details of the sub-matrices are presented in Appendix A.

Stiffness matrix

With respect to the stiffness matrix, it can be written as:

$$\boldsymbol{K} = \begin{bmatrix} \boldsymbol{K^{xx}} & \boldsymbol{K^{xy}} & \mathbf{0} \\ \mathbf{0} & \boldsymbol{K^{yy}} & \mathbf{0} \\ \mathbf{0} & \mathbf{0} & \boldsymbol{K^{zz}} \end{bmatrix}, \tag{6.87}$$

where $\boldsymbol{K^{xx}}$, $\boldsymbol{K^{yy}}$ and $\boldsymbol{K^{zz}}$ are the stiffness matrices of the horizontal, vertical and lateral motion of the hose, and $\boldsymbol{K^{xy}}$ is the coupling that appear in the horizontal stiffness matrix due to the vertical motion.

Grid fins forces matrix

The grid fins force matrix is formed by the following sub-matrices:

$$\boldsymbol{Q} = \begin{bmatrix} \boldsymbol{Q^{xx}} & \boldsymbol{Q^{xy}} & \boldsymbol{Q^{xz}} \\ \boldsymbol{Q^{yx}} & \boldsymbol{Q^{yy}} & \boldsymbol{Q^{yz}} \\ \boldsymbol{Q^{zx}} & \boldsymbol{Q^{zy}} & \boldsymbol{Q^{zz}} \end{bmatrix}, \tag{6.88}$$

As seen throughout the development of the formulation, the terms associated with the fins forces only appear at the boundary conditions at the hose-fins-drogue connection ($s = s_0$). Therefore, the sub-matrices of Eq.(6.88) can be defined as matrices of zeros except in the terms associated to this node:

$$Q^{lm}_{i,j} = 0, \tag{6.89}$$

$$Q^{lm}_{N_s+1,N_s+1} = \Delta Q^{lm}, \tag{6.90}$$

where $l = x, y, z$, $m = x, y, z$, $N_s{+}1$ represents the position of the hose-fins-drogue junction in the matrix, and ΔQ^{lm} the different terms that show up in the grid fins aerodynamic matrix defined in Appendix C.

6.5 Aeroelastic analysis

With the inertia, damping and stiffness matrices and with the aerodynamic forces of the fins it is possible to analyze the aeroelastic stability of the system. As in the model without grid fins, the objective is to determine the flutter speeds, frequencies and modal

shapes under different flight conditions and parameters. The analysis will primarily focus on the effect of including the fin model on the flutter behavior of the system. Therefore, the differences that arise compared to the model without fins will be analyzed, allowing conclusions to be drawn about the impact of the fins on the aeroelastic stability of the system. All considerations mentioned when calculating flutter in the system without fins in Chapter 4 (such as the influence of the static position on the system dynamics, the lag between aerodynamic and structural forces in the hose, etc), remain valid for the hose-drogue-fins model.

The stability of the system will be evaluated for different flight conditions (altitudes and speeds), for various values of the lag angle ψ (the angle will be increased until found unstable results) and for different fins steady configurations from those defined in Chapter 5. As discussed in that chapter, each fin can have a different initial steady configuration, associated with the position of the prototype itself and the ability of the fins to rotate around their own axes. The configurations studied were presented in Table 5.7.

However, the inclusion of the aerodynamic forces from the fins in the equations changes the approach for solving the aeroelastic stability of the system. As discussed in Chapter 4, flutter calculation for the model without fins used the tracing of the roots method, meaning that for each flight condition, the system's frequencies and damping coefficients were obtained, allowing for a direct stability analysis. In contrast, for the hose-drogue-fins model, this strategy is not feasible due to the inclusion of aerodynamic forces from the fins (which, as explained in Chapter 5, depend on both the Mach number and the reduced frequency of the motion and are not available in the Laplace domain). Therefore, another method for calculating flutter must be used. Among the available options, the analysis will be performed by using the K-Method (see [Rodden, 2011]).

6.5.1 K-Method

Assuming harmonic motion $\lambda = i\omega$, Eq.(6.84) can be rewritten as:

$$[-\omega^2 \boldsymbol{M} + i\omega \boldsymbol{B} + \boldsymbol{K} - q_\infty \boldsymbol{Q}(k, M_\infty)]\boldsymbol{u} = \boldsymbol{0}. \tag{6.91}$$

The aerodynamic force matrix is henceforth expressed as a function of the Mach number M_∞ and the reduced frequency k, since the grid fins aerodynamic coefficients are function of these parameters. As it is usually done in this type of analysis, in order to reduce the number of modes of the system a modal approximation is introduced:

$$\boldsymbol{u} = \boldsymbol{\phi_{ah}} \boldsymbol{u_h}, \tag{6.92}$$

where $\boldsymbol{\phi_{ah}}$ is the modal matrix of the conservative system, whose columns include the low frequency modes, and $\boldsymbol{u_h}$ is the vector of modal coordinates considered. Pre-multiplying by ${\boldsymbol{\phi_{ah}}}^T$ gives:

$$[-\omega^2 \boldsymbol{M_{hh}} + i\omega \boldsymbol{B_{hh}} + \boldsymbol{K_{hh}} - q_\infty \boldsymbol{Q_{hh}}(k, M_\infty)]\boldsymbol{u_h} = \boldsymbol{0}, \tag{6.93}$$

where $\boldsymbol{M_{hh}}$, $\boldsymbol{B_{hh}}$, $\boldsymbol{K_{hh}}$ and $\boldsymbol{Q_{hh}}$ are the generalized inertia, damping, stiffness and aero-

dynamic fins forces matrices, obtained as:

$$\boldsymbol{M_{hh}} = \boldsymbol{\phi_{ah}}^T \cdot \boldsymbol{M} \cdot \boldsymbol{\phi_{ah}}, \tag{6.94}$$

$$\boldsymbol{B_{hh}} = \boldsymbol{\phi_{ah}}^T \cdot \boldsymbol{B} \cdot \boldsymbol{\phi_{ah}}, \tag{6.95}$$

$$\boldsymbol{K_{hh}} = \boldsymbol{\phi_{ah}}^T \cdot \boldsymbol{K} \cdot \boldsymbol{\phi_{ah}}, \tag{6.96}$$

$$\boldsymbol{Q_{hh}} = \boldsymbol{\phi_{ah}}^T \cdot \boldsymbol{Q} \cdot \boldsymbol{\phi_{ah}}. \tag{6.97}$$

Following the K-Method, a fictitious damping coefficient g proportional to the displacement is introduced:

$$[-\omega^2 \boldsymbol{M_{hh}} + i\omega \boldsymbol{B_{hh}} + (1+ig)\boldsymbol{K_{hh}} - q_\infty \boldsymbol{Q_{hh}}(k, M_\infty)]\boldsymbol{u_h} = \boldsymbol{0}, \tag{6.98}$$

dividing by g and grouping the generalized mass matrix and the grid fins forces matrix the above Equation is expressed as:

$$\left[-\frac{\omega^2}{1+ig}\left(\boldsymbol{M_{hh}} + \frac{\rho_\infty}{2}\left(\frac{l_{ref}}{k}\right)^2 \boldsymbol{Q_{hh}}(k, M_\infty)\right) + \frac{i\omega}{\sqrt{1+ig}}\boldsymbol{B_{hh}} + \boldsymbol{K_{hh}}\right]\boldsymbol{u_h} = \boldsymbol{0}. \tag{6.99}$$

After manipulation of the different terms, Eq.(6.99) can be written as a explicit function of the flight speed:

$$\left\{-\frac{U_\infty^2}{1+ig}\left[\left(\frac{k}{l_{ref}}\right)^2 \boldsymbol{M_{hh}} + \frac{\rho_\infty}{2}\boldsymbol{Q_{hh}}(k, M_\infty)\right] + \frac{iU_\infty}{\sqrt{1+ig}}\left(\frac{k}{l_{ref}}\right)\boldsymbol{B_{hh}} + \boldsymbol{K_{hh}}\right\}\boldsymbol{u_h} = \boldsymbol{0}, \tag{6.100}$$

where the reduced frequency is written as $k = \omega l_{ref}/2U_\infty$, being l_{ref} the chord of the grid fins. The eigenvalue of Eq.(6.100) is:

$$p^2 = -\frac{U_\infty^2}{1+ig}, \tag{6.101}$$

which can be approximated by:

$$p = \frac{iU_\infty}{\sqrt{1+ig}} \simeq iU_\infty\left(1 - i\frac{g}{2}\right) = U_\infty\left(\frac{g}{2} + i\right). \tag{6.102}$$

Procedure of the flutter computation

The procedure to obtain the flutter boundaries in the hose-drogue-grid fins system will be the following:

1. The steady initial configuration of each grid fin (and therefore the values of the angles $\alpha_{e_i}^F$ and $\beta_{e_i}^F$) is selected.
2. The value of the phase lag angle ψ is fixed. As in the model without grid fins, the process will start at $\psi = 0$, increasing its value until the system becomes unstable.

3. The flight Mach Number M_∞ is fixed, ensuring that all the values will cover the range of flight speeds at which the refueling process can be performed.

4. The flight altitude H_∞, and, therefore, the speed of sound a_∞ and the air density ρ_∞ are fixed. The flight speed is $U_\infty = a_\infty M_\infty$, and the dynamic pressure $q_\infty = \frac{1}{2}\rho_\infty U_\infty^2$. The process will start at the maximum altitude at which the refueling process can be safely performed (as explained in previous chapters, 30000 ft) and will decrease until the minimum (5000 ft).

5. For each grid fins steady configuration, flight altitude and flight Mach number:

   a) The steady force coefficient from the UGF Method $C_{L\alpha i}(0, M_\infty)$ is computed and the steady grid fins forces are calculated.

   b) The static equilibrium of the system is obtained.

   the static equilibrium position of the system is obtained.

6. From the static equilibrium position:

   a) Mass, damping and stiffness matrices of the system $\boldsymbol{M}$, $\boldsymbol{B}$ and $\boldsymbol{K}$ are computed following the development of the unsteady equations of the system.

   b) With $\boldsymbol{M}$ and $\boldsymbol{K}$, the modal matrix of the conservative problem $\boldsymbol{\phi_{ah}}$, and, therefore, the generalized matrices $\boldsymbol{M_{hh}}$, $\boldsymbol{B_{hh}}$ and $\boldsymbol{K_{hh}}$ are obtained. Matrix $\boldsymbol{B_{hh}}$ will not be in general diagonal while matrices $\boldsymbol{M_{hh}}$ and $\boldsymbol{K_{hh}}$ will.

7. A range of interest of the reduced frequency is selected, ensuring that this range will cover all the necessary flight speeds. For each reduced frequency k_j:

   a) The unsteady force coefficient from the UGF Method $C_{L\alpha i}(k_j, M_\infty)$ is computed. Then, the unsteady grid fins force matrix $\boldsymbol{Q}$ is obtained, and, with $\boldsymbol{\phi_{ah}}$, the generalized matrix $\boldsymbol{Q_{hh}}$.

   b) The eigenvalues of Eq.(6.100) for each mode p_m are computed. Then, we obtain:

   - The flutter speed $U_{\infty_m} = \mathrm{Im}(p_m)$,
   - The damping $g_m = \dfrac{2\mathrm{Re}(p_m)}{\mathrm{Im}(p_m)}$,
   - The frequency $\omega_m = \dfrac{2k_j U_{\infty_m}}{l_{ref}} = 2\pi f_m$

8. $V - g - f$ diagrams, representing (U_{∞_m}, f_m) and (U_{∞_m}, g_m), are sketched.

9. The flutter speed U_F will be the lowest at which any of the damping coefficients g_m becomes positive. From the $V - f$ diagram at this speed the flutter frequency f_F is obtained.

6.6 Results

In this section the results obtained from the hose-drogue-fins model analysis are presented. The sequence of the results will follow the structure of the chapter: first, the results of the static equilibrium position will be presented, followed by an analysis of the results

related to the dynamic properties of the system and its flutter behavior.

Since this chapter focuses on the effect of the fins on the system, all results will center on comparing the complete hose-drogue-fins model to the model without fins. Therefore, the effect of the parameters previously considered in Chapter 4 (such as the downwash angle induced by the tanker, the lag between aerodynamic and structural forces, the hose bending, etc.) will not be revisited here. Instead, the results of the complete model will be presented and compared with those obtained under the same conditions but without the inclusion of the fin model.

One of the main computational advantages of the developed model is its ability to easily adjust and study variations in the flight condition as well as in the values of the parameters. Regarding the flight condition, a broad range of flight Mach numbers and flight altitudes have been studied:

- The Mach number range studied is M_∞=0.3 to M_∞=0.8, as away of this range the refueling process can not be carried out.
- Flight altitudes from 5000 ft (1424 m) to 30000 ft (9144 m) are computed, as in the model without grid fins. It is worth noting that with the Mach number and the altitude the flight speed is fixed.

Regarding some of the important parameters included in the model and analyzed during Chapter 4, the following considerations must be taken into account:

- With respect to the hose, it is important to remember that two cases could be considered: the hose empty and the hose filled with fuel. As will be shown throughout the section, in all the results of this chapter the hose will be considered empty of fuel.
- The impact of the downwash angle induced by the tanker aircraft. All the results will be obtained with this effect included.
- The bending force in the hose. Unlike in the results for the model without fins where an analysis of the inclusion of this force was carried out, in this chapter the bending force of the hose will always be included in all the results presented.
- The steady position of each grid fin: As discussed during the characterization of the grid fins presented at Chapter 5, all results associated with the fins are obtained from a specific static configuration of each of the fins. In this analysis of the results, a fixed fins steady configuration will be assumed in some sections, while in others, the potential changes that arise in both the static and dynamic aspects when this configuration changes will be examined.

The main parameters of the hose-drogue-fins model are summarized in Table 6.1.

6.6.1 Static results

The static equilibrium position of the system will be determined first. The different positions are obtained for the flight speeds and flight altitudes range explained previously, as well as for the values of the system parameters given at Table 6.1.

Table 6.1: Parameters of the hose-drogue-fins model.

Hose length, s_0	25.90 m
Hose external diameter, d_{ext}	0.0676 m
Hose internal diameter, d_{int}	0.0551 m
Mass per unit length of the hose empty, ρ_H	2.50 kg/m
Young Modulus of the hose, E	600 MPa
Moment of inertia of the hose empty, I	$5.71{\cdot}10^{-7}$ m^4
Drag without lift coefficient of the hose, C_{D0}	1.2
Friction drag coefficient of the hose, C_{Df}	$4.5995{\cdot}10^{-4}$
Drogue weight, W	101.80 N
Drogue drag, Q	925.01 N
Fins UGF surface, S_{UGF}	2256 mm^2
Fins span, a_f	190 mm
Fins height, b_f	270 mm
Fins chord, c_f	30 mm
Number of hose elements, N_s	3000

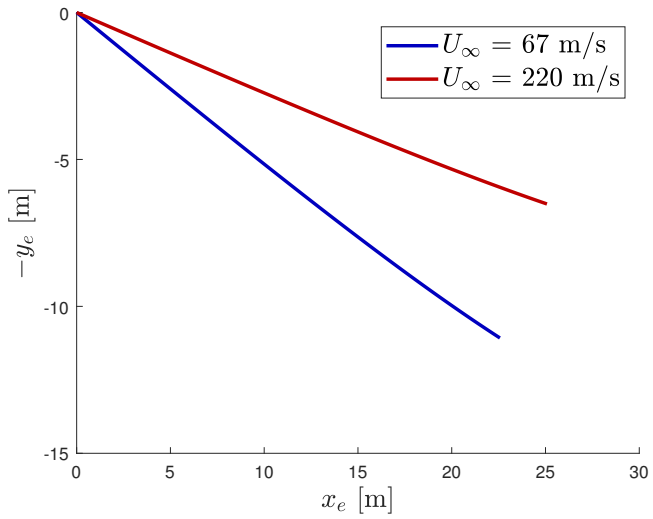

Figure 6.3: Static equilibrium position of the system for different flight speeds, (x, y) plane.

To analyze the influence of the grid fins in the steady position for different flight conditions, in Figures 6.3 and 6.4 the equilibrium positions (in a vertical and a lateral plane, respectively) are presented for two specific flight scenarios with the same altitude, H_∞ = 5000 ft, but different speeds: U_∞ = 67 m/s and U_∞ = 220 m/s. The hose is empty of fuel, and the fins steady configuration selected is the number 6 of those presented in Table 5.7 of Chapter 5. It can be observed that increasing the speed leads to significant changes in the equilibrium position. In addition, as mentioned during the development of

the formulation, in Figure 6.4 is shown that the lateral displacement of the hose is about one order of magnitude smaller than the vertical displacement given in Figure 6.3.

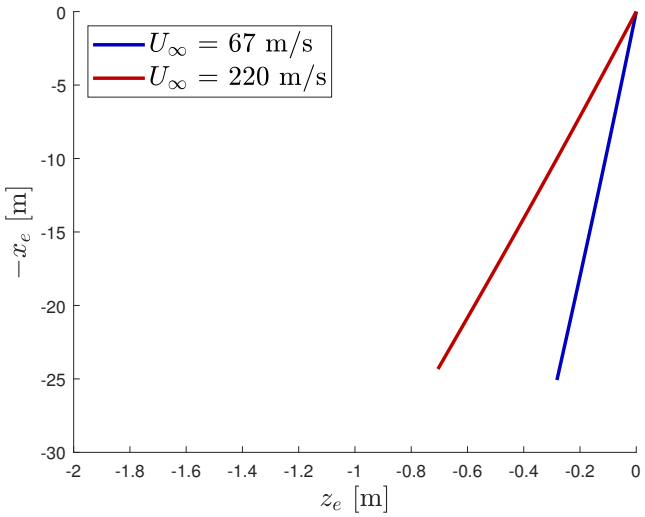

Figure 6.4: Static equilibrium position of the system for different flight speeds, (z, x) plane.

Next, to analyze the impact of the flight altitude, two scenarios with the same flight speed (U_∞ = 220 m/s) but different flight altitudes (H_∞ = 5000 ft and H_∞ = 30000 ft) with the hose empty of fuel and with the same steady configuration of the fins as the previous one are presented in Figures 6.5 and 6.6. As can be seen, changes in flight altitude result in relatively small differences in the equilibrium position of the system: At the maximum flight altitude the vertical drop at the hose-fins-drogue junction is reduced around an 8% with respect to the minimum altitude, while the lateral distance is a 7% higher, approximately.

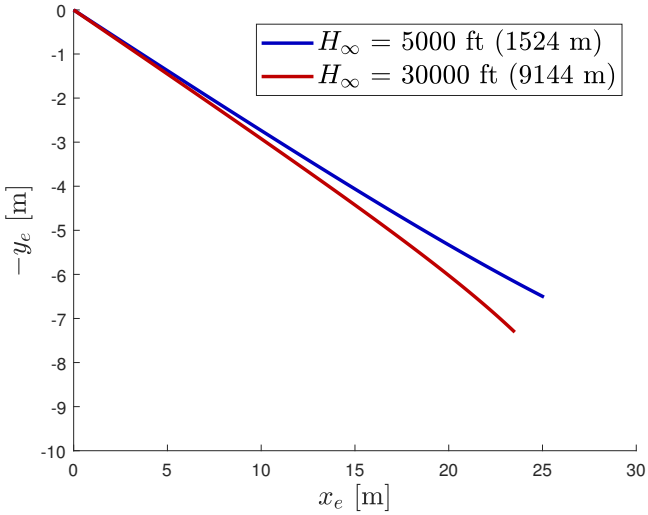

Figure 6.5: Static equilibrium position of the system for different flight altitudes, (x, y) plane.

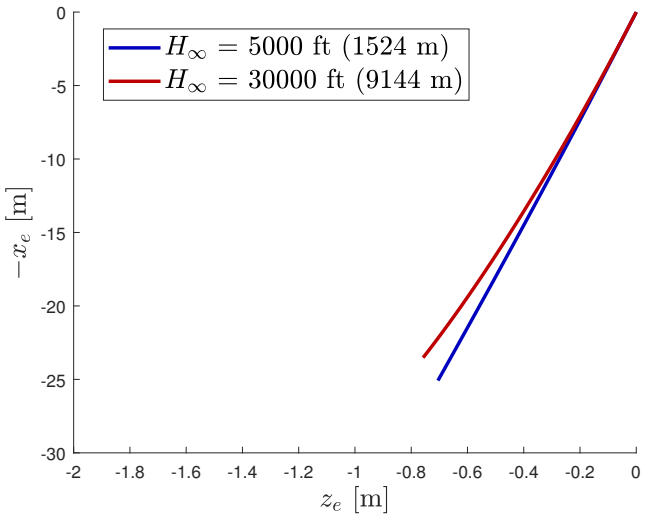

Figure 6.6: Static equilibrium position of the system for different flight altitudes, (z, x) plane.

To compare the results of the complete hose-drogue-fins model with the ones obtained from the model without fins, Figures 6.7 and 6.8 present the static position of both the systems with and without fins for two flight conditions with the same altitude H_∞=5000 ft but different flight speeds: U_∞=67 m/s and U_∞=220 m/s. The hose is empty of fuel and the steady configuration of the fins is the same as in the previous results.

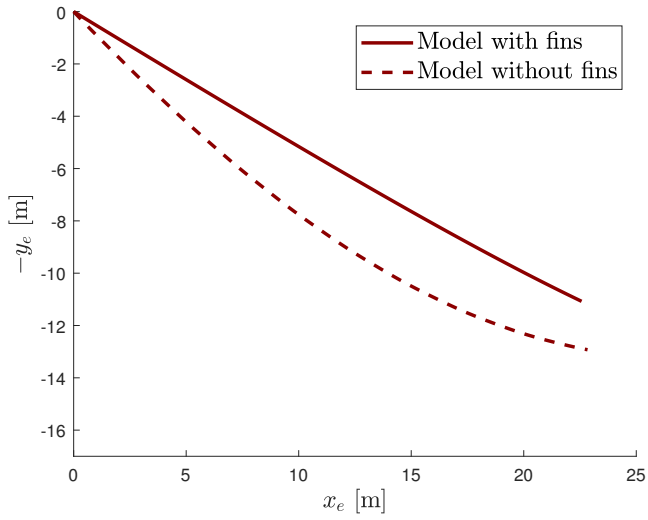

Figure 6.7: Static equilibrium position of the model with and without grid fins, U_∞=67 m/s and H_∞=5000 ft.

In both Figures 6.7 and 6.8 interesting differences between the two models are observed. Firstly, the model with fins shows a smaller hose-fins-drogue junction drop position with respect to the model without fins for both flight speeds. Although the steady configuration of each fin will affect this distance (in this case the configuration 6 is used, which, as shown in Table 5.7 from Chapter 5, the static lift of the fins is positive, while in other cases it may be negative), it is noteworthy that with the fin system, despite adding more weight, a smaller vertical distance in the hose-fins-drogue junction can be achieved due to

aerodynamics. Additionally, another important difference can be observed in the behavior of the hose along its length: the system with fins shows reduced deformation due to the added tension on the hose, leading to the conclusion that the hose is stiffer than in the case without fins. This change in hose behavior will be of great importance in the flutter analysis.

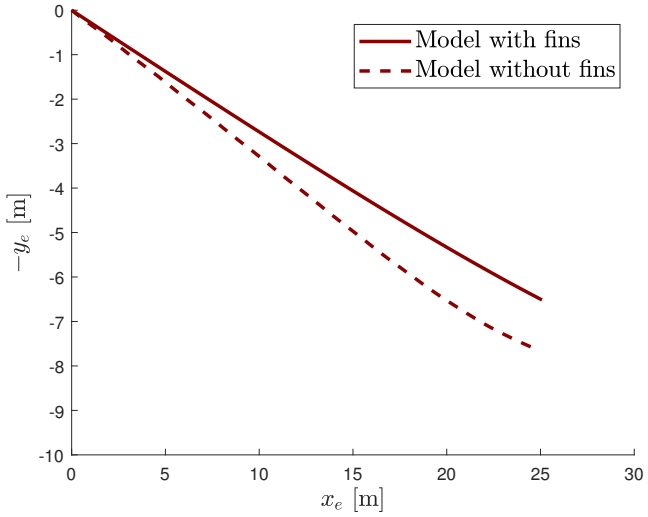

Figure 6.8: Static equilibrium position of the model with and without grid fins, U_∞=220 m/s and H_∞=5000 ft.

Finally, it is important to emphasize that all the results presented for the static position of the system correspond to one of the many possible steady configurations of each fin. These configurations are either fixed during the hose deployment or can be changed once the hose is fully deployed and before the contact with the receiver aircraft. Therefore, to analyze its influence on the static equilibrium positions three different steady fin configurations are used, and results are presented in Figures 6.9 and 6.10. Out of the eleven configurations shown in Table 5.7 from Chapter 5, configurations 6, 7 and 9 have been selected, see Table 6.2.

Table 6.2: Steady fins configurations used in the comparison of results.

Configuration	$\alpha^F_{e_1}$	$\alpha^F_{e_2}$	$\alpha^F_{e_3}$	$\alpha^F_{e_4}$	$\beta^F_{e_1}$	$\beta^F_{e_2}$	$\beta^F_{e_3}$	$\beta^F_{e_4}$	C^F_{Le}	C^F_{Ze}	C^F_{Me}
6	5	10	5	10	5	0	5	0	1.9087	-0.7386	6.8541
7	-5	0	-5	0	5	0	5	0	-0.1314	-0.7386	-2.9435
9	0	5	0	5	0	-5	0	-5	0.8608	0.1289	2.4288

Configuration six is the one used in all the previous results. Configuration seven was chosen because, in this case, the total static lift of the fins is negative, while in configuration nine, the change occurs in the static lateral force, which is positive instead of negative as it is in configurations six and seven. Table shows the angles of attack and sideslip and the aerodynamic coefficients for each of these three cases. The flight condition is U_∞=220 m/s and H_∞=5000 ft and the hose is again empty of fuel.

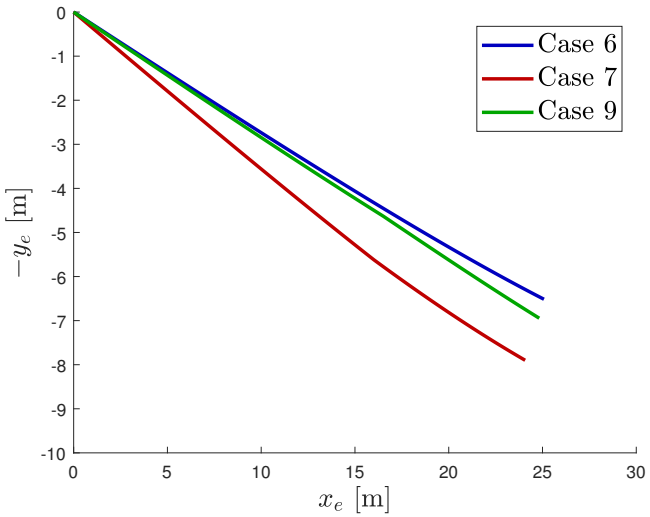

Figure 6.9: Static equilibrium position of the system for different fins configurations, U_∞=220 m/s and H_∞=5000 ft, (x, y) plane.

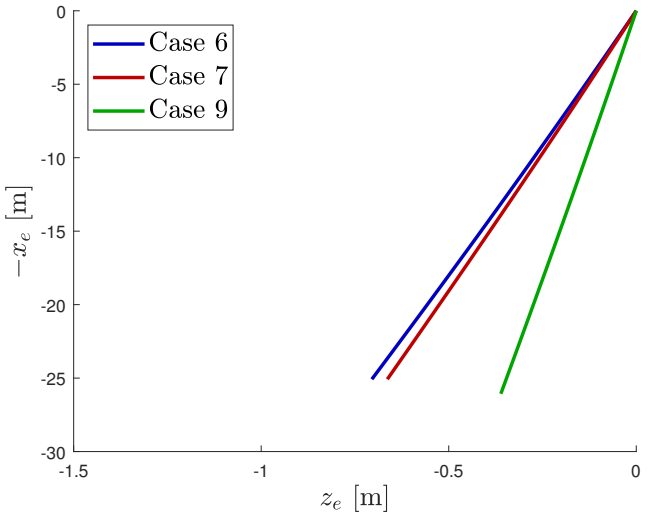

Figure 6.10: Static equilibrium position of the system for different fins configurations, U_∞=220 m/s and H_∞=5000 ft, (z, x) plane.

As shown in Figure 6.9, configuration 7 shows a greater vertical drop at the hose-fins-drogue junction compared to the other two configurations (an increase of 18.50% with respect to configuration 6). This is expected, as in this case the lift generated by the fins is negative, see Table 6.2. However this increase in the drogue's vertical drop is not particularly significant taking into account that the lift coefficient is much lower in configuration 7 compared to configuration 6 (a decrease of 93.11% in absolute value combined with the change in sign). Additionally, the fins continue to contribute an increase in stiffness along the hose, an effect absent in the original model without fins.

With respect to the lateral position presented in Figure 6.10, the main difference appears in configuration 9, where a smaller lateral distance is observed compared to configurations 6 and 7 (a reduction of 52.1% with respect to case 6). This behavior is associated with the fact that in configuration 9, the lateral force of the fins is positive and has a smaller

value than in the other two configurations, where it remains the same. Compared to the vertical position, this result shows that changes in lateral force strength have a more pronounced effect on the lateral position of the system than changes of lift in the vertical position.

It is important to mention that the ability to use different static fin configurations is a significant advantage, as changing the configuration allows for adjustments in the static equilibrium position. This, in turn, can be highly beneficial both for addressing potential stability issues within the system and for correctly aligning the drogue with the receiver's position, something that could not be achieved as easily without fins.

6.6.2 Flutter results

$V-g-f$ diagrams

The results of the flutter speeds, frequencies and modes of the system are presented next. To compare the results with the model without grid fins, the flutter boundaries will be computed for different values of both the phase lag angle ψ and the flight altitude H_∞. The initial steady configuration of each fin in the grid fins prototype will be fixed in the configuration 6 of those presented in Table 5.7 from Chapter 5, and the hose is considered empty of fuel in all the results. A wide range of values of the lag angle (from 0° to 20°) have been considered. However, once the results are obtained, the evaluation of if the value assumed has meaning physically must be done to really set the flight condition as a real one or not.

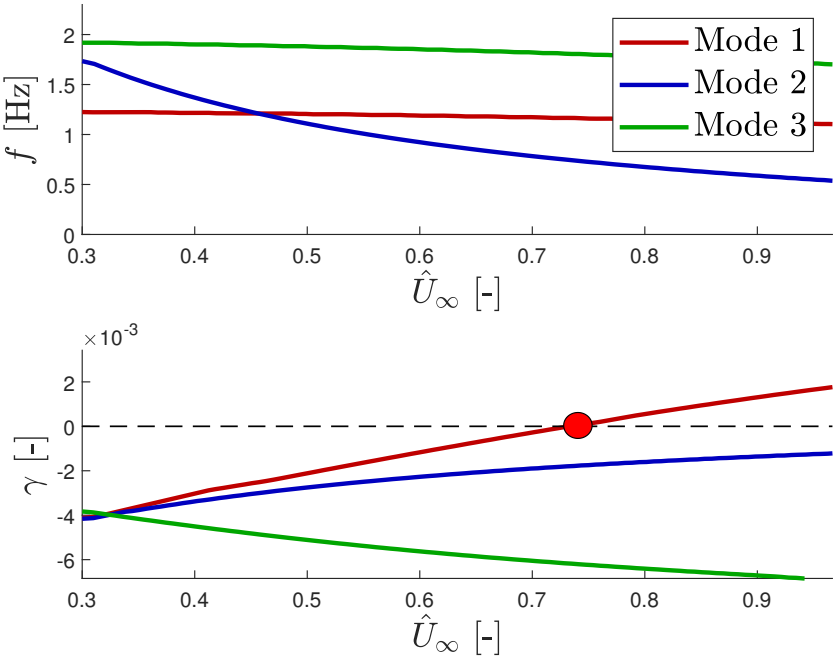

Figure 6.11: $V-g-f$ diagram for the first three modes. $\psi = 15°$ and $H_\infty = 5000$ ft.

Figures 6.11 and 6.12 show the evolution with the non-dimensional flight speed of the frequencies and damping coefficients for the first three vertical modes of the system (this

modes are selected to be able to compare the results to the ones obtained in the model without grid fins). Results are obtained for a lag value of ψ=15° (which, as will be explained afterwards, is the first value of ψ for which the system becomes unstable) and for two different flight altitudes. The flight speed is dimensionless with the same value of Chapter 4 (U_{max} = 300 m/s).

Important conclusions can be drawn from Figures 6.11 and 6.12. First, that the flutter always occurs by a single mode: there is no modal coupling in any of the cases. This type of flutter already appeared in the hose-drogue system without grid fin. In addition, the flutter mode in all the cases is the first mode associated with the vertical motion of the system, just like in the system without grid fins. Therefore, it is possible to conclude that the inclusion of the grid fins does not change the flutter mechanism of the hose-drogue system.

With respect to the evolution of the damping coefficients with the speed, it can be noticed that the results for both altitudes are very similar: The flutter speed for H_∞ = 5000 ft is $\hat{U}_F$ = 0.73, and for H_∞ = 30000 ft is $\hat{U}_F$ = 0.71 (a reduction of 2.74%). Thus, when the flight altitude increases the flutter speed decreases slightly. The damping coefficient for the second mode, although approaches zero for high flight speeds, it does not become positive in the range studied, and the damping coefficient for the third mode becomes more stable with the flight speed. With respect to the flutter frequencies, for H_∞ = 5000 ft we obtain f_F = 1.19 Hz and for H_∞ = 30000 ft f_F = 1.02 Hz, that is, a 14.29% of reduction. This variation is not as small as expected, and shows that the flight altitude variation does not affect significantly to the flutter speed but yes to the frequency.

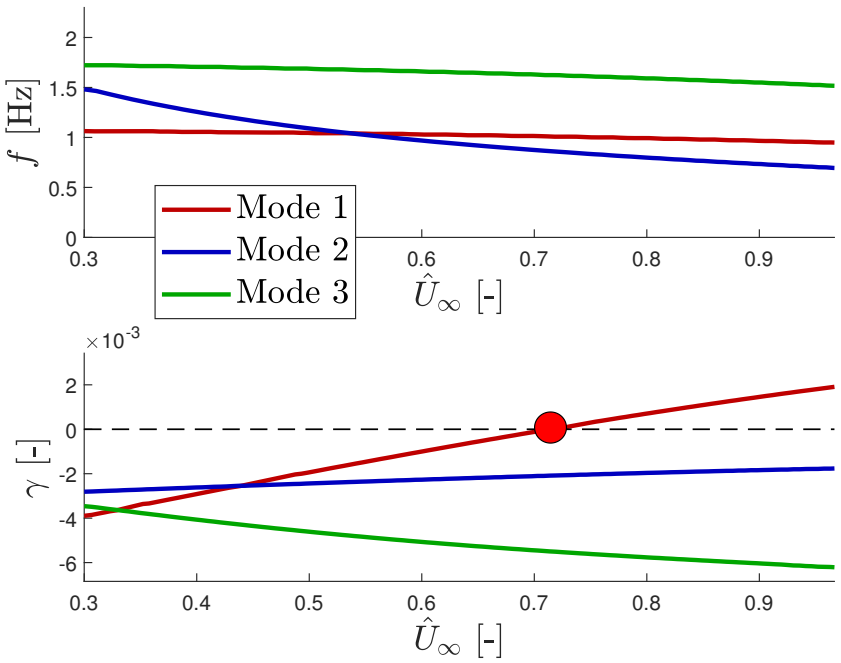

Figure 6.12: $V-g-f$ diagram for the first three modes. ψ = 15° and H_∞ = 30000 ft.

Figure 6.13 presents the flutter mode shape for a phase lag angle of ψ = 15° and different values of the flight altitude. As can be seen, the flutter mode is barely affected by the change in the flight altitude.

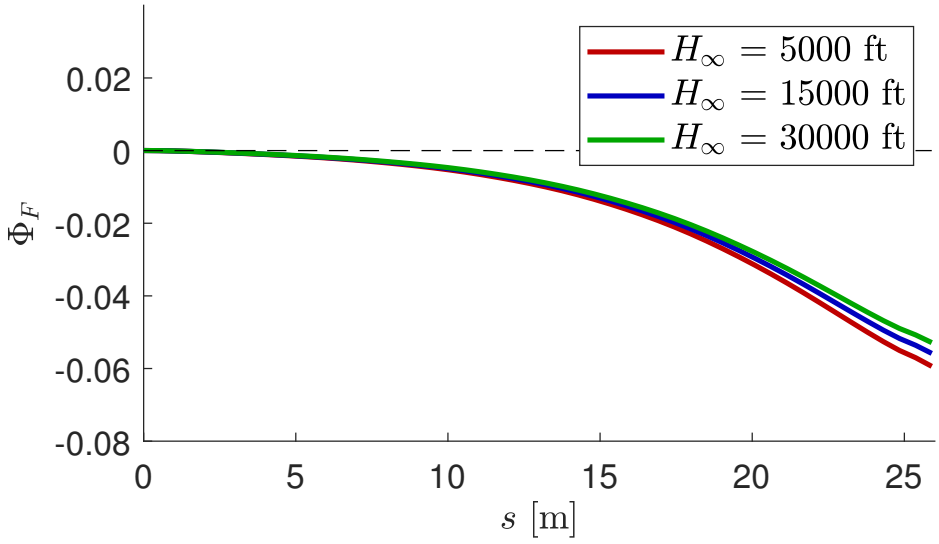

Figure 6.13: Flutter mode shape for different flight altitudes. $\psi = 15°$.

Comparison with the model without grid fins

Next, comparison with the results obtained for the model without grid fins (presented in Chapter 4) is done. It is interesting to mention that in the system with grid fins the first unstable cases appear for a phase lag angle around 15°, while in the system without grid fins, flutter appears for a phase lag angle around 10°. Therefore, one of the main conclusions is that the inclusion of the grid fins increases the aeroelastic stability of the hose-drogue system, in terms of a wider range of possible lags over which the system is stable (or, for a fixed value of the lag angle, a wider range of flight speeds). This fact remains consistent when different fin configurations are calculated, and therefore constitutes one of the most important conclusions of the chapter: The hose-drogue-fins model is more stable from the aeroelastic point of view (in terms of flutter) than the model without fins.

To show the effect of the grid fins, in Figures 6.14 and 6.15 the $V - g - f$ diagram (only for the first vertical mode, which is always the unstable one) of two cases with different values of ψ with and without grid fins are presented.

In Figure 6.14 it can be seen that for ψ=10° the system without grid fins (red line) reaches flutter, while the system with grid fins (blue line) is stable over the whole flight speed range studied. On the other hand, Figure 6.15 shows that for $\psi = 15°$ the system reaches flutter for both configurations. However, the flutter speed without grid fins is lower. Therefore, it is confirmed that the inclusion of the grid fins significantly delays the flutter of the system.

Regarding the frequencies of the system, it can be observed that with fins the frequencies are increased across the entire range of flight speeds studied compared to the system without fins. This is expected, as mentioned in the analysis of the static equilibrium position, since the fins significantly increase the tension and therefore the stiffness along the hose. Although they also increase the total weight of the system, this change in stiffness proves to be much more significant.

With respect to the damping coefficients, Figures 6.14 and 6.15 show the opposite effect: the inclusion of the fins results in significantly lower damping coefficients compared to the model without fins. However, this also makes sense since the fins induce new aerodynamic forces, causing a significant increase in the system's stiffness (and adding more weight, and therefore the inertia of the system is also increased), which explains why the damping coefficients are lower than in the model without them. Nevertheless, as shown, lower damping does not necessarily mean that the system is more unstable. In fact, the opposite occurs: while the damping is reduced, the effect of the fins is to delay the point at which any of these coefficients become positive, thus preventing the system from turning unstable. Table 6.3 summarizes the main differences that appear in the system with and without grid fins in the flutter speeds and frequencies.

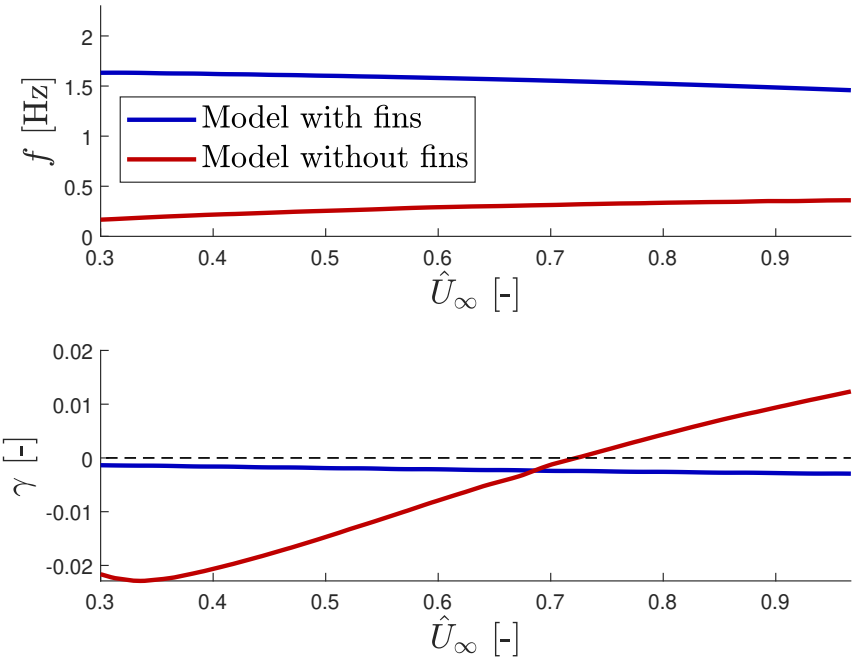

Figure 6.14: $V - g - f$ diagram comparison between the system without grid fins. $\psi = 10°$ and $H_\infty = 5000$ ft.

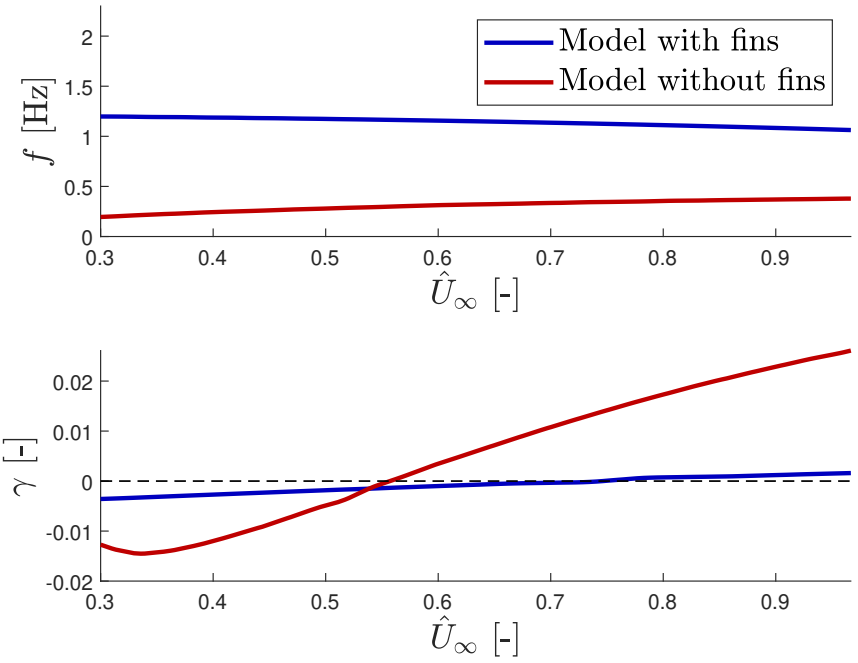

Figure 6.15: $V-g-f$ diagram comparison between the system without grid fins. $\psi = 15°$ and $H_\infty = 5000$ ft.

Table 6.3: Flutter results without and with grid fins.

	Without grid fins		**With grid fins**	
	U_F	f_F	U_F	f_F
$\psi = 10°$ $H_\infty = 5000$ ft	213.4 m/s	0.32 Hz	—	—
$\psi = 15°$ $H_\infty = 5000$ ft	165.1 m/s	0.29 Hz	219.3 m/s	1.13 Hz
$\psi = 15°$ $H_\infty = 30000$ ft	156.0 m/s	0.27 Hz	213.1 m/s	1.11 Hz

The variation of the non-dimensional flutter speed as a function of the phase lag angle and the flight altitude for both systems (with and without grid fins) is depicted in Figure 6.16. As previously explained, for the system without grid fins the unstable cases appear for phase lag angle values around 10° (left side of the Figure), while flutter in the system with grid fins appears around 15° (right side of the Figure). When the phase lag angle increases the flutter speed decreases, being this reduction less pronounced for higher values of ψ. Concerning the flight altitude, as shown in Figures 6.11 and 6.12 when the flight altitude increases the flutter speed decreases slightly. This effect is due to the influence of the static equilibrium position of the hose on the flutter speed.

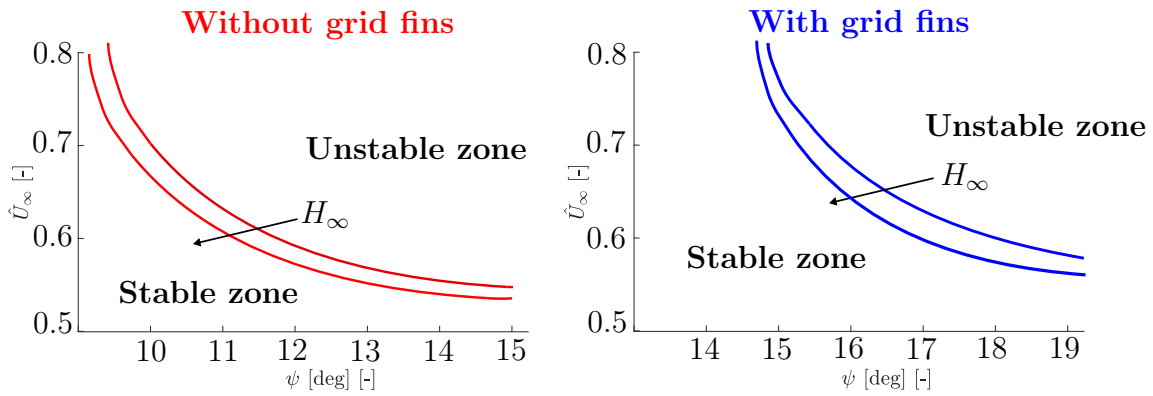

Figure 6.16: Non-dimensional flutter speed as a function of the lag angle and the flight altitude for the system without and with grid fins.

Finally, it is also of great interest to compare the flutter mode shape of the system with and without fins. As discussed earlier, in both models, the flutter involves a single degree of freedom without modal coupling, and it always occurs in the first mode associated with the vertical motion of the system. In Figure 6.17 the flutter mode of the system with and without grid fins is presented, for a flight altitude of $H_\infty = 5000$ ft and a lag angle of ψ =15°. As can be seen, the flutter mode in the model with fins (blue line) shows higher modal amplitude towards the end of the hose with respect to the mode in the model without fins (red line). This is expected, as the flutter speed of the model with fins is higher than that of the model without fins, and it was previously shown that the modal amplitude increases with speed. In addition, it can be observed that the modal behavior at the hose-fins-drogue junction is different: in the model with fins, the mode has a steeper slope compared to the model without fins. This is due to the modification of the boundary condition associated with the moment at that point: the inclusion of the pitching moment of the fins causes this change.

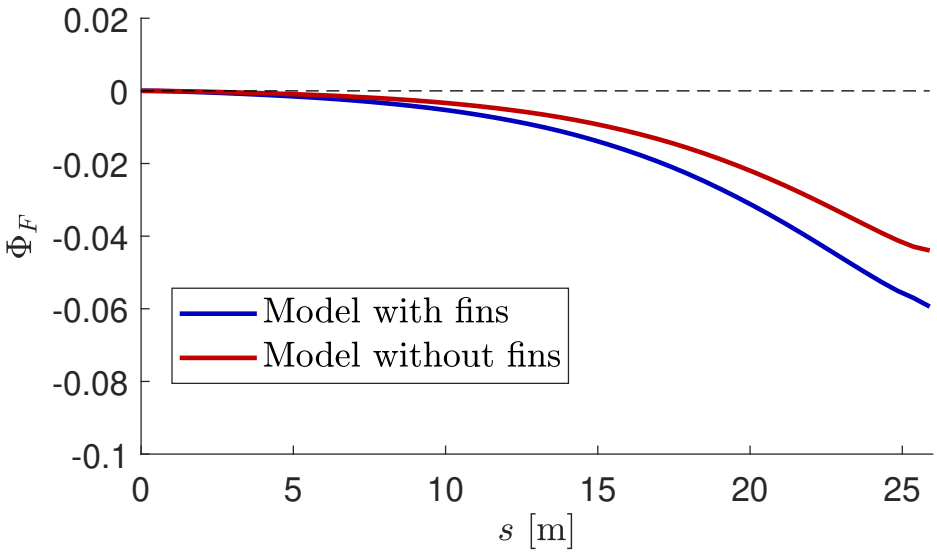

Figure 6.17: Flutter mode shape for the system with and without grid fins. $\psi = 15°$ and $H_\infty = 5000$ ft.

Effect of the steady fins configuration

As in the static results analysis, it is important to analyze the effect of the steady fins configuration in the flutter results. Thus, the V-g diagrams (for the mode that enters flutter) of the system with fins are presented in Figure 6.18 for a lag angle of $\psi = 15°$ and a flight altitude of $H_\infty = 5000$ ft, and for the steady fins configurations presented in Table 6.2. The same configurations used in the static results (6, 7, and 9 from the ones presented in shown in Table 5.7 of Chapter 5) are selected. The flutter results for each configuration are also summarized in Table 6.4.

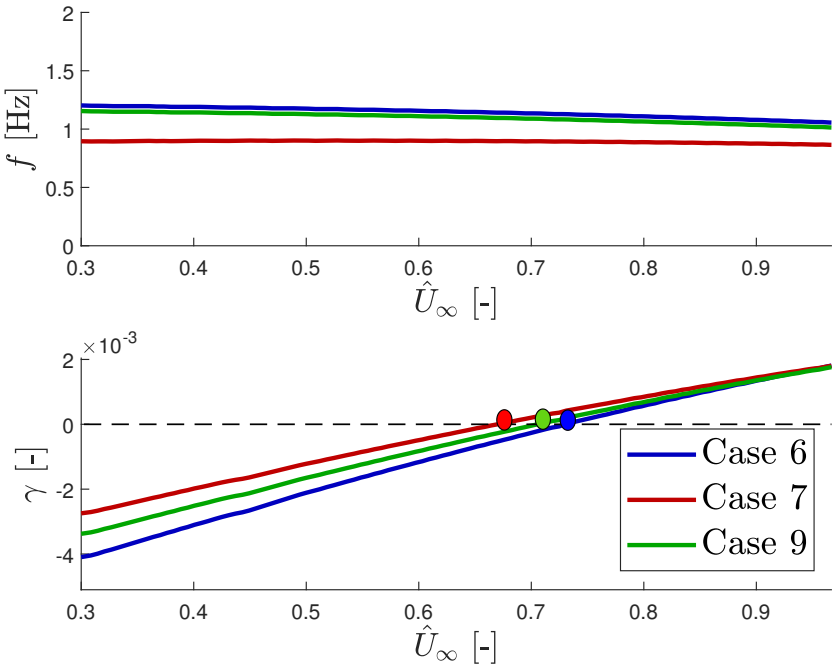

Figure 6.18: $V-g-f$ diagram for the flutter mode with different fins steady configurations. $\psi = 15°$ and $H_\infty = 5000$ ft.

Table 6.4: Flutter results without and with grid fins.

Fins steady configuration	U_F [m/s]	f_F [Hz]
Case 6	219.3	1.13
Case 7	204.1	0.90
Case 9	212.2	1.09

As can be seen in Figure 6.18 and in Table 6.4, the differences between case 6 and case 9 are very small: the flutter speed decreases from 219.3 m/s to 212.2 m/s (a reduction of 3.24%), while the flutter frequency remains almost the same in both cases (1.13 Hz and 1.09 Hz, respectively). However, the differences are more pronounced with configuration 7, where a flutter speed of 204.1 m/s is obtained (a reduction of 6.93% with respect to configuration 6) along with a lower frequency (0.9 Hz). Therefore, in all three cases flutter still occurs at much higher speeds than in the model without fins. Thus, it can once again

be concluded that the system with fins is more stable in terms of flutter than the system without fins.

Chapter 7

Discussion

Preceding the presentation of the main conclusions of the thesis, this chapter revisits the discussion of the results that have been explained and developed previously. While all of these analyses have already been addressed, and certain aspects will be reiterated in the conclusions of the thesis, it is a mandatory requirement set by the Polytechnic University of Madrid (UPM) to include this chapter with the discussion of results, even if previously covered within individual sections in the respective chapters. This discussion is structured to follow the same sequence presented throughout the thesis: starting with the characterization tests, then moving on to the original hose-drogue model, followed by the characterization of the grid fins, and concluding with the new hose-drogue-fins model.

7.1 Characterization tests

In Chapter 3 an static and a dynamic test of a sample of the hose were presented, with the aim to obtain reliable reference values of some important mechanical properties of the hose for its use in the rest of the work.

With respect to the static test, in Figures 3.4 and 3.5, as well as in Table 3.1, the results for the Elastic Modulus E were presented. As shown, results for each of the three different static tests performed provides significantly different values of the Elastic Modulus. Therefore, as expected, it is verified that the properties of the hose are different depending on the direction. However, the order of magnitude of the Elastic Modulus ($\simeq 10^8$) is consistent across all the tests, against the values found in some literature, so it can be concluded the values used by other works are not representative or the type of hose is very different to the one considered in this thesis. Finally, an Elastic Modulus of $E = 600$ MPa was selected to be used throughout the work.

The results obtained in the dynamic tests performed in the hose sample were presented in Table 3.5, where for each of the two modes analyzed the frequencies and the damping coefficients are given. The frequencies were estimated from the peaks of the FRF module. As shown, the adjustment for the first mode yields a consistent frequency and, except for the first function, an identical damping coefficient. By averaging all cases, the damping coefficient for the first mode is estimated to be $\gamma_1 \simeq 2.24\%$. For the second mode, the damping coefficient is estimated to be $\gamma_2 \simeq 3.93\%$. With the results of the vibration

test, it is concluded that the estimation of the structural damping of the hose for the two modes is reliable. Assuming that the coefficient of the first mode γ_1 is small enough, a conservative approach would be used: to assume the smallest value of γ_1 directly as the structural damping coefficient. Hence, a value of 2.22% was selected to be used for the structural damping of the hose.

7.2 Hose-drogue model

7.2.1 Static equilibrium position

Starting with the results of the static equilibrium position of the system, in order to illustrate the variations that appear under different flight conditions, Figure 4.4 displays the equilibrium positions for two specific flight scenarios with the same speed but different altitudes and in Figure 4.5 is presented the opposite: the same flight altitude but different flight speeds. Is shown that changes in flight altitude result in relatively small differences in the equilibrium position of the system. For instance, variations in the vertical position are approximately 4.5% at the junction between the hose and the drogue. Nevertheless, increasing the flight speed leads to significant changes in the equilibrium. In particular, a variation in the hose-drogue junction vertical position of more than 100% appear. From these two Figures it can be concluded that, as expected, the air density barely affects to the dynamic pressure while the flight speed strongly influence it. Although not applied in this work, the assumption of constant density flow could be adopted without compromising the results.

An analysis of the effect of different parameters on the steady position of the system was also performed during Chapter 4: Figure 4.6 shows the static equilibrium position for the same flight condition with the hose empty and with the hose filled with fuel, showing that the hose with fuel descends more than when it is empty. This behavior is expected, as the mass per unit length of the hose nearly doubles. However, the effect is less pronounced than one might anticipate because the bending forces in the hose filled with fuel also increase (due to the increased moment of inertia). The variation in the vertical position at the hose-drogue junction is approximately 10%. The static equilibrium position with and without the effect of the downwash angle ε is illustrated in Figure 4.7, where is shown that the main effect of the angle is to lower the equilibrium position of the hose. This effect involves a larger vertical distance between the tanker and the receiver, along with a more pronounced steady angle of attack on the hose, which markedly influence the dynamics of the system. The end position of the hose is lowered a 15% due to this angle (an effect much more pronounced than the one due to the air density). In addition, the effect of the hose bending on the static equilibrium position is analyzed in Figure 4.8, where is presented that the bending force inclusion results in a reduction in the vertical distance between the tanker and the drogue. Additionally, it can be observed that the hose is slightly stiffer (particularly towards the end, where the hose angle of attack is smaller with bending than without bending). This outcome is expected due to the increased stiffness of the hose when considering bending forces.

7.2.2 Dynamic problem

The dynamic characteristics of the system, including natural frequencies, damping coefficients, and mode shapes, were analyzed under various conditions to evaluate their dependence on flight parameters and system configurations. Using the eigenvalues and eigenvectors derived from Eq.(4.98), the natural frequencies and damping coefficients for different flight conditions were computed. These results, summarized in Tables 4.3 and 4.4, reveal the system's response under varying altitudes and speeds. The frequencies associated to the horizontal motion remained largely unaffected by altitude or speed, while frequencies related to the vertical motion increased markedly with speed. Table 4.4 shows that for vertical modes, damping increases with speed due to augmented aerodynamic effects. Given these findings, subsequent aeroelastic analyses focused solely on vertical modes, as flutter and instability issues were found to occur exclusively within these modes. Figures 4.9-4.11 illustrate the first three vertical modes, showing increased amplitudes at higher speeds while nodal points remain largely unchanged.

Results of the dynamic properties were compared with an empty hose and a fuel-filled hose. The analysis, focused on vertical modes (Table 4.5), highlights that frequencies were lower for the fuel-filled hose, attributed to the increased system mass outweighing the rise in stiffness. In addition, the presence of fuel caused a significant decrease in damping coefficients, consistent with the added inertia. Figures 4.12-4.14 depict the first three vertical modes for both cases, showing reduced modal amplitudes in the fuel-filled configuration but minimal structural changes. The impact of the downwash angle on dynamic properties was analyzed in Table 4.6, showing a slight decrease in natural frequencies due to the downwash-induced reduction in system stiffness, and a higher absolute damping coefficients due to the grew of aerodynamic damping with increased angles of attack. With respect to the influence of hose bending on the dynamic properties summarized in Table 4.7, is shown that significant frequency rises were observed when bending stiffness was included, reflecting the added stiffness's effect on system dynamics. With respect to the damping coefficients, a slight reduction was noted, consistent with the increase in stiffness, highlighting the importance of accounting for bending forces in flutter analyses to avoid overly conservative predictions.

The role of the phase lag angle ψ in system dynamics was also explored by comparing scenarios where $\psi = 0$ and $\psi \neq 0$. When $\psi \neq 0$, aerodynamic terms in the damping and stiffness matrices became complex, doubling the natural frequencies and damping coefficients. Tables 4.8 and 4.9, along with Figures 4.21 and 4.22, show that natural frequencies were largely unaffected by changes in ψ (less than 0.5% variation), while damping coefficients exhibited significant sensitivity, with the coefficient γ_{1V}^{+} (associated to one of the branches of the first vertical mode) becoming positive around $\psi = 7°$, indicating potential instability.

7.2.3 Aeroelastic analysis

The aeroelastic analysis were performed by means of the Tracing of the Roots method, obtaining flutter speeds, frequencies and modes of the hose-drogue system. To determine flutter boundaries, frequencies and damping coefficients were plotted against flight speed U_∞ for different values of the phase lag angles ψ. Flutter speed is obtained at the first

instance where a damping coefficient becomes positive. Three scenarios ($\psi = 0°$, $5°$, and $10°$) are depicted in Figures 4.23-4.25. Results can be summarized as follows:

- No Flutter for $\psi = 0°$ and $\psi = 5°$: In Figures 4.23 and 4.24, damping coefficients remain negative, indicating stable conditions.
- Flutter at $\psi = 10°$: For $\psi = 10°$ (Figure 4.25), the damping coefficient γ_{1V}^{+} crosses zero. Linear interpolation estimates the flutter speed U_F as 206 m/s for this case.

Flutter speeds, frequencies, and modes were analyzed under varying phase lag angles ψ and flight altitudes H_∞. Unlike prior results, structural damping was included, leading to differences from earlier analyses where structural damping was neglected. Across all the studied cases, flutter arises from a single mode—the first vertical mode of the system. Other vertical and all horizontal modes remain stable. Is shown that flutter occurs at $\psi \approx 9°$, with flutter speed decreasing as ψ increases. The effect diminishes for higher values of ψ. In addition, an increased altitude slightly reduces flutter speed due to equilibrium position variations. With respect to the flutter mechanism, in Figure 4.27 is showed for all cases, highlighting minimal impact on mode shapes from changes in ψ or H_∞. Phase lag ψ has a more significant impact on flutter speed than altitude. The root locus diagrams of Figures 4.31-4.33 show eigenvalue evolution with flight speed, emphasizing the importance of static equilibrium positions in flutter onset.

As in the static and dynamic results, the effect of different parameters were again studied in the aeroelastic analysis. The impact of fuel was examined in Table 4.5, where is showed that in the hose with fuel both frequencies and damping coefficients are decreased. As shown in Figure 4.34 the flutter speed decreases from $\hat{U}_\infty = 0.55$ (empty hose) to $\hat{U}_\infty = 0.52$ (fuel-filled hose), a 5.5% reduction. This aligns with reduced damping in the fuel-filled configuration. With respect to the downwash angle, its inclusion increases system damping while slightly reducing frequencies (Table 4.6). Figure 4.35 shows that flutter speed increases from $\hat{U}_\infty = 0.53$ (without downwash effect) to $\hat{U}_\infty = 0.55$, reflecting additional aerodynamic damping introduced by the downwash angle. Finally, is presented that the inclusion of hose bending significantly affects flutter boundaries. Table 4.7 shows that bending increases frequencies but decreases damping coefficients. Figure 4.36 demonstrates that excluding bending results in a higher flutter speed: $\hat{U}_\infty = 0.58$ compared to $\hat{U}_\infty = 0.55$ when bending is included. Therefore, neglecting bending forces can lead to overly non-conservative flutter predictions.

7.3 Grid fins characterization

In Chapter 5 the grid fins prototype were presented and the complete steady and unsteady aerodynamic characterization were performed.

First, the results for the steady aerodynamic coefficients (lift, side force and pitching moment) obtained with the DLM code and the proposed UGF Method were presented. The experimental cases available are used as a reference. As shown in Table 5.7, all the results are similar to those obtained experimentally, although minimal discrepancies in some cases appear, mainly due to the applicability of the interference factors, which are

derived from an adjustment across all cases.

With respect to the unsteady aerodynamic forces, the coefficients were first presented as a function of the reduced frequency for a fixed Mach number, followed by results for a fixed reduced frequency with varying Mach number. This approach enables the analysis of the influence of both parameters on the results. Starting from the known results for $k = 0$, the DLM code is executed for a Mach number $M_\infty = 0.5$ and for several reduced frequencies. Then, an unsteady UGF normal force coefficient $C_{N\alpha,\mathrm{UGF}}(M_\infty = 0.5, k)$ can be calculated. Using the previously explained UGF Method, the unsteady coefficients are obtained. In Figures 5.7-5.9, the magnitude and phase of each coefficient are represented as functions of the reduced frequency. As observed, the magnitudes of the three aerodynamic coefficients decrease with increasing reduced frequency, up to a value close to $k = 2$. Beyond this point, the trend reverses, and the magnitudes start to increase with the reduced frequency. Regarding the phases, for values of k up to approximately 1.5, the phases of all three coefficients increase with the reduced frequency. However, beyond this point, the phases decrease slightly as the reduced frequency increases.

Then, by setting $k = 0.2$, the DLM code is executed again but performing a sweep across the Mach number M_∞. This process yields $C_{N\alpha,\mathrm{UGF}}(M_\infty, k = 0.2)$. Following the same procedure as in the previous case, the coefficients are calculated. The magnitude and phase of each coefficient as functions of the Mach number are shown in Figures 5.10-5.12. Is shown that the magnitudes of the aerodynamic coefficients increase with the Mach number, with the rate of increase becoming more pronounced at higher Mach numbers. The phases exhibit a slight increase with the Mach number. However, this increase is minimal, leading to the conclusion that the Mach number's effect on the phase of the aerodynamic coefficients is practically negligible.

7.4 Hose-Drogue-Grid Fins model

Once the hose-drogue original system and the grid fins prototype were defined and studied, the new hose-drogue-fins was presented and analyzed in Chapter 6. All results were focused on comparing the complete hose-drogue-fins model to the model without fins. The effect of parameters previously analyzed in Chapter 4 (such as the effect of the fuel, the downwash angle and the hose bending) were not revisited. Instead, results for the complete model are compared under identical conditions but without including the grid fins prototype.

7.4.1 Static Equilibrium Position

To analyze the grid fins influence on the static equilibrium, Figures 6.3-6.4 and 6.5-6.6 present the steady positions of the complete system for different flight conditions. The results assume an empty hose and the same fins steady configuration. Increasing speed results in significant positional changes, with the lateral displacement approximately an order of magnitude smaller than the vertical. However, the change in the flight altitude produces less differences: at maximum altitude, the vertical drop at the hose-fins-drogue junction is reduced by 8%, and the lateral distance increases by 7%.

Comparison with the model without fins is shown in Figures 6.7 and 6.8. Key differences include that the system with fins shows a smaller vertical drop at the hose-fins-drogue junction due to aerodynamic lift generated by the fins. In addition, in the system with fins the hose deformation is reduced.

The equilibrium position was also studied for different fins steady configurations. Figures 6.9 and 6.10 present results for configurations 6, 7, and 9 (Table 6.2). Configuration 7 shows a larger vertical drop due to negative lift, while configuration 9 reduces lateral displacement. These results demonstrate that altering fin configurations can adjust static positions to optimize system stability or alignment with the receiver aircraft.

7.4.2 Aeroelastic Analysis

Flutter speeds, frequencies, and modes are obtained for various lag angles ψ and flight altitudes H_∞ by means of the K-Method. Figures 6.11 and 6.12 show the evolution of frequencies and damping coefficients with flight speed for the first three vertical modes. Is shown that in all cases flutter always occurs by a single mode (the first vertical mode), as in the model without fins. With respect to the flutter speeds and frequencies:

- Flutter speed decreases slightly with flight altitude: $\hat{U}_F = 0.73$ for $H_\infty = 5000$ ft and $\hat{U}_F = 0.71$ for $H_\infty = 30000$ ft, a 2.81% reduction.
- Flutter frequencies are more affected by flight altitude: $f_F = 1.19$ Hz at $H_\infty = 5000$ ft and $f_F = 1.02$ Hz at $H_\infty = 30000$ ft, a 14.29% reduction.

Results for the model without fins presented at Chapter 4 where compared to those obtained with the complete hose-drogue-fins model. Figures 6.14 and 6.15 show $V - g - f$ diagrams for the first vertical mode. At $\psi = 10°$, the system without fins enters into flutter, while the system with grid fins remains stable. At $\psi = 15°$, both systems enters into flutter, but the system with fins achieves higher flutter speeds, confirming enhanced aeroelastic stability with the grid fins prototype included. The fins increase stiffness and frequencies but reduce damping coefficients. However, lower damping does not imply instability; instead, fins delay flutter onset, as shown in Table 6.3.

In addition, the effect of steady fin configurations on flutter results is analyzed for configurations 6, 7, and 9 (of those presented at Table 6.2). Flutter speeds and frequencies are summarized in Table 6.4. Configuration 7 shows the lowest flutter speed and frequency, but all configurations are more stable than the model without fins.

Chapter 8

Conclusions

This thesis has focused on the study of an aerial refueling system with a hose-drogue configuration, analyzing the static and dynamic behavior as well as the aeroelastic stability of the system. The study was conducted first on a conventional hose-drogue system and then on a new development that includes a prototype of grid fins at the hose-drogue junction. This required the aerodynamic characterization of the fins and the subsequent analysis of their integration into the system. This chapter will conclude the work by discussing the main results and findings obtained throughout the various chapters, ending with potential future research directions based on the outcomes of this thesis.

8.1 Concluding remarks

This section will discuss the main results and contributions of the thesis, following the same order of presentation as in the previous chapters.

Chapter 3 presented the results of two characterization tests conducted on a hose sample: a static test to estimate the Elastic Modulus and a dynamic test to estimate the structural damping coefficient. Both estimations have been crucial in the following chapters, making these experimental tests a highly important part of the thesis.

In the static test, the objective was to estimate the Elastic Modulus of the hose by measuring its deformations under controlled loading conditions. Due to the structural complexity of the hose, multiple tests were conducted with varying positions of the extensometer to obtain reliable estimates. The tests confirmed that the mechanical properties of the hose vary directionally; however, all results remained within the same order of magnitude, supporting an approximate Elastic Modulus value. Therefore, an Elastic Modulus of 600 MPa was selected for use throughout this thesis, providing an adequate basis for subsequent analyses of hose bending behavior.

The vibration test aimed to estimate the structural damping coefficient of the hose by analyzing its dynamic response to controlled excitation. Using a shaker, a white noise signal was applied to the hose while accelerometers measured its response across several points. The Frequency Response Functions (FRFs) of the system were obtained, and the Peak-Picking Method was applied to the resulting data. The analysis of the main modes

obtained in the test yielded the damping coefficients. With the consideration of achieve a conservative and reliable estimation, the smaller damping coefficient (of 2.22%) was selected as the structural damping coefficient for the hose in the subsequent aeroelastic and dynamic analyses within the thesis. This approach provides a consistent and reasonable basis for evaluating the hose's behavior under dynamic conditions.

Chapter 4 presented the complete development and analysis of the hose-drogue model. The mathematical formulation of the system was first developed. This formulation defines the forces acting on both the hose and drogue components within a two-dimensional plane, simplifying the model through symmetry assumptions and setting up equations that enable the evaluation of system equilibrium and dynamic responses. Initially, the model establishes the governing equations for the hose's horizontal and vertical positions and the associated tension. Important effects such as the downwash effect induced by the tanker's wake and the bending forces on the hose are included. A significant aspect involved defining the aerodynamic forces on the hose based on aerodynamic characteristics of an inclined cylinder, leveraging findings from prior studies to enhance accuracy while maintaining computational efficiency. The equations were linearized under small perturbation assumptions, allowing the dynamic behavior to be modeled as oscillations around a static equilibrium. This approach enables a split between steady-state and perturbed components of the system's motion.

In the static analysis, the equilibrium position of the hose-drogue system is determined through a system of nonlinear differential equations that account for aerodynamic forces, hose tension and bending effects. Given the critical role of the static equilibrium position in influencing dynamic stability, this analysis examines how factors like flight speed, altitude, fuel presence (analyzing the hose empty and the hose filled with fuel), downwash angle, and bending forces impact the system's steady-state configuration. Results show that changes in altitude minimally affect equilibrium, highlighting the limited role of air density. The flight speed has a major impact, with a significant effect in the hose-drogue junction's vertical position, Furthermore, the addition of fuel in the hose increases its vertical drop to added weight, though bending forces offset this effect by enhancing structural stiffness. The downwash angle from the tanker significantly lowers the hose position, which increases the vertical gap between tanker and drogue, a factor with potential implications for hose stability. Lastly, the inclusion of bending effects reduces the overall vertical displacement, adding rigidity that could help maintain stability under flight conditions.

With the static results, the dynamics of the hose-drogue system to small perturbations relative to its equilibrium position are analyzed. The focus is on low-intensity disturbances applied at the drogue, enabling a linear approximation of the equations and allowing for the calculation of the natural frequencies, damping coefficients, and modal shapes of the system. Assuming small-amplitude oscillations, transient tension effects are considered negligible, and the unsteady equations are discretized along the hose using the Weighted Residual Method formulation, obtaining the inertia, damping and stiffness matrices of the system.

The effects of different flight conditions, fuel presence in the hose, downwash angle induced by the tanker's wake, and hose bending are evaluated in relation to the system's dynamic

properties. Regarding flight speed and altitude, frequencies associated to the horizontal motion remain largely constant across conditions, while vertical motion frequencies increase with flight speed due to the aerodynamic effects. In the hose filled with fuel the natural frequencies are reduced as a consequence of the added mass, despite the accompanying increase in stiffness from hose bending. The downwash angle slightly decreases natural frequencies and increases damping, due to the added aerodynamic forces, while including hose bending significantly raises natural frequencies due to added stiffness. Neglecting bending forces can yield oversimplified results with underestimated frequencies and overestimated damping, potentially leading to non-conservative flutter predictions. Finally, the phase lag between unsteady aerodynamic forces and structural oscillations is examined as an influence on stability. When phase lag is introduced, the system's eigenvalues are no longer complex conjugates, splitting each natural frequency and damping coefficient. Although phase lag has a minimal effect on natural frequencies, its influence on damping coefficients is significant, and above a certain value of the angle the system may become unstable.

The aeroelastic stability analysis of the hose-drogue system was focused on determining flutter speeds, frequencies, and modal shapes under varying flight conditions. The system's nonlinear static position and linearized dynamics necessitate precise solutions for accurate stability predictions. Unlike conventional flutter analysis, where only dynamic forces are considered, this approach accounts for the effects of static equilibrium on dynamic forces. As such, flutter solutions will depend on the static equilibrium configuration. The flutter analysis involves several steps. Starting with fixed values of the phase lag angle, altitude, and flight speed, the static equilibrium position is calculated. Subsequently, the dynamic problem is solved by computing inertia, damping, and stiffness matrices, followed by eigenvalues that reveal the system's frequencies and damping coefficients. Flutter speed is identified using a tracing of the roots method: if all eigenvalues have negative real parts, the system is deemed stable; if any real part becomes positive, the flutter condition is reached, and the corresponding speed, frequency, and mode are determined.

Flutter results demonstrate that as the phase lag increases, the flutter speed decreases, especially at lower lag values. Altitude also has a mild effect, slightly lowering flutter speed due to equilibrium position changes with altitude. Across all the studied cases, the system shows a single-mode flutter, with the first vertical mode consistently responsible for instability. The phase lag has a more significant effect on flutter speed than altitude, with higher lag values lowering the speed threshold for instability. Additional analyses examine the influence of specific parameters on aeroelastic stability. When the hose is filled with fuel, flutter speed decreases slightly, as the increased mass reduces damping, hastening instability onset. The downwash angle introduces additional aerodynamic damping, resulting in a small increase in flutter speed when included. The bending effect increases system stiffness and slightly lowers damping coefficients. Therefore, excluding bending forces can produce non-conservative results, overstating the stability and slightly elevating flutter speed predictions.

The hose-drogue model developed enables both stability analysis and dynamic response evaluation during key refueling events, like drogue-receiver contact. Initially, a vertical impulse was applied to the drogue to observe basic model behavior, especially bending effects. This impulse creates a wave along the hose, gradually dampening as the system

returns to equilibrium. Including bending forces generates multiple waves with reduced movement amplitude, indicating increased stiffness. For a more realistic scenario, a receiver speed profile was applied, covering both horizontal and vertical drogue movements upon contact. Analysis shows a significant initial force spike in the hose due to the sudden velocity shift, particularly in the vertical direction, which diminishes over time as the system stabilizes. These force peaks highlight critical moments in the refueling process where dynamic control is essential to avoid excessive strain on the system.

In Chapter 5 the grid fins prototype used for the new developed configuration is presented. The prototype used follow a cross configuration with four grid fins (two vertical and two horizontal), each capable of rotating around its axis, which influences local angles of attack and sideslip for aerodynamic analysis. The UGF Method approach is used for obtain the aerodynamic forces on the fins. In this method, the aerodynamic forces of the fins are computed by dividing it into individual Unit Grid Fins, each modeled separately. This approach includes both steady and unsteady aerodynamic forces, obtained via a Doublet-Lattice Method (DLM) code to capture dynamic aerodynamic coefficients over varied flight conditions.

Steady aerodynamic forces are validated through comparison with experimental data, showing close agreement and low error margins. The interference terms between the fins and other prototype components are integrated into calculations using experimental data. The aerodynamic coefficients, including lift, side force, drag, and pitching moment, are calculated and validated, with interference factors added for enhanced accuracy. The unsteady analysis explores changes in aerodynamic forces as functions of both reduced frequency and Mach number. The results of the modules and phases of the unsteady forces show that increased reduced frequency reduces the module of aerodynamic coefficients initially, then increases it beyond a certain value. Similarly, higher Mach numbers generally increase coefficient modules while minimally affecting phase angles.

With both the hose-drogue model and the grid fins prototype fully developed and studied, in Chapter 6 the complete development and analysis of the new hose-drogue-fins configuration was presented. As in the model without fins, this Chapter included the full mathematical modeling of the system, addressing both its static and dynamic behavior, focusing on the determination of the system's flutter conditions and comparing all the results with those obtained in the original system without fins.

The hose-drogue-fins mathematical formulation extends the two-dimensional hose-drogue framework into a three-dimensional space by incorporating the aerodynamic and structural effects of grid fins. This formulation includes forces and motions in the horizontal, vertical, and lateral axes, capturing lateral forces generated by the fins—forces that were previously unaccounted. The governing equations consider again the hose tension, the bending force on the hose and the downwash angle induced by the tanker aircraft.

The static equilibrium analysis of the hose-drogue-fins system shows how flight speed, altitude, and the different steady fin configurations impact in the position of the system. Results presented that increasing flight speed significantly alters the equilibrium position, with vertical displacement notably larger than lateral displacement. Additionally, altitude changes have a less pronounced effect than speed, with only a slight reduction in

vertical displacement at higher altitudes.

The comparison of the original hose-drogue system with the new hose-drogue-fins configuration reveals that the system with fins achieves a smaller vertical drop and a reduced hose deformation, despite the additional weight of the fins. This outcome highlights the aerodynamic benefit of fins in stabilizing the hose, making it more stiffer. Finally, varying the static fin configuration enables further control over the hose position. When comparing steady configurations with differing each fin position, results show how some configurations minimizes vertical and lateral displacements. This adaptability through fin adjustments provides a significant advantage, allowing the system to address stability concerns and improve drogue alignment with the receiver aircraft—a versatility unattainable in models lacking fins.

The aeroelastic analysis investigates the stability of the hose-drogue-fins system by determining flutter speeds, frequencies, and mode shapes with the K-Method under various flight conditions, with a focus on the impact of the fins addition to the model. The analysis considers different flight speeds, flight altitudes, phase lag angles, and steady configurations of the fins. The findings indicate that including fins enhances the system's stability. Flutter typically initiates at a higher phase lag angle (around 15°) compared to the model without fins (around 10°), suggesting a wider operational stability range with fins. The results show that in all cases, flutter occurs via the first vertical mode without modal coupling, similar to the system without fins. Thus, the addition of fins does not fundamentally alter the flutter mechanism but shifts the flutter speed and frequency to higher values.

Results show that the flutter speed is only slightly affected by altitude, with a minor decrease at higher altitudes. However, flutter frequency shows a more noticeable reduction with increasing altitude, showing that altitude affects frequency more than speed in the presence of fins. Comparing the model with and without fins, the finned configuration displays significantly higher flutter speeds, confirming that fins delay flutter. Moreover, adding fins lowers damping coefficients across the flight speed range due to increased stiffness and mass from the fins, yet it still effectively stabilizes the system, as the onset of instability is postponed.

Examining different steady configurations of the fins shows that certain configurations yield lower flutter speeds and frequencies, highlighting how adjustments to fin angles can influence stability. Despite these variations, all configurations with fins remain more stable than the non-finned model, underscoring the fins' stabilizing effect in terms of aeroelastic performance.

8.2 Future works

In this thesis, several valuable insights have been achieved, highlighting areas for further research and potential advancements. Future work could explore enhancements to the model, deeper investigations into the aerodynamic forces, or applications in different operational scenarios. Key recommendations could include:

- Extend the analysis to other phases of aerial refueling with the hose-drogue system, particularly the hose deployment and retrieval, and examine the behavior of the system in these stages. This would require incorporating the unsteady tension of the hose, and would make the small perturbation approach unsuitable, necessitating a simultaneous solution of the static and dynamic problems.

- With the inclusion of the fins developed, various active control strategies could be implemented and studied in the new hose-drogue-fins configuration to prevent instabilities in the system.

- Analyze the dynamic response of the system upon receiver-drogue contact within the complete model that includes grid fins. This thesis has presented results for the hose-drogue system without the fins, but extending this analysis to the configuration with fins would be highly valuable to assess the potential differences associated with their inclusion.

- Conduct unsteady tests on the fins to directly validate the complete dataset of unsteady aerodynamic forces. Additionally, perform in-flight tests of the hose-drogue system both with and without fins, allowing for validation of many of the obtained results against real flight data.

Appendix A

Development of the hose and drogue model

A.1 Discretized equations

Before the development of the equations, it is necessary to make a manipulation in certain terms, to avoid the appearance of derivatives in a greater order than the necessary in the equations. This manipulation is performed in the tension and bending terms:

A.1.1 Tension term

The application of the Weighted Residual Method to the tension terms of Eq.(4.81) yields the following integral, which can be written as:

$$\int_{s_{j-1}}^{s_j} \varphi_k^{(1)}(s) \frac{d}{ds}[T_e \hat{N}'(s)] ds = \varphi_k^{(1)}(s) T_e(s) \hat{N}'(s) \mid_0^{s_0} - \int_{s_{j-1}}^{s_j} \varphi_k^{\prime(1)}(s) T_e(s) \hat{N}'(s) ds.$$

With the application of the boundary conditions given in Eq.(4.88), the first term is:

$$\varphi_k^{(1)}(s) T_e(s) \hat{N}'(s) \mid_0^{s_0} = \varphi_k^{(1)}(s_0) T_e(s_0) \hat{N}'(s_0) - \cancelto{0}{\varphi_k^{(1)}(0) T_e(0) \hat{N}'(0)} = \varphi_k^{(1)}(s_0) T_e(s_0) \hat{N}'(s_0),$$

thus:

$$\int_{s_{j-1}}^{s_j} \varphi_k^{(1)}(s) \frac{d}{ds}[T_e \hat{N}'(s)] ds = \varphi_k^{(1)}(s_0) T_e(s_0) \hat{N}'(s_0) - \int_{s_{j-1}}^{s_j} \varphi_k^{\prime(1)}(s) T_e(s) \hat{N}'(s) ds. \quad \text{(A.1)}$$

It should be noted that the manipulation of the tension term in the horizontal variable $\hat{X}(s)$ will be the same.

A.1.2 Bending term

In this case, the application of the Weighted Residual Method to the bending term of Eq.(4.81) will be different for the displacements and for the rotations:

- ***Displacement***: Analyzing only the integral (not the complete term with EI, which will be added later):

$$\int_{s_{j-1}}^{s_j} \varphi_{k,d}^{(3)}(s)\hat{N}^{IV}(s)ds = \varphi_{k,d}^{(3)}(s)\hat{N}'''(s) \mid_0^{s_0} - \int_{s_{j-1}}^{s_j} \varphi_{k,d}^{'(3)}(s)\hat{N}'''(s)ds.$$

As in the case of the tension, the first term is:

$$\varphi_{k,d}^{(3)}(s)\hat{N}'''(s) \mid_0^{s_0} = \varphi_{k,d}^{(3)}(s_0)\hat{N}'''(s_0) - \cancelto{0}{\varphi_{k,d}^{(3)}(0)\hat{N}'''(0)} = \varphi_{k,d}^{(3)}(s_0)\hat{N}'''(s_0).$$

And the resulting integral is analyzed in a similar way:

$$-\int_{s_{j-1}}^{s_j} \varphi_{k,d}^{'(3)}(s)\hat{N}'''(s)ds = -\varphi_{k,d}^{'(3)}(s)\hat{N}''(s) \mid_0^{s_0} + \int_{s_{j-1}}^{s_j} \varphi_{k,d}^{''(3)}(s)\hat{N}''(s)ds.$$

And again, with the use of the boundary conditions presented in Table 4.1, the first term is:

$$-\varphi_{k,d}^{'(3)}(s)\hat{N}''(s) \mid_0^{s_0} = -\cancelto{0}{\varphi_{k,d}^{'(3)}(s_0)}\hat{N}''(s_0) + \cancelto{0}{\varphi_{k,d}^{''(3)}(0)}\hat{N}''(0) = 0.$$

Thus, with all the terms together:

$$-EI\int_{s_{j-1}}^{s_j} \varphi_{k,d}^{(3)}(s)\hat{N}^{IV}(s)ds = -EI\left(\int_{s_{j-1}}^{s_j} \varphi_{k,d}^{''(3)}(s)\hat{N}''(s)ds + \varphi_{k,d}^{(3)}(s_0)\hat{N}'''(s_0)\right). \tag{A.2}$$

- ***Rotation***: In a similar manner to the previous integrals:

$$\int_{s_{j-1}}^{s_j} \varphi_{k,r}^{(3)}(s)\hat{N}^{IV}(s)ds = \varphi_{k,r}^{(3)}(s)\hat{N}'''(s) \mid_0^{s_0} - \int_{s_{j-1}}^{s_j} \varphi_{k,r}^{'(3)}(s)\hat{N}'''(s)ds.$$

In this case, the first term is:

$$\varphi_{k,r}^{(3)}(s)\hat{N}'''(s) \mid_0^{s_0} = \cancelto{0}{\varphi_{k,r}^{(3)}(s_0)}\hat{N}'''(s_0) - \cancelto{0}{\varphi_{k,r}^{(3)}(0)}\hat{N}'''(0) = 0.$$

And, again, the resultant integral is analyzed in a similar way:

$$-\int_{s_{j-1}}^{s_j} \varphi_{k,r}^{'(3)}(s)\hat{N}'''(s)ds = -\varphi_{k,r}^{'(3)}(s)\hat{N}''(s) \mid_0^{s_0} + \int_{s_{j-1}}^{s_j} \varphi_{k,r}^{''(3)}(s)\hat{N}''(s)ds.$$

With the use of the boundary conditions presented in Table 4.1:

$$-\varphi_{k,r}^{'(3)}(s)\hat{N}''(s) \mid_0^{s_0} = -\varphi_{k,r}^{'(3)}(s_0)\hat{N}''(s_0) + \cancelto{0}{\varphi_{k,r}^{''(3)}(0)}\hat{N}''(0) = -\varphi_{k,r}^{'(3)}(s_0)\hat{N}''(s_0).$$

Thus, with all the terms together:

$$-EI\int_{s_{j-1}}^{s_j} \varphi_{k,r}^{(3)}(s)\hat{N}^{IV}(s)ds = -EI\left(\int_{s_{j-1}}^{s_j} \varphi_{k,r}^{''(3)}(s)\hat{N}''(s)ds - \varphi_{k,r}^{'(3)}(s_0)\hat{N}''(s_0)\right). \tag{A.3}$$

A.1.3 Horizontal and vertical discretized equations

The application of the Weighted Residual Method to the horizontal and vertical dynamic equations Eqs.(4.75) and (4.76) yields:

$$
\begin{aligned}
&- \lambda^2 \rho_H \int_{s_j}^{s_{j+1}} \varphi_k^{(1)}(s)\hat{X}(s)ds - \lambda c \int_{s_j}^{s_{j+1}} \varphi_k^{(1)}(s)\hat{X}(s)ds + \frac{\lambda}{U_\infty}\int_{s_j}^{s_{j+1}} \varphi_k^{(1)}(s)\hat{N}(s)\left.\frac{dq}{d\alpha}\right|_{\alpha_e}(s)ds \\
&+ \int_{s_j}^{s_{j+1}} \varphi_k^{(1)}(s)\hat{N}'(s)\left.\frac{dq}{d\alpha}\right|_{\alpha_e}(s)ds - \int_{s_j}^{s_{j+1}} \varphi_k^{'(1)}(s)T_e(s)\hat{X}'(s)ds \\
&+ \varphi_{N_s}^{(1)}(s)\left[\cancel{T_e(s_0)\hat{X}'(s_0)} - \cancel{T_e(s_0)\hat{X}'(s_0)}\right] = 0, \qquad \text{(A.4)}
\end{aligned}
$$

$$
\begin{aligned}
&- \lambda^2 \rho_H \int_{s_j}^{s_{j+1}} \varphi_k^{(1)}(s)\hat{N}(s)ds - \lambda c \int_{s_j}^{s_{j+1}} \varphi_k^{(1)}(s)\hat{N}(s)ds - \frac{\lambda}{U_\infty}\int_{s_j}^{s_{j+1}} \varphi_k^{(1)}(s)\hat{N}(s)\left.\frac{dp}{d\alpha}\right|_{\alpha_e}(s)ds \\
&- \int_{s_j}^{s_{j+1}} \varphi_k^{(1)}(s)\hat{N}'(s)\left.\frac{dp}{d\alpha}\right|_{\alpha_e}(s)ds - \int_{s_j}^{s_{j+1}} \varphi_k^{'(1)}(s)T_e(s)\hat{N}'(s)ds - EI\int_{s_j}^{s_{j+1}} \varphi_{k,d}^{''(3)}(s)\hat{N}''(s)ds \\
&- EI\int_{s_j}^{s_{j+1}} \varphi_{k,r}^{''(3)}(s)\hat{N}''(s)ds + \varphi_k^{(1)}(s_0)\left[-\lambda^2\frac{W}{g}\hat{N}(s_0) + \cancel{T_e(s_0)\hat{N}'(s_0)} - \cancel{T_e(s_0)\hat{N}'(s_0)}\right] \\
&+ \varphi_{N_s,d}^{(3)}(s)[-EI\cdot\hat{N}'''(s_0) - EI\cdot\hat{N}'''(s_0)] + \cancel{\varphi_{N_s,g}^{(3)}(s)\cdot EI\hat{N}''(s_0)}^{\,0} + \\
&\varphi_{N_s,d}^{'(3)}(s)[EI\cdot\hat{N}''(s_0)] = 0. \qquad \text{(A.5)}
\end{aligned}
$$

Eqs.(A.4) and (A.5) can be rewritten as:

$$
\begin{aligned}
&- \lambda^2 \rho_H \int_{s_j}^{s_{j+1}} \varphi_k^{(1)}(s)\hat{X}(s)ds - \lambda c \int_{s_j}^{s_{j+1}} \varphi_k^{(1)}(s)\hat{X}(s)ds + \frac{\lambda}{U_\infty}\int_{s_j}^{s_{j+1}} \varphi_k^{(1)}(s)\hat{N}(s)\left.\frac{dq}{d\alpha}\right|_{\alpha_e}(s)ds \\
&+ \int_{s_j}^{s_{j+1}} \varphi_k^{(1)}(s)\hat{N}'(s)\left.\frac{dq}{d\alpha}\right|_{\alpha_e}(s)ds - \int_{s_j}^{s_{j+1}} \varphi_k^{'(1)}(s)T_e(s)\hat{X}'(s)ds = 0, \qquad \text{(A.6)}
\end{aligned}
$$

$$
\begin{aligned}
&- \lambda^2 \rho_H \int_{s_j}^{s_{j+1}} \varphi_k^{(1)}(s)\hat{N}(s)ds - \lambda c \int_{s_j}^{s_{j+1}} \varphi_k^{(1)}(s)\hat{N}(s)ds - \frac{\lambda}{U_\infty}\int_{s_j}^{s_{j+1}} \varphi_k^{(1)}(s)\hat{N}(s)\left.\frac{dp}{d\alpha}\right|_{\alpha_e}(s)ds \\
&- \int_{s_j}^{s_{j+1}} \varphi_k^{(1)}(s)\hat{N}'(s)\left.\frac{dp}{d\alpha}\right|_{\alpha_e}(s)ds - \int_{s_j}^{s_{j+1}} \varphi_k^{'(1)}(s)T_e(s)\hat{N}'(s)ds - EI\int_{s_j}^{s_{j+1}} \varphi_{k,d}^{''(3)}(s)\hat{N}''(s)ds \\
&- EI\int_{s_j}^{s_{j+1}} \varphi_{k,r}^{''(3)}(s)\hat{N}''(s)ds - \varphi_k^{(1)}(s_0)\lambda^2\frac{W}{g}\hat{N}(s_0) - 2EI\varphi_{N_s,d}^{(3)}(s)\cdot\hat{N}'''(s_0) \\
&+ EI\varphi_{N_s,d}^{'(3)}(s)\cdot\hat{N}''(s_0) = 0. \qquad \text{(A.7)}
\end{aligned}
$$

And by approaching $\hat{X}(s)$ and $\hat{N}(s)$ (and their respective derivatives) with the different form functions:

$$-\lambda^2\rho_H\int_{s_j}^{s_{j+1}}\varphi_k^{(1)}(s)\cdot v_j\cdot\varphi_j^{(1)}(s)ds-\lambda c\int_{s_j}^{s_{j+1}}\varphi_k^{(1)}(s)\cdot v_j\cdot\varphi_j^{(1)}(s)ds+$$

$$\frac{\lambda}{U_\infty}\int_{s_j}^{s_{j+1}}\varphi_k^{(1)}(s)\cdot w_j\cdot\varphi_j^{(1)}(s)\left.\frac{dq}{d\alpha}\right|_{\alpha_e}(s)ds+\int_{s_j}^{s_{j+1}}\varphi_k^{(1)}(s)\cdot w_j\cdot\varphi_j^{'(1)}(s)\left.\frac{dq}{d\alpha}\right|_{\alpha_e}(s)ds$$

$$-\int_{s_j}^{s_{j+1}}\varphi_k^{'(1)}(s)\cdot T_e(s)\cdot v_j\cdot\varphi_j^{'(1)}(s)ds=0, \tag{A.8}$$

$$-\lambda^2\rho_H\int_{s_j}^{s_{j+1}}\varphi_k^{(1)}(s)\cdot w_j\cdot\varphi_j^{(1)}(s)ds-\lambda c\int_{s_j}^{s_{j+1}}\varphi_k^{(1)}(s)\cdot w_j\cdot\varphi_j^{(1)}(s)ds-$$

$$\frac{\lambda}{U_\infty}\int_{s_j}^{s_{j+1}}\varphi_k^{(1)}(s)\cdot w_j\cdot\varphi_j^{(1)}(s)\left.\frac{dp}{d\alpha}\right|_{\alpha_e}(s)ds-\int_{s_j}^{s_{j+1}}\varphi_k^{(1)}(s)\cdot w_j\cdot\varphi_j^{'(1)}(s)\left.\frac{dp}{d\alpha}\right|_{\alpha_e}(s)ds-$$

$$\int_{s_j}^{s_{j+1}}\varphi_k^{'(1)}(s)T_e(s)\cdot w_j\cdot\varphi_j^{(1)}(s)ds-EI\int_{s_j}^{s_{j+1}}\varphi_{k,d}^{''(3)}(s)\cdot w_j\cdot\varphi_{j,d}^{''(3)}(s)ds-$$

$$EI\int_{s_j}^{s_{j+1}}\varphi_{k,r}^{''(3)}(s)\hat{N}''(s)ds-\varphi_{N_s}^{(1)}(s)\cdot\lambda^2\frac{W}{g}\cdot w_{N_s+1}\cdot\varphi_{N_s}^{(1)}(s)-$$

$$2EI\varphi_{N_s,d}^{'(3)}(s)\cdot w_{N_s+1}\cdot\varphi_{N_s,d}^{''(3)}(s)+EI\varphi_{N_s,d}^{'(3)}(s)\cdot w_{N_s+1}\cdot\varphi_{N_s,d}^{''(3)}(s)=0. \tag{A.9}$$

It is important to mention that in the bending terms of Eq.(A.9), as will be presented below, only the part related to the displacements appear.

A.2 Inertia matrix

Both $\hat{X}(s)$ and $\hat{N}(s)$ are approximated by the linear form functions. Therefore, the expressions for the inertia matrix are:

$$M_{i,i}^{xx}=M_{i,i}^{yy}=-\rho_H\int_{s_{i-1}}^{s_i}\varphi_i^{(1)^2}(s)\cdot ds-\rho_H\int_{s_i}^{s_{i+1}}\varphi_i^{(1)^2}(s)\cdot ds, \tag{A.10}$$

$$M_{i,i-1}^{xx}=M_{i,i-1}^{yy}=-\rho_H\int_{s_{i-1}}^{s_i}\varphi_i^{(1)}(s)\cdot\varphi_{i-1}^{(1)}(s)\cdot ds, \tag{A.11}$$

$$M_{i,i-1}^{xx}=M_{i,i+1}^{yy}=-\rho_H\int_{s_i}^{s_{i+1}}\varphi_i^{(1)}(s)\cdot\varphi_{i+1}^{(1)}(s)\cdot ds, \tag{A.12}$$

$$M_{N_s,N_s}^{xx}=-\rho_H\int_{s_{N_s-1}}^{s_{N_s}}\varphi_{N_s}^{(1)^2}(s)\cdot ds. \tag{A.13}$$

$$M_{N_s,N_s}^{yy}=-\rho_H\int_{s_{N_s-1}}^{s_{N_s}}\varphi_{N_s}^{(1)^2}(s)\cdot ds-\frac{W}{g}. \tag{A.14}$$

As can be seen in Eqs.(A.10)-(A.14), all the inertia matrix terms along the hose are identical for the horizontal and the vertical motion except Eq.(A.14), which represent the last node (where in the vertical motion the drogue weight effect must be included).

A.3 Damping matrix

The terms of the sub-matrices are here developed. Starting with $\boldsymbol{B^{xx}}$:

$$B^{xx}_{i,i} = -c\int_{s_{i-1}}^{s_i} \varphi_i^{(1)^2}(s)\cdot ds - c\int_{s_i}^{s_{i+1}} \varphi_i^{(1)^2}(s)\cdot ds, \tag{A.15}$$

$$B^{xx}_{i,i-1} = -c\int_{s_{i-1}}^{s_i} \varphi_i^{(1)}(s)\cdot \varphi_{i-1}^{(1)}(s)\cdot ds, \tag{A.16}$$

$$B^{xx}_{i,i-1} = -c\int_{s_i}^{s_{i+1}} \varphi_i^{(1)}(s)\cdot \varphi_{i+1}^{(1)}(s)\cdot ds, \tag{A.17}$$

$$B^{xx}_{N_s,N_s} = -c\int_{s_{N_s-1}}^{s_{N_s}} \varphi_{N_s}^{(1)^2}(s)\cdot ds. \tag{A.18}$$

As seen in Eqs.(A.15)-(A.18), in $\boldsymbol{B^{xx}}$ the only source of damping is structural. In contrast, for the coupled sub-matrix $\boldsymbol{B^{xy}}$ the only damping source is aerodynamic:

$$B^{xy}_{i,i} = \frac{1}{U_\infty}\int_{s_{i-1}}^{s_i} \varphi_i^{(1)^2}(s)\cdot \left.\frac{dq}{d\alpha}\right|_{\alpha_e}(s)\cdot ds + \frac{1}{U_\infty}\int_{s_i}^{s_{i+1}} \varphi_i^{(1)^2}(s)\cdot \left.\frac{dq}{d\alpha}\right|_{\alpha_e}(s)\cdot ds, \tag{A.19}$$

$$B^{xy}_{i,i-1} = \frac{1}{U_\infty}\int_{s_{i-1}}^{s_i} \varphi_i^{(1)}(s)\cdot \varphi_{i-1}^{(1)}(s)\cdot \left.\frac{dq}{d\alpha}\right|_{\alpha_e}(s)\cdot ds, \tag{A.20}$$

$$B^{xy}_{i,i+1} = \frac{1}{U_\infty}\int_{s_i}^{s_{i+1}} \varphi_i^{(1)}(s)\cdot \varphi_{i+1}^{(1)}(s)\cdot \left.\frac{dq}{d\alpha}\right|_{\alpha_e}(s)\cdot ds, \tag{A.21}$$

$$B^{xy}_{N_s,N_s} = \frac{1}{U_\infty}\int_{s_{N_s-1}}^{s_{N_s}} \varphi_{N_s}^{(1)^2}(s)\cdot \left.\frac{dq}{d\alpha}\right|_{\alpha_e}(s)\cdot ds. \tag{A.22}$$

Finally, the expressions for $\boldsymbol{B^{yy}}$ will be presented. In this sub-matrix both sources of damping (structural and aerodynamic) will appear:

$$B^{yy}_{i,i} = -c\int_{s_{i-1}}^{s_i} \varphi_i^{(1)^2}(s)\cdot ds - c\int_{s_i}^{s_{i+1}} \varphi_i^{(1)^2}(s)\cdot ds,$$

$$-\frac{1}{U_\infty}\int_{s_{i-1}}^{s_i} \varphi_i^{(1)^2}(s)\cdot \left.\frac{dp}{d\alpha}\right|_{\alpha_e}(s)\cdot ds - \frac{1}{U_\infty}\int_{s_i}^{s_{i+1}} \varphi_i^{(1)^2}(s)\cdot \left.\frac{dp}{d\alpha}\right|_{\alpha_e}(s)\cdot ds, \tag{A.23}$$

$$B^{yy}_{i,i-1} = -c\int_{s_{i-1}}^{s_i} \varphi_i^{(1)}(s)\cdot \varphi_{i-1}^{(1)}(s)\cdot ds - \frac{1}{U_\infty}\int_{s_{i-1}}^{s_i} \varphi_i^{(1)}(s)\cdot \varphi_{i-1}^{(1)}(s)\cdot \left.\frac{dp}{d\alpha}\right|_{\alpha_e}(s)\cdot ds, \tag{A.24}$$

$$B^{yy}_{i,i+1} = -c\int_{s_i}^{s_{i+1}} \varphi_i^{(1)}(s)\cdot\varphi_{i+1}^{(1)}(s)\cdot ds - \frac{1}{U_\infty}\int_{s_i}^{s_{i+1}} \varphi_i^{(1)}(s)\cdot\varphi_{i+1}^{(1)}(s)\cdot \left.\frac{dp}{d\alpha}\right|_{\alpha_e}(s)\cdot ds, \tag{A.25}$$

$$B^{yy}_{N_s,N_s} = -c\int_{s_{N_s-1}}^{s_{N_s}} \varphi_{N_s}^{(1)^2}(s)\cdot ds - \frac{1}{U_\infty}\int_{s_{N_s-1}}^{s_{N_s}} \varphi_{N_s}^{(1)^2}(s)\cdot \left.\frac{dp}{d\alpha}\right|_{\alpha_e}(s)\cdot ds. \tag{A.26}$$

A.4 Stiffness matrix

Starting with the horizontal sub-matrix $\boldsymbol{K^{xx}}$, as observed in Eqs.(A.6) and (A.7) it has only one contribution: the terms associated to the tension of the hose (last term of Eq.(4.75)):

$$K^{xx}_{i,i} = -\int_{s_{i-1}}^{s_i} T_e(s)\cdot\varphi_i^{'(1)^2}(s)\cdot ds - \int_{s_i}^{s_{i+1}} T_e(s)\cdot\varphi_i^{'(1)^2}(s)\cdot ds, \tag{A.27}$$

$$K^{xx}_{i,i-1} = -\int_{s_{i-1}}^{s_i} T_e(s)\cdot\varphi_i^{'(1)}(s)\cdot\varphi_{i-1}^{'(1)}(s)\cdot ds, \tag{A.28}$$

$$K^{xx}_{i,i+1} = -\int_{s_i}^{s_{i+1}} T_e(s)\cdot\varphi_i^{'(1)}(s)\cdot\varphi_{i+1}^{'(1)}(s)\cdot ds, \tag{A.29}$$

$$K^{xx}_{N_s,N_s} = -\int_{s_{N_s-1}}^{s_{N_s}} T_e(s)\cdot\varphi_{N_s}^{'(1)^2}(s)\cdot ds. \tag{A.30}$$

Regarding the coupling between horizontal and the vertical motion, the stiffness sub-matrix $\boldsymbol{K^{xy}}$, there is only one source of stiffness: the one due to the aerodynamic terms of Eqs.(A.6).

$$K^{xy}_{i,i} = \int_{s_{i-1}}^{s_i} \varphi_i^{(1)^2}(s)\cdot \left.\frac{dq}{d\alpha}\right|_{\alpha_e}(s)\cdot ds + \int_{s_i}^{s_{i+1}} \varphi_i^{(1)^2}(s)\cdot \left.\frac{dq}{d\alpha}\right|_{\alpha_e}(s)\cdot ds, \tag{A.31}$$

$$K^{xy}_{i,i-1} = \int_{s_{i-1}}^{s_i} \varphi_i^{(1)}(s)\cdot\varphi_{i-1}^{(1)}(s)\cdot \left.\frac{dq}{d\alpha}\right|_{\alpha_e}(s)\cdot ds, \tag{A.32}$$

$$K^{xy}_{i,i+1} = \int_{s_i}^{s_{i+1}} \varphi_i^{(1)}(s)\cdot\varphi_{i+1}^{(1)}(s)\cdot \left.\frac{dq}{d\alpha}\right|_{\alpha_e}(s)\cdot ds, \tag{A.33}$$

$$K^{xy}_{N_s,N_s} = \int_{s_{N_s-1}}^{s_{N_s}} \varphi_{N_s}^{(1)^2}(s)\cdot \left.\frac{dq}{d\alpha}\right|_{\alpha_e}(s)\cdot ds. \tag{A.34}$$

Concerning $\boldsymbol{K^{yy}}$, as can be seen in Eq.(A.7) it has three contributions: one associated with the tension of the hose (fifth term of Eq.(A.7)), another associated with the aerodynamic stiffness (third term of Eq.(A.7)) and the last one associated to the bending stiffness (last term of Eq.(A.7)). In order to clarify the different terms, the sub-matrix will be divided as follows:

$$\boldsymbol{K^{yy}} = \boldsymbol{K^{yy,T}} + \boldsymbol{K^{yy,A}} + \boldsymbol{K^{yy,B}}, \tag{A.35}$$

where the super-index T denotes tension, A aerodynamic and B bending. Starting with the tension, analogous expressions to Eqs.(A.27)-(A.30) are achieved:

$$K_{i,i}^{yy,T} = -\int_{s_{i-1}}^{s_i} T_e(s)\cdot \varphi_i^{'(1)^2}(s)\cdot ds - \int_{s_i}^{s_{i+1}} T_e(s)\cdot \varphi_i^{'(1)^2}(s)\cdot ds, \tag{A.36}$$

$$K_{i,i-1}^{yy,T} = -\int_{s_{i-1}}^{s_i} T_e(s)\cdot \varphi_i^{'(1)}(s)\cdot \varphi_{i-1}^{'(1)}(s)\cdot ds, \tag{A.37}$$

$$K_{i,i+1}^{yy,T} = -\int_{s_i}^{s_{i+1}} T_e(s)\cdot \varphi_i^{'(1)}(s)\cdot \varphi_{i+1}^{'(1)}(s)\cdot ds, \tag{A.38}$$

$$K_{N_s,N_s}^{yy,T} = -\int_{s_{N_s-1}}^{s_{N_s}} T_e(s)\cdot \varphi_{N_s}^{'(1)^2}(s)\cdot ds. \tag{A.39}$$

With respect to the aerodynamic stiffness terms, we obtain:

$$K_{i,i}^{yy,A} = -\int_{s_{i-1}}^{s_i} \varphi_i^{(1)^2}(s)\cdot \left.\frac{dp}{d\alpha}\right|_{\alpha_e}(s)\cdot ds - \int_{s_i}^{s_{i+1}} \varphi_i^{(1)^2}(s)\cdot \left.\frac{dp}{d\alpha}\right|_{\alpha_e}(s)\cdot ds, \tag{A.40}$$

$$K_{i,i-1}^{yy,A} = -\int_{s_{i-1}}^{s_i} \varphi_i^{(1)}(s)\cdot \varphi_{i-1}^{(1)}(s)\cdot \left.\frac{dp}{d\alpha}\right|_{\alpha_e}(s)\cdot ds, \tag{A.41}$$

$$K_{i,i+1}^{yy,A} = -\int_{s_i}^{s_{i+1}} \varphi_i^{(1)}(s)\cdot \varphi_{i+1}^{(1)}(s)\cdot \left.\frac{dp}{d\alpha}\right|_{\alpha_e}(s)\cdot ds, \tag{A.42}$$

$$K_{N_s,N_s}^{yy,A} = -\int_{s_{N_s-1}}^{s_{N_s}} \varphi_{N_s}^{(1)^2}(s)\cdot \left.\frac{dp}{d\alpha}\right|_{\alpha_e}(s)\cdot ds. \tag{A.43}$$

Finally, to analyze the bending terms of the stiffness matrix $\boldsymbol{K^{yy,B}}$ it is important to remember that this matrix includes the degrees of freedom of displacement and rotation of each node of the hose, i.e., it is twice larger than the other two matrices. In order to be able to add them, it is necessary that the three matrices be of the same size. One option would be to fill the degrees of freedom of the rotations with zeros in $\boldsymbol{K^{yy,T}}$ and $\boldsymbol{K^{yy,A}}$. Another option, which will be the one adopted in this thesis, is to apply a Guyan Reduction [Guyan, 1965] in $\boldsymbol{K^{yy,B}}$. Following this procedure, the hose displacements are considered as the active coordinates a, while the hose rotations are the slave coordinates o. Defining the bending stiffness matrix as:

$$\boldsymbol{K^{yy,B}} = \begin{bmatrix} \boldsymbol{K_{aa}^{yy,B}} & \boldsymbol{K_{ao}^{yy,B}} \\ \boldsymbol{K_{oa}^{yy,B}} & \boldsymbol{K_{oo}^{yy,B}} \end{bmatrix}, \tag{A.44}$$

The Guyan Reduction gives:

$$\boldsymbol{\hat{K}^{yy,B}} = \boldsymbol{K_{aa}^{yy,B}} - \boldsymbol{K_{ao}^{yy,B}}\boldsymbol{K_{oo}^{yy,B^{-1}}}\boldsymbol{K_{oa}^{yy,B}} \tag{A.45}$$

The resulting reduced matrix $\boldsymbol{\hat{K}^{yy,B}}$ will be used in Eq.(A.35) instead of $\boldsymbol{K^{yy,B}}$.

The displacement and rotation contributions are:

$$K_{aa,i,i}^{yy,B} = -EI \int_{s_{i-1}}^{s_i} \varphi_{i,d}^{''(3)^2}(s) \cdot ds - EI \int_{s_i}^{s_{i+1}} \varphi_{i,d}^{''(3)^2}(s) \cdot ds, \tag{A.46}$$

$$K_{aa,i,i-1}^{yy,B} = -EI \int_{s_{i-1}}^{s_i} \varphi_{i,d}^{''(3)}(s) \cdot \varphi_{i-1,d}^{''(3)}(s) \cdot ds, \tag{A.47}$$

$$K_{aa,i,i+1}^{yy,B} = -EI \int_{s_i}^{s_{i+1}} \varphi_{i,d}^{''(3)}(s) \cdot \varphi_{i+1,d}^{''(3)}(s) \cdot ds, \tag{A.48}$$

$$K_{aa,N_s,N_s}^{yy,B} = -EI \int_{s_{N_s-1}}^{s_{N_s}} \varphi_{N_s,d}^{''(3)^2}(s) \cdot ds - 2EI \cdot \varphi_{N_s,d}^{(3)}(s_0) \cdot \varphi_{N_s,d}^{'''(3)}(s_0), \tag{A.49}$$

$$K_{oo,i,i}^{yy,B} = -EI \int_{s_{i-1}}^{s_i} \varphi_{i,r}^{''(3)^2}(s) \cdot ds - EI \int_{s_i}^{s_{i+1}} \varphi_{i,r}^{''(3)^2}(s) \cdot ds, \tag{A.50}$$

$$K_{oo,i,i-1}^{yy,B} = -EI \int_{s_{i-1}}^{s_i} \varphi_{i,r}^{''(3)}(s) \cdot \varphi_{i-1,r}^{''(3)}(s) \cdot ds, \tag{A.51}$$

$$K_{oo,i,i+1}^{yy,B} = -EI \int_{s_i}^{s_{i+1}} \varphi_{i,r}^{''(3)}(s) \cdot \varphi_{i+1,r}^{''(3)}(s) \cdot ds, \tag{A.52}$$

$$K_{oo,N_s,N_s}^{yy,B} = -EI \int_{s_{N_s-1}}^{s_{N_s}} \varphi_{N_s,r}^{''(3)^2}(s) \cdot ds + EI \cdot \varphi_{N_s,r}^{'(3)}(s_0) \cdot \varphi_{N_s,r}^{''(3)}(s_0). \tag{A.53}$$

And the cross sub-matrices $\boldsymbol{K_{ao}^{yy,B}}$ and $\boldsymbol{K_{oa}^{yy,B}}$ are obtained in the same way with their respective form functions:

$$K_{ao,i,i}^{yy,B} = -EI \int_{s_{i-1}}^{s_i} \varphi_{i,d}^{''(3)}(s) \cdot \varphi_{i,r}^{''(3)}(s) \cdot ds - EI \int_{s_i}^{s_{i+1}} \cdot \varphi_{i,d}^{''(3)}(s) \varphi_{i,r}^{''(3)}(s) \cdot ds, \tag{A.54}$$

$$K_{ao,i,i-1}^{yy,B} = -EI \int_{s_{i-1}}^{s_i} \varphi_{i,d}^{''(3)}(s) \cdot \varphi_{i-1,r}^{''(3)}(s) \cdot ds, \tag{A.55}$$

$$K_{ao,i,i+1}^{yy,B} = -EI \int_{s_i}^{s_{i+1}} \varphi_{i,d}^{''(3)}(s) \cdot \varphi_{i+1,r}^{''(3)}(s) \cdot ds, \tag{A.56}$$

$$K_{ao,N_s,N_s}^{yy,B} = -EI \int_{s_{N_s-1}}^{s_{N_s}} \varphi_{N_s,d}^{''(3)}(s) \cdot \varphi_{N_s,d}^{''(3)}(s) \cdot ds - 2EI \cdot \varphi_{N_s,d}^{(3)}(s_0) \cdot \varphi_{N_s,r}^{'''(3)}(s_0), \tag{A.57}$$

$$K_{oa,i,i}^{yy,B} = -EI \int_{s_{i-1}}^{s_i} \varphi_{i,r}^{''(3)}(s) \cdot \varphi_{i,d}^{''(3)}(s) \cdot ds - EI \int_{s_i}^{s_{i+1}} \varphi_{i,r}^{''(3)}(s) \cdot \varphi_{i,d}^{''(3)}(s) \cdot ds, \tag{A.58}$$

$$K_{oa,i,i-1}^{yy,B} = -EI \int_{s_{i-1}}^{s_i} \varphi_{i,r}^{''(3)}(s) \cdot \varphi_{i-1,d}^{''(3)}(s) \cdot ds, \tag{A.59}$$

$$K_{oa,i,i+1}^{yy,B} = -EI \int_{s_i}^{s_{i+1}} \varphi_{i,r}^{''(3)}(s) \cdot \varphi_{i+1,d}^{''(3)}(s) \cdot ds, \tag{A.60}$$

$$K_{oa,N_s,N_s}^{yy,B} = -EI \int_{s_{N_s-1}}^{s_{N_s}} \varphi_{N_s,r}^{''(3)}(s) \cdot \varphi_{N_s,d}^{''(3)}(s) \cdot ds + EI \cdot \varphi_{N_s,r}^{'(3)}(s_0) \cdot \varphi_{N_s,d}^{''(3)}(s_0). \tag{A.61}$$

Appendix B

Grid fins aerodynamic dataset

This appendix presents the complete development of the aerodynamic coefficients (lift, side force, and pitching moment) for the fins, including both the steady and unsteady components. Although many of the coefficients presented below have already been explained or even written in a more compact form during the development of Chapter 5, this appendix provides each of them in full, to serve as a reference in case there is a need to analyze any of the coefficients in detail.

B.1 Lift force coefficient

B.1.1 Steady coefficient

The steady lift force coefficients for each fin are:

$$C^F_{Le_1} = C_{L\alpha 1} \cdot \alpha^F_{e_1} \cdot \cos\beta^F_{e_1}, \tag{B.1}$$

$$C^F_{Le_2} = C_{L\alpha 2} \cdot \alpha^F_{e_2} \cdot \cos\beta^F_{e_2}, \tag{B.2}$$

$$C^F_{Le_3} = C_{L\alpha 1} \cdot \alpha^F_{e_3} \cdot \cos\beta^F_{e_3}, \tag{B.3}$$

$$C^F_{Le_4} = C_{L\alpha 2} \cdot \alpha^F_{e_4} \cdot \cos\beta^F_{e_4}, \tag{B.4}$$

and the total steady coefficient is:

$$C^F_{Le} = C_{L\alpha 1}\left(\hat{f}_{1L} \cdot \alpha^F_{e_1} \cdot \cos\beta^F_{e_1} + \hat{f}_{3L} \cdot \alpha^F_{e_3} \cdot \cos\beta^F_{e_3}\right) + C_{L\alpha 2}\left(\hat{f}_{2L} \cdot \alpha^F_{e_2} \cdot \cos\beta^F_{e_2} + \hat{f}_{4L} \cdot \alpha^F_{e_4} \cdot \cos\beta^F_{e_4}\right) \tag{B.5}$$

B.1.2 Unsteady coefficient

The unsteady lift force coefficients for each fin are:

$$\Delta C_{L1}^{F} = C_{L\alpha 1} \cdot \cos\beta_{e_1}^{F} \cdot \Delta\alpha_{1}^{F} - C_{L\alpha 1} \cdot \alpha_{e_1}^{F} \cdot \sin\beta_{e_1}^{F} \cdot \Delta\beta_{1}^{F}, \tag{B.6}$$

$$\Delta C_{L2}^{F} = C_{L\alpha 2} \cdot \cos\beta_{e_2}^{F} \cdot \Delta\alpha_{2}^{F} - C_{L\alpha 2} \cdot \alpha_{e_2}^{F} \cdot \sin\beta_{e_2}^{F} \cdot \Delta\beta_{2}^{F}, \tag{B.7}$$

$$\Delta C_{L3}^{F} = C_{L\alpha 1} \cdot \cos\beta_{e_3}^{F} \cdot \Delta\alpha_{3}^{F} - C_{L\alpha 1} \cdot \alpha_{e_3}^{F} \cdot \sin\beta_{e_3}^{F} \cdot \Delta\beta_{3}^{F}, \tag{B.8}$$

$$\Delta C_{L4}^{F} = C_{L\alpha 2} \cdot \cos\beta_{e_4}^{F} \cdot \Delta\alpha_{4}^{F} - C_{L\alpha 2} \cdot \alpha_{e_4}^{F} \cdot \sin\beta_{e_4}^{F} \cdot \Delta\beta_{4}^{F}, \tag{B.9}$$

and the total unsteady coefficient is:

$$\begin{aligned}\Delta C_{L}^{F} = {} & C_{L\alpha 1}\left[\hat{f}_{1L}\left(\cos\beta_{e_1}^{F} \cdot \Delta\alpha_{1}^{F} - \alpha_{e_1}^{F} \cdot \sin\beta_{e_1}^{F} \cdot \Delta\beta_{1}^{F}\right) + \hat{f}_{3L}\left(\cos\beta_{e_3}^{F} \cdot \Delta\alpha_{3}^{F} - \alpha_{e_3}^{F} \cdot \sin\beta_{e_3}^{F} \cdot \Delta\beta_{3}^{F}\right)\right] \\ & + C_{L\alpha 2}\left[\hat{f}_{2L}\left(\cos\beta_{e_2}^{F} \cdot \Delta\alpha_{2}^{F} - \alpha_{e_2}^{F} \cdot \sin\beta_{e_2}^{F} \cdot \Delta\beta_{2}^{F}\right) + \hat{f}_{4L}\left(\cos\beta_{e_4}^{F} \cdot \Delta\alpha_{4}^{F} - \alpha_{e_4}^{F} \cdot \sin\beta_{e_4}^{F} \cdot \Delta\beta_{4}^{F}\right)\right]\end{aligned} \tag{B.10}$$

B.2 Side force coefficient

B.2.1 Steady coefficient

The side force coefficients for each fin are:

$$C_{Ze_1}^{F} = C_{Z\beta 1} \cdot (-\beta_{e_1}^{F}) \cdot \cos\alpha_{e_1}^{F}, \tag{B.11}$$

$$C_{Ze_2}^{F} = C_{Z\beta 2} \cdot (-\beta_{e_2}^{F}) \cdot \cos\alpha_{e_2}^{F}, \tag{B.12}$$

$$C_{Ze_3}^{F} = C_{Z\beta 1} \cdot (-\beta_{e_3}^{F}) \cdot \cos\alpha_{e_3}^{F}, \tag{B.13}$$

$$C_{Ze_4}^{F} = C_{Z\beta 2} \cdot (-\beta_{e_4}^{F}) \cdot \cos\alpha_{e_4}^{F}, \tag{B.14}$$

and the total steady coefficient is:

$$C_{Ze}^{F} = -C_{Z\beta 1}\left(\hat{f}_{1Z} \cdot \beta_{e_1}^{F} \cdot \cos\alpha_{e_1}^{F} + \hat{f}_{3Z} \cdot \beta_{e_3}^{F} \cdot \cos\alpha_{e_3}^{F}\right) - C_{Z\beta 2}\left(\hat{f}_{2Z} \cdot \beta_{e_2}^{F} \cdot \cos\alpha_{e_2}^{F} + \hat{f}_{4Z} \cdot \beta_{e_4}^{F} \cdot \cos\alpha_{e_4}^{F}\right) \tag{B.15}$$

B.2.2 Unsteady coefficient

The unsteady side force coefficients for each fin are:

$$\Delta C_{Z1}^{F} = C_{Z\beta 1} \cdot \cos\alpha_{e_1}^{F} \cdot \Delta\beta_{1}^{F} + C_{Z\beta 1} \cdot \beta_{e_1}^{F} \cdot \sin\alpha_{e_1}^{F} \cdot \Delta\alpha_{1}^{F}, \tag{B.16}$$

$$\Delta C_{Z2}^{F} = C_{Z\beta 2} \cdot \cos\alpha_{e_2}^{F} \cdot \Delta\beta_{2}^{F} + C_{Z\beta 2} \cdot \beta_{e_2}^{F} \cdot \sin\alpha_{e_2}^{F} \cdot \Delta\alpha_{2}^{F}, \tag{B.17}$$

$$\Delta C_{Z3}^{F} = C_{Z\beta 1} \cdot \cos\alpha_{e_3}^{F} \cdot \Delta\beta_{3}^{F} + C_{Z\beta 1} \cdot \beta_{e_3}^{F} \cdot \sin\alpha_{e_3}^{F} \cdot \Delta\alpha_{3}^{F}, \tag{B.18}$$

$$\Delta C_{Z4}^{F} = C_{Z\beta 2} \cdot \cos\alpha_{e_4}^{F} \cdot \Delta\beta_{4}^{F} + C_{Z\beta 2} \cdot \beta_{e_4}^{F} \cdot \sin\alpha_{e_4}^{F} \cdot \Delta\alpha_{4}^{F}, \tag{B.19}$$

and the total unsteady coefficient is:

$$\Delta C_Z^F = C_{Z\beta 1}\left[\hat{f}_{1Z}\left(\cos\alpha_{e_1}^F\cdot\Delta\beta_1^F+\cdot\beta_{e_1}^F\cdot\sin\alpha_{e_1}^F\cdot\Delta\alpha_1^F\right)+\hat{f}_{3Z}\left(\cos\alpha_{e_3}^F\cdot\Delta\beta_3^F+\cdot\beta_{e_3}^F\cdot\sin\alpha_{e_3}^F\cdot\Delta\alpha_3^F\right)\right]+$$
$$C_{Z\beta 2}\left[\hat{f}_{2Z}\left(\cos\alpha_{e_2}^F\cdot\Delta\beta_2^F+\cdot\beta_{e_2}^F\cdot\sin\alpha_{e_2}^F\cdot\Delta\alpha_2^F\right)+\hat{f}_{4Z}\left(\cos\alpha_{e_4}^F\cdot\Delta\beta_4^F+\cdot\beta_{e_4}^F\cdot\sin\alpha_{e_4}^F\cdot\Delta\alpha_4^F\right)\right] \tag{B.20}$$

B.3 Pitching moment coefficient

B.3.1 Steady coefficient

The steady pitching moment coefficients for each fin are:

$$C_{Me_1}^F=\frac{r_{z1}}{a_f}\left(-\hat{f}_{1L}\cdot C_{L\alpha 1}\cdot\alpha_{e_1}^F\cdot\cos\beta_{e_1}^F\cdot\sin\alpha_{e_1}^F+C_{D1}^F\cdot\cos\alpha_{e_1}^F\right)+$$
$$\frac{x_{ref}}{a_f}\left(\hat{f}_{1L}\cdot C_{L\alpha 1}\cdot\alpha_{e_1}^F\cdot\cos\beta_{e_1}^F\cdot\cos\alpha_{e_1}^F+C_{D1}^F\cdot\sin\alpha_{e_1}^F\right), \tag{B.21}$$

$$C_{Me_2}^F=\frac{r_{z2}}{a_f}\left(-\hat{f}_{2L}\cdot C_{L\alpha 2}\cdot\alpha_{e_2}^F\cdot\cos\beta_{e_2}^F\cdot\sin\alpha_{e_2}^F+C_{D2}^F\cdot\cos\alpha_{e_2}^F\right)+$$
$$\frac{x_{ref}}{a_f}\left(\hat{f}_{2L}\cdot C_{L\alpha 2}\cdot\alpha_{e_2}^F\cdot\cos\beta_{e_2}^F\cdot\cos\alpha_{e_2}^F+C_{D2}^F\cdot\sin\alpha_{e_2}^F\right), \tag{B.22}$$

$$C_{Me_3}^F=\frac{r_{z3}}{a_f}\left(-\hat{f}_{3L}\cdot C_{L\alpha 1}\cdot\alpha_{e_3}^F\cdot\cos\beta_{e_3}^F\cdot\sin\alpha_{e_3}^F+C_{D3}^F\cdot\cos\alpha_{e_3}^F\right)+$$
$$\frac{x_{ref}}{a_f}\left(\hat{f}_{3L}\cdot C_{L\alpha 1}\cdot\alpha_{e_3}^F\cdot\cos\beta_{e_3}^F\cdot\cos\alpha_{e_3}^F+C_{D3}^F\cdot\sin\alpha_{e_3}^F\right), \tag{B.23}$$

$$C_{Me_4}^F=\frac{r_{z4}}{a_f}\left(-\hat{f}_{4L}\cdot C_{L\alpha 2}\cdot\alpha_{e_4}^F\cdot\cos\beta_{e_4}^F\cdot\sin\alpha_{e_4}^F+C_{D4}^F\cdot\cos\alpha_{e_4}^F\right)+$$
$$\frac{x_{ref}}{a_f}\left(\hat{f}_{4L}\cdot C_{L\alpha 2}\cdot\alpha_{e_4}^F\cdot\cos\beta_{e_4}^F\cdot\cos\alpha_{e_4}^F+C_{D4}^F\cdot\sin\alpha_{e_4}^F\right), \tag{B.24}$$

and the total steady pitching moment coefficient:

$$C_{Me}^F = \frac{r_{z1}}{a_f}\left(-\hat{f}_{1L}\cdot C_{L\alpha 1}\cdot \alpha_{e_1}^F\cdot\cos\beta_{e_1}^F\cdot\sin\alpha_{e_1}^F + C_{D1}^F\cdot\cos\alpha_{e_1}^F\right)+$$

$$\frac{r_{z2}}{a_f}\left(-\hat{f}_{2L}\cdot C_{L\alpha 2}\cdot \alpha_{e_2}^F\cdot\cos\beta_{e_2}^F\cdot\sin\alpha_{e_2}^F + C_{D2}^F\cdot\cos\alpha_{e_2}^F\right)+$$

$$\frac{r_{z3}}{a_f}\left(-\hat{f}_{3L}\cdot C_{L\alpha 1}\cdot \alpha_{e_3}^F\cdot\cos\beta_{e_3}^F\cdot\sin\alpha_{e_3}^F + C_{D3}^F\cdot\cos\alpha_{e_3}^F\right)+$$

$$\frac{r_{z4}}{a_f}\left(-\hat{f}_{4L}\cdot C_{L\alpha 2}\cdot \alpha_{e_4}^F\cdot\cos\beta_{e_4}^F\cdot\sin\alpha_{e_4}^F + C_{D4}^F\cdot\cos\alpha_{e_4}^F\right)+$$

$$\frac{x_{ref}}{a_f}\Big(\hat{f}_{1L}\cdot C_{L\alpha 1}\cdot \alpha_{e_1}^F\cdot\cos\beta_{e_1}^F\cdot\cos\alpha_{e_1}^F + C_{D1}^F\cdot\sin\alpha_{e_1}^F+$$

$$\hat{f}_{2L}\cdot C_{L\alpha 2}\cdot \alpha_{e_2}^F\cdot\cos\beta_{e_2}^F\cdot\cos\alpha_{e_2}^F + C_{D2}^F\cdot\sin\alpha_{e_2}^F+$$

$$\hat{f}_{3L}\cdot C_{L\alpha 1}\cdot \alpha_{e_3}^F\cdot\cos\beta_{e_3}^F\cdot\cos\alpha_{e_3}^F + C_{D3}^F\cdot\sin\alpha_{e_3}^F+$$

$$\hat{f}_{4L}\cdot C_{L\alpha 2}\cdot \alpha_{e_4}^F\cdot\cos\beta_{e_4}^F\cdot\cos\alpha_{e_4}^F + C_{D4}^F\cdot\sin\alpha_{e_4}^F\Big). \tag{B.25}$$

B.3.2 Unsteady coefficient

The unsteady pitching moment coefficient for each fin is:

$$\Delta C_{M1}^F = \frac{r_{z1}}{a_f}\Big[-\hat{f}_{1L}\cdot\sin\alpha_{e_1}^F\cdot C_{L\alpha 1}\cdot(\Delta\alpha_1^F\cos\beta_{e_1}^F - \alpha_{e_1}^F\Delta\beta_1^F\sin\beta_{e_1}^F)-$$

$$\hat{f}_{1L}\cdot C_{L\alpha 1}\cdot\alpha_{e_1}^F\cdot\cos\beta_{e_1}^F\cdot\cos\alpha_{e_1}^F\cdot\Delta\alpha_1^F - C_{De1}^F\cdot\sin\alpha_{e_1}^F\cdot\Delta\alpha_1^F\Big]+$$

$$\frac{x_{ref}}{a_f}\Big[\hat{f}_{1L}\cdot C_{L\alpha 1}\cdot\alpha_{e_1}^F\cdot\cos\beta_{e_1}^F\cdot\sin\alpha_{e_1}^F\cdot\Delta\alpha_1^F+$$

$$\hat{f}_{1L}\cdot\cos\alpha_{e_1}^F\cdot C_{L\alpha 1}\cdot(\Delta\alpha_1^F\cos\beta_{e_1}^F - \alpha_{e_1}^F\Delta\beta_1^F\sin\beta_{e_1}^F) + C_{De1}^F\cdot\cos\alpha_{e_1}^F\cdot\Delta\alpha_1^F\Big]. \tag{B.26}$$

$$\Delta C_{M2}^F = \frac{r_{z2}}{a_f}\Big[-\hat{f}_{2L}\cdot\sin\alpha_{e_2}^F\cdot C_{L\alpha 2}\cdot(\Delta\alpha_2^F\cos\beta_{e_2}^F - \alpha_{e_2}^F\Delta\beta_2^F\sin\beta_{e_2}^F)-$$

$$\hat{f}_{2L}\cdot C_{L\alpha 2}\cdot\alpha_{e_2}^F\cdot\cos\beta_{e_2}^F\cdot\cos\alpha_{e_2}^F\cdot\Delta\alpha_2^F - C_{De2}^F\cdot\sin\alpha_{e_2}^F\cdot\Delta\alpha_2^F\Big]+$$

$$\frac{x_{ref}}{a_f}\Big[\hat{f}_{2L}\cdot C_{L\alpha 2}\cdot\alpha_{e_2}^F\cdot\cos\beta_{e_2}^F\cdot\sin\alpha_{e_2}^F\cdot\Delta\alpha_2^F+$$

$$\hat{f}_{2L}\cdot\cos\alpha_{e_2}^F\cdot C_{L\alpha 2}\cdot(\Delta\alpha_2^F\cos\beta_{e_2}^F - \alpha_{e_2}^F\Delta\beta_2^F\sin\beta_{e_2}^F) + C_{De2}^F\cdot\cos\alpha_{e_2}^F\cdot\Delta\alpha_2^F\Big]. \tag{B.27}$$

$$\Delta C^F_{M3} = \frac{r_{z3}}{a_f}\Big[-\hat{f}_{3L}\cdot\sin\alpha^F_{e_3}\cdot C_{L\alpha 1}\cdot(\Delta\alpha^F_3\cos\beta^F_{e_3}-\alpha^F_{e_3}\Delta\beta^F_3\sin\beta^F_{e_3})-$$

$$\hat{f}_{3L}\cdot C_{L\alpha 1}\cdot\alpha^F_{e_3}\cdot\cos\beta^F_{e_3}\cdot\cos\alpha^F_{e_3}\cdot\Delta\alpha^F_3 - C^F_{De3}\cdot\sin\alpha^F_{e_3}\cdot\Delta\alpha^F_3\Big]+$$

$$\frac{x_{ref}}{a_f}\Big[\hat{f}_{3L}\cdot C_{L\alpha 1}\cdot\alpha^F_{e_3}\cdot\cos\beta^F_{e_3}\cdot\sin\alpha^F_{e_3}\cdot\Delta\alpha^F_3+$$

$$\hat{f}_{3L}\cdot\cos\alpha^F_{e_3}\cdot C_{L\alpha 1}\cdot(\Delta\alpha^F_3\cos\beta^F_{e_3}-\alpha^F_{e_3}\Delta\beta^F_3\sin\beta^F_{e_3})+C^F_{De3}\cdot\cos\alpha^F_{e_3}\cdot\Delta\alpha^F_3\Big]. \tag{B.28}$$

$$\Delta C^F_{M4} = \frac{r_{z4}}{a_f}\Big[-\hat{f}_{4L}\cdot\sin\alpha^F_{e_4}\cdot C_{L\alpha 2}\cdot(\Delta\alpha^F_4\cos\beta^F_{e_4}-\alpha^F_{e_4}\Delta\beta^F_4\sin\beta^F_{e_4})-$$

$$\hat{f}_{4L}\cdot C_{L\alpha 2}\cdot\alpha^F_{e_4}\cdot\cos\beta^F_{e_4}\cdot\cos\alpha^F_{e_4}\cdot\Delta\alpha^F_4 - C^F_{De4}\cdot\sin\alpha^F_{e_4}\cdot\Delta\alpha^F_4\Big]+$$

$$\frac{x_{ref}}{a_f}\Big[\hat{f}_{4L}\cdot C_{L\alpha 2}\cdot\alpha^F_{e_4}\cdot\cos\beta^F_{e_4}\cdot\sin\alpha^F_{e_4}\cdot\Delta\alpha^F_4+$$

$$\hat{f}_{4L}\cdot\cos\alpha^F_{e_4}\cdot C_{L\alpha 2}\cdot(\Delta\alpha^F_4\cos\beta^F_{e_4}-\alpha^F_{e_4}\Delta\beta^F_4\sin\beta^F_{e_4})+C^F_{De4}\cdot\cos\alpha^F_{e_4}\cdot\Delta\alpha^F_4\Big]. \tag{B.29}$$

And the total unsteady pitching moment coefficient is:

$$\Delta C^F_M = \frac{r_{z1}}{a_f}\Big[-\hat{f}_{1L}\cdot\sin\alpha^F_{e_1}\cdot C_{L\alpha 1}\cdot(\Delta\alpha^F_1\cos\beta^F_{e_1}-\alpha^F_{e_1}\Delta\beta^F_1\sin\beta^F_{e_1})-$$

$$\hat{f}_{1L}\cdot C_{L\alpha 1}\cdot\alpha^F_{e_1}\cdot\cos\beta^F_{e_1}\cdot\cos\alpha^F_{e_1}\cdot\Delta\alpha^F_1 - C^F_{De1}\cdot\sin\alpha^F_{e_1}\cdot\Delta\alpha^F_1\Big]+$$

$$\frac{r_{z2}}{a_f}\Big[-\hat{f}_{2L}\cdot\sin\alpha^F_{e_2}\cdot C_{L\alpha 2}\cdot(\Delta\alpha^F_2\cos\beta^F_{e_2}-\alpha^F_{e_2}\Delta\beta^F_2\sin\beta^F_{e_2})-$$

$$\hat{f}_{2L}\cdot C_{L\alpha 2}\cdot\alpha^F_{e_2}\cdot\cos\beta^F_{e_2}\cdot\cos\alpha^F_{e_2}\cdot\Delta\alpha^F_2 - C^F_{De2}\cdot\sin\alpha^F_{e_2}\cdot\Delta\alpha^F_2\Big]+$$

$$\frac{r_{z3}}{a_f}\Big[-\hat{f}_{3L}\cdot\sin\alpha^F_{e_3}\cdot C_{L\alpha 1}\cdot(\Delta\alpha^F_3\cos\beta^F_{e_3}-\alpha^F_{e_3}\Delta\beta^F_3\sin\beta^F_{e_3})-$$

$$\hat{f}_{3L}\cdot C_{L\alpha 1}\cdot\alpha^F_{e_3}\cdot\cos\beta^F_{e_3}\cdot\cos\alpha^F_{e_3}\cdot\Delta\alpha^F_3 - C^F_{De3}\cdot\sin\alpha^F_{e_3}\cdot\Delta\alpha^F_3\Big]+$$

$$\frac{r_{z4}}{a_f}\Big[-\hat{f}_{4L}\cdot\sin\alpha^F_{e_4}\cdot C_{L\alpha 2}\cdot(\Delta\alpha^F_4\cos\beta^F_{e_4}-\alpha^F_{e_4}\Delta\beta^F_4\sin\beta^F_{e_4})-$$

$$\hat{f}_{4L}\cdot C_{L\alpha 2}\cdot\alpha^F_{e_4}\cdot\cos\beta^F_{e_4}\cdot\cos\alpha^F_{e_4}\cdot\Delta\alpha^F_4 - C^F_{De4}\cdot\sin\alpha^F_{e_4}\cdot\Delta\alpha^F_4\Big]+$$

$$\frac{x_{ref}}{a_f}\Big[\hat{f}_{1L}\cdot C_{L\alpha 1}\cdot\alpha^F_{e_1}\cdot\cos\beta^F_{e_1}\cdot\sin\alpha^F_{e_1}\cdot\Delta\alpha^F_1+$$

$$\hat{f}_{1L}\cdot\cos\alpha^F_{e_1}\cdot C_{L\alpha 1}\cdot(\Delta\alpha^F_1\cos\beta^F_{e_1}-\alpha^F_{e_1}\Delta\beta^F_1\sin\beta^F_{e_1})+C^F_{De1}\cdot\cos\alpha^F_{e_1}\cdot\Delta\alpha^F_1+$$

$$\hat{f}_{2L}\cdot C_{L\alpha 2}\cdot\alpha^F_{e_2}\cdot\cos\beta^F_{e_2}\cdot\sin\alpha^F_{e_2}\cdot\Delta\alpha^F_2+$$

$$\hat{f}_{2L} \cdot \cos\alpha_{e_2}^F \cdot C_{L\alpha 2} \cdot (\Delta\alpha_2^F \cos\beta_{e_2}^F - \alpha_{e_2}^F \Delta\beta_2^F \sin\beta_{e_2}^F) + C_{De2}^F \cdot \cos\alpha_{e_2}^F \cdot \Delta\alpha_2^F +$$

$$\hat{f}_{3L} \cdot C_{L\alpha 1} \cdot \alpha_{e_3}^F \cdot \cos\beta_{e_3}^F \cdot \sin\alpha_{e_3}^F \cdot \Delta\alpha_3^F + .$$

$$\hat{f}_{3L} \cdot \cos\alpha_{e_3}^F \cdot C_{L\alpha 1} \cdot (\Delta\alpha_3^F \cos\beta_{e_3}^F - \alpha_{e_3}^F \Delta\beta_3^F \sin\beta_{e_3}^F) + C_{De3}^F \cdot \cos\alpha_{e_3}^F \cdot \Delta\alpha_3^F +$$

$$\hat{f}_{4L} \cdot C_{L\alpha 2} \cdot \alpha_{e_4}^F \cdot \cos\beta_{e_4}^F \cdot \sin\alpha_{e_4}^F \cdot \Delta\alpha_4^F + .$$

$$\hat{f}_{4L} \cdot \cos\alpha_{e_4}^F \cdot C_{L\alpha 2} \cdot (\Delta\alpha_4^F \cos\beta_{e_4}^F - \alpha_{e_4}^F \Delta\beta_4^F \sin\beta_{e_4}^F) + C_{De4}^F \cdot \cos\alpha_{e_4}^F \cdot \Delta\alpha_4^F \Big] . \tag{B.30}$$

B.3.3 Unsteady forces as a function of the fins angles

During the development of the aerodynamic coefficients, Eqs.(5.76)-(5.78) present the three unsteady coefficients as a function of the unsteady angles of attack and sideslip of each fin. This way of expressing the coefficients is of great interest for the subsequent development at Chapter 6, where the fin prototype is included in the complete hose-drogue system. Therefore, the different components of the unsteady coefficients expressed in this form are presented below.

Lift coefficient

$$\Delta C_{L\alpha_1} = C_{L\alpha 1} \cdot \cos\beta_{e_1}^F, \tag{B.31}$$

$$\Delta C_{L\beta_1} = C_{L\alpha 1} \cdot \alpha_{e_1}^F \cdot \sin\beta_{e_1}^F, \tag{B.32}$$

$$\Delta C_{L\alpha_2} = C_{L\alpha 2} \cdot \cos\beta_{e_2}^F, \tag{B.33}$$

$$\Delta C_{L\beta_2} = C_{L\alpha 2} \cdot \alpha_{e_2}^F \cdot \sin\beta_{e_2}^F, \tag{B.34}$$

$$\Delta C_{L\alpha_3} = C_{L\alpha 1} \cdot \cos\beta_{e_3}^F, \tag{B.35}$$

$$\Delta C_{L\beta_3} = C_{L\alpha 1} \cdot \alpha_{e_3}^F \cdot \sin\beta_{e_3}^F, \tag{B.36}$$

$$\Delta C_{L\alpha_4} = C_{L\alpha 2} \cdot \cos\beta_{e_4}^F, \tag{B.37}$$

$$\Delta C_{L\beta_4} = C_{L\alpha 2} \cdot \alpha_{e_4}^F \cdot \sin\beta_{e_4}^F. \tag{B.38}$$

Side force coefficient

$$\Delta C_{Z\alpha_1} = C_{Z\beta 1} \cdot \beta_{e_1}^F \cdot \sin\alpha_{e_1}^F, \tag{B.39}$$

$$\Delta C_{Z\beta_1} = C_{Z\beta 1} \cdot \cos\alpha_{e_1}^F, \tag{B.40}$$

$$\Delta C_{Z\alpha_2} = C_{Z\beta 2} \cdot \beta_{e_2}^F \cdot \sin\alpha_{e_2}^F, \tag{B.41}$$

$$\Delta C_{Z\beta_2} = C_{Z\beta 2} \cdot \cos\alpha_{e_2}^F, \tag{B.42}$$

$$\Delta C_{Z\alpha_3} = C_{Z\beta 1} \cdot \beta_{e_3}^F \cdot \sin\alpha_{e_3}^F, \tag{B.43}$$

$$\Delta C_{Z\beta_3} = C_{Z\beta 1} \cdot \cos\alpha_{e_3}^F, \tag{B.44}$$

$$\Delta C_{Z\alpha_4} = C_{Z\beta 2} \cdot \beta_{e_4}^F \cdot \sin\alpha_{e_4}^F, \tag{B.45}$$

$$\Delta C_{Z\beta_4} = C_{Z\beta 2} \cdot \cos\alpha_{e_4}^F. \tag{B.46}$$

Pitching moment coefficient

$$\Delta C_{M\alpha_1} = \frac{r_{z1}}{a_f}\left[-\hat{f}_{1L}\cdot\sin\alpha^F_{e_1}\cdot C_{L\alpha 1}\cdot\cos\beta^F_{e_1} - \hat{f}_{1L}\cdot C_{L\alpha 1}\cdot\alpha^F_{e_1}\cdot\cos\beta^F_{e_1}\cdot\cos\alpha^F_{e_1} - C^F_{De1}\cdot\sin\alpha^F_{e_1}\right]$$

$$+\frac{x_{ref}}{a_f}\left[\hat{f}_{1L}\cdot C_{L\alpha 1}\cdot\alpha^F_{e_1}\cdot\cos\beta^F_{e_1}\cdot\sin\alpha^F_{e_1} + \hat{f}_{1L}\cdot\cos\alpha^F_{e_1}\cdot C_{L\alpha 1}\cdot\cos\beta^F_{e_1} + C^F_{De1}\cdot\cos\alpha^F_{e_1}\right], \tag{B.47}$$

$$\Delta C_{M\beta_1} = \frac{r_{z1}}{a_f}\cdot\hat{f}_{1L}\cdot\sin\alpha^F_{e_1}\cdot C_{L\alpha 1}\cdot\alpha^F_{e_1}\cdot\sin\beta^F_{e_1} - \frac{x_{ref}}{a_f}\cdot\hat{f}_{1L}\cdot\cos\alpha^F_{e_1}\cdot C_{L\alpha 1}\cdot\alpha^F_{e_1}\sin\beta^F_{e_1}, \tag{B.48}$$

$$\Delta C_{M\alpha_2} = \frac{r_{z2}}{a_f}\left[-\hat{f}_{2L}\cdot\sin\alpha^F_{e_2}\cdot C_{L\alpha 2}\cdot\cos\beta^F_{e_2} - \hat{f}_{2L}\cdot C_{L\alpha 2}\cdot\alpha^F_{e_2}\cdot\cos\beta^F_{e_2}\cdot\cos\alpha^F_{e_2} - C^F_{De2}\cdot\sin\alpha^F_{e_2}\right]$$

$$+\frac{x_{ref}}{a_f}\left[\hat{f}_{2L}\cdot C_{L\alpha 2}\cdot\alpha^F_{e_2}\cdot\cos\beta^F_{e_2}\cdot\sin\alpha^F_{e_2} + \hat{f}_{2L}\cdot\cos\alpha^F_{e_2}\cdot C_{L\alpha 2}\cdot\cos\beta^F_{e_2} + C^F_{De2}\cdot\cos\alpha^F_{e_2}\right], \tag{B.49}$$

$$\Delta C_{M\beta_2} = \frac{r_{z2}}{a_f}\cdot\hat{f}_{2L}\cdot\sin\alpha^F_{e_2}\cdot C_{L\alpha 2}\cdot\alpha^F_{e_2}\cdot\sin\beta^F_{e_2} - \frac{x_{ref}}{a_f}\cdot\hat{f}_{2L}\cdot\cos\alpha^F_{e_2}\cdot C_{L\alpha 2}\cdot\alpha^F_{e_2}\sin\beta^F_{e_2}, \tag{B.50}$$

$$\Delta C_{M\alpha_3} = \frac{r_{z3}}{a_f}\left[-\hat{f}_{3L}\cdot\sin\alpha^F_{e_3}\cdot C_{L\alpha 1}\cdot\cos\beta^F_{e_3} - \hat{f}_{3L}\cdot C_{L\alpha 1}\cdot\alpha^F_{e_3}\cdot\cos\beta^F_{e_3}\cdot\cos\alpha^F_{e_3} - C^F_{De3}\cdot\sin\alpha^F_{e_3}\right]$$

$$+\frac{x_{ref}}{a_f}\left[\hat{f}_{3L}\cdot C_{L\alpha 1}\cdot\alpha^F_{e_3}\cdot\cos\beta^F_{e_3}\cdot\sin\alpha^F_{e_3} + \hat{f}_{3L}\cdot\cos\alpha^F_{e_3}\cdot C_{L\alpha 1}\cdot\cos\beta^F_{e_3} + C^F_{De3}\cdot\cos\alpha^F_{e_3}\right], \tag{B.51}$$

$$\Delta C_{M\beta_3} = \frac{r_{z3}}{a_f}\cdot\hat{f}_{3L}\cdot\sin\alpha^F_{e_3}\cdot C_{L\alpha 1}\cdot\alpha^F_{e_3}\cdot\sin\beta^F_{e_3} - \frac{x_{ref}}{a_f}\cdot\hat{f}_{3L}\cdot\cos\alpha^F_{e_3}\cdot C_{L\alpha 1}\cdot\alpha^F_{e_3}\sin\beta^F_{e_3}, \tag{B.52}$$

$$\Delta C_{M\alpha_4} = \frac{r_{z4}}{a_f}\left[-\hat{f}_{4L}\cdot\sin\alpha^F_{e_4}\cdot C_{L\alpha 2}\cdot\cos\beta^F_{e_4} - \hat{f}_{4L}\cdot C_{L\alpha 2}\cdot\alpha^F_{e_4}\cdot\cos\beta^F_{e_4}\cdot\cos\alpha^F_{e_4} - C^F_{De4}\cdot\sin\alpha^F_{e_4}\right]$$

$$+\frac{x_{ref}}{a_f}\left[\hat{f}_{4L}\cdot C_{L\alpha 2}\cdot\alpha^F_{e_4}\cdot\cos\beta^F_{e_4}\cdot\sin\alpha^F_{e_4} + \hat{f}_{4L}\cdot\cos\alpha^F_{e_4}\cdot C_{L\alpha 2}\cdot\cos\beta^F_{e_4} + C^F_{De4}\cdot\cos\alpha^F_{e_4}\right], \tag{B.53}$$

$$\Delta C_{M\beta_4} = \frac{r_{z4}}{a_f}\cdot\hat{f}_{4L}\cdot\sin\alpha^F_{e_4}\cdot C_{L\alpha 2}\cdot\alpha^F_{e_4}\cdot\sin\beta^F_{e_4} - \frac{x_{ref}}{a_f}\cdot\hat{f}_{4L}\cdot\cos\alpha^F_{e_4}\cdot C_{L\alpha 2}\cdot\alpha^F_{e_4}\sin\beta^F_{e_4}. \tag{B.54}$$

Appendix C

Development of the hose-drogue-fins model

C.1 Discretized equations

To obtain the dynamic equations of the system, the Weighted Residual Method is applied to the horizontal, vertical and lateral dynamic equations Eqs.(6.72) and (6.74) including their respective boundary conditions. Starting with the horizontal motion:

$$
\begin{aligned}
&- \lambda^2 \rho_H \int_{s_j}^{s_{j+1}} \varphi_k^{(1)}(s)\hat{X}(s)ds - \lambda c \int_{s_j}^{s_{j+1}} \varphi_k^{(1)}(s)\hat{X}(s)ds + \frac{\lambda}{U_\infty}\int_{s_j}^{s_{j+1}} \varphi_k^{(1)}(s)\hat{N}(s)\left.\frac{dq}{d\alpha}\right|_{\alpha_e}(s)ds \\
&+ \int_{s_j}^{s_{j+1}} \varphi_k^{(1)}(s)\hat{N}'(s)\left.\frac{dq}{d\alpha}\right|_{\alpha_e}(s)ds - \int_{s_j}^{s_{j+1}} \varphi_k^{'(1)}(s)T_e(s)\hat{X}'(s)ds + +\varphi_{N_s}^{(1)}(s)\left[\cancel{T_e(s_0)\hat{X}'(s_0)}\right. \\
&\left.- \cancel{T_e(s_0)\hat{X}'(s_0)}\right] + \varphi_{N_s}^{(1)}(s)\left[Z_{F_e}\hat{\Gamma}'(s_0) + \left.\frac{dz_e}{ds}\right|_{s_0}\cdot q_\infty S_{UGF}[\Delta Q_{Zx}\hat{X}'(s_0)\right. \\
&\left.+ \Delta Q_{Zy}\hat{N}'(s_0) + \Delta Q_{Zz}\hat{\Gamma}'(s_0)] + q_\infty S_{UGF} c_f \Delta Q_{Mx}\hat{X}'(s_0)\right] = 0,
\end{aligned}
\tag{C.1}
$$

applying the method next to the vertical motion:

$$
\begin{aligned}
&- \lambda^2 \rho_H \int_{s_j}^{s_{j+1}} \varphi_k^{(1)}(s)\hat{N}(s)ds - \lambda c \int_{s_j}^{s_{j+1}} \varphi_k^{(1)}(s)\hat{N}(s)ds - \frac{\lambda}{U_\infty}\int_{s_j}^{s_{j+1}} \varphi_k^{(1)}(s)\hat{N}(s)\left.\frac{dp}{d\alpha}\right|_{\alpha_e}(s)ds \\
&- \int_{s_j}^{s_{j+1}} \varphi_k^{(1)}(s)\hat{N}'(s)\left.\frac{dp}{d\alpha}\right|_{\alpha_e}(s)ds - \int_{s_j}^{s_{j+1}} \varphi_k^{'(1)}(s)T_e(s)\hat{N}'(s)ds - EI\int_{s_j}^{s_{j+1}} \varphi_{k,d}^{''(3)}(s)\hat{N}''(s)ds \\
&- EI\int_{s_j}^{s_{j+1}} \varphi_{k,r}^{''(3)}(s)\hat{N}''(s)ds + \varphi_{N_s}^{(1)}(s)\left[-\lambda^2\frac{W}{g}\hat{N}(s_0) + \cancel{T_e(s_0)\hat{N}'(s_0)} - \cancel{T_e(s_0)\hat{N}'(s_0)}\right] \\
&+ \varphi_{N_s,d}^{(3)}(s)[-EI\cdot\hat{N}'''(s_0) - EI\cdot\hat{N}'''(s_0)] + \cancel{\varphi_{N_s,r}^{(3)}(s)\cdot EI\hat{N}''(s_0)}^{\to 0} \\
&+ \varphi_{N_s,d}^{'(3)}(s)[EI\cdot\hat{N}''(s_0)] + \varphi_{N_s}^{(1)}(s)\left[q_\infty S_{UGF}[\Delta Q_{Lx}\hat{X}'(s_0) + \Delta Q_{Ly}\hat{N}'(s_0)\right. \\
&\left.+ \Delta Q_{Lz}\hat{\Gamma}'(s_0)] + q_\infty S_{UGF} c_f \Delta Q_{My}\hat{N}'(s_0)\right] = 0,
\end{aligned}
\tag{C.2}
$$

and finally to the lateral motion:

$$
\begin{aligned}
&- \lambda^2 \rho_H \int_{s_j}^{s_{j+1}} \varphi_k^{(1)}(s)\hat{\Gamma}(s)ds - \lambda c \int_{s_j}^{s_{j+1}} \varphi_k^{(1)}(s)\hat{\Gamma}(s)ds - \int_{s_j}^{s_{j+1}} \varphi_k^{'(1)}(s)T_e(s)\hat{\Gamma}'(s)ds \\
&+ \varphi_{N_s}^{(1)}(s)\left[\cancel{T_e(s_0)\hat{\Gamma}'(s_0)} + \cancel{T_e(s_0)\hat{\Gamma}'(s_0)}\right] + \varphi_{N_s}^{(1)}(s)\Big[D_{F_e}\hat{\Gamma}'(s_0) + q_\infty S_{UGF}[\Delta Q_{Zx}\hat{X}'(s_0) \\
&+ \Delta Q_{Zy}\hat{N}'(s_0) + \Delta Q_{Zz}\hat{\Gamma}'(s_0)] + q_\infty S_{UGF} c_f \Delta Q_{Mz}\hat{\Gamma}'(s_0)\Big] = 0, \qquad \text{(C.3)}
\end{aligned}
$$

where the bending term in the vertical motion and the tension term in all the motions were manipulated in a similar way to the model without grid fins, in order to avoid derivatives of higher order.

The next step is approaching $\hat{X}(s)$, $\hat{N}(s)$ and $\hat{\Gamma(s)}$ (and their respective derivatives) with the different form functions, obtaining the following equations: And by approaching $\hat{X}(s)$ and $\hat{N}(s)$ (and their respective derivatives) with the different form functions:

$$
\begin{aligned}
&- \lambda^2 \rho_H \int_{s_j}^{s_{j+1}} \varphi_k^{(1)}(s)\cdot v_j \cdot \varphi_j^{(1)}(s)ds - \lambda c \int_{s_j}^{s_{j+1}} \varphi_k^{(1)}(s)\cdot v_j \cdot \varphi_j^{(1)}(s)ds + \\
&\frac{\lambda}{U_\infty}\int_{s_j}^{s_{j+1}} \varphi_k^{(1)}(s)\cdot w_j \cdot \varphi_j^{(1)}(s)\left.\frac{dq}{d\alpha}\right|_{\alpha_e}(s)ds + \int_{s_j}^{s_{j+1}} \varphi_k^{(1)}(s)\cdot w_j \cdot \varphi_j^{'(1)}(s)\left.\frac{dq}{d\alpha}\right|_{\alpha_e}(s)ds \\
&- \int_{s_j}^{s_{j+1}} \varphi_k^{'(1)}(s)T_e(s)\cdot v_j \cdot \varphi_j^{'(1)}(s)ds + \varphi_{N_s}^{(1)}(s)\Big[Z_{F_e}\cdot z_{N_s+1}\cdot \varphi_{N_s}^{'(1)}(s) \\
&+ \left.\frac{dz_e}{ds}\right|_{s_0}\cdot q_\infty S_{UGF}[\Delta Q_{Zx}\cdot v_{N_s+1}\cdot \varphi_{N_s}^{'(1)}(s) + \Delta Q_{Zy}\cdot w_{N_s+1}\cdot \varphi_{N_s}^{'(1)}(s) + \Delta Q_{Zz}\cdot z_{N_s+1}\cdot \varphi_{N_s}^{'(1)}(s)] \\
&+ q_\infty S_{UGF} c_f \cdot \Delta Q_{Mx}\cdot v_{N_s+1}\cdot \varphi_{N_s}^{'(1)}(s)\Big] = 0. \qquad \text{(C.4)}
\end{aligned}
$$

$$
\begin{aligned}
&- \lambda^2 \rho_H \int_{s_j}^{s_{j+1}} \varphi_k^{(1)}(s)\cdot w_j \cdot \varphi_j^{(1)}(s)ds - \lambda c \int_{s_j}^{s_{j+1}} \varphi_k^{(1)}(s)\cdot w_j \cdot \varphi_j^{(1)}(s)ds - \\
&\frac{\lambda}{U_\infty}\int_{s_j}^{s_{j+1}} \varphi_k^{(1)}(s)\cdot w_j \cdot \varphi_j^{(1)}(s)\left.\frac{dp}{d\alpha}\right|_{\alpha_e}(s)ds - \int_{s_j}^{s_{j+1}} \varphi_k^{(1)}(s)\cdot w_j \cdot \varphi_j^{'(1)}(s)\left.\frac{dp}{d\alpha}\right|_{\alpha_e}(s)ds - \\
&\int_{s_j}^{s_{j+1}} \varphi_k^{'(1)}(s)T_e(s)\cdot w_j \cdot \varphi_j^{(1)}(s)ds - EI\int_{s_j}^{s_{j+1}} \varphi_{k,d}^{''(3)}(s)\cdot w_j \cdot \varphi_{j,d}^{''(3)}(s)ds - \\
&EI\int_{s_j}^{s_{j+1}} \varphi_{k,r}^{''(3)}(s)\hat{N}''(s)ds - \varphi_{N_s}^{(1)}(s)\lambda^2\frac{W}{g}\cdot w_j \cdot \varphi_{N_s}^{(1)}(s) \\
&- 2EI\varphi_{N_s,d}^{'(3)}(s)\cdot w_j \cdot \varphi_{N_s,d}^{''(3)}(s) + EI\varphi_{N_s,d}^{'(3)}(s)\cdot w_j \cdot \varphi_{N_s,d}^{''(3)}(s) \\
&+ \varphi_{N_s}^{(1)}(s)\Big[q_\infty S_{UGF}[\Delta Q_{Lx}\cdot v_{N_s+1}\cdot \varphi_{N_s}^{'(1)}(s) + \Delta Q_{Ly}\cdot w_{N_s+1}\cdot \varphi_{N_s}^{'(1)}(s) \\
&+ \Delta Q_{Lz}\cdot z_{N_s+1}\cdot \varphi_{N_s}^{'(1)}(s)] + q_\infty S_{UGF} c_f \cdot \Delta Q_{My}\cdot w_{N_s+1}\cdot \varphi_{N_s}^{'(1)}(s)\Big] = 0. \qquad \text{(C.5)}
\end{aligned}
$$

$$
\begin{aligned}
&- \lambda^2 \rho_H \int_{s_j}^{s_{j+1}} \varphi_k^{(1)}(s) \cdot z_j \cdot \varphi_j^{(1)}(s) ds - \lambda c \int_{s_j}^{s_{j+1}} \varphi_k^{(1)}(s) \cdot z_j \cdot \varphi_j^{(1)}(s) ds \\
&- \int_{s_j}^{s_{j+1}} \varphi_k^{'(1)}(s) T_e(s) \cdot z_j \cdot \varphi_j^{'(1)}(s) ds + \varphi_{N_s}^{(1)}(s) \Big[D_{F_e} \cdot z_{N_s+1} \cdot \varphi_{N_s}^{'(1)}(s) \\
&+ q_\infty S_{UGF} [\Delta Q_{Zx} \cdot v_{N_s+1} \cdot \varphi_{N_s}^{'(1)}(s) + \Delta Q_{Zy} \cdot w_{N_s+1} \cdot \varphi_{N_s}^{'(1)}(s) + \Delta Q_{Zz} \cdot z_{N_s+1} \cdot \varphi_{N_s}^{'(1)}(s)] \\
&+ q_\infty S_{UGF} c_f \Delta Q_{Mz} \cdot z_{N_s+1} \cdot \varphi_{N_s}^{'(1)}(s) \Big] = 0,
\end{aligned} \tag{C.6}
$$

C.2 Inertia matrix

For the terms related to λ^2, as shown in the previous equations, $\hat{X}(s)$, $\hat{N}(s)$ and $\hat{\Gamma}(s)$ are approximated by the linear form functions. Therefore, the expressions for the inertia matrix are:

$$
M_{i,i}^{xx} = M_{i,i}^{yy} = M_{i,i}^{zz} = -\rho_H \int_{s_{i-1}}^{s_i} \varphi_i^{(1)^2}(s) \cdot ds - \rho_H \int_{s_i}^{s_{i+1}} \varphi_i^{(1)^2}(s) \cdot ds, \tag{C.7}
$$

$$
M_{i,i-1}^{xx} = M_{i,i-1}^{yy} = M_{i,i-1}^{zz} = -\rho_H \int_{s_{i-1}}^{s_i} \varphi_i^{(1)}(s) \cdot \varphi_{i-1}^{(1)}(s) \cdot ds, \tag{C.8}
$$

$$
M_{i,i-1}^{xx} = M_{i,i+1}^{yy} = M_{i,i+1}^{zz} = -\rho_H \int_{s_i}^{s_{i+1}} \varphi_i^{(1)}(s) \cdot \varphi_{i+1}^{(1)}(s) \cdot ds, \tag{C.9}
$$

$$
M_{N_s,N_s}^{xx} = M_{N_s,N_s}^{zz} = -\rho_H \int_{s_{N_s-1}}^{s_{N_s}} \varphi_{N_s}^{(1)^2}(s) \cdot ds. \tag{C.10}
$$

$$
M_{N_s,N_s}^{yy} = -\rho_H \int_{s_{N_s-1}}^{s_{N_s}} \varphi_{N_s}^{(1)^2}(s) \cdot ds - \frac{W}{g}. \tag{C.11}
$$

C.3 Damping matrix

The terms of the sub-matrices are here developed. Starting with $\boldsymbol{B^{xx}}$ and $\boldsymbol{B^{zz}}$, we obtain identical results:

$$
B_{i,i}^{xx} = B_{i,i}^{zz} = -c \int_{s_{i-1}}^{s_i} \varphi_i^{(1)^2}(s) \cdot ds - c \int_{s_i}^{s_{i+1}} \varphi_i^{(1)^2}(s) \cdot ds, \tag{C.12}
$$

$$
B_{i,i-1}^{xx} = B_{i,i-1}^{zz} = -c \int_{s_{i-1}}^{s_i} \varphi_i^{(1)}(s) \cdot \varphi_{i-1}^{(1)}(s) \cdot ds, \tag{C.13}
$$

$$
B_{i,i+1}^{xx} = B_{i,i+1}^{zz} = -c \int_{s_i}^{s_{i+1}} \varphi_i^{(1)}(s) \cdot \varphi_{i+1}^{(1)}(s) \cdot ds, \tag{C.14}
$$

$$
B_{N_s,N_s}^{xx} = B_{N_s,N_s}^{zz} = -c \int_{s_{N_s-1}}^{s_{N_s}} \varphi_{N_s}^{(1)^2}(s) \cdot ds. \tag{C.15}
$$

As seen in Eqs.(C.12)-(C.15), in $\boldsymbol{B^{xx}}$ and $\boldsymbol{B^{zz}}$ the only source of damping is structural. In contrast, for the coupled sub-matrix between the horizontal and vertical motion $\boldsymbol{B^{xy}}$ the only

damping source is aerodynamic:

$$B_{i,i}^{xy} = \frac{1}{U_\infty}\int_{s_{i-1}}^{s_i} {\varphi_i^{(1)}}^2(s)\cdot\left.\frac{dq}{d\alpha}\right|_{\alpha_e}(s)\cdot ds + \frac{1}{U_\infty}\int_{s_i}^{s_{i+1}} {\varphi_i^{(1)}}^2(s)\cdot\left.\frac{dq}{d\alpha}\right|_{\alpha_e}(s)\cdot ds, \tag{C.16}$$

$$B_{i,i-1}^{xy} = \frac{1}{U_\infty}\int_{s_{i-1}}^{s_i} \varphi_i^{(1)}(s)\cdot\varphi_{i-1}^{(1)}(s)\cdot\left.\frac{dq}{d\alpha}\right|_{\alpha_e}(s)\cdot ds, \tag{C.17}$$

$$B_{i,i+1}^{xy} = \frac{1}{U_\infty}\int_{s_i}^{s_{i+1}} \varphi_i^{(1)}(s)\cdot\varphi_{i+1}^{(1)}(s)\cdot\left.\frac{dq}{d\alpha}\right|_{\alpha_e}(s)\cdot ds, \tag{C.18}$$

$$B_{N_s,N_s}^{xy} = \frac{1}{U_\infty}\int_{s_{N_s-1}}^{s_{N_s}} {\varphi_{N_s}^{(1)}}^2(s)\cdot\left.\frac{dq}{d\alpha}\right|_{\alpha_e}(s)\cdot ds. \tag{C.19}$$

Next, the expressions for $\boldsymbol{B^{yy}}$ will be presented. In this sub-matrix both sources of damping (structural and aerodynamic) will appear:

$$\begin{aligned} B_{i,i}^{yy} &= -c\int_{s_{i-1}}^{s_i} {\varphi_i^{(1)}}^2(s)\cdot ds - c\int_{s_i}^{s_{i+1}} {\varphi_i^{(1)}}^2(s)\cdot ds, \\ &- \frac{1}{U_\infty}\int_{s_{i-1}}^{s_i} {\varphi_i^{(1)}}^2(s)\cdot\left.\frac{dp}{d\alpha}\right|_{\alpha_e}(s)\cdot ds - \frac{1}{U_\infty}\int_{s_i}^{s_{i+1}} {\varphi_i^{(1)}}^2(s)\cdot\left.\frac{dp}{d\alpha}\right|_{\alpha_e}(s)\cdot ds, \end{aligned} \tag{C.20}$$

$$B_{i,i-1}^{yy} = -c\int_{s_{i-1}}^{s_i} \varphi_i^{(1)}(s)\cdot\varphi_{i-1}^{(1)}(s)\cdot ds - \frac{1}{U_\infty}\int_{s_{i-1}}^{s_i} \varphi_i^{(1)}(s)\cdot\varphi_{i-1}^{(1)}(s)\cdot\left.\frac{dp}{d\alpha}\right|_{\alpha_e}(s)\cdot ds, \tag{C.21}$$

$$B_{i,i+1}^{yy} = -c\int_{s_i}^{s_{i+1}} \varphi_i^{(1)}(s)\cdot\varphi_{i+1}^{(1)}(s)\cdot ds - \frac{1}{U_\infty}\int_{s_i}^{s_{i+1}} \varphi_i^{(1)}(s)\cdot\varphi_{i+1}^{(1)}(s)\cdot\left.\frac{dp}{d\alpha}\right|_{\alpha_e}(s)\cdot ds, \tag{C.22}$$

$$B_{N_s,N_s}^{yy} = -c\int_{s_{N_s-1}}^{s_{N_s}} {\varphi_{N_s}^{(1)}}^2(s)\cdot ds - \frac{1}{U_\infty}\int_{s_{N_s-1}}^{s_{N_s}} {\varphi_{N_s}^{(1)}}^2(s)\cdot\left.\frac{dp}{d\alpha}\right|_{\alpha_e}(s)\cdot ds. \tag{C.23}$$

C.4 Stiffness matrix

For the horizontal and lateral sub-matrices $\boldsymbol{K^{xx}}$ and $\boldsymbol{K^{zz}}$ there are only one contribution: the terms associated to the tension of the hose:

$$K_{i,i}^{xx} = K_{i,i}^{zz} = -\int_{s_{i-1}}^{s_i} T_e(s)\cdot {\varphi_i'^{(1)}}^2(s)\cdot ds - \int_{s_i}^{s_{i+1}} T_e(s)\cdot {\varphi_i'^{(1)}}^2(s)\cdot ds, \tag{C.24}$$

$$K_{i,i-1}^{xx} = K_{i,i-1}^{zz} = -\int_{s_{i-1}}^{s_i} T_e(s)\cdot \varphi_i'^{(1)}(s)\cdot \varphi_{i-1}'^{(1)}(s)\cdot ds, \tag{C.25}$$

$$K_{i,i+1}^{xx} = K_{i,i+1}^{zz} = -\int_{s_i}^{s_{i+1}} T_e(s)\cdot \varphi_i'^{(1)}(s)\cdot \varphi_{i+1}'^{(1)}(s)\cdot ds, \tag{C.26}$$

$$K_{N_s,N_s}^{xx} = K_{N_s,N_s}^{zz} - \int_{s_{N_s-1}}^{s_{N_s}} T_e(s)\cdot {\varphi_{N_s}'^{(1)}}^2(s)\cdot ds. \tag{C.27}$$

Regarding the coupling between horizontal and the vertical motion, the stiffness sub-matrix

$\boldsymbol{K^{xy}}$, there is only one source of stiffness: the one due to the aerodynamic terms.

$$K_{i,i}^{xy} = \int_{s_{i-1}}^{s_i} \varphi_i^{(1)^2}(s) \cdot \left.\frac{dq}{d\alpha}\right|_{\alpha_e}(s) \cdot ds + \int_{s_i}^{s_{i+1}} \varphi_i^{(1)^2}(s) \cdot \left.\frac{dq}{d\alpha}\right|_{\alpha_e}(s) \cdot ds, \tag{C.28}$$

$$K_{i,i-1}^{xy} = \int_{s_{i-1}}^{s_i} \varphi_i^{(1)}(s) \cdot \varphi_{i-1}^{(1)}(s) \cdot \left.\frac{dq}{d\alpha}\right|_{\alpha_e}(s) \cdot ds, \tag{C.29}$$

$$K_{i,i+1}^{xy} = \int_{s_i}^{s_{i+1}} \varphi_i^{(1)}(s) \cdot \varphi_{i+1}^{(1)}(s) \cdot \left.\frac{dq}{d\alpha}\right|_{\alpha_e}(s) \cdot ds, \tag{C.30}$$

$$K_{N_s,N_s}^{xy} = \int_{s_{N_s-1}}^{s_{N_s}} \varphi_{N_s}^{(1)^2}(s) \cdot \left.\frac{dq}{d\alpha}\right|_{\alpha_e}(s) \cdot ds. \tag{C.31}$$

Concerning $\boldsymbol{K^{yy}}$, as can be seen in Eq.(A.7) it has three contributions: one associated with the tension of the hose (fifth term of Eq.(A.7)), another associated with the aerodynamic stiffness (third term of Eq.(A.7)) and the last one associated to the bending stiffness (last term of Eq.(A.7)). In order to clarify the different terms, the sub-matrix will be divided as follows:

$$\boldsymbol{K^{yy}} = \boldsymbol{K^{yy,T}} + \boldsymbol{K^{yy,A}} + \boldsymbol{K^{yy,B}}, \tag{C.32}$$

where the super-index T denotes tension, A aerodynamic and B bending. Starting with the tension, analogous expressions to Eqs.(C.24)-(C.27) are achieved:

$$K_{i,i}^{yy,T} = -\int_{s_{i-1}}^{s_i} T_e(s) \cdot \varphi_i^{'(1)^2}(s) \cdot ds - \int_{s_i}^{s_{i+1}} T_e(s) \cdot \varphi_i^{'(1)^2}(s) \cdot ds, \tag{C.33}$$

$$K_{i,i-1}^{yy,T} = -\int_{s_{i-1}}^{s_i} T_e(s) \cdot \varphi_i^{'(1)}(s) \cdot \varphi_{i-1}^{'(1)}(s) \cdot ds, \tag{C.34}$$

$$K_{i,i+1}^{yy,T} = -\int_{s_i}^{s_{i+1}} T_e(s) \cdot \varphi_i^{'(1)}(s) \cdot \varphi_{i+1}^{'(1)}(s) \cdot ds, \tag{C.35}$$

$$K_{N_s,N_s}^{yy,T} = -\int_{s_{N_s-1}}^{s_{N_s}} T_e(s) \cdot \varphi_{N_s}^{'(1)^2}(s) \cdot ds. \tag{C.36}$$

With respect to the aerodynamic stiffness terms, we obtain:

$$K_{i,i}^{yy,A} = -\int_{s_{i-1}}^{s_i} \varphi_i^{(1)^2}(s) \cdot \left.\frac{dp}{d\alpha}\right|_{\alpha_e}(s) \cdot ds - \int_{s_i}^{s_{i+1}} \varphi_i^{(1)^2}(s) \cdot \left.\frac{dp}{d\alpha}\right|_{\alpha_e}(s) \cdot ds, \tag{C.37}$$

$$K_{i,i-1}^{yy,A} = -\int_{s_{i-1}}^{s_i} \varphi_i^{(1)}(s) \cdot \varphi_{i-1}^{(1)}(s) \cdot \left.\frac{dp}{d\alpha}\right|_{\alpha_e}(s) \cdot ds, \tag{C.38}$$

$$K_{i,i+1}^{yy,A} = -\int_{s_i}^{s_{i+1}} \varphi_i^{(1)}(s) \cdot \varphi_{i+1}^{(1)}(s) \cdot \left.\frac{dp}{d\alpha}\right|_{\alpha_e}(s) \cdot ds, \tag{C.39}$$

$$K_{N_s,N_s}^{yy,A} = -\int_{s_{N_s-1}}^{s_{N_s}} \varphi_{N_s}^{(1)^2}(s) \cdot \left.\frac{dp}{d\alpha}\right|_{\alpha_e}(s) \cdot ds. \tag{C.40}$$

Finally, to analyze the bending terms of the stiffness matrix $\boldsymbol{K^{yy,B}}$ it is important to remember that this matrix includes the degrees of freedom of displacement and rotation of each node of

the hose, i.e., it is twice larger than the other two matrices. In order to be able to add them, it is necessary that the three matrices be of the same size. As in the equations of the model without grid fins, the Guyan Reduction will be used. The full development of this approach is presented in Appendix A, and it will not be done again.

C.5 Grid fins aerodynamic forces matrix

From the terms of Eqs.(A.8)-(C.6) it is possible to write the aerodynamic forces of the grid fins as a compact matrix in the following way:

$$\boldsymbol{Q^F} = \begin{bmatrix} \Delta Q^{xx} & \Delta Q^{xy} & \Delta Q^{xz} \\ \Delta Q^{yx} & \Delta Q^{yy} & \Delta Q^{yz} \\ \Delta Q^{zx} & \Delta Q^{zy} & \Delta Q^{zz} \end{bmatrix}. \tag{C.41}$$

It should be noted that, unlike the rest of the matrices presented, the terms of Eq.(C.41) are not other matrices, but scalar values (this matrix is defined only at the hose-fins-drogue junction, not for every node of the hose). The expressions of every term can be obtained from Eqs.(A.8)-(C.6) as:

$$\Delta Q^{xx} = \varphi^{(1)}_{N_s}(s_0) \cdot \varphi'^{(1)}_{N_s}(s_0) \cdot \left(\left.\frac{dz_e}{ds}\right|_{s_0} \cdot q_\infty S_{UGF} \cdot \Delta Q_{Zx} + q_\infty S_{UGF} c_f \cdot \Delta Q_{Mx} \right), \tag{C.42}$$

$$\Delta Q^{xy} = \varphi^{(1)}_{N_s}(s_0) \cdot \varphi'^{(1)}_{N_s}(s_0) \cdot \left.\frac{dz_e}{ds}\right|_{s_0} \cdot q_\infty S_{UGF} \cdot \cdot \Delta Q_{Zy}, \tag{C.43}$$

$$\Delta Q^{xz} = \varphi^{(1)}_{N_s}(s_0) \cdot \varphi'^{(1)}_{N_s}(s_0) \cdot \left(\left.\frac{dz_e}{ds}\right|_{s_0} \cdot q_\infty S_{UGF} \cdot \Delta Q_{Zz} - Z_{F_e} \right), \tag{C.44}$$

$$\Delta Q^{yx} = \varphi^{(1)}_{N_s}(s_0) \cdot \varphi'^{(1)}_{N_s}(s_0) \cdot q_\infty S_{UGF} \cdot \Delta Q_{Lx}, \tag{C.45}$$

$$\Delta Q^{yy} = \varphi^{(1)}_{N_s}(s_0) \cdot \varphi'^{(1)}_{N_s}(s_0) \cdot (q_\infty S_{UGF} \cdot \Delta Q_{Ly} + q_\infty S_{UGF} c_f \cdot \Delta Q_{My}), \tag{C.46}$$

$$\Delta Q^{yz} = \varphi^{(1)}_{N_s}(s_0) \cdot \varphi'^{(1)}_{N_s}(s_0) \cdot q_\infty S_{UGF} \cdot \Delta Q_{Lz}, \tag{C.47}$$

$$\Delta Q^{zx} = \varphi^{(1)}_{N_s}(s_0) \cdot \varphi'^{(1)}_{N_s}(s_0) \cdot q_\infty S_{UGF} \cdot \Delta Q_{Zx}, \tag{C.48}$$

$$\Delta Q^{zy} = \varphi^{(1)}_{N_s}(s_0) \cdot \varphi'^{(1)}_{N_s}(s_0) \cdot q_\infty S_{UGF} \cdot \Delta Q_{Zy}, \tag{C.49}$$

$$\Delta Q^{zz} = \varphi^{(1)}_{N_s}(s_0) \cdot \varphi'^{(1)}_{N_s}(s_0) \cdot (q_\infty S_{UGF} \cdot \Delta Q_{Zz} + q_\infty S_{UGF} c_f \Delta Q_{Mz} + D_{F_e}). \tag{C.50}$$

Bibliography

[Belotserkovsky et al., 1985] Belotserkovsky, S. M., Odnovol, L. A., Safin, Y. Z., Tylenev, A. I., a. F. V. P., and Shitov, V. A. (1985). *Reshetchatye Krylya (Lattice Wings)*. Mashinostroenie, Moscow. 9

[Bertin and Smith, 1979] Bertin, J. and Smith, M. (1979). *Aerodynamics for Engineers*. Prentice Hall. 45

[Bloy and Jouma'a, 1995] Bloy, A. and Jouma'a, M. (1995). Lateral and directional stability and control in air-to-air refueling. *Proceedings of the Institution of Mechanical Engineers*, 209, 4:299–305. 18

[Bloy and Khan, 2001] Bloy, A. and Khan, M. (2001). Modeling of the Receiver Aircraft in Air-To-Air Refueling. *AIAA Journal*, 38, 2:393–396. 18

[Bloy and Khan, 2002] Bloy, A. and Khan, M. (2002). Modelling of the hose and drogue in air-to-air refuelling. *The Aeronautical Journal*, 106:17–26. 15, 16

[Bloy and Trochalidis, 1989] Bloy, A. and Trochalidis, V. (1989). The performance and longitudinal stability and control of large receiver aircraft during air to air refuelling. *The Aeronautical Journal*, 93:367–378. 16, 18

[Bloy and Trochalidis, 1990] Bloy, A. and Trochalidis, V. (1990). The aerodynamic interference between tanker and receiver aircraft during air-to-air refuelling. *The Aeronautical Journal*, 94:165–171. 16, 18

[Brooks and Burkhalter, 1989] Brooks, R. A. and Burkhalter, J. E. (1989). Experimental and analytical analysis of grid fin configurations. *Journal of Aircraft*, 26:885–887. 20, 21

[Burkhalter and Frank, 1996] Burkhalter, J. E. and Frank, H. M. (1996). Grid Fin Aerodynamics for Missile Applications in Subsonic Flow. *Journal of Spacecraft and Rockets*, 33:38–44. 20, 22

[Burkhalter et al., 1995] Burkhalter, J. E., Hartfield, R., and Leleux, T. (1995). Nonlinear Aerodynamic Analysis of Grid Fin Configurations. *Journal of Aircraft*, 32:547–554. 9, 21, 22, 110, 111

[Cai, 2009] Cai, J. (2009). Numerical study on choked flow over grid-fin configurations. *Journal of Spacecraft and Rockets*, 46:949–956. 20, 22

[Cestino et al., 2019] Cestino, E., Frulla, G., Spina, M., Catelani, D., and Linari, M. (2019). Numerical simulation and experimental validation of slender wings flutter behaviour. *Proceedings of the Institution of Mechanical Engineers, Part G: Journal of Aerospace Engineering*, 233:5913–5928. 61

[Chavan et al., 2022] Chavan, B., Bali, S. R., and Kavipriya, J. (2022). Aerodynamic Study of Grid Fin with Sharp Edges using CFD Method Aerodynamic Study of Grid Fin with Sharp Edges using CFD Method. (May). 20, 23

[Crespo da Silva et al., 1991] Crespo da Silva, M., Zaretzky, C., and Hodges, D. H. (1991). Effects of approximations on the static and dynamic response of a cantilever with a tip mass. *International Journal of Solids and Structures*, 27:565–583. 61

[Dai et al., 2018] Dai, X., Quan, Q., Ren, J., and Cai, K.-Y. (2018). Iterative learning control and initial value estimation for probe–drogue autonomous aerial refueling of UAVs. *Aerospace Science and Technology*, 82:583–593. 17, 20

[Dai et al., 2016] Dai, X., Wei, Z., and Quan, Q. (2016). Modeling and simulation of bow wave effect in probe and drogue aerial refueling. *Chinese Journal of Aeronautics*, 29:448–461. 16, 19

[Debiasi, 2020] Debiasi, M. (2020). Forces and moments generated by swept-forward grid fins and planar fins. *Journal of Aircraft*, 57:167–172. 21, 23

[Despeyroux et al., 2015] Despeyroux, A., Hickey, J. P., Desaulnier, R., Luciano, R., Piotrowski, M., and Hamel, N. (2015). Numerical analysis of static and dynamic performances of grid fin controlled missiles. *Journal of Spacecraft and Rockets*, 52:1236–1252. 21, 23

[DeSpirito et al., 2000] DeSpirito, J., Edge, H. L., Weinacht, P., Sahu, J., and Dinavhi, S. P. (2000). CFD analysis of grid fins for maneuvering missiles. *38th Aerospace Sciences Meeting and Exhibit*, (January). 20, 22

[Despirito et al., 2003] Despirito, J., Vaughn, M. E., and Washington, W. D. (2003). Numerical Investigation of Canard-Controlled Missile with Planar and Grid Fins. *Journal of Spacecraft and Rockets*, (40(3)):363–370. 21, 22

[Despirito et al., 2004] Despirito, J., Vaughn, M. E., and Washington, W. D. (2004). *Numerical Investigation of Aerodynamics of Canard-Controlled Missile Using Planar and Grid Tail Fins , Part II : Subsonic and Transonic Flow*. Number March. 20, 22, 105

[Dikbas et al., 2018] Dikbas, E., Baran, O., and Sert, C. (2018). Simplified Numerical Approach for the Prediction of Aerodynamic Forces on Grid Fins. *Journal of Spacecraft and Rockets*, 55. 11, 21, 23, 105, 107, 108, 110

[Dinh et al., 2023] Dinh, V.-S., Dinh, C.-T., and Pham, V.-S. (2023). Numerical study on aerodynamic characteristics of the grid fins with different grid patterns. *Physics of Fluids*, 35(123117). 21, 23

[Dogan et al., 2008] Dogan, A., Lewis, T., and Blake, W. (2008). Flight Data Analysis and Simulation of Wind Effects During Aerial Refueling. *Journal of Aircraft*, 45(6):2036–2048. 19

[Dowell, 2015] Dowell, E. (2015). *A Modern Course in Aeroelasticity, 5th edition*. Springer, Switzerland. 55, 61, 86

[Dupuis and Berner, 2001] Dupuis, A. and Berner, C. (2001). Aerodynamic aspects of a grid finned projectile at subsonic and supersonic velocities. *19th International Symposium of Ballistics, 7–11 May 2001, Interlaken, Switzerland*. 21, 22

[Eichler, 1978] Eichler, J. (1978). Dynamic Analysis of an In-Flight Refueling System. *Journal of Aircraft*, 15:311–318. 15, 16, 18, 47, 52, 54

[Erickson and Richards, 2019] Erickson, A. and Richards, P. (2019). Aeroelastic Modeling of Hose and Drogue Aerial Refueling Systems Including a Hose Reeling Mechanism. *American Institute of Aeronautics and Astronautics Journal*. 16, 20

[Ewins, 1984] Ewins, D. (1984). *Modal Testing: Theory and Practice*. Research studies press LTD. 30, 37

[Fezans and Jann, 2017] Fezans, N. and Jann, T. (2017). Modeling and Simulation for the Automation of Aerial Refueling of Military Transport Aircraft with the Probe-and-Drogue System. (June):1–17. 17, 19

[Finlayson, 1972] Finlayson, B. (1972). *The Method of Weighted Residuals and Variational Principles*. Academic Press. 57

[Fournier, 2001] Fournier, E. (2001). Wind Tunnel Investigation of a High L/D Projectile with Grid Fin and Conventional Planar Control Surfaces. *19th International Symposium of Ballistics, Thun, Switzerland*, pages 511–520. 21, 22

[Fravolini et al., 2004] Fravolini, M. L., Ficola, A., Campa, G., Napolitano, M. R., and Seanor, B. (2004). Modeling and control issues for autonomous aerial refueling for uavs using a probe–drogue refueling system. *Aerospace Science and Technology*, 8(7):611–618. 17, 18

[Fung, 1993] Fung, Y. (1993). *An Introduction to the Theory of Aeroelasticity*. Dover Publications, Inc. New York. 11, 61

[García-Fogeda Núñez and Sanz Andrés, 2014] García-Fogeda Núñez, P. and Sanz Andrés, A. (2014). *Introducción a las Vibraciones*. Ibergarceta Publicaciones. 36, 82, 100

[García-Fogeda and Arévalo, 2015] García-Fogeda, P. and Arévalo, F. (2015). Dynamic stability of a hose-drogue-wing system for aerial refueling. *International Forum on Aeroelasticity and Structural Dynamics, IFASD 2015*, (2015-74). 16

[García-Fogeda et al., 2018] García-Fogeda, P., Esteban Molina, J., and Arévalo, F. (2018). Dynamic Response of Aerial Refueling Hose-Drogue System with Automated Control Surfaces. *Journal of Aerospace Engineering*, 31(6): 04018110. 7, 8, 16, 20, 50, 51, 52, 53, 54, 62

[Gates and McCarthy, 2000] Gates, W. and McCarthy, M. (2000). United states marine corps aerial refueling requirements analysis. *2000 Winter Simulation Conference Proceedings*, 1:1075–1081. 18

[Goyal and Perkins, 2007] Goyal, S. and Perkins, N. (2007). Modeling of Cables with High and Low Tension Zones using a Hybrid Rod-Catenary Formulation. *Proceedings of Sixth International Symposium on Cable Dynamics*, 2125. 16, 18, 50, 53

[Guyan, 1965] Guyan, R. (1965). Reduction of Stiffness and Mass Matrices. *AIAA Journal*, 3:380–387. 177

[Hansen et al., 2004] Hansen, J., Murray, J., and Campos, N. (2004). The NASA Dryden AAR Project: A Flight Test Approach to an Aerial Refueling System. *AIAA Atmospheric Flight Mechanics Conference and Exhibit*, (4939). 17, 18

[Hao and Quan, 2021] Hao, L. and Quan, Q. (2021). Autonomous Aerial Refueling of Multiple UAVs: An Efficient Rendezvous Scheduling Approach. *Proceeding - 2021 China Automation Congress, CAC 2021*, pages 7463–7468. 17, 20

[He et al., 2017] He, Q., Wang, H., Chen, Y., Xu, M., and Jin, W. (2017). Command filtered backstepping sliding mode control for the hose whipping phenomenon in aerial refueling. *Aerospace Science and Technology*, 67:495–505. 19

[Hoerner, 1965] Hoerner, S. (1965). *Fluid-dynamic drag: practical information on aerodynamic drag and hydrodynamic resistance*. Hoerner, S.F., Bakersfield, CA, USA. 47, 48

[Jackson et al., 2007] Jackson, D., Tyler, C., and Blake, W. (2007). Computational Analysis of Air-to-Air Refueling. *25th AIAA Applied Aerodynamics Conference, Miami, Florida*, (4289). 17, 18

[Kamman and Huston, 1985] Kamman, J. and Huston, R. (1985). Modelling of submerged cable dynamics. *Journal of Computers and Structures*, 20:623–629. 18

[Khanafseh and Pervan, 2007] Khanafseh, S. and Pervan, B. (2007). Autonomous Airborne Refueling of Unmanned Air Vehicles Using the Global Positioning System. *Journal of Aircraft*, 44(5):1670–1682. 18

[Kiyak et al., 2014] Kiyak, Z. J., Hartfield, R. J., and Ledlow, T. W. (2014). Missile trajectory optimization using a modified ant colony algorithm. *IEEE Aerospace Conference Proceedings*. 21, 23

[Koh et al., 1999] Koh, C., Zhang, Y., and Quek, S. (1999). Low-Tension Cable Dynamics: Numerical and Experimental Studies. *Journal of Engineering Mechanics*, 125(3):347–354. 18

[Kreiselmaier and Laschka, 2000] Kreiselmaier, E. and Laschka, B. (2000). Small disturbance Euler equations efficient and accurate tool for unsteady load prediction. *Journal of Aircraft*, 37(5):770–778. 62

[Kuk and Ro, 2013] Kuk, T. and Ro, K. (2013). Design, test and evaluation of an actively stabilized drogue refueling system. *The Aeronautical Journal*, 117:1103–1118. 8, 16, 19

[Ledlow and Burkhalter, 2015] Ledlow, T. W. and Burkhalter, J. (2015). Integration of Grid Fins for the Optimal Design of Missile Systems. *AIAA Atmospheric Flight Mechanics Conference, Kissimmee, Florida*, (AIAA 2015-1017). 21, 23

[Liggieri, 2012] Liggieri, A. (2012). Refuelling tanker aerodynamics and hose characteristics. *PhD Thesis, Cranfield University*. 52

[Lin and Huang, 2003] Lin, H. and Huang, J. C. (2003). Navier – Stokes Computations for Body / Cruciform Grid Fin Con guration Introduction. *Journal of Spacecraft and Rockets*, 40. 22

[Meng and Chen, 2012] Meng, D. and Chen, L. (2012). Nonlinear free vibrations and vortex-induced vibrations of fluid-conveying steel catenary riser. *Applied Ocean Research*, 34:52–67. 17, 19

[Miller and Washington, 1994] Miller, M. S. and Washington, W. D. (1994). An experimental investigation of grid fin drag reduction techniques. *AIAA Journal*, 94-1914-CP. 20, 22

[Munawar, 2010] Munawar, S. (2010). Analysis of grid fins as efficient control surface in comparison to conventional planar fins. *27th Congress of the International Council of the Aeronautical Sciences 2010, ICAS 2010*, 3:1732–1737. 21, 22

[Nawrocki, 1996] Nawrocki, D. (1996). *Investigation of aerodynamic alterations for improving the KC-135 boom performance during aerial refueling*. PhD thesis. 2

[Ng and Tan, 2009] Ng, H. and Tan, E. (2009). Simulation of fuel behaviour during aircraft in-flight refueling. *Aircraft Engineering and Aerospace Technology: An International Journal*, 81/2:99–105. 17, 19

[Patil et al., 2001] Patil, M. J., Hodges, D. H., and Cesnik, C. E. (2001). Nonlinear aeroelasticity and flight dynamics of high-altitude long-endurance aircraft. *Journal of Aircraft*, 38:88–94. 61

[Poulin and Larsen, 2007] Poulin, S. and Larsen, A. (2007). Drag loading of circular cylinders inclined in the along-wind direction. *Journal of Wind Engineering and Industrial Aerodynamics*, 95:1350–1363. 47, 48

[Price et al., 2014] Price, M., Morscheck, F., Korn, B., Early, J. M., and McRoberts, R. (2014). Tanker Mission Implication on a Civil Aerial Refuelling Transport System's Benefit Evaluation. *Journal of Aircraft*, 52:320–328. 17, 19

[Purdy, 2010] Purdy, S. (2010). Probe and Drogue Aerial Refueling Systems. *Encyclopedia of Aerospace Engineering*. 17, 19

[Ren and Quan, 2024] Ren, J. and Quan, Q. (2024). Progress in Modeling and Control of Probe and Drogue Autonomous Aerial Refueling. *Chinese Journal of Aeronautics*, 37(5):6–26. 4, 20

[Reynier et al., 2006] Reynier, P., , Longo, J. M., and Schulein, E. (2006). Simulation of Missiles with Grid Fins using an Actuator Disc. *Journal of Spacecraft and Rockets*, 43(1). 22

[Reynier et al., 2004] Reynier, P., Reisch, U., Longo, J. M., and Radespiel, R. (2004). Flow predictions around a missile with lattice wings using the actuator disc concept. *Aerospace Science and Technology*, 8:377–388. 20, 22

[Ribbens et al., 2012] Ribbens, W., Saggio, F., Wierenga, R., and Feldmann, M. (2012). Dynamic Modeling of an Aerial Refueling Hose & Drogue System. *25th AIAA Applied Aerodynamics Conference, Miami, FL, USA*, (3802). 16, 19, 50, 53

[Ro and Kamman, 2009] Ro, K. and Kamman, J. (2009). Modeling and Simulation of Hose-Paradrogue Aerial Refueling Systems. *Journal of Guidance, Control and Dynamics*, 33:53–63. 8, 16, 19

[Ro et al., 2010] Ro, K., Kuk, T., and Kamman, J. (2010). Active Control of Aerial Refueling Hose-Drogue Systems. *AIAA Guidance, Navigation and Control Conference, Toronto, ON, Canada*, (8400). 16

[Rodden, 2011] Rodden, W. (2011). *Theoretical and Computational Aeroelasticity*. Crest Publishing. 141

[Romeo et al., 2006] Romeo, G., Frulla, G., Cestino, E., Marzocca, P., and Tuzcu, I. (2006). Non-linear aeroelastic modeling and experiments of flexible wings. *Collection of Technical Papers - AIAA/ASME/ASCE/AHS/ASC Structures, Structural Dynamics and Materials Conference*, 10:7063–7077. 61

[Roskam and Edward Lan, 1997] Roskam, J. and Edward Lan, C. (1997). *Airplane Aerodynamics and Performance*. Design, Analysis and Research Corporation. 48

[Sahin, 2010] Sahin, B. (2010). *Analysis of wake vortices of medium range twinpropeller military cargo aircraft using statistically designed experiments*. PhD thesis. 7, 6

[Sarpkaya, 2004] Sarpkaya, T. (2004). A critical review of the intrinsic nature of vortex-induced vibrations. *Journal of Fluids and Structures*, 19:389–447. 55, 84

[Shabana, 1991] Shabana, A. (1991). *Theory of Vibrations, Vol. II: Discrete and Continuous Systems)*. Springer-Verlag. 64

[Shannon, 1949] Shannon, C. (1949). Communication in the Presence of Noise. *Proceedings of the IRE*, 37(1):10–21. 65

[Smith, 1998] Smith, R. (1998). *Seventy-Five Years of Inflight Refueling)*. Air Force History and Museums Program. 2

[Styuart et al., 2011] Styuart, A., Yamashiro, H., Stirling, R., Mor, M., and Gaston, R. (2011). Numerical Simulation of Hose Whip Phenomenon in Aerial Refueling. *AIAA Atmospheric Flight Mechanics Conference, Minneapolis, MN, USA*, (6211). 19

[Tang and Dowell, 2001] Tang, D. and Dowell, E. H. (2001). Experimental and theoretical study on aeroelastic response of high-aspect-ratio wings. *AIAA Journal*, 39:1430–1441. 61

[Theerthamalai, 2007] Theerthamalai, P. (2007). Aerodynamic Characterization of Grid Fins at Subsonic Speeds. *Journal of Aircraft*, 44(2):694–697. 21, 22

[Theerthamalai and Nagarathinam, 2006] Theerthamalai, P. and Nagarathinam, M. (2006). Aerodynamic Analysis of Grid-Fin Configurations. *Journal of Spacecraft and Rockets*, 43. 20, 22

[Theodorsen, 1934] Theodorsen, T. (1934). General Theory of Aerodynamic Instability and the Mechanism of Flutter. *National Advisory Committee for Aeronautics Reports*, (496). 55

[Thomas et al., 2014] Thomas, P., Bhandari, U., Bullock, S., Richardson, T., and du Bois, J. (2014). Advances in air to air refueling. *Progress in Aerospace Sciences*, 71:14–35. 10, 1, 3, 6, 7, 16, 17, 19

[Timoshenko, 1945] Timoshenko, S. (1945). *Theory of Structures*. McGraw Hill. 39, 41

[Torenbeek, 1982] Torenbeek, E. (1982). *Synthesis of Subsonic Airplane Design*. Springer. 49

[Tripathi et al., 2019] Tripathi, M., Sucheendran, M. M., and Misra, A. (2019). Flow field characterization and visualization of grid fin subsonic flow. *Journal of Fluids Engineering, Transactions of the ASME*, 141. 21, 23

[Tripathi et al., 2020] Tripathi, M., Sucheendran, M. M., and Misra, A. (2020). Experimental analysis of cell pattern on grid fin aerodynamics in subsonic flow. *Proceedings of the Institution of Mechanical Engineers, Part G: Journal of Aerospace Engineering*, 234(3):537–562. 21, 23

[Vachon and Ray, 2004] Vachon, M. and Ray, R. (2004). Calculated Drag of an Aerial Refueling Assembly Through Airplane Performance Analysis. *42nd AIAA Aerospace Sciences Meeting and Exhibit, Reno, Nevada*, (0381). 17, 18

[Vassberg et al., 2003] Vassberg, J., Yeh, D., Blair, A., and Evert, J. (2003). Numerical Simulations of KC-10 Wing-Mount Aerial Refueling Hose-Drogue Dynamics with a Reel Take-Up System. *21th AIAA Applied Aerodynamics Conference, Orlando, FL, USA*, (3508). 8, 16, 18

[Vess et al., 2018] Vess, R., Koehler, E., Knoblauch, E., Boothe, K. E., and McLaughlin, S. (2018). An Introduction to the Navy's Physics Based Model of the Hose and Drogue Refueling System - Design and Validation. (January):1–13. 20

[Wang et al., 2014] Wang, H., Dong, X., Xue, J., and Liu, J. (2014). Dynamic modeling of a hose-drogue aerial refueling system and integral sliding mode backstepping control for the hose whipping phenomenon. *Chinese Journal of Aeronautics*, 27:930–946. 19

[Wang et al., 2017] Wang, X., Dong, X., Kong, X., Li, J., and Zhang, B. (2017). Drogue detection for autonomous aerial refueling based on convolutional neural networks. *Chinese Journal of Aeronautics*, 30(1):380–390. 17, 20

[Washingtion and Miller, 1993] Washingtion, W. and Miller, M. (1993). Grid fins - A new concept for missile stability and control. *31th Aerospace Sciences Meeting and Exhibit*, (93-0035). 9, 20, 21

[Washington and Miller, 1998] Washington, W. and Miller, M. (1998). Experimental Investigations of Grid Fin Aerodynamics: A Synopsis of nine wind tunnel and three flight tests. *RTO AVT Symposium on Missile Aerodynamics*. 9, 110, 111

[Weinerfelt and Nilsson, 2010] Weinerfelt, P. and Nilsson, A. (2010). A dynamic real time model for Air-To-Air refueling. *27th Congress of the International Council of the Aeronautical Sciences 2010, ICAS 2010*, 4:3348–3354. 19

[Williamson et al., 2010] Williamson, W. R., Reed, E., Glenn, G. J., Stecko, S. M., Musgrave, J., and Takacs, J. M. (2010). Controllable Drogue for Automated Aerial Refueling. *Journal of Aircraft*, 47: No.2:515–527. 8, 16, 19

[Wu et al., 2003] Wu, Q., Takahashi, K., and Nakamura, S. (2003). Non-linear vibrations of cables considering loosening. *Journal of Sound and Vibration*, 261:385–402. 16, 18

[Xun and Xinguo, 2013] Xun, S. and Xinguo, Z. (2013). The UAV Autonomous Aerial Refueling Controller Based on Predictor Auto Disturbances Rejection Method. *Applied Mechanics and Materials*, 380–384:347–352. 17, 19

[Yamamoto et al., 2004] Yamamoto, C. T., Meneghini, J. R., Saltara, F., Fregonesi, R. A., and Ferrari, J. A. (2004). Numerical simulations of vortex-induced vibration on flexible cylinders. *Journal of Fluids and Structures*, 19:467–489. 18

[Yamashiro et al., 2011] Yamashiro, H., Gaston, R., Stirling, R., Mor, M., and Styuart, A. (2011). Numerical Simulation of Hose Whip Phenomenon in Aerial Refueling. *AIAA Atmospheric Flight Mechanics Conference, 2011*, (AIAA 2011-6211). 16, 63

[Ye et al., 2022] Ye, K., Zhang, Y., Chen, Z., and Ye, Z. (2022). Numerical Investigation of Aeroelastic Characteristics of Grid Fin. *AIAA Journal*, 60:3107–3121. 21, 23

[Yuan et al., 2017] Yuan, D.and Zhao, T., Hou, X., Cheng, X., Qu, Y., Yan, J., and Xing, X. (2017). Study on the controllability of a drogue for hose-drogue aerial refueling system. *2017 11th Asian Control Conference (ASCC)*, pages 2592–2595. 8, 19

[Zhang et al., 2012] Zhang, Z., Yang, S., and Chen, P. C. (2012). Linearized Euler solver for rapid frequency-domain aeroelastic analysis. *Journal of Aircraft*, 49:922–932. 62

[Zhu, 2008] Zhu, Z. (2008). Dynamic stability analysis of aerial refueling hose/drogue system by Finite Element Method. *ASME 2008 International Mechanical Engineering Congress and Exposition, Boston, MA, USA*, (67103). 5, 15, 17, 19

[Zhu and Meguid, 2006] Zhu, Z. and Meguid, S. (2006). Elastodynamic Analysis of Aerial Refueling Hose using Curved Beam Element. *American Institute of Aeronautics and Astronautics Journal*, 44(6). 17, 63

[Zhu and Meguid, 2007] Zhu, Z. and Meguid, S. (2007). Modeling and simulation of aerial refueling by finite element method. *International Journal of Solids and Structures*, 44:8057–8073. 17, 18, 54, 78